THE UNIVERSITY *of* EDINBURGH

Exploring Thiophene Oligomers and Ruthenium(II) Complexes for their use in Dye-Sensitised Solar Cells

Yue Hu

Thesis submitted for the degree of PhD

The University of Edinburgh

2015

Declaration

I hereby declare that this thesis is entirely my own work and composed by myself except where clearly indicated in the acknowledgements, references or text. This work has not been submitted in whole or part for any other degree, diploma or professional qualification.

Yue Hu

Acknowledgement

I would like to take this opportunity to thank so many people for helping me get through my PhD.

Firstly and foremost, my supervisor Prof. Neil Robertson deserves much praise for his support and guidance throughout this past three years. I am lucky to have a supervisor that suits me so much for giving me a lot of freedom and support whenever I need. I've enjoyed my time working on solar cells and coordinating the Solar Spark outreach project.

I would like to express my gratitude to Prof. Michael Graetzel, Dr. Shaik Mohammed Zakeeruddin and Dr. Antonio Abate for allowing me to carry out research in EPFL and made me feel welcome. I thoroughly enjoyed all the discussions and the home-made pasta. I would also like to acknowledge my friend Xiaoyu Zhang, who provide me accommodation and keep me company.

A special thanks to Dr. Irene Sanchez-Molina and Dr. Saif A. Haque for measuring the emission of Ru complexes and time-correlated single photon counting measurements, also for welcoming me to Imperial College to measure the transient absorption spectroscopy.

I would like to thank Prof. Jianli Hua and Prof. Yun Chi for offering me the opportunity to collaborate with them and encouraging me all the time.

A special mention needs to go to Dr. Aruna Ivaturi from our group and Dr. Yiming Cao from EPFL for making liquid dye-sensitised solar cells on my dyes.

Thanks to Rosinda for being my best friend over the three years, Rosinda's mum for the yummy super spicy Mexican food and her thousands of cousins for celebrating my 25th birthday in Mexico City. Also thanks to Qing and Xiaocheng, for hotpot and gossip from time to time. Thanks Jacqueline and her family for the best Christmas on

Rhode Island. I have never received so many Christmas gifts in my life. Thanks Ke for travelling around with me, taking loots of nice pictures and cooking delicious food. Thanks Miquel, Farmin, Sara and Yoko for my first alcohol in Edinburgh and hanging out from time to time. Thanks Madeleine for the 'list of things you have to do in Edinburgh' and lots of fun together doing the Solar Spark. Thanks to Akash for all the precious suggestions and encouragements and holding party every night. Also thanks to Yeyuan, Han, Ziyue, Xiao, Jiabao, Xing, Yunning, Xiaoyun, Wei, Yutong, Jing for having fun together and giving me place to stay all over the world.

Finally I would like to thank my country for awarding me the CSC scholarship and my family for continual support and love.

Abstract

Despite offering relatively high conversion efficiencies, dye-sensitised solar cells using liquid electrolytes containing either I^-/I_3^- redox couple or Co^{2+}/Co^{3+} redox couple suffer from durability problems, such as electrode corrosion and electrolyte leakage. Replacements for liquid electrolytes have been extensively studied, but the efficiencies of the resulting devices remain low. One of the factors that limit the efficiency is the sensitising dye. Large sized hole-transport material results in poor pore-filling and thus leads to a fast back electron recombination that reduces the effective electron diffusion length to few micrometeres. The optimal TiO_2 layer thickness (2 μm) for maximal power conversion in solid-state dye-sensitised solar cell is much smaller than the 6-10 μm layer thickness required for quantitative light absorption by many dye molecules. Thus, dyes that can absorb in both visible and near-IR region with high extinction coefficient are needed. In order to achieve this, novel oligomers and ruthenium (II) complexes are designed, synthesized and studied as sensitisers for both liquid state and solid state dye-sensitised solar cells in this thesis.

Series of 'donor-free' dyes including oligo(3-hexylthiophene) (oligo-3HT) (Chapter 3) and oligo(4,4-dihexyl-4H-cyclopenta[1,2-b:5,4-b']dithiophene) (oligo-CPDTs) (Chapter 4) functionalized with cyanoacrylic end groups are easily synthesized using cross-coupling. They were fully characterised through electrochemical, spectroscopic and computational techniques, showing versatile colour-tuning, as well as outstanding absorption coefficients up to 75000 $M^{-1}cm^{-1}$. Liquid and solid-state DSSCs device performances are studied and discussed in terms of the dye structures. These dyes are effective sensitisers for liquid-state and solid-state dye-sensitised solar cells, although they do not contain a typical donor group, thus open a new strategy of designing dyes in the future.

New dyes containing different azo ligands as an additional chromophore moiety to enhance light harvesting of Ru complexes (Chapter 5) have been prepared using a protection/deprotection strategy that allows for convenient purification. The

absorption spectrum of the dyes showed an enhanced light harvesting compared to the N719 dye that lacks the azo ligand and electrochemical study also showed properties suitable for application as sensitisers in DSSCs. Following hydrolysis, the complexes were investigated in DSSCs, with performance investigated using I-V measurements. Poor performance was observed and we attribute this as mostly likely due to poor charge injection due to short excited-state lifetime. Although the application of these current dyes in DSSCs is not feasible due to their poor performance, this study allowed us to determine the positions of the HOMO and LUMO orbitals and correlate it to the π-acidity of the dyes.

Contents

Abbreviations

^{1}H NMR	Proton Nuclear Magnetic Resonance
AM1.5G	Air Mass 1.5 Global
azpy	2-Phenylazopyridine
B3LYP	Becke's three parameter exchange functional with the Lee-Yang-Parr
B3PW91	Becke's three parameter exchange functional with the Perdew Wang
bipy	Bipyridine
BMII	1-butyl-3-methylimidazolium iodide
COSY	Correlated Spectroscopy
CV	cyclic voltammetry
dcbpy	4, 4'-dicarboxylic acid-2,2'-bipyridine
DCM	Dichloromethane
DFT	Density Functional Theory
dmazpy	4-(2-pyridylazo)-N,N-dimethylaniline
DMF	Dimethylformamide
DMSO	Dimethylsulfoxide
DPV	Differential Pulse Voltammetry
DSSC	Dye-Sensitized Solar Cells
ESI-MS	Electrospray Ionnisation Mass Spectrometry
FF	Fill Factor
FTO	Fluorine Doped Tin Oxide
GuNCS	guanidinium thiocyanate
HOMO	Highest Occupied Molecular Orbital
$^{i}bu_2$dcbpy	bis(2-methylpropyl)-2,2'-bipyridine-4,4'-dicarboxylate
ILCT	intra-ligand charge transfer
IPCE	Incident Photon-to-current Conversion Efficiency
ISC	Intersystem Crossing
J_{SC}	Short Circuit Current Density
J-V	Photocurrent density-Voltage
LANL2DZ	Los Alamos National Laboratory 2-double-z
LC	ligand-centered
LLCT	ligand-to-ligand charge transfer
LUMO	Lowest Unoccupied Molecular Orbital
MeOH	Methanol
MLCT	Metal-to-ligand charge transfer

NCS	Thiocyanate
NOESY	Nuclear Overhauser Effect Spectroscopy
pai	[4-(N,N-dimethylamino)benzeneazo]imidazole
pai-Me	1-Methyl-2-[4-(N,N-dimethylamino)benzeneazo]imidazole
PCM	Polarisable Continuum Model
PES	Potential Energy Surface
ppm	Parts Per Million
TBAOH	Tetrabutylammonium hydroxide
TBP	4-*tert*-butylpyridine
TD-DFT	Time-dependent DFT calculations
V_{OC}	Open Circuit Voltage

Structures

Oligo(3-hexylthiophene) dyes

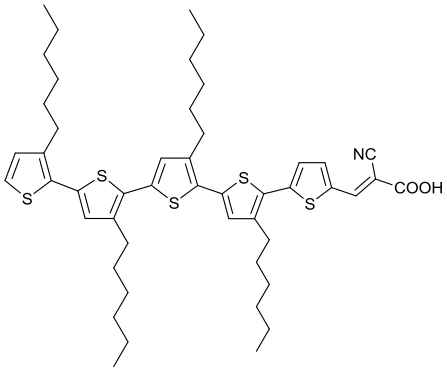

5T

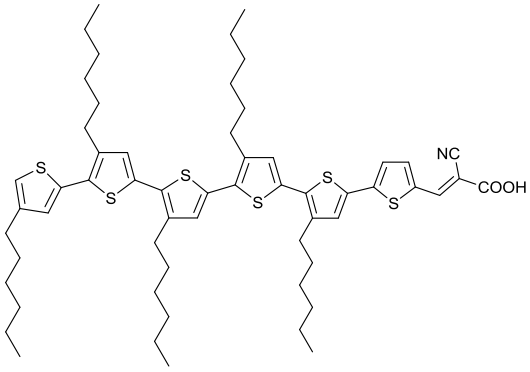

6T

Oligo(4,4-dihexyl-4H-cyclopenta[1,2-b:5,4-b']dithiophene) dyes

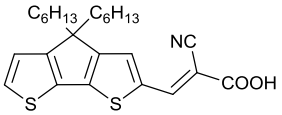

trans-CPDT-1

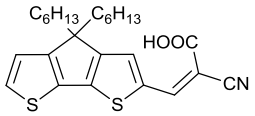

cis-CPDT-1

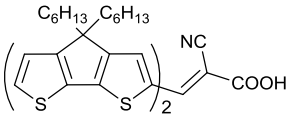

CPDT-2

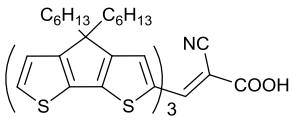

CPDT-3

Ruthenium (II) dyes

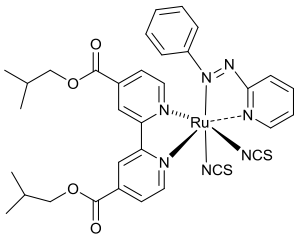

HY-1

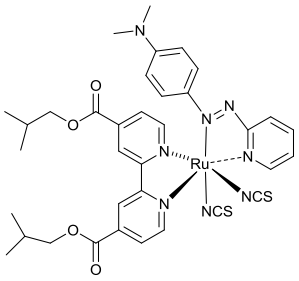

HY-2

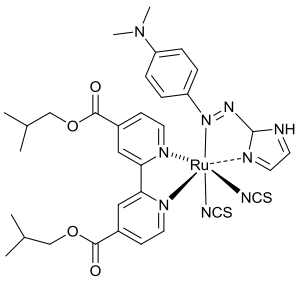

HY-3a

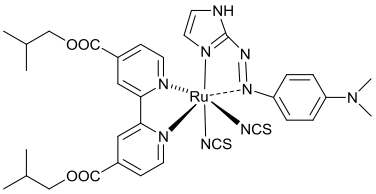

HY-3b

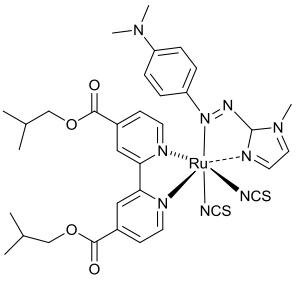

HY-4

Chapter 1 Introduction

1 Introduction

There is no more urgent and serious challenge facing human beings today than meeting the growing global energy demand. Until now, the most widely used energy source is fossil fuel including the solid state coal, the liquid state petroleum and the gaseous state natural gas. Ever since fossil fuels powered the Industrial Revolution in the 18th and 19th century, this energy has dominated the world and rapidly realized a twentyfold increase in use. However, the environmental impact of fossil fuel is often negative. The use of fossil fuel without restraint has already caused a lot of environmental problems such as global warming and climate change, ozone depletion and acid rain.[1] Fortunately, people have started to see this and recent years have witnessed a fundamental change in the way governments approach energy-related environmental issues.[2] The common consensus to solve this problem is to develop sustainable energy and the new sustainable energy technologies need to be improved in six important fields, namely, higher efficiency, lower cost, less resources use, easier design and analysis, better energy security and less environmental impact. The total world energy consumption by source for 2013 is shown in Figure 1.1. Despite a vast proportion of energy demand coming from fossil fuel resources, the proportion of renewable energy is increasing.

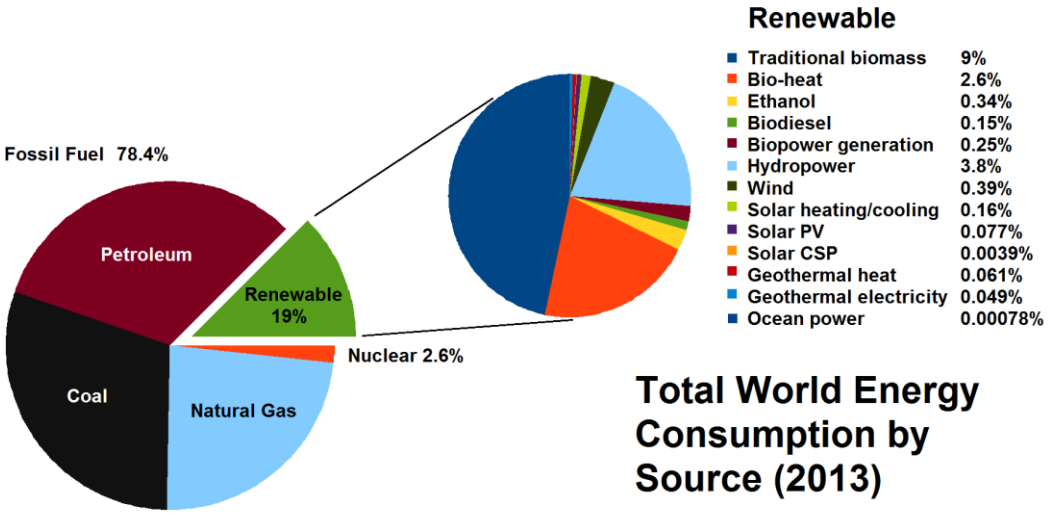

Figure 1.1 Total world energy consumption by source for 2013. [3]

The mainstream renewable technologies include wind power, hydropower, solar energy, biomass, biofuel, geothermal energy, oceanogenic power and so on. Among these, solar energy displays the largest potential for the huge amount of energy the sun radiates.[4] Even if a small fraction of sunlight could be converted to alternative and usable energy forms, the energy crisis could be vastly improved. So this makes harnessing of solar energy a very attractive proposition.

2 Solar techniques

Chemists have been interested for a long time in collecting sunlight, either to drive chemical transformations or to convert sunlight into electricity. Devices that convert sunlight into electricity are called photovoltaic solar cells.[5] The development of solar cell technology began with the 1839 research of Becquerel.[6] A photovoltaic effect was observed when he put a solid electrode in an electrolyte solution with light shining upon the electrode. The first solar cell was built around 1883 by Charles Fritts, who used junctions formed by coating selenium with an extremely thin layer of gold. The photoelectric effect was explained by Albert Einstein in 1905 for which he was awarded the Nobel Prize.[7]

Photovoltaic solar cells can be grouped into three major categories based on their material, maximum conversion efficiency and the associated cost of photovoltaic power. The first generation solar cells are based on silicon wafers that demonstrate a performance of about 15%~20%. The second generation solar cells are called thin film solar cells, which are based on amorphous silicon, CIGS and CdTe. The third generation solar cells cover all new techniques, including organic photovoltaics, multi-junction solar cells, perovskite solar cells and so on. Regardless of all the different materials and techniques that different solar cells use, the principles remain the same and includes three basic steps: 1) The absorption of light; 2) The separation of electrons and holes; 3) The extraction of electrons and holes to an external circuit.

2.1 Silicon solar cells

The silicon solar cell was invented by Russell Ohl in 1941 and the first practical device was made at Bell Laboratories in 1954. It was a crystalline silicon solar cell

capable of 6% power conversion efficiency.[8] Silicon solar cells achieve charge separation by generating an internal electric field across a p-n junction. (Figure 1.2)

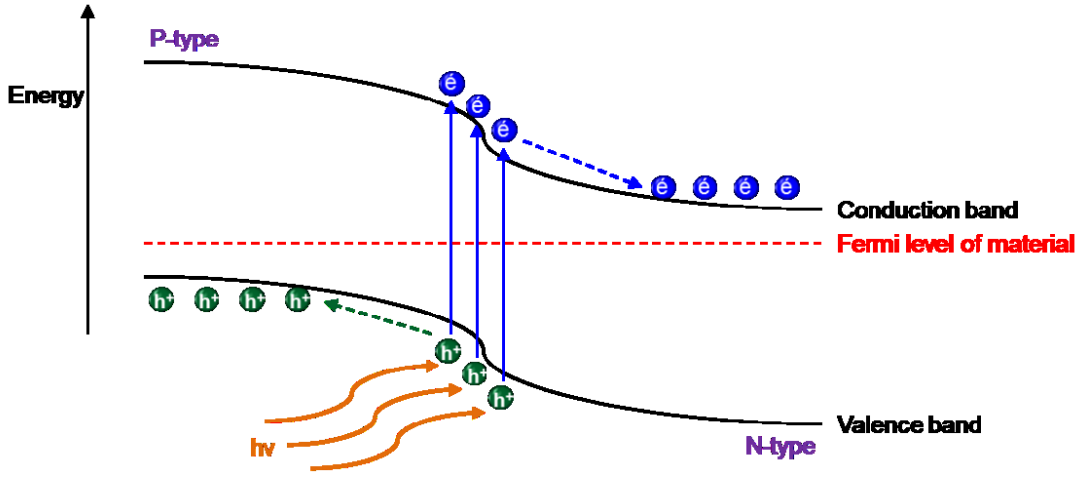

Figure 1.2 Charge separation across a p-n junction. [9]

The current solar cell market is dominated by crystalline silicon photovoltaic cells. [10] The record efficiency of this kind of solar cell was achieved as 25.6% [11] in 2014. The theoretical limiting power conversion efficiency of a single-junction solar cell is 33.7%, noted as the Shockley-Queisser limit in 1961.[12] This limit was first calculated by William Shockley and Hans Queisser by examining the amount of electricity that is extracted per photon of the incoming sunlight. Three main factors were considered in the calculation, namely, blackbody radiation, radiative recombination and spectrum losses. It only applies to cells with a single p-n junction. One of the main problems with the cell is the use of expensive pure silicon which leads to a high production cost. The fact that a relatively thick layer of silicon has to be used to absorb enough sunlight, due to the indirect band gap of silicon, also increases the cost and makes silicon solar cells heavy and rigid. This limits their application, especially in the portable power market. The standard blue colour also limits their incorporation into architecture.

2.2 Thin-film solar cells

Thin film solar cells have a reduced manufacturing cost with a relatively high efficiency. Cadmium telluride (CdTe) and copper indium gallium diselenide (CIGS)

are commonly used as the material in thin film solar cells. They work in a generally similar manner to silicon solar cells. However, both CdTe and CIGS can absorb light better than silicon, which enables the use of a thinner film. The highest efficiency of CIGS solar cell has reached 21.7% in 2015.[13] The main limitation of thin-film solar cells is the concern about the future availability due to the low natural abundance of indium, tellurium and selenium, and the toxicity of cadmium is also a problem. Most recently, copper zinc tin sulphide (CZTS) solar cell has emerged as a less-toxic alternative, which achieved 12.6% efficiency in 2014.[14]

2.3 Tandem solar cells

Tandem cells, or multijunction photovoltaic cells are able to outperform the Shockley-Queisser limit. By using a stack of different solar cells optimised to target a certain region of solar spectrum, the problem of spectrum losses is reduced. To fully use sunlight, a high-bandgap (blue) solar cell sits on top, absorbing high frequency light and transmitting the rest. $InGaP_2$ with a bandgap of 1.8-1.9eV is usually chosen as the material for the top sub-cell. Below that is a lower-bandgap (yellow) solar cell made of GaAs (the bandgap is 1.4eV) that absorbs some of the lower frequency light. Finally, a lowest-bandgap (red) solar cell made of germanium (the bandgap is 0.67eV) sits at the bottom. In addition, light concentrator systems are often integrated with the tandem solar cells to further boost the efficiency thus reducing the cost/efficiency ratio. In 2011, Solar Junction [15] has achieved an efficiency of 43.5% using a $5.5mm^2$ multijunction cell with light concentrated with mirrors.

Despite the high efficiency, the complex structure and the high price of tandem solar cells limit their applications. They are currently utilized in the space where high efficiency is the greatest priority compared to any other factors.

2.4 OPV & DSSC

One area of great promise in recent years is the organic photovoltaic solar cell (OPV). This technology is receiving enormous research attention from scientists with different background due to the possibility of low-cost production and fabrication on

flexible substrates. Dye-sensitised solar cells are often included in the OPV family because of the organic nature of at least part of their constituents. Over 20 years have passed since the first high efficiency DSSC was reported by Michael Grätzel and Brian O'Regan in 1991.[16] This genius work offers fresh challenges and hope for solar energy research. The DSSC is the only photovoltaic device that mimics natural photosynthesis which separates the process of light-harvesting and charge carrier transport. The main advantages of this solar cell are the ease of manufacture, non-toxicity of the materials, and the possibility to fabricate solar cells on any substrates. However, the DSSCs still have limitations such as the comparatively low efficiency (the record certified efficiency is 11.4% [17]) compared with silicon solar cells and poor long-term stability, thus, research is still needed.

2.5 Perovskite solar cells

Perovskite solar cells have recently emerged as low-cost, high-efficiency solar cells. The efficiency of these solar cells has increased dramatically in the last few years, which has revolutionized the solar cell research field. In 2009, Miyasaka et al. used organometallic perovskite $CH_3NH_3PbI_3$ as a sensitiser in liquid electrolyte dye-sensitised solar cells and achieved an efficiency of 3.8%. [18] Three years later, Park and Gratzel[19] replaced the liquid electrolyte with a solid-state hole transport material spiro-OMeTAD and the efficiency was increased to 9.7%. The efficiency was rapidly increased to 19.3% in 2014 by Yang. [20] On the other hand, Snaith [21] replaced the mesoporous titanium dioxide with an insulator (Al_2O_3) and achieved an efficiency of 15.4% using vapor deposition. This work questioned the principle of perovskite solar cells and suggested a different mechanism of operation from dye-sensitised solar cells. In 2015, the record certified efficiency of perovskite reached 21.02%. [22]

Other developments in this field include optimizing hole transport materials [23-25], tuning perovskite properties through chemical composition [26] and so on. The challenges of making perovskite solar cells commercial include the environmental friendly issues, photo-stabilities and how to scale up. In order to achieve this, encapsulation technology and materials with humidity-resistance and photo-stability

should be developed.[27] Substitution of other elements for Pb to make the solar cells environmental friendly is also a challenge.

3 Structure and mechanism of DSSC

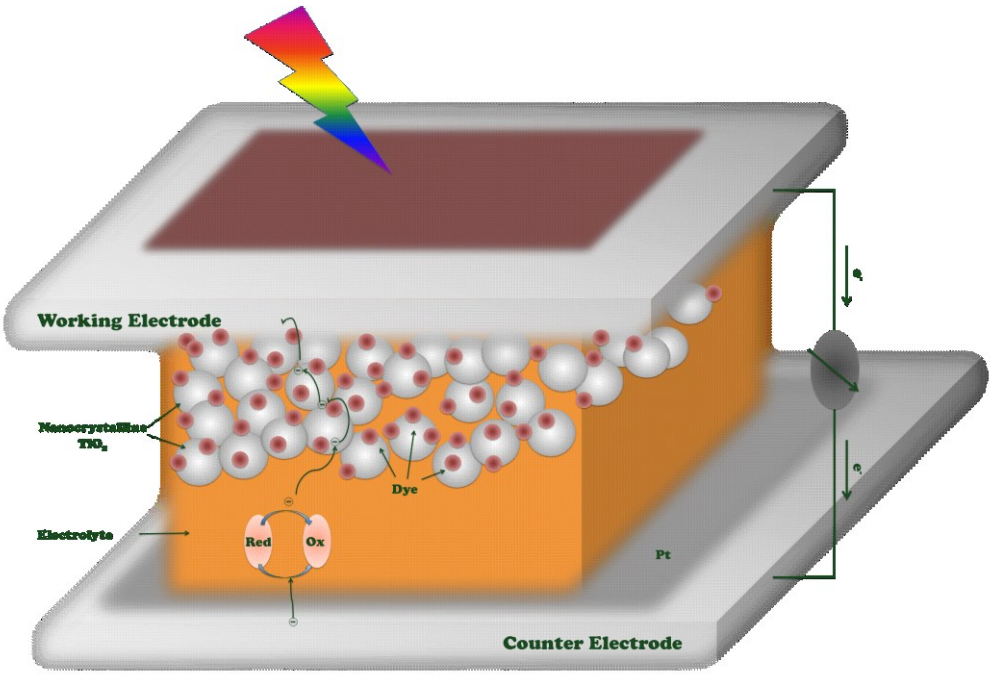

Figure 1.3 Schematic structure of a DSSC

In the case of the original Grätzel and O'Regan design, the DSSC has five main components (Figure 1.3): (i) a conductive transparent anode, typically fluorine-doped tin dioxide (SnO_2:F or FTO) coated glass; (ii) a nanocrystalline semiconducting oxide with a highly porous structure and high surface area, typically titanium dioxide (TiO_2); (iii) a sensitising dye such as a ruthenium bipyridyl complex; (iv) an organic electrolyte containing a redox mediator, usually a mixture of iodide/triiodide (I^-/I_3^-) in a low viscosity organic solvent such as acetonitrile and (v) another FTO coated glass with a platinum catalyst coating working as counter electrode.

In terms of solid-state dye-sensitised solar cells, the liquid electrolyte is replaced by solid state organic or p-type conducting polymer hole-transport materials (HTMs).

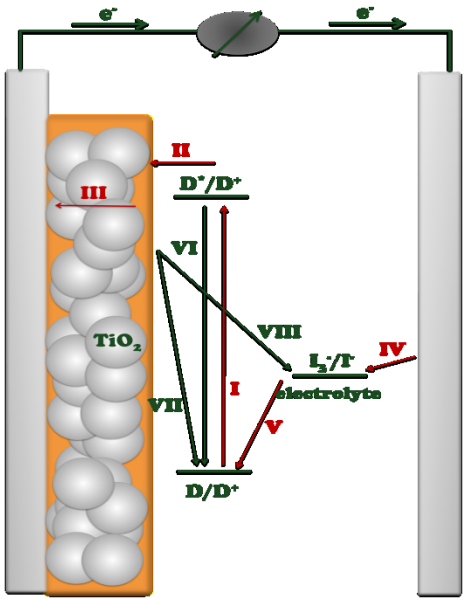

Figure 1.4 Summary of working processes in a DSSC

Figure 1.4 summarises all the working processes I – VIII in a DSSC. The details of these processes are as follows:

(I) The absorption of a photon by the dye D leads to formation of its electronically excited state D*:

$D + h\nu \rightarrow D^*$

(II) The molecule in the excited state undergoes oxidative quenching, injecting electrons into the conduction band of TiO_2 and leading to the oxidation of the sensitiser:

$D^* \rightarrow D^+ + e^-CB$

(III) The injected electrons travel through the mesoporous network of particles to reach the back-collector electrode to propagate around the external circuit to the platinum coated cathode.

(IV) The electrons reaching the counter electrode through the external circuit reduce the oxidized iodide (I_3^-) back to iodide (I^-). The platinum catalyst enables this reaction to proceed with minimal over-potential:

$I_3^- + 2e^- \rightarrow 3I^-$

(V) The oxidized dye is regenerated rapidly to the neutral state by the electrolyte:

$2D^+ + 3I^- \rightarrow 2D + I_3^-$

(VI) The dye in the excited state can decay back to the ground state when there is competition between the electron injection into the metal oxide and the radiative and non-radiative decay of the excited state dye:

$D^* \rightarrow D + h\nu/heat$

(VII) The oxidized dye is recombined with an injected electron in the conduction band of TiO_2:

$D^+ + e^-CB \rightarrow D$

(VIII) The electron in the conduction band recombines with the oxidised redox species in the electrolyte.

$I_3^- + 2\ e^-CB \rightarrow 3I^-$

Forward processes of light absorption, electron injection, dye regeneration, and charge transport I–V (red arrows) should ideally be kinetically favoured over competing loss pathways of excited-state decay to ground and electron recombination processes VI–VIII (green arrows).[28, 29]

3.1 Basic concepts in solar science

3.1.1 Air mass

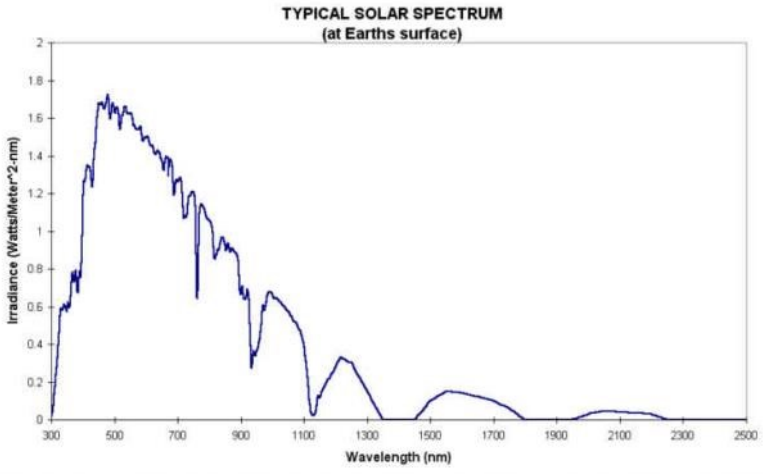

Figure 1.5 Standard intensity AM 1.5 spectrum for light incident on the Earth's surface

At any given place on the earth, the solar radiation is dependent on a number of factors. Before entering the atmosphere, the energy power density has a value of j_E,

$_{AM0}$ = 1353Wm^{-2}.[30] However, the solar radiation is partially absorbed during its passage through the atmosphere. The infrared region can be absorbed by water vapour (H_2O), carbon dioxide (CO_2), nitrous oxide (N_2O), methane (CH_4), fluorinated hydrocarbons and dust. At the same time, the ultraviolet region can be absorbed by ozone (O_3) and oxygen (O_2). When the sunlight shines on the earth at different angles, there will be a different spectrum. It is often characterized by the air mass coefficient or *AM*. For a thickness l_0 of the atmosphere, the path length l through the atmosphere for radiation from the sun incident at an angle α relative to the normal to the earth's surface is given by $l=l_0/\cos\alpha$. The ratio l/l_0 is called the air mass coefficient. It characterizes the real solar spectrum resulting from the absorption of a layer of air of thickness *l*. The spectrum outside the atmosphere is designated by *AM*0. The spectrum when the sun shines vertically on the surface of the earth for normal incidence is designated by *AM*1 which is 1.07kW/m^2. In that case, the angle of incidence is 90°.

A typical spectrum that is often used in the field of solar cells is *AM*1.5, which corresponds to an angle of incidence of solar radiation of 48.19° relative to the surface normal. This spectrum (Figure 1.5) is defined as the standard condition for solar cell testing and comparison. For convenience, the integral over this spectrum, or the energy current density onto a surface normal to the sun for a cloudless sky, is defined to be $j_{E,\,AM1.5}$ = 1.0 kW/m^2.

3.1.2 Monochromatic incident photon-to-current conversion efficiency (IPCE)

Monochromatic incident photon-to-current conversion efficiency (IPCE) [31] can be defined as the percentage of photons that are converted to electric current when the cell is operated under short circuit conditions. The value corresponds to the photocurrent density produced in the external circuit under monochromatic illumination of the cell divided by the photon flux that strikes the solar cell.

$$IPCE\ (\lambda) = N_e / N_p \times 100\% = 1240\ I_{sc} / (\lambda \times P_{in}) \qquad \text{Equation 1.1}$$

Here, N_e is the number of electrons generated in the external circuit, N_p is the number of incident monochromatic photons, I_{sc} is the short circuit current density, λ is the wavelength, P_{in} is the luminous flux. The units used are A cm^{-2}, nm, W cm^{-2}, respectively.

Considering the process of how the current is generated, the equation can also be:

$$IPCE\ (\lambda) = \mathrm{LHE}(\lambda)\phi_{\mathrm{inj}}\eta_{\mathrm{coll}} \qquad \text{Equation 1.2}$$

Here, LHE(λ) is the light-harvesting efficiency for photons of wavelength λ , ϕ_{inj} is the quantum yield for electron injection from the excited state dye in the conduction band of the semiconductor oxide. η_{coll} is the electron collection efficiency on the back contact of semiconductor oxide and the conducting glass.

3.1.3 I-V curves

The performance of a photovoltaic device can be compared according to overall power-conversion efficiency of the solar cell. Current-voltage (I-V) relationships, which measure the electrical characteristics of PV devices, are depicted by *I-V curves*. A typical I-V curve is shown in Figure 1.6.

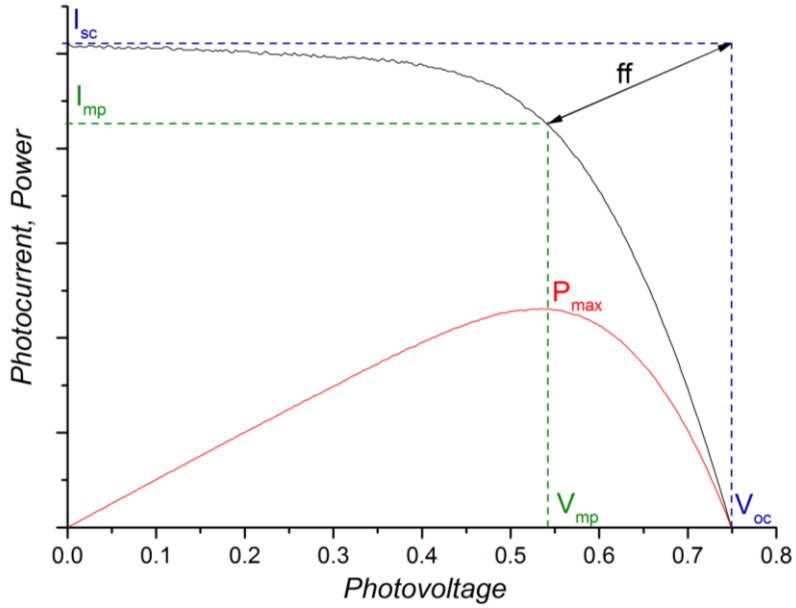

Figure 1.6 Typical I-V curve (black line) for a DSSC

From an I-V curve, a number of parameters can be obtained in order to determine the efficiency of the cell.

The short circuit current I_{sc} is the current through the solar cell when the voltage across the solar cell is zero (i.e., when the solar cell is at short circuit). In a DSSC, it is related to a few factors: 1) The light absorption ability of the sensitiser; 2) The electron-injection efficiency from the excited dye to the TiO_2; 3) The regeneration efficiency of the oxidized dye by the electrolyte.

The open-circuit voltage V_{oc} is the maximum voltage available from a solar cell, and this occurs at zero current. In a DSSC, this corresponds to the difference between the quasi-Fermi energy of electrons in the TiO_2 and the redox potential of the electrolyte. The fill factor (*ff*) is the ratio of the maximum power from the solar cell to the product of V_{oc} and I_{sc}. P_{max}, maximum power obtained, is the product of two terms current I_{mp} and voltage V_{mp}.

$$ff = P_{max} / (I_{sc} \times V_{oc}) = (I_{mp} \times V_{mp}) / (I_{sc} \times V_{oc}) \qquad \text{Equation 1.3}$$

The fill factor value is attenuated by the series resistance of the cell including the sheet resistances of both electrodes, electron transport resistance of the working electrode, hole transport resistance in the electrolyte and charge-transfer resistance at the counter electrode. It depends a lot on the fabrication process.

The efficiency (η) is defined as the ratio of maximum electrical power out (P_{out}) to the solar power input (P_{in}) into the cell.

$$\eta = P_{max} / P_{in} = (ff \times I_{sc} \times V_{oc}) / P_{in} \qquad \text{Equation 1.4}$$

3.2 Substrates for DSSC

Different substrates can be used in DSSCs including conducting glass, metal foil and flexible polymer film. Among them, the glass substrate is most widely used in academic research because it confers good protection against penetration of oxygen

or water. The glass used has a surface coating of a transparent conductive oxide (TCO). TCOs are used in a wide range of applications, such as optoelectronic devices, LEDs and transparent contacts for solar cells due to their low sheet resistance and high transparency to solar radiation in the visible-IR region. TCOs are generally n-type wide bandgap semiconductors that consist of a relatively high concentration of free electrons in the conduction band. The high optical transmittance is provided by the wide bandgap and the electrical conductivity is increased by the free electrons. The most commonly used TCO in DSSC are Indium Tin Oxide (In: SnO_2, ITO) and Fluorine doped Tin Oxide (F: SnO2, FTO). ITO is the 'gold standard' of TCOs due to its high transmittance (around 80% to 90%) and high conductivity.[32] However, when ITO is placed at a temperature over 300℃, there will be a decrease in the oxygen vacancies and this phenomenon leads to a decrease of electric carriers and a dramatic drop in conductivity. FTO is a preferable choice when making DSSC not only because of its good stability at high temperature, but also because of its competitive cost in comparison with ITO. The transmittance of FTO can be as high as 80% to 85% depending on the thickness, and the resistivity can be as low as 2×10^{-4} ohms per square. Other alternative material like Aluminium doped Zinc Oxide (Al:ZnO, AZO) are also used.

3.3 Nanocrystalline semiconductors

Semiconductor oxides used in dye-sensitised solar cells serve as the carrier for the monolayers of the dye and the path for electrons diffusing to the conducting substrate. Many wide-bandgap oxide semiconductors including TiO_2, ZnO, SnO_2, Nb_2O_5 and so on, have been examined as potential candidates for DSSCs. TiO_2 turned out to be the most popular choice due to its chemical stability, ready abundance in the market, nontoxicity, low-cost and biocompatibility. TiO_2 has a wide 3.2eV band gap and can be found in nature as anatase, rutile or brookite. Anatase is the most common structure used in high performance solar cells.

Various techniques are used to synthesize nanocrystalline TiO_2 particles, including vapour-liquid-solid process (VLS), sol-gel, solution-based process, electrodeposition

and polymer-assisted growth. Among them, the sol-gel procedure is the most commonly used.[33]

Three traditional deposition methods, spin-coating, doctor-blading and screen-printing, are used to prepare the nanocrystalline titania film on a conducting glass before sintering at high temperature. Usually, four layers are needed for a good TiO_2 electrode. (i) A dense TiO_2 blocking layer coating on the whole FTO glass to prevent contact between the redox mediator in the electrolyte and the FTO, (ii) a nanocrystalline sensitiser absorption layer for dye absorption and electron transport, (iii) a light scattering layer comprising larger particles to give effective light scattering, (iv) another thin coating layer on the whole assembly. However, when it comes to DSSCs based on organic flexible substrates, the traditional methods are no longer suitable because the substrates are not durable at high temperature. Accordingly, new methods have been studied and reported, such as low-temperature annealing [34] at a temperature below 150℃ and liftoff technique [35] to transfer pre-sintered porous layers from conducting glass substrate to a flexible substrate while maintaining the original electrical properties.

The typical film thickness is 2-15μm using nanosized particles of 10-30nm. A large surface area allows the film to absorb more dye, but also increases the recombination in process (VIII). New research to coat the TiO_2 film with a thin overcoat of another metal oxide with a higher conduction band edge has been investigated in an attempt to solve this problem by increasing the physical separation of injected electrons from the oxidized dye.[36, 37]

3.4 Electrolyte

The electrolyte plays a very important role in the DSSCs. It is responsible for regenerating the oxidized dye and transporting the electrons. According to the different states of matter, the electrolyte can be divided into three types: liquid electrolyte, quasi-solid state electrolyte and solid electrolyte.

3.4.1 Liquid electrolyte

The liquid electrolyte is the most classic electrolyte for DSSCs and the world record efficiency is always achieved by liquid electrolyte DSSCs. Usually, a liquid electrolyte contains four elements, including electron mediators like I^-/I_3^-, cations working as the counter ions for the electron mediators, additives like *tert*-butylpyridine (*t*-BP) and organic solvents used to dissolve everything. Different redox couples have been studied. The most common choice is iodide/triiodide dissolved in a mixture of acetonitrile and valeronitrile. However, it also has been noticed that the triiodide absorbs a non-negligible portion of the visible light and thus is competitive with the dye. Also, its low redox potential sets a limitation of the open-circuit voltage and its corrosive nature also causes a problem. Efforts to find new electron mediators have been made and polypyridyl cobalt (II/III) complexes as well as the $(SeCN)_3^-/SeCN^-$ couple have been found to be the most promising replacements. An efficiency of 12.3% (uncertified) is achieved by incorporating $Co^{(II/III)}$tris(bipyridyl)–based redox electrolyte in conjunction with a custom synthesized donor-π-bridge-acceptor zinc porphyrin dye **YD-2-o-C8** and organic dye **Y123** (Figure 1.7) as co-sensitiser.[38] Despite the high efficiency, co-sensitising makes the fabrication and optimisation of these devices technically challenging. The idea of developing a single sensitiser with a panchromatic light response in a DSSC leads to the new record (uncertified) efficiency of 13% at full sun illumination using a big donor-π-bridge-acceptor zinc porphyrin dye **SM315** (Figure 1.7) without the requirement of a co-sensitiser.

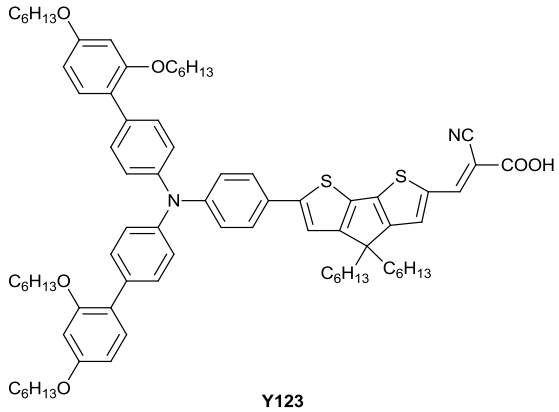

Y123

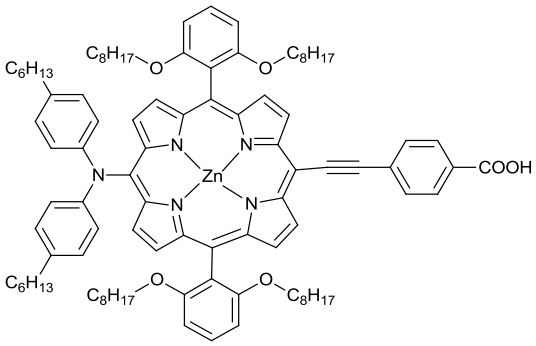

YD-2-o-C8

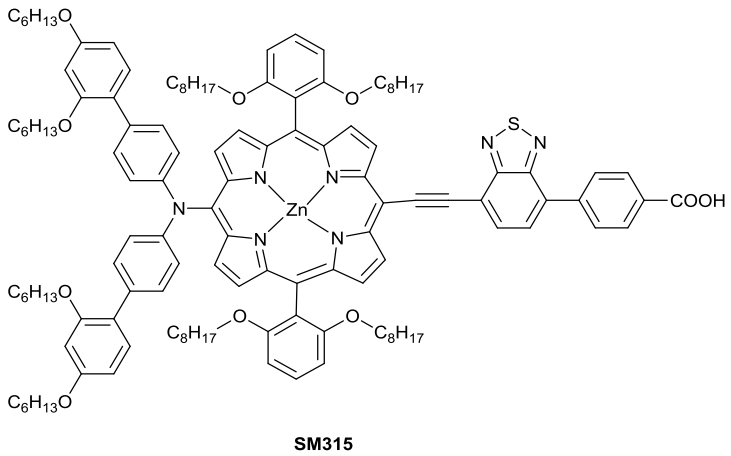

SM315

Figure 1.7 Molecular structures of **YD-2-o-C8**, **Y123** and **SM315**

3.4.2 Ionic liquid and quasi-solid state electrolyte

A room-temperature ionic liquid is a salt in the liquid state at room temperature. These can have excellent thermal and chemical stability, negligible vapor pressure, high ionic conductivity and a wide electrochemical window.

Most ionic liquids applied in DSSCs are iodide salts, especially alkylimidazolium-based. Their special properties allow them to be both the source of iodide and the solvent. The limitation of ionic liquids is their viscosity, which slows down the transport of I_3^- in the electrolyte and decreases the current density and the solar efficiency. It has been shown that the viscosity of the ionic liquid increases with increasing alkyl chain length due to van der Waals forces, whereas the conductivity decreases with increasing viscosity.[39] To improve the mobility, low viscosity ionic liquids were developed [40] and different ionic liquids were used together as a mixture to adjust the viscosity and conductivity. A high efficiency of 7.6% was achieved by Kuang et al. in 2004 using **K77** as the dye (Figure 1.8) and binary ionic liquids, 1-propyl-3-methylimidazolium iodide (PMII) and 1-ethyl-3-methylimidazolium tetracyanoborate ($EMIB(CN)_4$) with I^-/I_3^- as the electrolyte (Figure 1.8).[41] Two additives are also often used in the electrolyte, *N*-butylbenzoimidazole (NBB) and guanidinium thiocyanate (GNCS). A very impressive efficiency of 9.1% with high stability could be achieved using DMII/EMII/$EMIB(CN)_4$/I_2/NBB/GNCS (molar ratio: 12/12/16/1.67/3.33/0.67) as the

electrolyte and **C103** as the dye (Figure 1.8).[42] An alternative redox couple has also been studied. By using a low viscosity ionic liquid EMISeCN with an iodine-free $SeCN^-/(SeCN)_3^-$ electrolyte, an efficiency of 7.5% can be reached.[43]

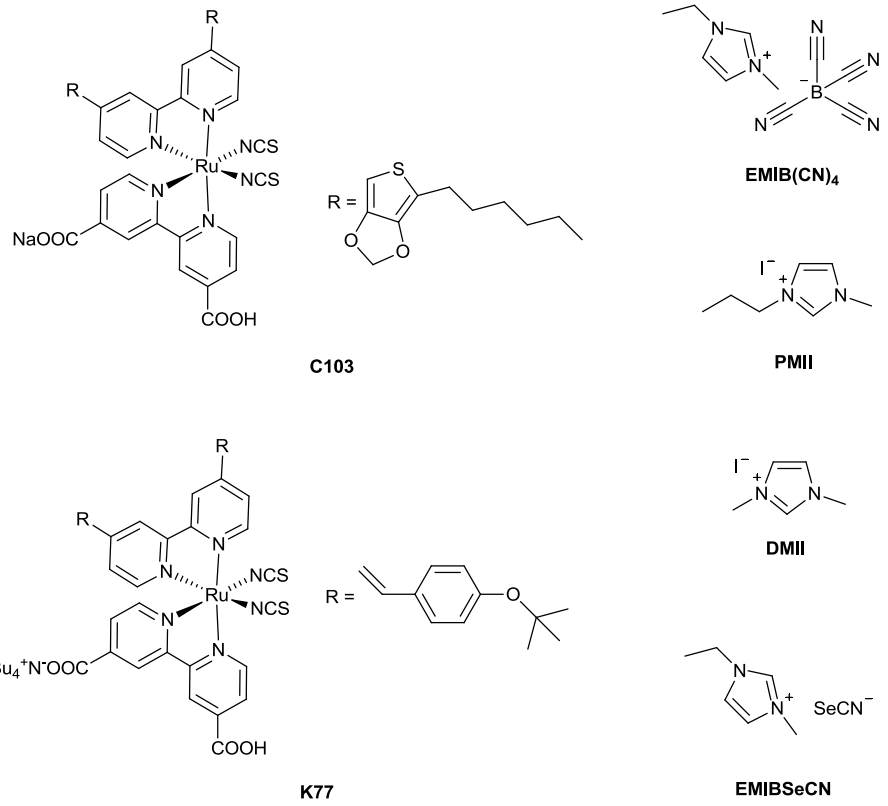

Figure 1.8 Molecular structures of **C103** and **K77** and the ionic liquids used with these dyes

3.4.3 Solid electrolyte

In order to increase the long-term performance and durability of DSSCs and to fully solve the inevitable problems of any liquid electrolyte, such as leakage, corrosion, volatility and photoreactivity, purely solid state dye-sensitised solar cells (SSDSSCs) need to be developed. Currently, efforts have been focused on using inorganic conducting polymer or organic hole-transport materials (HTMs).

The HTMs used for DSSCs should meet a number of requirements. (i) The redox potential of the HTM should be less positive than that of the dye so it can accept

holes from the oxidized dye before the electron recombination, (ii) the HTM needs to have good hole mobility, (iii) the HTM must have a good penetration into the pores of the nanoparticle film, (iv) there must be a way to deposit the HTM without dissolving or degrading the dye on TiO_2, (v) the HTM should not absorb light in the visible spectrum, where the dye absorbs light.[44, 45]

Copper(I) iodide (CuI) [46-48], copper(I) thiocyanate (CuSCN) [49], and NiO [50] are representative of inorganic HTMs used in DSSCs. In the work of Kumara, they used 1-ethyl-3-methylimidazolium thiocyanate (EMISCN) as a CuI crystal growth inhibitor and make CuI crystallites fine to fill the pores. The cells can be optimised to 3.75% (AM1.5). The highest conversion efficiency using CuI as the HTM is 7.4% reported by Sakamoto *et al.* [51] Comparing with CuI, CuSCN has an even better stability, but results in low efficiency. NiO showed low efficiency cells as well. This is mainly due to the low hole mobilities of these materials. In 2012, Kanatzidis [52] developed a new type of HTM, which is a solution-processable p-type direct bandgap semiconductor $CsSnI_3$. $CsSnI_3$ has an energy gap of 1.3eV and a remarkably high mobility of μ_h = 585 $cm^2V^{-1}s^{-1}$ at room temperature. The optimum cell exhibits an efficiency of 8.51% under AM 1.5 irradiation when doping of $CsSnI_3$ with 5% F and 5% SnF_2. What's more, the good solubility of $CsSnI_3$ in polar organic solvents allows the use of solution-processing to fabricate solar cells.

Polymers have also been investigated much in the past decades due to their advantages of low cost, high stability, good adaptability and the possibility to use an easy spin-coating process. In the meantime, they suffer from insufficient penetration into the TiO_2. The most studied examples of these polymers are poly(3,4-ethylenedioxythiophene) (PEDOT) [53, 54] and poly(3-hexylthiophene) (P3HT) (Figure 1.9), [55] leading to 6.8% and 7.4%, respectively.

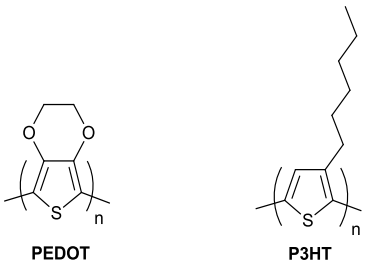

Figure 1.9 Molecular structures of representative polymers used as HTM

The use of small organic molecules as HTM in SSDSSCs leads to the highest efficiency for 2,2',7,7'-tetrakis(N,N-di-p-methoxyphenyl-amine)9,9'-spirobifluorene (spiro-OMeTAD) (Figure 3.8).[49] Since it was first reported by Bach and Grätzel in 1998, giving an overall efficiency of 0.74% based on a Ru-complex dye, the efficiency of spiro-OMeTAD-based SSDSSCs increased dramatically through dye development, TiO_2 modification, and addition of additives. Now it can reach 5.0% using a Ru-complex dye **C106** (Figure 1.10) and 7.2% using metal-free organic dye **Y123**.

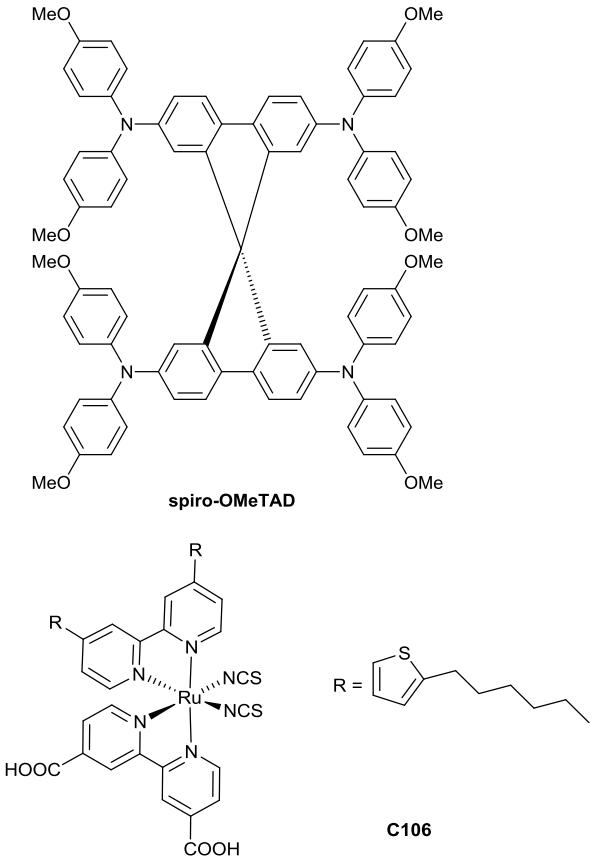

Figure 1.10 Molecular structures of spiro-OMeTAD and the dyes used with it to reach high efficiency

Spiro-OMeTAD has been used as a standard HTM in both solid-state dye-sensitised solar cells and perovskite solar cells. However, it still needs to be investigated and improved. For example, the slow charge transport in Spiro-OMeTAD limits the device performance.[56] One solution to this problem is to add strong oxidants as p-dopants in order to increase the conductivity in Spiro-OMeTAD.[57, 58] Other alternatives would be designing new materials to improve hole mobility.[59] Previous HTM work in our group has been based on triphenylamine. By introducing different electron-donating functional groups, the oxidation potential of these HTM can be precisely controlled and tuned. [60]

3.5 Sensitising dye

One of the most important components in DSSCs is the sensitising dye. A number of features are needed for the dye to enable high power conversion efficiency (PCE) in the DSSC. (i) The dye should have a panchromatic absorption envelope in the visible and near infra-red region with high molar extinction coefficient. Ideally, all photons below wavelength of 920nm should be harvested and converted into electric current, (ii) the ground state and excited state redox potentials should be positioned suitably for both injection and regeneration, (iii) the dye excitation should be a charge-transfer transition with the electron density moving towards the anchoring group to the TiO_2 surface in order to facilitate electron injection. There are several anchoring groups that are commonly used, such as carboxylic acid (–COOH), sulfonic acid -SO_3H, phosphonic acid (-PO_3H_2), (iv) the dyes need to have reasonably good thermal and chemical stabilities.[61, 62]

Up till now, there are two main categories of sensitising dyes: metal complexes and metal-free organic dyes. The solar cells using metal complexes lead to high efficiency and good stability while the purification is more complicated. Organic dyes are easier to purify and design, but their efficiency and stability are still in debate and the best-performing examples often require complex multi-step synthesis.

3.5.1 Ruthenium complexes

Over the past two decades, ruthenium complexes endowed with thiocyanate ligands have led the performance in DSSCs over hundreds of dyes. The reasons why ruthenium is chosen as the metal for DSSC dyes are as follows. (i) its octahedral geometry allows ligands to be introduced in a controllable way, (ii) the metal can exist in oxidation states from +1 to +4 with good stability, (iii) the photophysical, photochemical and electrochemical properties of these complexes can be predictably tuned.

The first DSSC to exhibit efficiency over 10% used complex $Ru(dcbpy)_2(NCS)_2$ (dcbpy=4,4'-dicarboxy-2,2'-bipyridine), better known as **N3** (Figure 1.12). It is now often used as a standard for comparative assessment of new dyes. In **N3**, the highest occupied molecular orbital (HOMO) is localized primarily on the metal-thiocyanate fragment while the lowest unoccupied molecular orbital (LUMO) is positioned on the dcbpy anchoring ligands. This allows efficient charge injection to the TiO_2 after photoexcitation. Also, this complex was discovered to have a broad visible absorption spectrum which displays maximum absorption at 380 nm and 518 nm which are dependent on intraligand absorption and singlet metal to ligand charge transfer (^{1}MLCT), respectively. In addition, this complex has a sufficiently long excited state lifetime and strong adsorption on TiO_2. Based on variations of **N3**, hundreds of dyes have been designed and studied.

Protons carried by the dye will have an effect on DSSC performance because the conduction band energy of the TiO_2 has a dependence on pH.[63, 64] The effect was systematically studied by comparing the N3 dye with no protons **D1**, two protons **N719** and four protons **N3**. (Figure 1.12) [61, 65, 66] It was found that the fully protonated sensitiser will give a higher photocurrent, but lower open-circuit potential because of the positive shift of the conduction band edge induced by TiO_2 surface protonation. On the other hand, the sensitiser that carries no protons shows high open-circuit potential compared to the fully protonated one at the sacrifice of a lower short-circuit photocurrent. Thus, an optimal degree of protonation of the sensitiser to obtain both good short-circuit photocurrent and open-circuit potential is the doubly

protonated **N3** analogue, also known as the famous dye **N719**.[66] In **N719**, tetrabutylammonium (TBA) was used as the cation. Other cations like sodium ion or potassium ion can also be used and a single conclusion cannot be drawn about which cation is the best because the effect of cation substitution depends on the electrolyte composition.

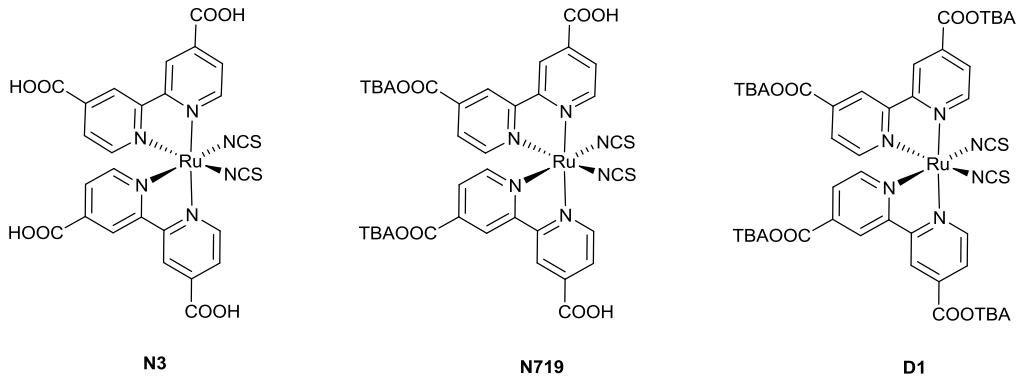

Figure 1.12 Molecular structures of **N3** with four protons, two protons (**N719**) and no protons

Two different bpy ligands can be used in the Ru complexes. One of them can be dcbpy ligand in order to attach the dye to the TiO_2, the other one can be used to tune the properties of the dye. For example, the length of alkyl chains on the bpy ligand has an effect, mainly on the stability of the solar cells. The sensitiser goes through water-induced desorption from the TiO_2 surface over time. By introducing long alkyl chains in the ligand, the hydrophobic properties increase and thus increase the thermal stability of the solar cells. A key example regards **Z907** (Figure 1.13).[67] The long chains of the sensitiser can also retard the charge recombination in process (VIII) by forming an aliphatic network to prevent the oxidized redox couple I_3^- in the electrolyte from reaching the surface of TiO_2. However, in the meantime, the dye regeneration process (V) is also suppressed, resulting in a reduced PCE.

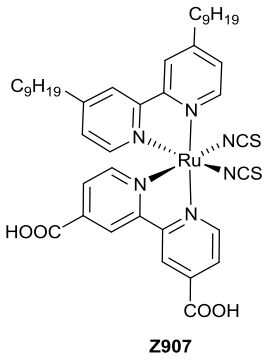

Z907

Figure 1.13 Molecular structure of sensitiser with long alkyl chains (**Z907**)

The expansion of π-conjugation of the polypyridyl ligand will enhance the molar extinction coefficient of the sensitiser. By endowing it further with electron donating alkoxy groups, the LUMO energy level can be fine-tuned and the directioniality in the excited state can be guaranteed. Good examples for this theory are dyes with conjugated aromatic rings including, but not limited to, methoxystyryl group **Z910**[68] and **N945H**[69], thiophene **C101**[70] and **C106**[71], 3,4-ethylenedioxythiophene **C103**[28], selenophene **C105**[72], triarylamine **D2** and **D3**. (Figure 1.14)[73] Other dyes use a tridentate ligand to make **N749**[74] (also called the 'black dye') and tetradentate ligand **N886** (Figure 1.14)[75] have also been tried and these dyes give an obvious panchromatic absorption spectrum (up to 900 nm).

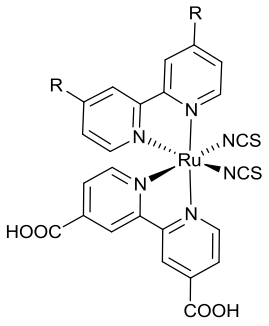

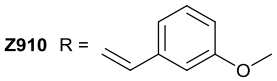

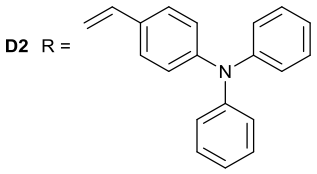

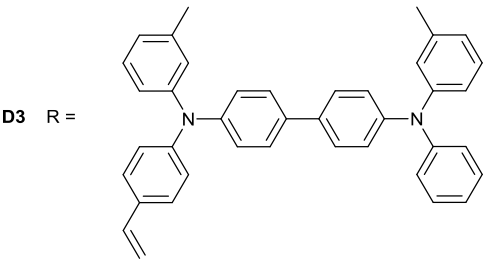

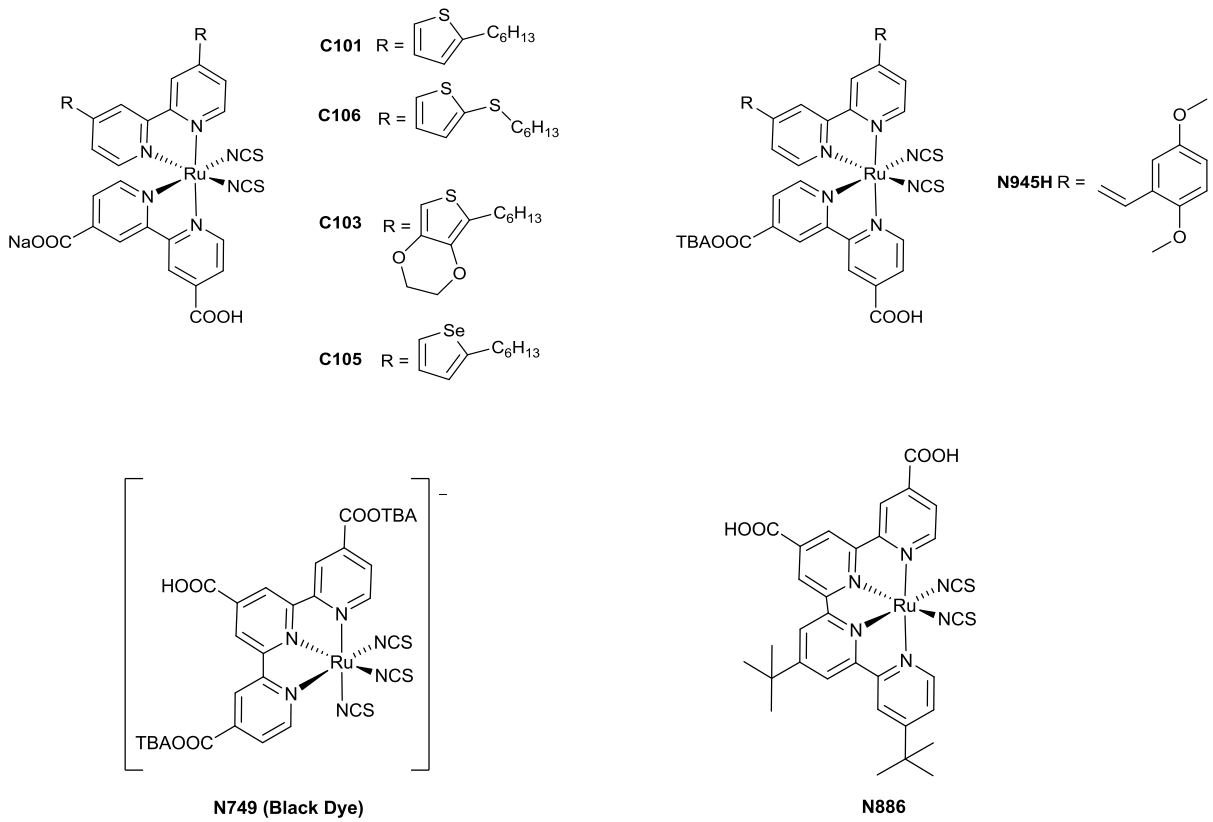

Figure 1.14 Molecular structures of sensitiser with π-conjugated system

Thiocyanate (NCS^-) ligands have also been taken into consideration. It has been employed as the electron-donating group for most efficient Ru dyes. However, from the prospect of chemical stability, the NCS^- seems to be the most labile part of the complex. Over time, the dyes will lose the monodentate, labile NCS^- ligands. Efforts have been made to overcome this problem by replacing NCS^- with other ligands. In 2011, the efficiency of this kind of DSSCs reached 10.7% by using dye **TF-3** [76] (Figure 1.15) containing a 4,4',4"-tricarboxy-2,2':6,2"-terpyridine ligand and a styrene-substituted pyridylpyrazolate (pypz) auxochrome. More thiocyanate-free Ru dyes were studied by Yun Chi, et al. [77]

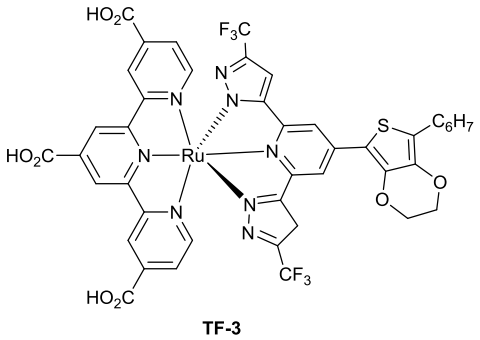

TF-3

Figure 1.15 Molecular structures of example NCS-free sensitisers [76]

3.5.2 Porphyrin and phthalocyanine dyes

Phthalocyanine is an intensely blue-green coloured aromatic macrocyclic compound. In contrast to Ru complexes, porphyrin and phthalocyanine dyes exhibit an intense Soret band in the 400-450 nm region and Q-band in the 500-700 nm region with good chemical, photochemistry, and thermal stability. Among all the porphyrin and phthalocyanine dyes, the diamagnetic metalloporphyrins containing zinc with carboxylic binding groups have shown the best performance. In the work of Nazeeruddin and co-workers, they use dye **D4** to achieve a high IPCE value of 75% and overall efficiency of 4.8%.[78] One problem in this kind of dye is that the HOMO and LUMO are both localized in the macrocycle, so the charge separation is not good and thus causes a difficulty for the electrons to inject into TiO_2. In order to separate the HOMO and LUMO, strong electron donors and acceptors with anchoring groups are introduced. Dye **YD-2** (Figure 1.16) is designed based on this idea and its derivative **YD-2-o-C8** (Figure 1.7) is one of the dyes used in the world-record solar cell.

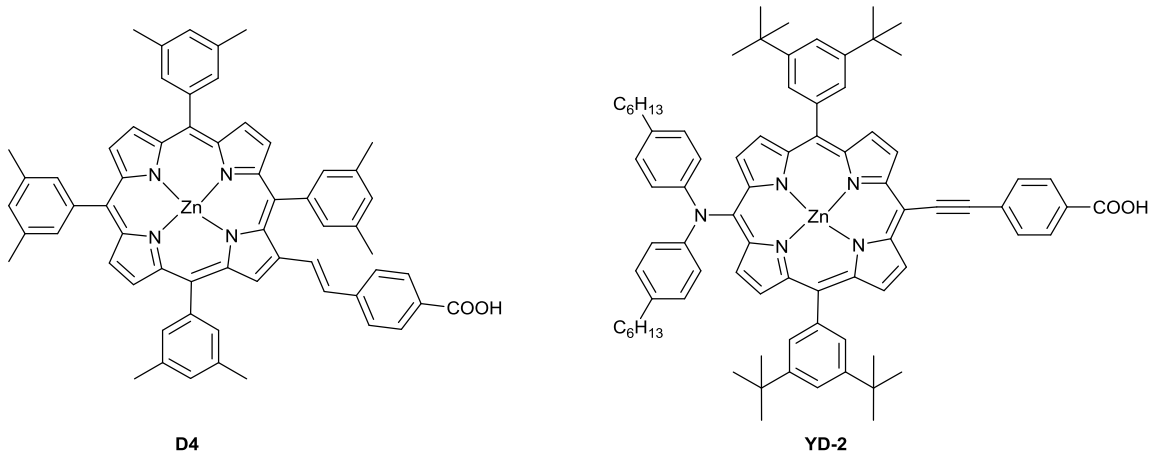

Figure 1.16 Molecular structures of asymmetric a D-A type Zn porphyrin dyes

3.5.3 Metal-free organic dye

Metal-free organic dyes typically show higher molar extinction coefficients than Ru polypyridyl complexes. The structures are very diverse and can be easily designed. In addition, without using a rare metal, the cost of this kind of dye may also be lower. The metal-free organic dye is designed based on a donor - π spacer - acceptor (D- π -A) architecture. In this case, the donor and the π spacer part will contain the HOMO of the dye while the LUMO is distributed on the acceptor part and the anchoring group. Upon excitation, the electrons move from donor to acceptor through the π-bridge. Cyanoacrylic acid is a commonly used acceptor which decreases the gap between HOMO and LUMO, thus leading to a red shift of the lowest energy absorption maximum.[79] Various organic dyes have been investigated, including anthraquinone dyes, boradiazaindacene dyes, carbazole dyes, coumarin dyes, *N,N*-diakylaniline dyes, hemicyanine dyes, heteroanthracene dyes, indoline dyes, merocyanine dyes, oligothiophene dyes, tetrahydroquinoline dyes, triarylamine dyes, squaraine dyes, perylene dyes, polymeric dyes, and natural dyes.[80]

The problems that organic dyes have are dye-aggregation due to the strong π- π stacking, the lack of absorption in the red region of the visible spectrum and the low

stability. Molecular aggregation has negative influence on the solar cell efficiency because it may lead to intermolecular excited-state quenching. Also, the aggregated molecules are not attached to the TiO_2 directly, therefore are not efficient in charge transfer. [81] Although dye aggregation causes redshifts and broadening of the absorption spectra, it results in lowering the J_{SC} in the solar cell.

In order to prevent the aggregation, sterically hindered substituents, such as long alkyl chains and bulky aromatic units have been introduced into the dye molecules to disturb the π- π stacking. The alkyl substitution of dyes can block the oxidized species in the electrolyte away from the injected electrons, thus preventing charge recombination and increasing the V_{OC} of the cell. Hara et al. carried out a systematic study on the how thiophene alkyl-chain length and positions in the π-conjugation bridge of organic dyes affect the photovoltaic performance and the kinetics for electron injection and charge recombination. [82] The series of MK dyes (Figure 1.17) they synthesised have a carbazole derivative as an electron donor and cyanoacrylic acid moiety as an electron acceptor. The donor and acceptor are connected by n-hexyl-substituted oligothiophenes. By comparing with **MK-1** and **MK-3**, or **MK-2** and **MK-4**, **MK-5** and **MK-7**, it was observed that less hexyl chains in the dye led to a blue shift accompanied with a broadening of the absorption spectrum, suggesting the influence of number and position of hexyl chains on the intermolecular interaction of the dyes. The relatively sharp absorption peaks on the TiO_2 surface of **MK-1**, **MK-2** and **MK-8** also suggested a decrease of the π- π stacking when more hexyl chains were present. In addition, the V_{OC} of dye **MK-1** and **MK-2** were 80mV higher than **MK-3**, **MK-4**, **MK-5** and **MK-7**, due to their longer electron lifetimes as a result of the alkyl chains.

Studies have also been done on the electron-donor groups. It was found that a bulky donor group is usually preferred in order to reduce the electron recombination between redox electrolyte and the TiO_2 surface and to stabilize the oxidized dye. The influence of the donor size in D - π - A dye was studied by Yang etc.[83] A higher voltage was observed when they introduced a bulky-indoline moiety as donor into the reported **IQ4** dye (Figure 1.18).[84] The bis(2,4-dihexyloxy)benzene substitution

on the quinoxaline of **YA421** and **YA422** (Figure 1.18) reduced the electron recombination between the oxidised species in the electrolyte and the injected electrons in TiO_2, especially when using Co(II/III) electrolyte.

Some groups have also introduce another electron-donating group to help inhibit the approaching I_3^- ions to TiO_2 surface, thus forming the so-called donor – donor - π spacer - acceptor (D – D - π -A) architecture. This will increase the distance between the dye cation centre and the TiO_2 surface and retard the charge recombination.[85-88]

Other solutions to solve the aggregation problem include adding a co-adsorbent, chenodeoxylcholic acid (CDCA) into the dye solution. However, as a co-adsorbent, CDCA competes with the dyes adsorbed on the TiO_2, thus resulting in a reduction of injected electrons. It is important to tune the amount of CDCA to effectively reduce dye aggregation.

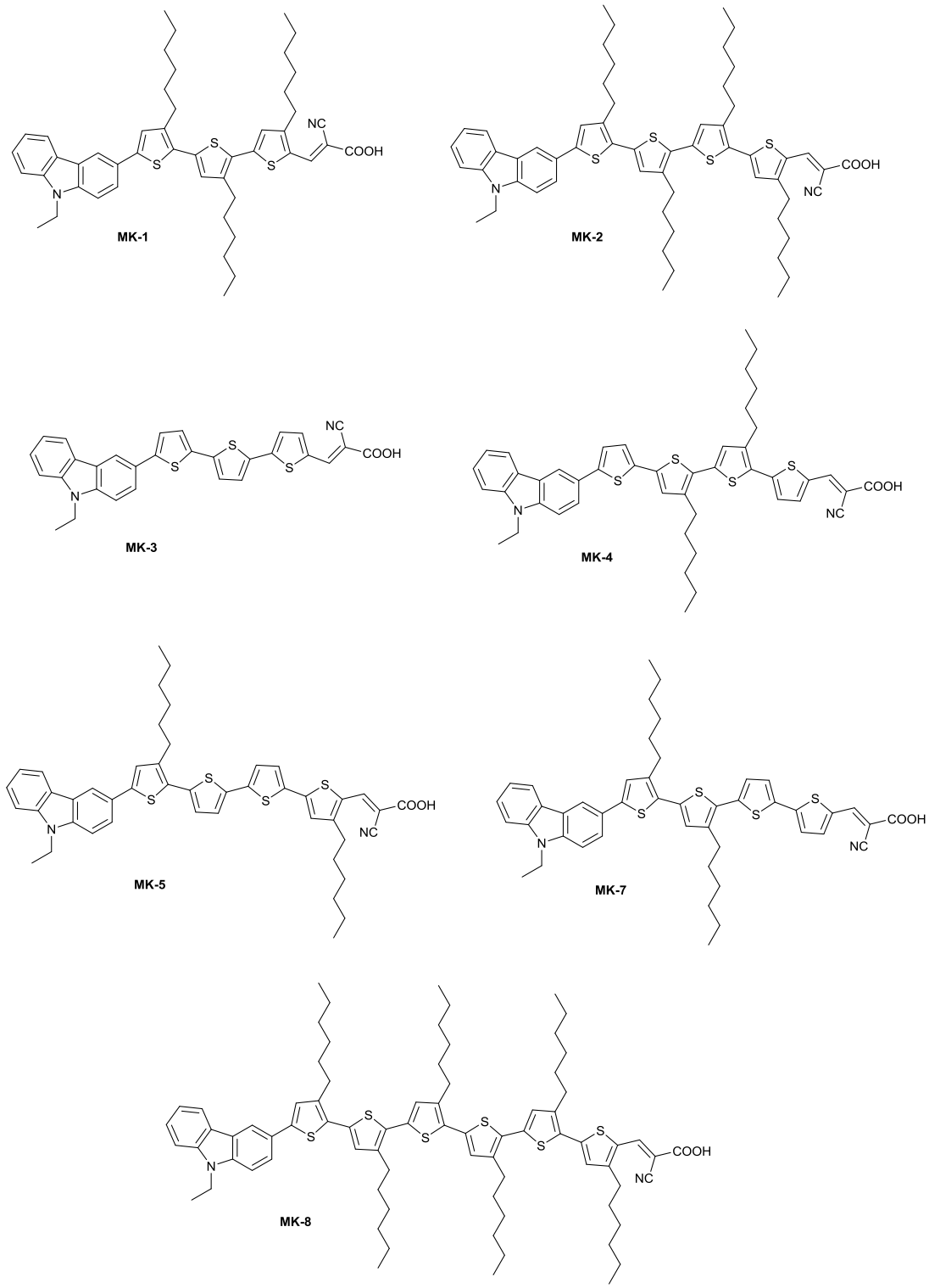

Figure 1.17 Molecular structures of organic dye MK series

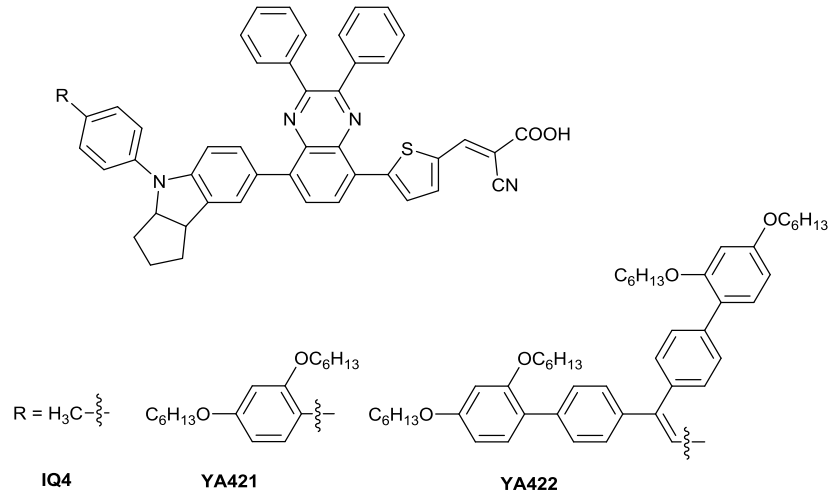

Figure 1.18 Molecular structures of quinoxaline-based dyes

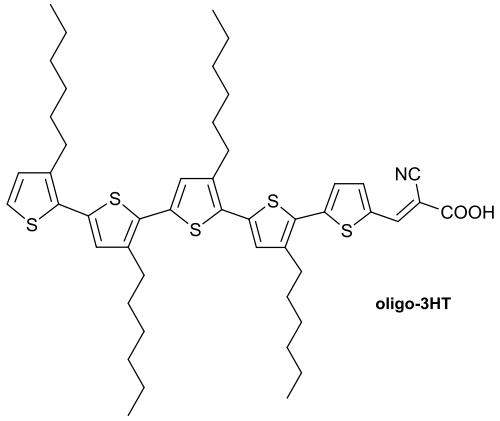

Figure 1.19 Molecular structures of a donor-free dye **oligo-3HT**

Most D - π - A structured dyes were first designed for DSSCs based on liquid redox electrolytes. For those cells, the electron-donating group is necessary due to the reasons discussed before. However, for solid-state dye sensitised solar cells, where the liquid electrolyte is replaced by mild oxidant hole transport material, the donor group may be unnecessary. Abate and Planells [89] investigated a 'donor-free' dye **oligo-3HT** (Figure 1.19) and applied it in a solid-state dye-sensitised solar cell. Given the same basic molecular structure, **oligo-3HT** was compared with **MK-2**. A significantly higher V_{OC} was achieved while J_{SC} remained the same. It was discovered that under operating conditions, the **oligo-3HT** dye has a significant fraction of dye in the oxidised form and the higher V_{OC} was attributed to this. This result proposed a new strategy to obtain efficient solid-state solar cells.

3.5.4 Co-sensitisers

In order to further improve the spectral response of the solar cells, multi-sensitisers with different absorption spectra can be used to extend the light absorption spectrum. A co-sensitiser should meet the following requirements. (i) It needs to have a strong light absorption in the desired region; (ii) the co-sensitiser should not cause a competition with the other dye when anchoring with TiO_2; (iii) no aggregation should result among the different dyes.[90]

4 Research Proposal

Despite offering relatively high conversion efficiencies, dye-sensitised solar cells using liquid electrolytes containing either I^-/I_3^- redox couple or Co^{2+}/Co^{3+} redox couple suffer from durability problems, such as electrode corrosion and electrolyte leakage. Replacements for liquid electrolytes have been extensively studied, but the efficiencies of the resulting devices remain low. One of the factors that limit the efficiency is the sensitising dye. Large sized hole-transport material results in poor pore-filling and thus leads to a fast back electron recombination that reduces the effective electron diffusion length to few micrometeres. The optimal TiO_2 layer thickness (2μm) for maximal power conversion in solid-state dye-sensitised solar cell is much smaller than the 6-10 μm layer thickness required for quantitative light absorption by many dye molecules. [5] Thus, dyes that can absorb in both visible and near-IR region with high extinction coefficient are needed. In order to achieve this, novel oligomers and ruthenium (II) complexes are designed, synthesized and studied as sensitisers for both liquid state and solid state dye-sensitised solar cells in this thesis.

Series of 'donor-free' dyes including oligo(3-hexylthiophene) (oligo-3HT) (Chapter 3) and oligo(4,4-dihexyl-4H-cyclopenta[1,2-b:5,4-b']dithiophene) (oligo-CPDTs) (Chapter 4) functionalized with cyanoacrylic end groups are easily synthesized using cross-coupling. Liquid and solid-state DSSCs device performances are studied and discussed in terms of the dye structures. These dyes are effective sensitisers for liquid-state and solid-state dye-sensitised solar cells, although they do not contain a typical donor group, thus open a new strategy of designing dyes in the future.

Different azo ligands as an additional chromophore moiety have been introduced into Ru complexes to enhance light harvesting. (Chapter 5) These dyes were prepared using a protection/deprotection strategy that allows for convenient purification. Following hydrolysis, the complexes were investigated in DSSCs, with performance investigated using I-V measurements.

Each chapter begins with a relevant literature review to introduce the project in question.

References

1. Houghton, J.T., *Global warming : the complete briefing*. 4th ed. 2009, Cambridge: Cambridge University Press. xviii, p. 438.
2. *CO2 Emissions from Fuel Combustion,* 2012, International Energy Agency.
3. https://commons.wikimedia.org
4. Lewis, N.S.N., D. G., *Powering the planet: chemical challenges in solar energy utilization.* Proceedings of the National Academy of Sciences of the United States of America, 2006. **103**: p. 15729-15735.
5. Kalyanasundaram, K., *Dye-sensitized solar cells*. 2010: CRC Press Inc.
6. Becquerel, E., *Mémoire sur les effets électriques produits sous l'influence des rayons solaires.* Comptes rendus de l'Académie des Sciences, 1839. **9**: p. 561-567.
7. *The Nobel Prize in Physics 1921*. 2013; Available from: http://www.nobelprize.org/nobel_prizes/physics/laureates/1921/index.html.
8. Chapin, D.M., C.S. Fuller, and G.L. Pearson, *A New Silicon P-N Junction Photocell for Converting Solar Radiation into Electrical Power.* Journal of Applied Physics, 1954. **25**(5): p. 676-677.
9. Chadwick, N., *Ruthenium dyes for Dye Sensitised Solar Cells (DSSCs). Exploring dye synthesis and TiO2-dye-I-/I3- electron transfer reactions in a DSSC.* 2014, University of Edinburgh.
10. Green, M.A., *Crystalline Silicon Solar Cells*, in *Clean Electricity from Photovoltaics*. 2001, Imperial College Press. p. 1-49.
11. Masuko, K., et al., *Achievement of More Than 25% Conversion Efficiency With Crystalline Silicon Heterojunction Solar Cell.* Ieee Journal of Photovoltaics, 2014. **4**(6): p. 1433-1435.
12. Shockley, W. and H.J. Queisser, *Detailed Balance Limit of Efficiency of P-N Junction Solar Cells.* Journal of Applied Physics, 1961. **32**(3): p. 510.
13. Jackson, P., et al., *Properties of Cu(In,Ga)Se-2 solar cells with new record efficiencies up to 21.7%.* Physica Status Solidi-Rapid Research Letters, 2015. **9**(1): p. 28-31.
14. Wang, W., et al., *Device Characteristics of CZTSSe Thin-Film Solar Cells with 12.6% Efficiency.* Advanced Energy Materials, 2014. **4**(7): p. 1301465.
15. http://www.sj-solar.com/downloads/Solar_Junction_World_Record_%20Efficiency_14April11.pdf.
16. O'Regan, B. and M. Graetzel, *A low-cost, high-efficiency solar cell based on dye-sensitized colloidal titanium dioxide films.* Nature, 1991. **353**(6346): p. 737-40.
17. Han, L.Y., et al., *High-efficiency dye-sensitized solar cell with a novel co-adsorbent.* Energy & Environmental Science, 2012. **5**(3): p. 6057-6060.
18. Kojima, A., et al., *Organometal Halide Perovskites as Visible-Light Sensitizers for Photovoltaic Cells.* Journal of the American Chemical Society, 2009. **131**(17): p. 6050-6051.

19. Kim, H.S., et al., *Lead Iodide Perovskite Sensitized All-Solid-State Submicron Thin Film Mesoscopic Solar Cell with Efficiency Exceeding 9%.* Scientific Reports, 2012. **2**: 591.
20. Zhou, H.P., et al., *Interface engineering of highly efficient perovskite solar cells.* Science, 2014. **345**(6196): p. 542-546.
21. Liu, M.Z., M.B. Johnston, and H.J. Snaith, *Efficient planar heterojunction perovskite solar cells by vapour deposition.* Nature, 2013. **501**(7467): p. 395-398.
22. Jeon, N.J., et al., *Compositional engineering of perovskite materials for high-performance solar cells.* Nature, 2015. **517**(7535): p. 476-480.
23. Jeon, N.J., et al., *o-Methoxy Substituents in Spiro-OMeTAD for Efficient Inorganic-Organic Hybrid Perovskite Solar Cells.* Journal of the American Chemical Society, 2014. **136**(22): p. 7837-7840.
24. Jeon, N.J., et al., *Efficient Inorganic Organic Hybrid Perovskite Solar Cells Based on Pyrene Arylamine Derivatives as Hole-Transporting Materials.* Journal of the American Chemical Society, 2013. **135**(51): p. 19087-19090.
25. Abate, A., et al., *Hole-transport materials with greatly-differing redox potentials give efficient TiO2- [CH3NH3][PbX3] perovskite solar cells.* Physical Chemistry Chemical Physics, 2015. **17**(4): p. 2335-2338.
26. Ogomi, Y., et al., *CH3NH3SnxPb(1-x)I3 Perovskite Solar Cells Covering up to 1060 nm.* Journal of Physical Chemistry Letters, 2014. **5**(6): p. 1004-1011.
27. Park, N.G., *Perovskite solar cells: an emerging photovoltaic technology.* Materials Today, 2015. **18**(2): p. 65-72.
28. Robson, K.C.D., P.G. Bomben, and C.P. Berlinguette, *Cycloruthenated sensitizers: improving the dye-sensitized solar cell with classical inorganic chemistry principles.* Dalton Transactions, 2012. **41**(26): p. 7814-7829.
29. Listorti, A., B. O'Regan, and J.R. Durrant, *Electron Transfer Dynamics in Dye-Sensitized Solar Cells.* Chemistry of Materials, 2011. **23**(15): p. 3381-3399.
30. Würfel, P. and U. Würfel, *Physics of solar cells: from basic principles to advanced concepts*. 2009, Wiley-VCH Verlag GmbH & Co. KGaA, Weinheim.
31. Gratzel, M., *Recent advances in sensitized mesoscopic solar cells.* Accounts of Chemical Research, 2009. **42**(11): p. 1788-1798.
32. Chen, S.C., *The properities of transparent ductivite oxides ITO deposited on flexible substrate*, in *Department of Materials Science and Engineering*. 2003, National Cheng Kung University: Tainan: Taiwan.
33. Kalyanasundaram, K., ed. *Dye-sensitized Solar Cells*. 2010, EPFL Press.
34. Longo, C., et al., *Solid-state and flexible dye-sensitized TiO2 solar cells: a study by electrochemical impedance spectroscopy.* Journal of Physical Chemistry B, 2002. **106**(23): p. 5925-5930.
35. Durr, M., et al., *Low-temperature fabrication of dye-sensitized solar cells by transfer of composite porous layers.* Nature Materials, 2005. **4**(8): p. 607-611.
36. Wang, M.L., Y. Wang, and J.B. Li, *ZnO nanowire arrays coating on TiO2 nanoparticles as a composite photoanode for a high efficiency DSSC.* Chemical communications, 2011. **47**(40): p. 11246-11248.

37. Palomares, E., et al., *Control of charge recombination dynamics in dye sensitized solar cells by the use of conformally deposited metal oxide blocking layers.* Journal of the American Chemical Society, 2003. **125**(2): p. 475-482.
38. Yella, A., et al., *Porphyrin-Sensitized Solar Cells with Cobalt (II/III)-Based Redox Electrolyte Exceed 12 Percent Efficiency.* Science, 2011. **334**(6056): p. 629-634.
39. Kuang, D.B., et al., *Stable mesoscopic dye-sensitized solar cells based on tetracyanoborate ionic liquid electrolyte.* Journal of the American Chemical Society, 2006. **128**(24): p. 7732-7733.
40. Fei, Z.F., et al., *A supercooled imidazolium iodide ionic liquid as a low-viscosity electrolyte for dye-sensitized solar cells.* Inorganic Chemistry, 2006. **45**(26): p. 10407-10409.
41. Kuang, D.B., et al., *Stable, high-efficiency ionic-liquid-based mesoscopic dye-sensitized solar cells.* Small, 2007. **3**(12): p. 2094-2102.
42. Shi, D., et al., *New Efficiency Records for Stable Dye-Sensitized Solar Cells with Low-Volatility and Ionic Liquid Electrolytes.* Journal of Physical Chemistry C, 2008. **112**(44): p. 17046-17050.
43. Wang, P., et al., *A solvent-free, SeCN-/(SeCN)(3)(-) based ionic liquid electrolyte for high-efficiency dye-sensitized nanocrystalline solar cells.* Journal of the American Chemical Society, 2004. **126**(23): p. 7164-7165.
44. Garcia-Canadas, J., et al., *Determination of electron and hole energy levels in mesoporous nanocrystalline TiO2 solid-state dye solar cell.* Synthetic Metals, 2006. **156**(14-15): p. 944-948.
45. Tennakone, K., G.R. Kumara, and A.R. Kumarasinghe, *A dye-sensitized nano-porous solid-state photovoltaic cell.* Semiconductor Science and Technology, 1995. **10**(12): p. 1689-1693.
46. Tennakone, K., et al., *An efficient dye-sensitized photoelectrochemical solar cell made from oxides of tin and zinc.* Chemical communications, 1999(1): p. 15-16.
47. Taguchi, T., et al., *Improving the performance of solid-state dye-sensitized solar cell using MgO-coated TiO2 nanoporous film.* Chemical communications, 2003(19): p. 2480-2481.
48. Konno, A., et al., *The effect of particle size and conductivity of CuI layer on the performance of solid-state dye-sensitized photovoltaic cells.* Current Applied Physics, 2005. **5**(2): p. 149-151.
49. Bach, U., et al., *Solid-state dye-sensitized mesoporous TiO2 solar cells with high photon-to-electron conversion efficiencies.* Nature, 1998. **395**(6702): p. 583-585.
50. Bandara, J. and H. Weerasinghe, *Solid-state dye-sensitized solar cell with p-type NiO as a hole collector.* Solar Energy Materials & Solar Cells, 2005. **85**(3): p. 385-390.
51. Sakamoto, H., et al., *Highly efficient all solid state dye-sensitized solar cells by the specific interaction of CuI with NCS groups II. Enhancement of the photovoltaic characteristics.* Organic Electronics, 2012. **13**(3): p. 514-518.

52. Chung, I., et al., *All-solid-state dye-sensitized solar cells with high efficiency.* Nature, 2012. **485**(7399): p. 486-498.
53. Liu, X.Z., et al., *An Efficient Organic-Dye-Sensitized Solar Cell with in situ Polymerized Poly(3,4-ethylenedioxythiophene) as a Hole-Transporting Material.* Advanced Materials, 2010. **22**(20): p. E150-E155.
54. Kim, J., et al., *Enhanced Performance of I2-Free Solid-State Dye-Sensitized Solar Cells with Conductive Polymer up to 6.8%.* Advanced Functional Materials, 2011. **21**(24): p. 4633-4639.
55. Guo, X., et al., *High efficiency polymer solar cells based on poly(3-hexylthiophene)/indeneC70 bisadduct with solvent additive.* Energy & Environmental Science, 2012. **5**: p. 7943-7949.
56. Fabregat-Santiago, F., et al., *Electron Transport and Recombination in Solid-State Dye Solar Cell with Spiro-OMeTAD as Hole Conductor.* Journal of the American Chemical Society, 2009. **131**(2): p. 558-562.
57. Burschka, J., et al., *Tris(2-(1H-pyrazol-1-yl)pyridine)cobalt(III) as p-Type Dopant for Organic Semiconductors and Its Application in Highly Efficient Solid-State Dye-Sensitized Solar Cells.* Journal of the American Chemical Society, 2011. **133**(45): p. 18042-18045.
58. Abate, A., et al., *Lithium salts as "redox active" p-type dopants for organic semiconductors and their impact in solid-state dye-sensitized solar cells.* Physical Chemistry Chemical Physics, 2013. **15**(7): p. 2572-2579.
59. Abate, A., et al., *Anisotropic ionic conductivity in fluorinated ionic liquid crystals suitable for optoelectronic applications.* Journal of Materials Chemistry A, 2013. **1**(22): p. 6572-6578.
60. Planells, M., et al., *Diacetylene bridged triphenylamines as hole transport materials for solid state dye sensitized solar cells.* Journal of Materials Chemistry A, 2013. **1**(23): p. 6949-6960.
61. Nazeeruddin, M.K., et al., *Investigation of sensitizer adsorption and the influence of protons on current and voltage of a dye-sensitized nanocrystalline TiO2 solar cell.* Journal of Physical Chemistry B, 2003. **107**(34): p. 8981-8987.
62. Robertson, N., *Optimizing dyes for dye-sensitized solar cells.* Angewandte Chemie, 2006. **45**(15): p. 2338-2345.
63. Yan, S.G. and J.T. Hupp, *Semiconductor-based interfacial electron-transfer reactivity: Decoupling kinetics from pH-dependent band energetics in a dye-sensitized titanium dioxide aqueous solution system.* Journal of Physical Chemistry, 1996. **100**(17): p. 6867-6870.
64. Tachibana, Y., et al., *Modulation of the rate of electron injection in dye-sensitized nanocrystalline TiO2 films by externally applied bias.* Journal of Physical Chemistry B, 2001. **105**(31): p. 7424-7431.
65. Wolfbauer, G., et al., *Experimental and theoretical investigations of the effect of deprotonation on electronic spectra and reversible potentials of photovoltaic sensitizers: Deprotonation of cis-L(2)RuX(2) (L=2,2 '-bipyridine-4,4 '-dicarboxylic acid; X = CN(-), NCS(-)) by electrochemical reduction at*

platinum electrodes. Journal of the American Chemical Society, 2000. **122**(1): p. 130-142.
66. Nazeeruddin, M.K., et al., *Acid-Base Equilibria of (2,2'-Bipyridyl-4,4'-dicarboxylic acid)ruthenium(II) Complexes and the Effect of Protonation on Charge-Transfer Sensitization of Nanocrystalline Titania.* Inorganic Chemistry, 1999. **38**(26): p. 6298-6305.
67. Wang, P., et al., *High efficiency dye-sensitized nanocrystalline solar cells based on ionic liquid polymer gel electrolyte.* Chemical communications, 2002(24): p. 2972-2973.
68. Wang, P., et al., *Stable new sensitizer with improved light harvesting for nanocrystalline dye-sensitized solar cells.* Advanced Materials, 2004. **16**(20): p. 1806-1811.
69. Nazeeruddin, M.K., et al., *DFT-INDO/S modeling of new high molar extinction coefficient charge-transfer sensitizers for solar cell applications.* Inorganic Chemistry, 2006. **45**(2): p. 787-797.
70. Gao, F., et al., *Enhance the optical absorptivity of nanocrystalline TiO(2) film with high molar extinction coefficient ruthenium sensitizers for high performance dye-sensitized solar cells.* Journal of the American Chemical Society, 2008. **130**(32): p. 10720-10728.
71. Gao, F.F., et al., *A new heteroleptic ruthenium sensitizer enhances the absorptivity of mesoporous titania film for a high efficiency dye-sensitized solar cell.* Chemical communications, 2008(23): p. 2635-2637.
72. Gao, F.F., et al., *Conjugation of Selenophene with Bipyridine for a High Molar Extinction Coefficient Sensitizer in Dye-Sensitized Solar Cells.* Inorganic Chemistry, 2009. **48**(6): p. 2664-2669.
73. Handa, S., et al., *Reducing charge recombination losses in solid state dye sensitized solar cells: the use of donor-acceptor sensitizer dyes.* Chemical communications, 2007(17): p. 1725-1727.
74. Nazeeruddin, M.K., et al., *Engineering of efficient panchromatic sensitizers for nanocrystalline TiO2-based solar cells.* Journal of the American Chemical Society, 2001. **123**(8): p. 1613-1624.
75. Barolo, C., et al., *Synthesis, characterization, and DFT-TDDFT computational study of a ruthenium complex containing a functionalized tetradentate ligand.* Inorganic Chemistry, 2006. **45**(12): p. 4642-4653.
76. Chou, C.C., et al., *Ruthenium(II) Sensitizers with Heteroleptic Tridentate Chelates for Dye-Sensitized Solar Cells.* Angewandte Chemie-International Edition, 2011. **50**(9): p. 2054-2058.
77. Wu, K.L., et al., *Dye sensitized solar cells with cobalt and iodine-based electrolyte: the role of thiocyanate-free ruthenium sensitizers.* Journal of Materials Chemistry A, 2014. **2**(45): p. 19556-19565.
78. Nazeeruddin, M.K., et al., *Application of metalloporphyrins in nanocrystalline dye-sensitized solar cells for conversion of sunlight into electricity.* Langmuir, 2004. **20**(15): p. 6514-6517.
79. Wang, Z.S., et al., *A high-light-harvesting-efficiency coumarin dye for stable dye-sensitized solar cells.* Advanced Materials, 2007. **19**(8): p. 1138-1141.

80. Hagfeldt, A., et al., *Dye-Sensitized Solar Cells.* Chemical Reviews, 2010. **110**(11): p. 6595-6663.
81. Khazraji, A.C., et al., *Controlling dye (Merocyanine-540) aggregation on nanostructured TiO2 films. An organized assembly approach for enhancing the efficiency of photosensitization.* Journal of Physical Chemistry B, 1999. **103**(22): p. 4693-4700.
82. Wang, Z.S., et al., *Hexylthiophene-functionalized carbazole dyes for efficient molecular photovoltaics: Tuning of solar-cell performance by structural modification.* Chemistry of Materials, 2008. **20**(12): p. 3993-4003.
83. Yang, J.B., et al., *Influence of the Donor Size in D-pi-A Organic Dyes for Dye-Sensitized Solar Cells.* Journal of the American Chemical Society, 2014. **136**(15): p. 5722-5730.
84. Pei, K., et al., *Constructing High-Efficiency D-A-pi-A-Featured Solar Cell Sensitizers: a Promising Building Block of 2,3-Diphenylquinoxaline for Antiaggregation and Photostability.* Acs Applied Materials & Interfaces, 2013. **5**(11): p. 4986-4995.
85. Ning, Z.J. and H. Tian, *Triarylamine: a promising core unit for efficient photovoltaic materials.* Chemical Communications, 2009(37): p. 5483-5495.
86. Ning, Z.J., Y. Fu, and H. Tian, *Improvement of dye-sensitized solar cells: what we know and what we need to know.* Energy & Environmental Science, 2010. **3**(9): p. 1170-1181.
87. Ning, Z.J., et al., *Starburst triarylamine based dyes for efficient dye-sensitized solar cells.* Journal of Organic Chemistry, 2008. **73**(10): p. 3791-3797.
88. Ning, Z.J., et al., *Photovoltage Improvement for Dye-Sensitized Solar Cells via Cone-Shaped Structural Design.* Journal of Physical Chemistry C, 2009. **113**(23): p. 10307-10313.
89. Abate, A., et al., *An Organic "Donor-Free" Dye with Enhanced Open-Circuit Voltage in Solid-State Sensitized Solar Cells.* Advanced Energy Materials, 2014. **4**(13): p. 1400166.
90. Zhang, S.F., et al., *Highly efficient dye-sensitized solar cells: progress and future challenges.* Energy & Environmental Science, 2013. **6**(5): p. 1443-1464.

Chapter 2 Experimental Methods

1 General techniques

To confirm the structure of each dye synthesised, a variety of techniques was used, including NMR spectroscopy, mass spectrometry, elemental analysis, IR spectroscopy and X-ray crystallography.

1.1 General experimental details

^{1}H NMR, ^{13}C NMR, 2D COSY and 2D NOESY spectroscopy were performed on Bruker 400 MHz, 500 MHz or 600 MHz FT-NMR spectrometers. The reported chemical shifts were against TMS. Electron Ionization Mass Spectrometry (EI-MS), Electrospray Ionisation Mass Spectrometry (ESI-MS) and Fast Atom Bombardment Mass Spectrometry (FAB-MS) were recorded on ThermoElectron MAT 900. Elemental analyses were carried out by Stephen Boyer at London Metropolitan University using a Carlo Erba CE1108 Elemental Analyser. Crystals of ruthenium complexes were grown by slow diffusion from acetone/hexane. Single crystal data were collected using Cu-Kα radiation (λ=1.54184Å) on a Bruker Smart Apex CCD diffractometer equipped with an Oxford Cryostreams low temperature device operating at 120 K. The structure was solved by Patterson synthesis and refined by Full-matrix least-squares on F^2.[1] Figures were prepared using the programme Mercury.[2]

2 Electronic Absorption Spectroscopy

2.1 The technique

Electronic absorption spectroscopy is a very useful tool to study the photophysical properties of dyes.

In Ru complexes, metal-centred excitations (d-d), ligand centred transitions (π-π*) and metal to ligand charge transfer (MLCT) are commonly observed. In organic dyes, we usually find a mixture of π-π* transitions and intramolecular charge transfer (CT). Bands observed in the UV-vis spectrum each have their particular band-widths and intensities. These are determined by the nature of the transitions, thus can provide information about the electronic processes and the vibronic coupling nature of the molecules.

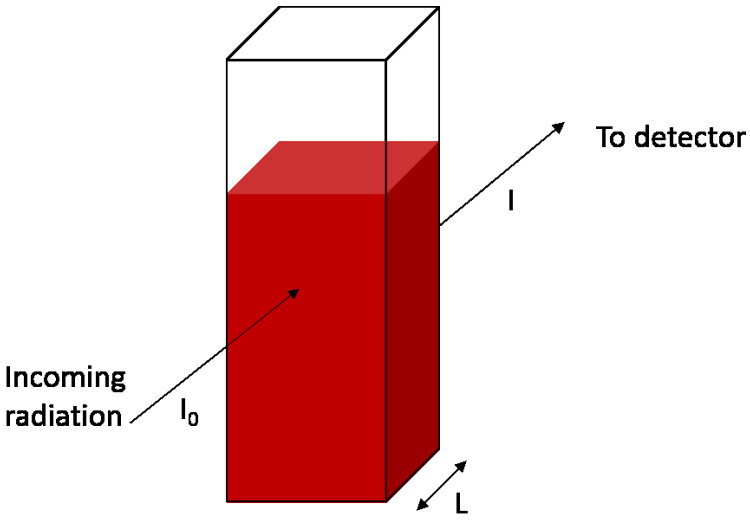

Figure 2.1 The set-up of an absorption spectroscopy experiment. I_0 is the incident light; I is the light transmitted through sample; L is the cuvette length in cm.

This technique works by passing a beam of light through the sample (Figure 2.1). The intensity of the light which is transmitted through the sample (I) is compared with the original intensity (I_0). The ratio is called transmittance, T, which is shown in Equation 2.1. Thus the absorbance (A) can be calculated according to Equation 2.2. By plotting the absorbance against the wavelength of light, a UV-vis spectrum is obtained.

$$T = I / I_0 \qquad \text{Equation 2.1}$$

$$A = -log_{10} T \qquad \text{Equation 2.2}$$

It is also important to determine the probability of an electronic transition occurring, which shows as the intensity of a band in the UV-vis spectrum. The Beer-Lambert Law is used to measure the molar absorption coefficient, Ɛ. (Equation 2.3)

$$A = \varepsilon cl \qquad \text{Equation 2.3}$$

Where c is the concentration of the sample and l is the path length.

Usually, a graph of absorbance against concentration is plotted and the molar extinction co-efficient is calculated by determining the gradient of the resulting straight line. For example, in Figure 2.2, the extinction coefficient is determined to be 4.1×10^4 M^{-1} cm^{-1}. If the Beer-Lambert plot turns out to be non-linear, then it means the absorption is independent of concentration. This can happen when i) the molecules aggregate in the solution, which is common for organic molecules at high concentration; ii) the sample is not fully dissolved in the solution. Measuring the UV-vis at a low concentration can usually avoid this.

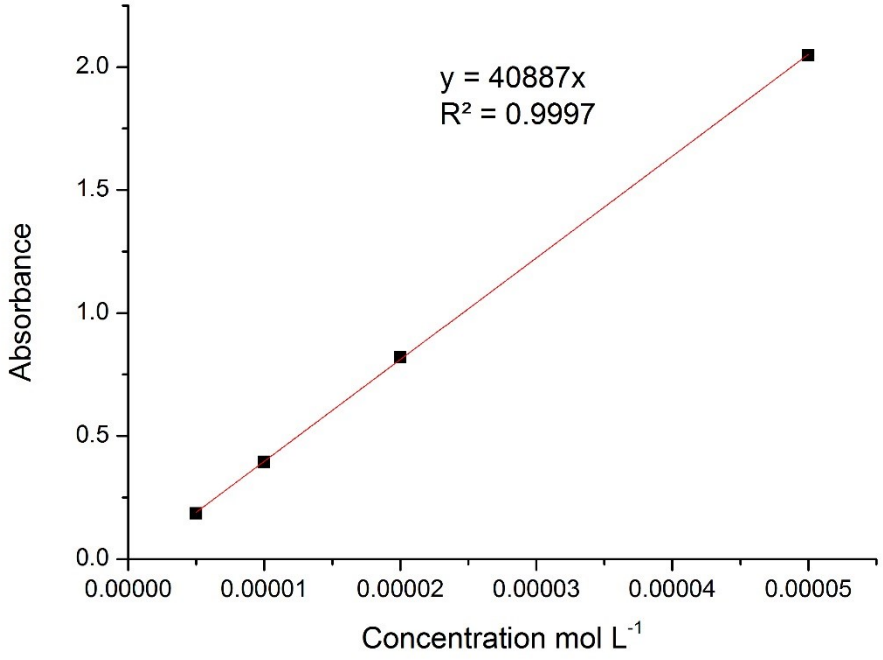

Figure 2.2 An example of a Beer-Lambert plot

2.2 Experimental details

UV-Visible absorption spectra were recorded using Jasco V-670 UV/Vis/NIR spectrophotometer controlled using the Spectra Manager software. All measurements were made using a quartz cell of 1 cm path length at room temperature using methanol, dichloromethane, acetonitrile, dimethylformamide, dimethylsulfoxide or chloroform as the solvents. The molar absorption coefficient was calculated by a Beer-Lambert plot.

3 Photoluminescence

3.1 The technique

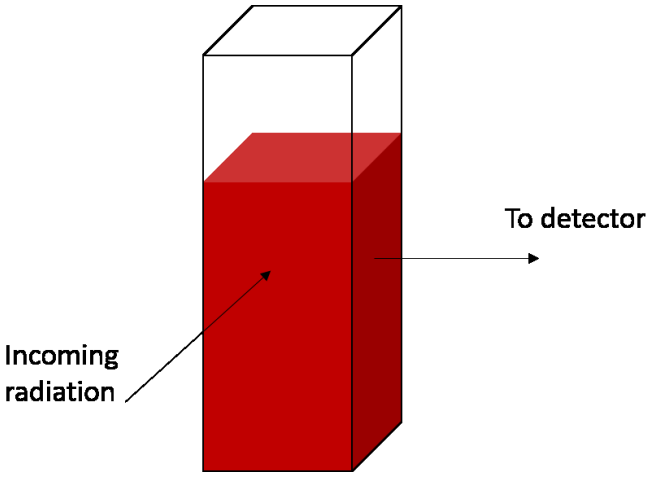

Figure 2.3 The set-up of an emission spectroscopy experiment.

After excitation, the excited state relaxes back to the ground state by various relaxation processes, namely, non-radiative decay or radiative decay. By using a fluorimeter, radiative decay can be measured by determining the energy of an emitted photon. It uses a monochromator to stimulate electronic excitation at a particular wavelength and an emission spectrum is produced when the detector collects the photons emitted across a range of wavelengths. On the contrary, an excitation spectrum can be produced if the fluorimeter is set to stimulate excitation across a range of wavelengths and only measure the emission of photons at a particular energy. (Figure 2.3) Generally, the excitation spectrum is similar to the absorption spectrum measured by UV-vis spectroscopy.

When an organic dye molecule is excited by an incoming photon, the electrons move from the ground state to the excited singlet states (S_1, S_2 …), followed by vibrational relaxation and internal conversion of excited state electrons to the lowest energy level and eventually emit back to the ground state. This is known as Kasha's rule, which can also be stated as the emission wavelength is independent of the excitation wavelength.[3]

On the other hand, due to a significant mixing of singlet and triplet excited states in ruthenium complexes, the excited photon undergoes an intersystem crossing process into the triplet state, which has a lower energy than the singlet state. Then the photon again, may relax either vibrationally or emit light by phosphorescence. Phosphorescence can be quenched by oxygen, therefore, measurement of frozen dye solutions from which oxygen is removed is usually required to observe phosphorescence. All these processes can be summarized in a Jablonski diagram. (Figure 2.4)

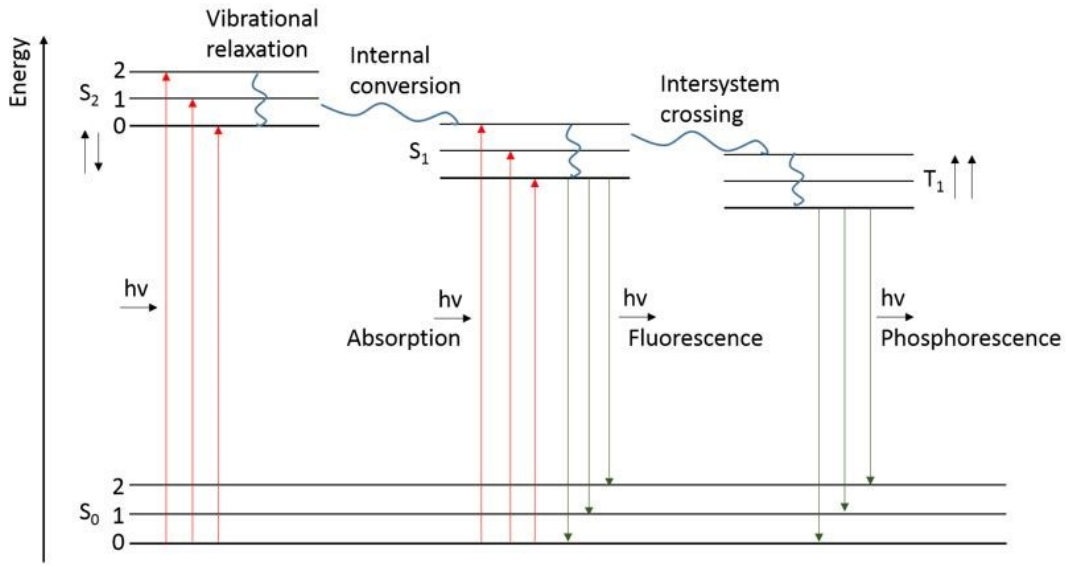

Figure 2.4 A Jablonski diagram

3.2 Experimental details

Photoluminescence (PL) spectra were recorded with Fluoromax-3 fluorimeter controlled by the ISAMain software. All samples were measured in a 1 cm cell. The PL of organic dyes was performed in dichloromethane at room temperature while the PL of ruthenium dyes was performed by Dr. Irene Sanchez-Molina in Imperial College.

4 Electrochemistry

Electrochemistry is very important in dye characterisation. It can not only provide information of the energy levels of the novel dyes, but also can test the reversibility of redox processes. In order for a dye to function in a solar cell, the dye needs to have the right energy levels to inject electrons into the TiO_2 conduction band and to regenerate by I^- in the electrolyte. During injection, the excited state dye is oxidized and during regeneration, the oxidized dye is reduced by I^-. This corresponds to the oxidation process and re-reduction process of the dye measured in electrochemistry.

4.1 The three electrode system

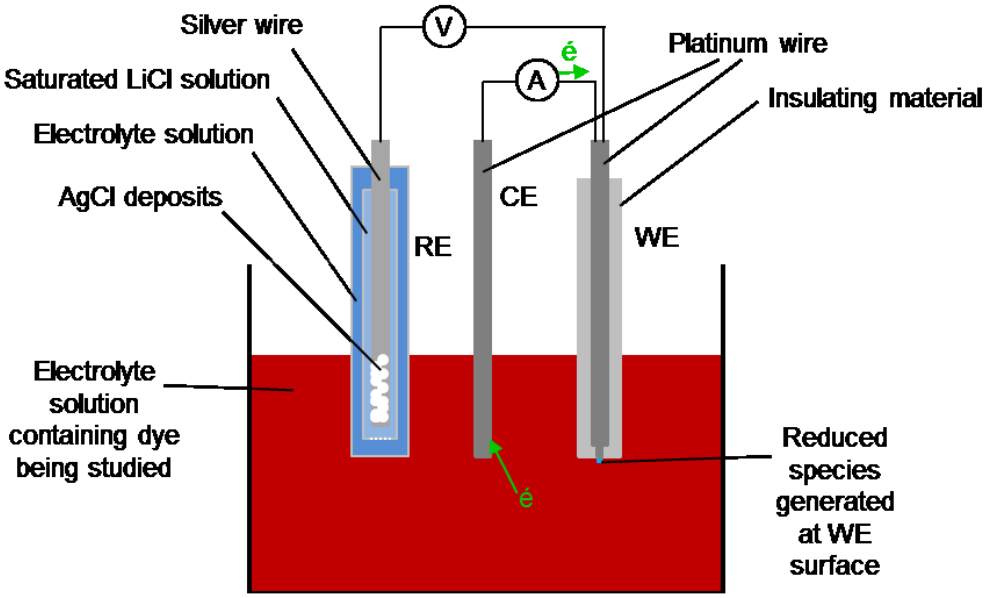

Figure 2.5 The three electrode system. Reproduced from reference [4].

The three-electrode system, shown above (Figure 2.5), is the most common method of measuring electrochemistry. In a three electrode system, three electrodes are used, a working electrode, a counter electrode and a reference electrode. The reference electrode has a known potential. The high stability of the electrode potential is realized by employing a redox system with excess amount of each component of the redox reaction. The one in this work is a Ag/AgCl reference electrode which has a silver wire coated with a thin layer of silver chloride and surrounded by saturated

LiCl solution. So the electrode functions as a redox electrode and the reaction is between the silver metal and silver chloride, as follows.

$$AgCl\ (s) + e^- \leftrightarrow Ag(s) + Cl^- \qquad \text{Equation 2.4}$$

The working electrode is where the redox reactions of molecules take place. Common working electrodes consist of materials such as gold, silver, platinum or glassy carbon. The one used in this work is a platinum wire with a small surface area. Finally, a counter electrode, with high surface area, is connected with the working electrode to modulate the charge at the working electrode. The reference electrode is not able to do this job because a constant and known potential cannot be maintained when redox processes take place at the reference electrode. Large surface area of counter electrode is used to ensure that the half-reaction occurring at the counter electrode can occur fast enough as so not to limit the process at the working electrode. Therefore, the current is measured across the counter and working electrodes. The electrodes are all connected by the electrolyte solution.

During the electrochemical process, mass transfers from the solution to the electrode surface and reacts there, then the resulting product transfers from the electrode surface to the bulk solution. There are three mass transfer regimes, including diffusion, migration and convection. The electrolyte solution ensures that the electroactive species is not affected by migration.

In this thesis, three electrochemistry techniques are used, namely, cyclic voltammetry (CV), differential pulse voltammetry (DPV) and square wave voltammetry (SWV).

4.2 Cyclic Voltammetry

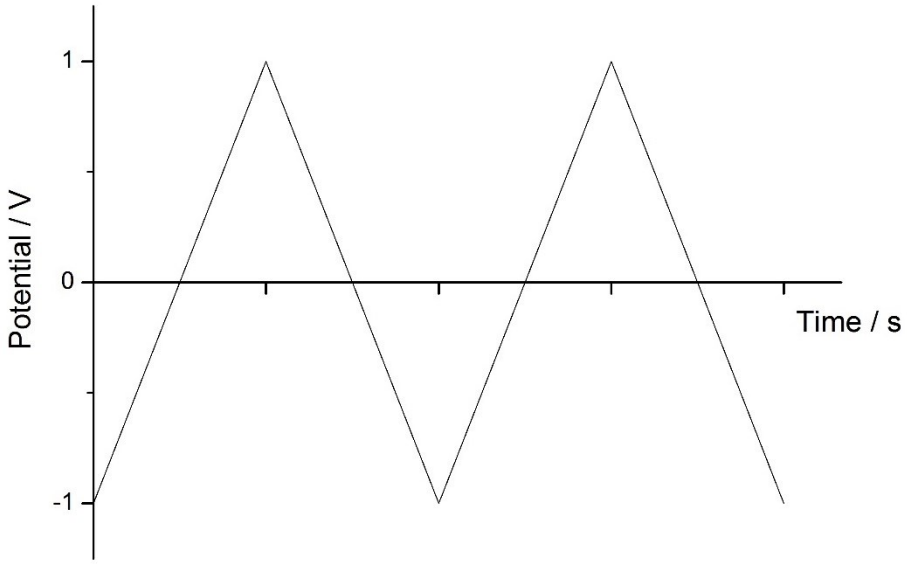

Figure 2.6 The waveform used for cyclic voltammetry

Cyclic voltammetry is performed by cycling the potential of the working electrode and measuring the resulting current. (Figure 2.6) Current against applied voltage is then plotted. In Figure 2.7, the oxidation process occurs when the potential is scanned positively. Initially there is no current as the potential applied is insufficient to oxidize the sample (point a). With further scan, the oxidation process begins and leads to an exponential rise of current (point b). When more oxidized species accumulate between the surface of the working electrode and the bulk phase, a diffusion layer is created and prevents the non-oxidized species from reaching the electrode. Thus, at some point, all the substrate on the surface of the working electrode is oxidized and a peak current (point c) is reached. This resulting current is called the anodic peak current (i_{pa}) and the corresponding peak potential is called the anodic peak potential (E_{pa}). Then the current begins to decrease as the mass transport becomes the limiting factor (point d). When the potential is switched, the oxidized substrate stays in the oxidised form until the applied potential is sufficient to re-reduce the oxidized species (point e). The peak resulting from this process is characterised by the cathodic peak current (i_{pc}) and cathodic peak potential (E_{pc}),

respectively. The standard electrochemical potential for a process ($E_{1/2}$) is calculated then according to Equation 2.5.

$$E_{1/2} = (E_{pa} + E_{pc}) / 2 \qquad \text{Equation 2.5}$$

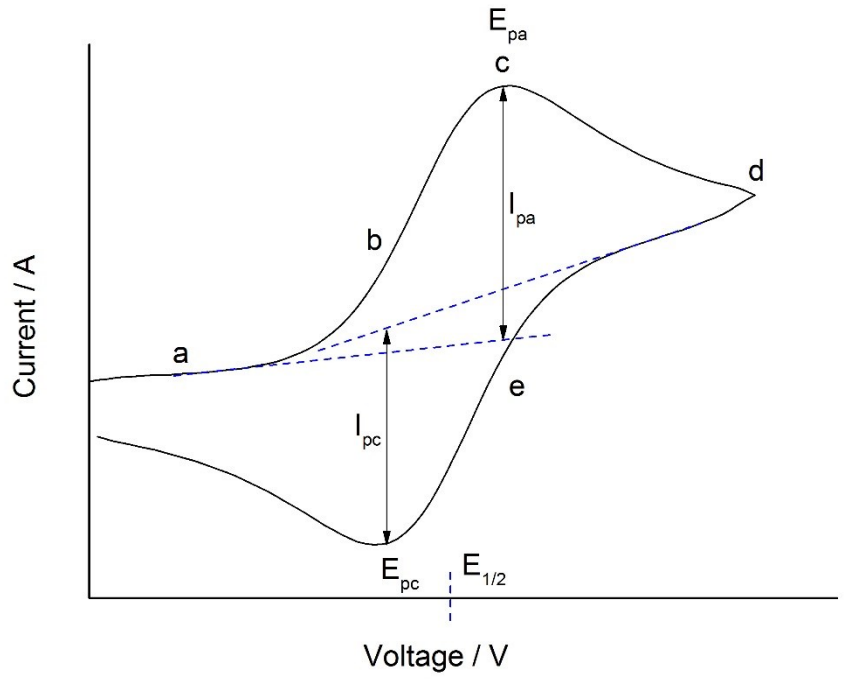

Figure 2.7 A reversible cyclic voltammgram

For a reversible electrochemical reaction, the CV recorded has a few well defined characteristics.

1) The ratio of the peak currents is equal to one.

$$i_{pa} = i_{pc} \qquad \text{Equation 2.6}$$

2) The voltage separation between the current peaks is

$$E_{pa} - E_{pc} = 59/n \text{ mV} \qquad \text{Equation 2.7}$$

Where n is the number of electrons transferred.

3) The positions of E_{pa} and E_{pc} do not change with different scan rates.
4) The peak currents are proportional to the square root of the scan rate, in other words, there is a linearity relationship between the square root of the scan rate and the peak current.

If the reaction is electrochemically irreversible, the separation of E_{pa} and E_{pc} will increase with increasing scan rates because the electron transfer rate is slower than

the timescale of the experiment. If the reaction is chemically irreversible, the electrochemically produced product cannot return to its original form, thus no return peak can be observed.[5]

4.3 Differential Pulse Voltammetry

In a differential pulse voltammetry, the potential of the working electrode is stepped from the initial potential to the final potential. A profile of this potential versus time waveform is shown in Figure 2.8. The current is sampled twice during a single pulse, once just before the application of a pulse (i_1), once at the end of the pulse (i_2). The current difference (i_2 - i_1) is plotted against potential to give a voltammogram that displays redox processes with characteristic peaks. This decreases the effect of the charging current and results in enhanced sensitivity as compared with cyclic voltammetry. It is very useful at separating the overlapping peaks that may be shown in a cyclic voltammetry experiment.

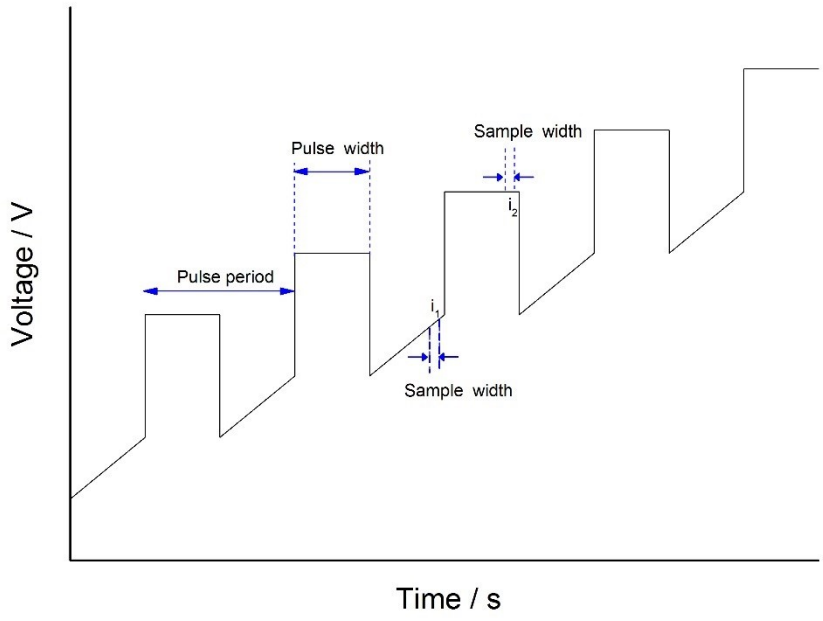

Figure 2.8 The waveform used for differential pulse voltammetry

The voltage at the peak current in differential pulse voltammetry is the same with $E_{1/2}$ in cyclic voltammetry. In differential pulse voltammetry, reversible reactions

show symmetrical peaks. Irreversible reactions show asymmetrical peaks. The return peak usually shifts to more extreme potentials, with a broader peak. An example of differential pulse voltammetry can be seen in Figure 2.9.

Differential pulse is a very useful technique. However, the scan rate of this is typically at 0.02 V/s. It takes more time than a cyclic voltammetry and may lead to problems if the sample produces unstable products in electrochemistry.

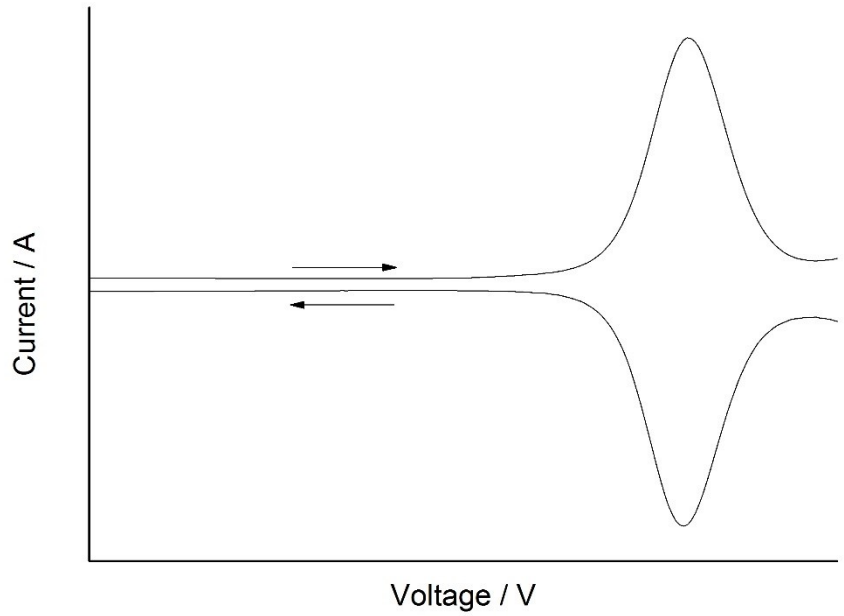

Figure 2.9 An example of differential pulse voltammetry

4.4 Square Wave Voltammetry

The waveform of square wave voltammetry is shown in Figure 2.10. The current is sampled at the end of the forward potential pulse as well as at the end of the reverse potential pulse.

Comparing to a normal differential pulse voltammetry, square wave voltammetry is not only more sensitive and more precise, but also faster to perform. The

voltammogram of square wave voltammetry is very similar to the one of differential pulse.

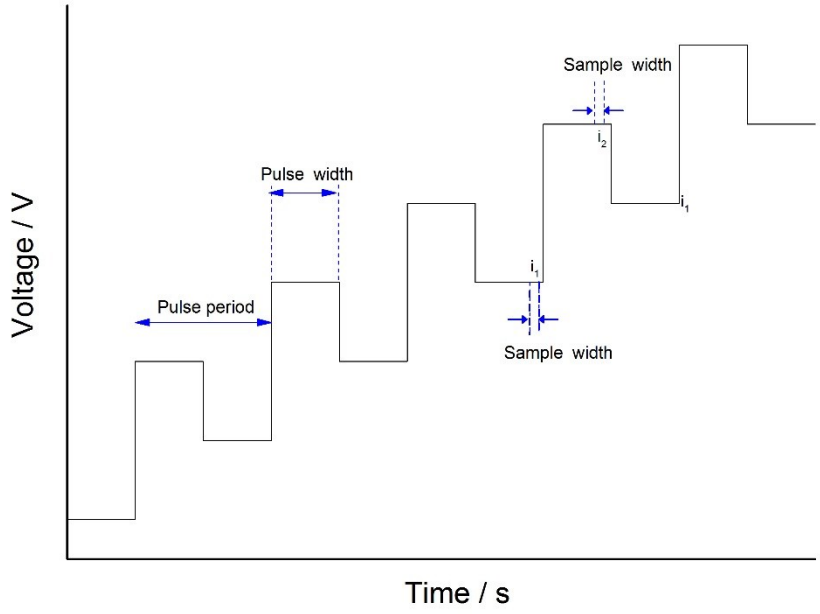

Figure 2.10 The waveform used for square wave voltammetry

4.5 Experimental details

Electrochemical studies were obtained by cyclic voltammetry (CV), differential pulse voltammetry (DPV) and square wave voltammetry (SWV) using a μ autolab type III potentistat, controlled using General Purpose Electrochemical System (GPES) software. A platinum rod counter electrode, a 0.5 mm diameter platinum working electrode and a Ag/AgCl reference electrode were used. The experiment was carried out in a cell sealed with a Teflon lid. Three electrodes were submerged in the electrolyte solution. Oxygen was removed using a nitrogen bubbler to bubble nitrogen gently for 15 minutes before testing. Ferrocene/ferrocenium (Fc/Fc^+) redox couple was used as an internal standard. Tetrabutylammonium tetrafluoroborate ($TBABF_4$) or tetrabutylammonium hexafluorophosphate was used as the supporting electrolyte. The experiment was performed in nitrogen purged 0.1 M $[TBA]^+[BF_4]^-$

or 0.1 M $[TBA]^+[BF_6]^-$ solution in acetonitrile or 0.3 M $[TBA]^+[BF_6]^-$ in DCM. The data were recorded against ferrocene and converted to NHE by addition of 0.63V.

5 Computational Studies

An increasing importance of computational calculation has been seen in chemistry in recent years. It can be used to give theoretical support to experimental results. In the case of sensitisers in sensitised solar cells, computation studies can provide approximate values of the energies of highest occupied molecular orbitals (HOMOs), lowest unoccupied molecular orbitals (LUMOs) and other orbitals. It can also give information about how much each component of the molecule contributes to the molecular orbitals.

5.1 *Ab Initio* Molecular Orbital Theory

$$\hat{H}\psi = E\psi \qquad \text{Equation 2.8}$$

The term '*Ab Initio*' is Latin for 'from the beginning'. It is a quantum mechanics approach of theoretical modelling of a molecule. The principal aim is to solve the Schrödinger equation, shown in Equation 2.8. $\hat{H}$ is the Hamiltonian operator, which includes all energy in a system, it operates on ψ, which is the wavefunction, to determine permitted energy levels (E) of a molecule. However, the Schrödinger equation can only be solved for the hydrogen atom exactly. For systems with more than one electron, approximations have to be made to find a solution. Several basic approximations are made in the *ab initio* calculation. The first one is called Born-Oppenheimer approximation. By considering this approximation, nuclei are stationary and therefore we only need to consider the movement of the electrons. The second theory is called Hartree theory. All the nuclear and electronic motions are decoupled and treated separately. As a consequence, the total energy of the system is a sum of the nuclear energy with the electronic energy. However, Hartree theory does not consider Pauli's exclusion principle, in which two electrons cannot have the same spin in an orbital. To solve this problem, another theory called Fock theory, is

combined with Hartree theory. This is known as Hartree-Fock theory. In this case electron exchange is acknowledged, so a good approximation of the overall energy of the system is obtained. Hartree-Fock theory is the most basic level of *ab initio* calculation.

5.2 Density Functional Theory (DFT)

Density functional theory (DFT) is a computational quantum mechanical modelling method based only on spatial coordinates. It is among the most popular and versatile methods in computational chemistry. The approximations most commonly used in chemistry are generalised gradient approximations, including LYP, PW91 and so on. DFT approximates e^-/e^- correlation and e^-/e^- exchange while HF theory ignores e^-/e^- correlation and is exact in the e^-/e^- exchange. So usually, DFT is combined with HF theory to create hybrid DFT, like B3LYP. By doing this, we obtain approximates in e^-/e^- correlation and exact e^-/e^- exchange, which is accurate enough in many cases.

As discussed before, the Hamiltonian operator operates on ψ, the wavefunction. Based on Born-Oppenheimer approximation, nuclei are fixed, so the wavefunction actually describes the region of space where the electron is located. The most common way to do this is to approximate the atomic radial distribution functions (ARFs). These functions can be mimicked by sum a series of Gaussian functions, with varying exponents. (Equation 2.9) c is the weighting function. φ is the Gaussian function. The value of 'c' is varied until HF self-consistent field (SCF) energy is minimised. When it stops changing, the Ψ is optimised for that particular geometry. The collection of functions is described as a basis set.

$$\Psi = \sum_i c_i \varphi_i \qquad \text{Equation 2.9}$$

Basis sets are optimised for atoms, not molecules. When an atom becomes part of the molecule, the size, charge and shape may change. So polarisation functions and diffuse functions are added on the Guassian functions, labelling as '*' and '+', respectively. Some commonly used basis sets including 3-21G*, 6-31G*, 6-311G* and so on. The higher the numbers are, the better the basis set is. However, it also takes more time and money to calculate. For heavy atoms like ruthenium, effective

core potential basis set are used. These basis sets have the core electrons replaced by an effective potential to allow correct modelling of valence electrons. One of the most common used basis set for heavy metals is LANL2DZ. It is an effective core potential basis set, in which case the core electrons are replaced by an effective potential, so only the valence electrons need to be considered. This can help simplify the calculation of molecules containing heavy atoms (e.g. Ru).

5.3 Geometry Optimisation & Solvent Effect

In the geometry optimisation method, the positions of atoms in a molecule are iteratively adjusted. The potential energy surface (PES) is calculated after each adjustment until a stationary point is reached. In practice, calculating the molecule's minimum energy takes a lot of time and money, so the forces acting on the atoms are calculated instead to determine the gradient of energy with respect to their position, as in Equation 2.10.

$$dE / dx = kx \qquad \text{Equation 2.10}$$

However, when the gradient of PES is equal to zero, the stationary point reached may not be the minimum of the system, it can be a minimum, maximum or saddle point on the PES. In this case, a frequency calculation is carried out after the structure is optimised, which computes the force constants of the system, according to the 2nd derivative. (Equation 2.11). The minimum is indicated by the absence of any negative frequencies.

$$d^2E / dx^2 = k \qquad \text{Equation 2.11}$$

Generally geometry optimisations are performed in the gas phase or vacuum. However, in this work, no experiments were done with single molecule in vacuum. In order to compare the calculation more accurately with the experimental results, the geometry can be further optimised in the presence of a solvent. This can be achieved by incorporating a polarisable continuum model (PCM)[6] in the calculation. The PCM is a medium of specified dielectric constant, which describes a sphere of

solvent around the molecule with a given density and dielectric field. In more complicated systems where the molecule has some particular relationship with the solvent, such as the structures with strong dipole moments in polar or hydrogen-bonding solvents, PCM does not work very well. In those cases, calculations can require more complicated modelling of the solvent.

5.4 Time-Dependent Density Functional Theory (TD-DFT)

Time-dependent density functional theory (TD-DFT) is a quantum mechanical theory used to investigate the theoretical absorption spectrum, excitation energies and frequency-dependent response properties in the presence of time-dependent potentials, such as electric or magnetic fields. It is useful for explaining the appearance and origins of the electronic absorption peaks that are observed experimentally in the electronic absorption spectrum. Molecular orbital transitions can be assigned for each peak and compared with the experimental data.

Choosing the right functional is important in TDDFT because different functional usually gives totally different positions (wavelengths) of peaks. Although B3LYP has been used a lot, the failure of TDDFT using B3LYP method in highly delocalized charge transfer system has been reported, which is usually the case in the calculation of sensitisers for dye-sensitised solar cells. This is due to the fact that the exchange-correlation potentials generated by B3LYP functional decay too fast in the asymptotic region.[7] In a recent work, Tretiak and Magyar have reported the computational study of a series of D-π-A molecules with better correlation with experimental result.[8] By introducing a large fraction of HF exchange, they successfully corrected the asymptotic behaviour of the charge transfer states. The newly designed functional, long-range Coulomb attenuating method (CAM-B3LYP) comprised 19% of HF and 81% of B88 exchange at short-range and 65% of HF and 35% of B88 at long-range. CAM-B3LYP gives results better matching the experimental data, although it is never able to give fully accurate values.

In conclusion, TD-DFT is more useful in explaining the experimental results rather than predicting. What's more, it can be useful in qualifying trends exhibited within a series of compounds.

5.5 Experimental details

For Ru complexes, the molecular structures were optimised in vacuum, using the software Avogadro[9, 10] to enter the starting geometry. Then the structure was optimised using the methanol polarisable-continuum model, starting from the optimised structure from vacuum. All calculations were carried out using the Gaussian 09 program[11] with the Becke three parameter exchange functional with the Perdew Wang 1991 correlation functional (B3PW91)[12, 13] level of theory together with 6-31+G* basis set for C, H, N, O and S atoms. The Ru atom was treated with the Hay-Wadt VDZ (n+1) ECP basis set.[14-16] After running the frequency calculations, the molecular orbital isosurfaces were generated by Avogadro. This illustrates where the HOMO and LUMO are located on the molecules. The percentage of each orbital located on each atom of the entire molecule was obtained by 'getocc' input in Gaussian 09. Time-dependent DFT calculations (TD-DFT)[17, 18] were performed using Gaussian 09 program[11] with a methanol polarisable continuum model (PCM).[6] The 70 lowest singlet electronic transitions were calculated and processed with the GaussSum software package.[19] Calculations for the organic dyes were carried out in an analogous manner, using Lee-Yang-Parr for the correlation functional and 6-31+G* as the basis set. [20]

6 Solar Cells

6.1 Fabrication

6.1.1 Liquid-electrolyte Dye-sensitised Solar Cells

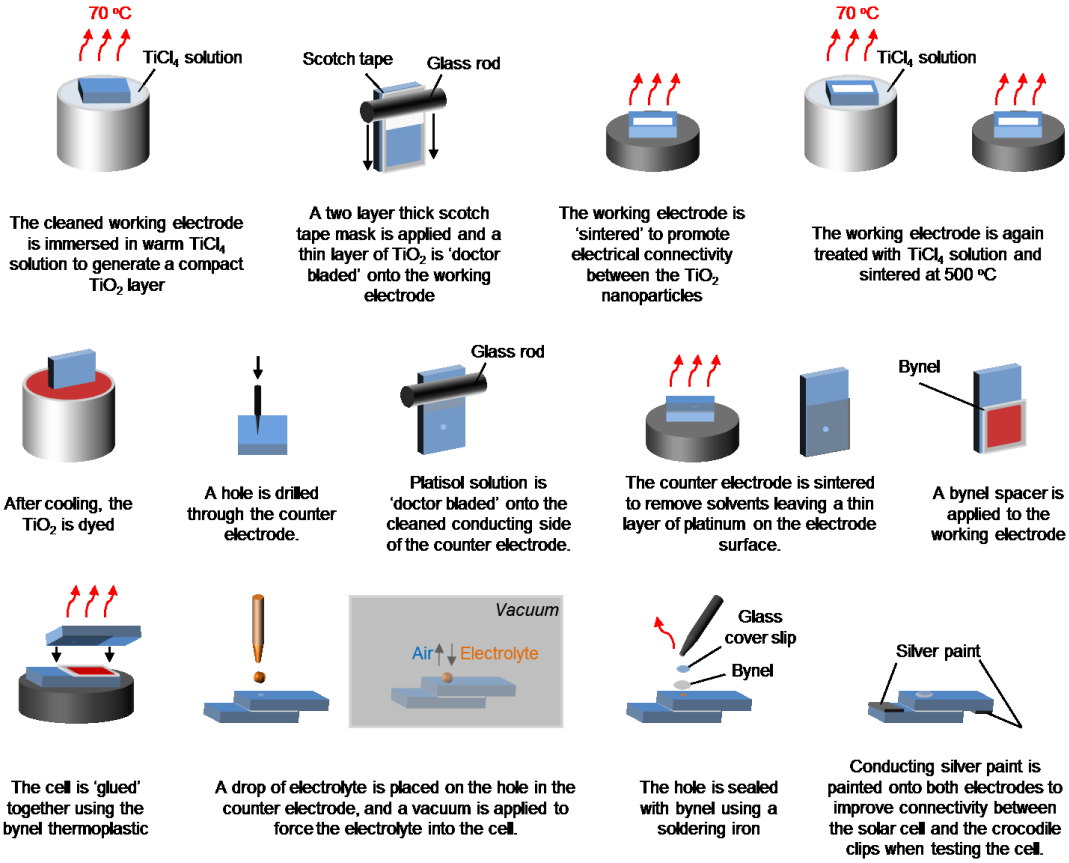

Figure 2.11 Fabrication of a dye-sensitised solar cell. Reproduced from reference [21]

To make the working electrode, a fluorine doped tin oxide (FTO) coated conductive glass (15 Ω/sq, Solaronix) was cut into 1.5 × 2.5 cm^2 plates and washed by sonication in detergent, distilled water, acetone and ethanol. The cleaned glass was pre-treated with a solution of $TiCl_4$ (40mM in water) at 75 ℃ for 30 mins, rinsed with water and ethanol. For cells based on ruthenium complexes, a film of titanium dioxide paste was coated onto the conductive side by doctor blading (shown in Figure 2.11). The liquid cells based on oligothiophene dyes and oligo-CPDT dyes were made by Dr. Aruna Ivaturi and Dr. Yiming Cao, respectively, using screen printing method (not shown in figure) to put on TiO_2 film. The film was then dried at

125℃ for 6 mins and gradually heated using the controllable hotplate (325℃ for 5 mins; 375℃ for 5 mins; 425℃ for 5 mins; 475℃ for 10 mins; 510℃ for 10 mins). The slides were allowed to cool to room temperature and post-treated with $TiCl_4$ (40mM in water) again at 75 ℃ for 30 mins and sintered at 500 ℃ for 30 mins. When the temperature dropped to about 80-100 ℃, the working electrode was put into dye solution and soaked for an amount of time. The concentration of dye solution and the soaking time for each dye will be indicated in later chapters. After that, the electrodes were removed and washed with ethanol, to remove any unbound dye.
Counter electrode was prepared by drilling a hole into pre-cut FTO glass (1.5 × 2.5 cm^2) and washed with distilled water, 0.1M HCl in ethanol and finally acetone. The electrode was heated at 400 ℃ for 15 mins both before and after a layer of Platisol solution was applied.

The solar cells were then assembled by superimposing the two electrodes together using thermal plastic (Surlyn) and an electrolyte was introduced into the hole and the hole was sealed by sticky tin foil. The electrolyte used was a mixture of 1-butyl-3-methylimidazolium iodide, I_2, 4-tert butylpyridine, guanidine in acetonitrile:valeronitrile (17:3). The concentration of each component will be indicated in later chapters.

6.1.2 Solid-state Dye-sensitised Solar Cells

After laser etching, the FTO substrates (15Ω/sq, Pilkington) were cleaned with Hellmanex (2% by volume in water), de-ionized water and ethanol. The last traces of organic residues were removed by a 15min UV-O_3 treatment. The FTO sheets were subsequently coated with a compact layer of TiO_2 by aerosol spray pyrolysis deposition at 450°C, using oxygen as the carrier gas. Films of 0.9μm thick mesoporous TiO_2 were then deposited by spin-coating a diluted commercial paste (Dyesol 30NR-D: ethanol = 2:3, by weight ratio). The TiO_2 films were slowly heated to 450°C and allowed to sinter for 30min in air. Once cooled down to 80°C, the substrates were immersed into a 0.2mM dye solution in 3:7 mixture of chloroform and ethanol, for 1h at room temperature. After the dyed films were rinsed in acetonitrile, the HTM layer was applied by spin-coating at 2000 rpm for 30s in dry

box. The solutions for spin coating consisted of (2,2',7,7'-tetrakis(N,N-di-p-methoxyphenylamine)-9,9-spirobifluorene) (spiro-MeOTAD, from Merck), lithium bis(trifluoromethylsulfonyl)imide (Li-TFSI, from Aldrich), 4-tertbutylpyridine (TBP, from Aldrich) and tris(2-(1H-pyrazol-1-yl)-4-tert-butylpyridine)-cobalt(III) tris(bis(trifluoromethylsulfonyl)imide) (FK209, from Dyenamo) in chlorobenzene. The concentration will be indicated in later chapters. Finally 80nm of gold was thermally evaporated on top of the device under high vacuum.

6.2 Testing the efficiency of the solar cells

6.2.1 Parameters used in determining the efficiency

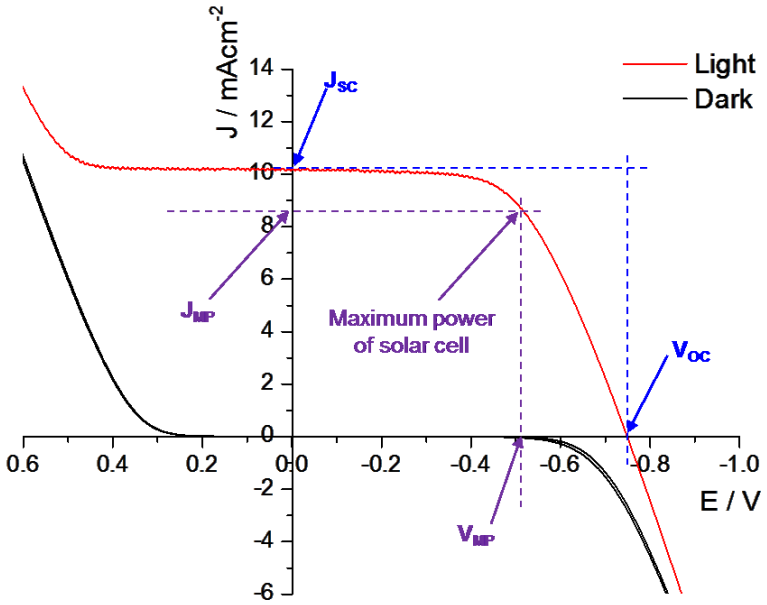

Figure 2.12 Typical J-V curves under light and dark

The efficiency (η) of a solar cell is determined by the ratio of the power generated by the cell to the solar power put into the cell. The power input is controlled by the light intensity of the lamp used for testing, which is set to be AM1.5 (1000W m^{-2}). During testing, a load voltage (V) is applied to the solar cell and current (I) produced is measured. As the current is dependent on the surface area, current density (J) is used instead of the current in practice and plot against voltage. (Figure 2.12) With the J-V curves, important parameters such as short-circuit current density (J_{SC}), open-circuit voltage (V_{OC}) and fill factor (FF) can be obtained. The product of these factors

determines the solar power conversion efficiency (η). The meanings of these parameters were discussed in Chapter 1.

6.2.2 Experimental details

For liquid cells, the working area of the liquid cells was masked to 0.1257 cm^2, and current-voltage characteristics in the dark and in the light were tested using the AUTOLAB PGSTAT30 potentiostat controlled by GPES version 4.9.007. AM 1.5 solar illumination (1000 Wm^{-2}) was provided by a Sciencetech Inc. solar simulator (Model SF150, 1kW Xe lamp) with an AM 1.5 filter (Müller). The power output was calibrated by a silicon diode; itself calibrated at 1000 Wm^{-2} by GBSOL. IPCE was measured two days after preparation by Dr. A. Orbelli Biroli from Istituto di Scienze e Tecnologie Molecolari del CNR (CNR-ISTM) in Italy.

The solid cells were fabricated and measured in EPFL. Current–voltage characteristics were recorded with a digital source meter (Keithley Model 2400). The light source was a 450W Xenon lamp (Oriel) equipped with a Schott K113 Tempax sunlight filter (Praezisions Glas und Optik GmbH) to match the emission spectrum of the lamp to the AM1.5G standard. Before each measurement, the exact light intensity was determined using a calibrated Si reference diode equipped with an infrared cut-off filter (KG-3, Schott). Analysis of the data and automated curve fitting was performed using Igor Pro data collection and analysis software. IPCE spectra were recorded as functions of wavelength under a constant white light bias of approximately 5mW cm^2 supplied by an array of white light-emitting diodes. The excitation beam coming from a 300W Xenon lamp (ILC Technology) was focused through a Gemini-180 double monochromator (Jobin Yvon Ltd) and chopped at approximately 2 Hz. The signal was recorded using a Model SR830 DSP Lock-In Amplifier (Stanford Research Systems). All measurements were conducted using a non-reflective metal mask of 0.16 cm^2 to define the active area of the device and avoid light scattering through the sides.

6.3 Electrochemical Impedance Spectroscopy (EIS)

6.3.1 The technique

In DSSC study, electrochemical impedance spectroscopy is used to investigate the properties and quality of whole devices or components such as blocking layers or platinum cathodes. It measures the frequency response of the device – the rate at which the current responds to a small perturbation at a certain applied voltage. The impedance response of a DSSC is related to the response of the various components of the device.

The measurements are relatively straightforward with a frequency response analyser (FRA). In contrast, the interpretation of the results is challenging due to the complicated structure of DSSC has. The data are usually analysed by fitting a model. The selection of a correct and appropriate equivalent circuit then becomes significantly important. An equivalent circuit of a DSSC is shown in Figure 2.13 which contains linear elements representing all of the processes taking place in the DSSC. [22] The mesoporous electrode can be modelled by a transmission line model [23] with a distributed network of resistive and capacitive elements that describes the transport, accumulation and recombination of electrons in the semiconductor phase of the cells. The impedance related with electron transport is in parallel with the transmission line. The impedance related with transport of ions in the electrolyte is modelled by a finite Warburg element. Other elements include the series resistance of the device and the charge-transfer resistance and interfacial capacitance at the counter electrode. This model allows the study of different interfaces in DSSCs separately, namely, the TiO_2/dye/electrolyte interface, FTO/TiO_2/electrolyte interface and counter electrode/electrolyte interface.

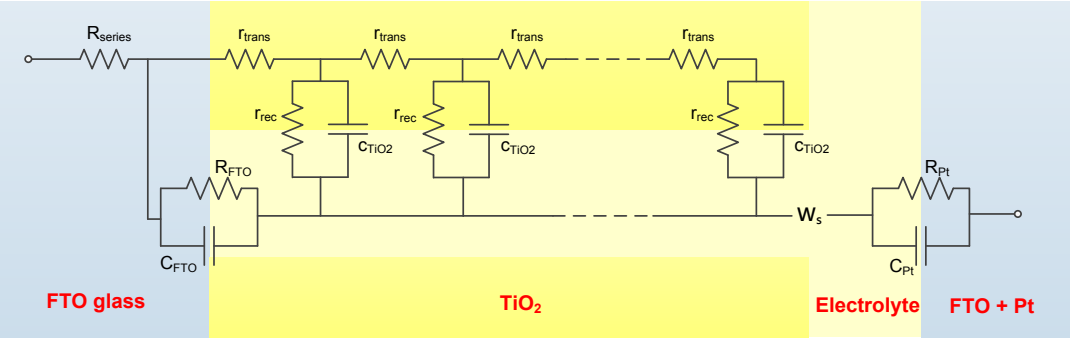

Figure 2.13 An equivalent circuit of the DSSC. R_{series} is the series resistance of the cell; R_{FTO} is the charge transfer resistance for electron recombination from the uncovered layer of the FTO to the electrolyte; C_{FTO} is the capacitance at the FTO/TiO_2/electrolyte interface; r_{trans} is the electron transport resistance; r_{rec} is the recombination resistance across the TiO_2/dye/electrolyte interface; c_{TiO2} is the chemical capacitance that represents the electron density as a function of the Fermi level; W_o is the Warburg impedance of electrolyte diffusion; R_{Pt} is the charge transfer resistance at the counter electrode/electrolyte interface; C_{Pt} is the capacitance at the counter electrode/electrolyte interface.

At high voltages, the TiO_2 film becomes conducting [22], so the resistance to transport through the TiO_2 film is negligible, thus the circuit can be simplified as Figure 2.14.

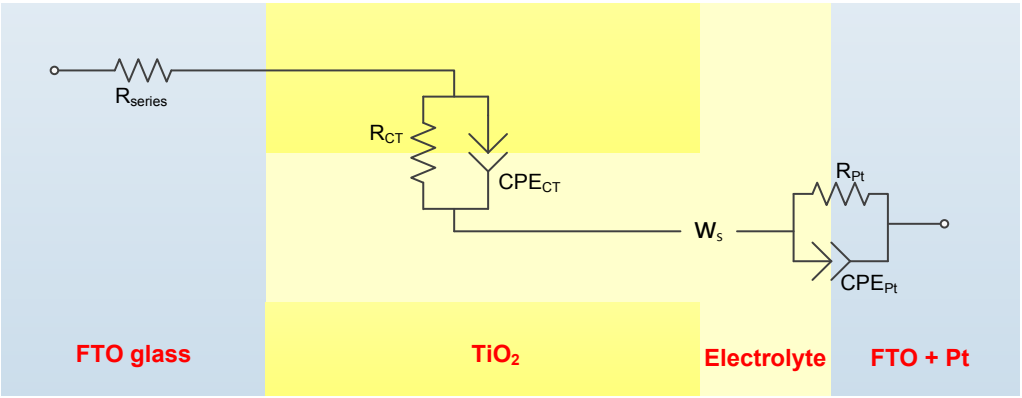

Figure 2.14 A simplified equivalent circuit of the DSSC. R_{series} is the series resistance of the cell; R_{CT} is the resistance to electron recombination; CPE_{CT} is the chemical capacitance that represents the electron density as a function of the Fermi level; W_o is Warburg impedance of electrolyte diffusion; R_{Pt} is the charge transfer resistance at the counter electrode/electrolyte interface; CPE_{Pt} is the capacitance at the counter electrode/electrolyte interface. In practice, a constant phase element (CPE) was used to model all capacitive processes to account for the ubiquitous dispersion observed in the measurements. [24]

One of the most common way of expressing the measured results is using Nyquist plots as shown in Figure 2.15. A typical Nyquist plot can be divided into three regions, namely, low, medium and high frequency regions.[25, 26] The first semi-circle (from the left) at high frequency represents the counter electrode/electrolyte interface, the second represents the TiO_2/dye/electrolyte interface and the third represents the electrolyte diffusion. As the only parameter varying in this study is the dye, the second semi-circle is the part of most interest. From a Nyquist plot, the resistance to an electron transfer process can be determined by measuring the diameter of the semi-circle representing that particular electron transfer process. The capacitance of that process is related to the height of the semi-circle and the imperfection of the capacitor is described by using a constant phase element. Another popular presentation method is the Bode plot. There are two kinds of Bode plot. In one kind, the impedance is plotted with log frequency on the x-axis and the absolute value of the impedance on the y-axis. (Figure 2.16 up) In the other, the phase-shift is plotted against the log frequency. (Figure 2.16 down) Unlike the Nyquist plot, the Bode plot explicitly shows frequency information.

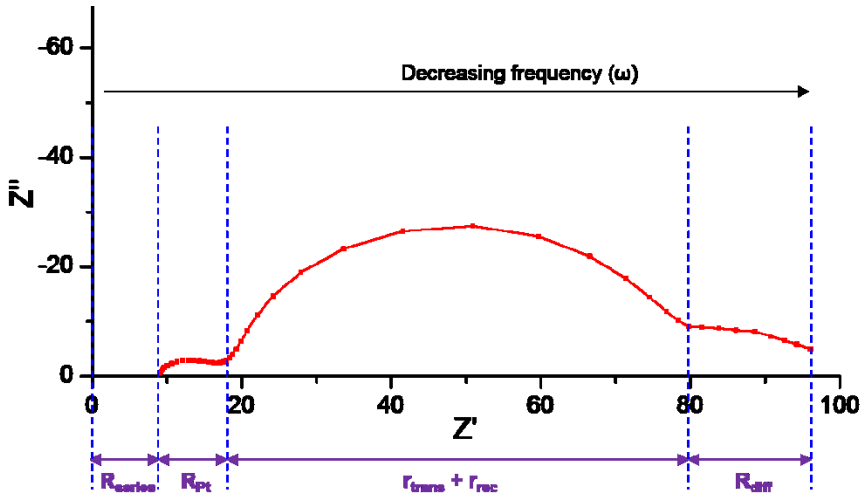

Figure 2.15 A typical Nyquist plot of a DSSC when performing electrochemical impedance spectroscopy at V_{OC}.

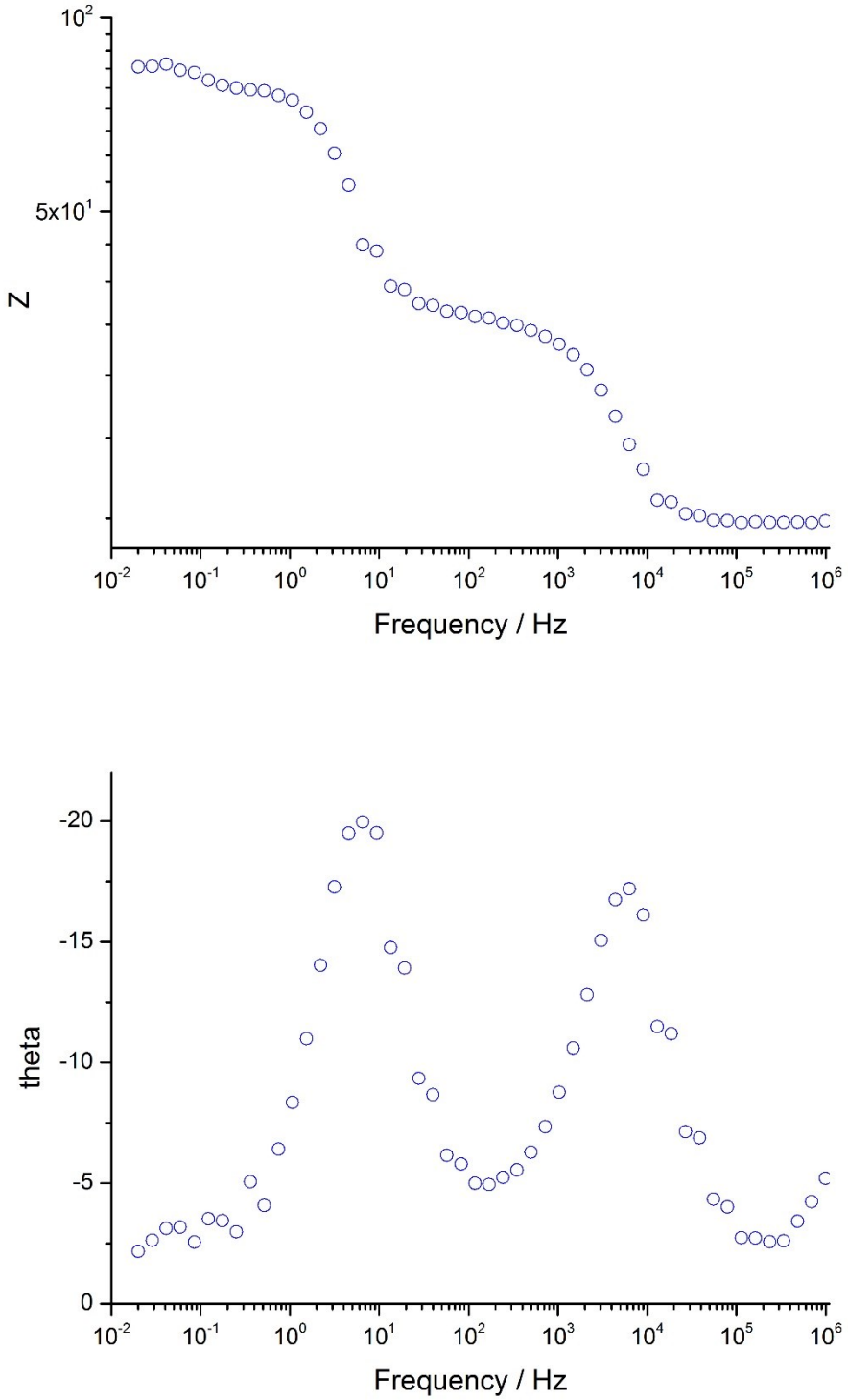

Figure 2.16 Typical Bode plots of a DSSC.

A useful analysis of the solar cells requires the EIS measurements to be made at several different voltage points. With different applied voltage, the shapes of the

semi-circles in the Nyquist plot can vary. At low voltages (less than the V_{OC} of the cell), the high frequency end of the second semi-circle looks nearly like a straight line because of the contribution of resistance to electron transport thought the TiO_2. At high voltages (greater than the V_{OC} of the cell), the TiO_2 film is in the conducting state, thus the second semi-circle looks almost like a perfect semi-circle and it is fully responsible for the resistance to recombination. Thus, appropriate models need to be selected during fitting.

Many parameters extracted from EIS show an exponential dependence on voltage due to an exponential distribution of delocalised trapping states below the conduction band edge where the electrons build up. [24] Figure 2.17 shows an example of the consequence of a conduction band edge shift on the relationship between a number of measured parameters including the small perturbation electron lifetime (τ_n), diffusion coefficient (D_n), total charge concentration (n) and applied voltage (V). The charge concentration is directly related to chemical capacitance. They can both act as the reference for the relative position of the conduction band edge position. [27] However, some recent research has shown that some electrolyte additives or dyes can not only change the concentration of charge for a given voltage, but also the concentration of charge for a given current.[28] If the distribution (or concentration) of trapping states changes, the transport and recombination parameters will change accordingly as shown in Figure 2.18.

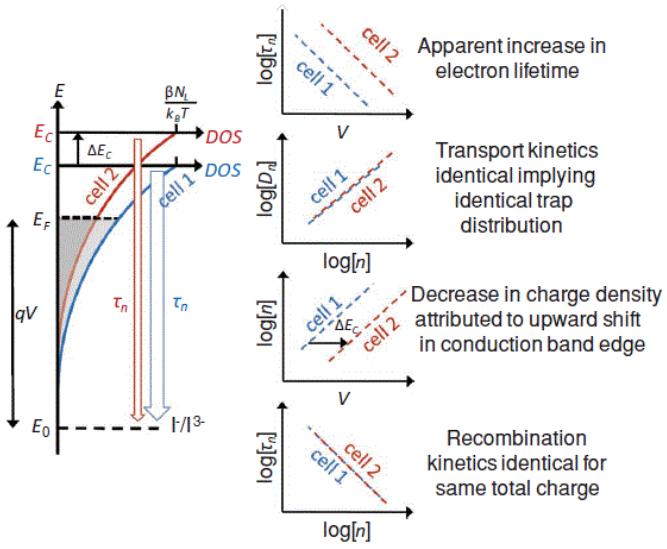

Figure 2.17 Schematic diagram showing an example of the consequence of a conduction band edge shift (ΔE_C) on the relationship between the measured parameters of small perturbation electron lifetime (τ_n), diffusion coefficient (D_n), total charge concentration (n) and voltage (V). Reproduced from reference [24].

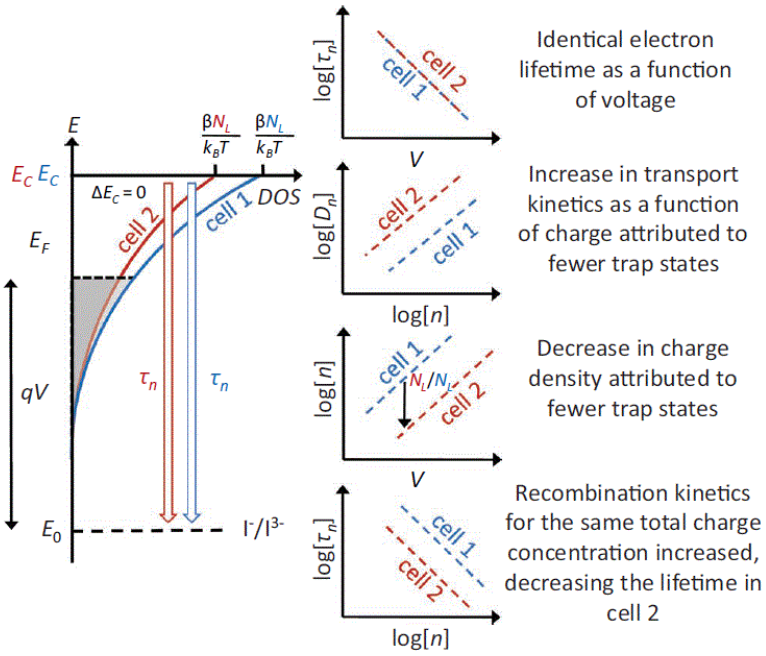

Figure 2.18 Schematic diagram showing an example of the consequence of a change in the total density of electronic trapping states (N_L). Reproduced from reference [24].

6.3.2 Experimental details

Electrochemical impedance spectroscopy (EIS) was performed using the AUTOLAB PGSTAT30 potentiostat controlled by FRA software, version 4.9.007. The cells were measured in a frequency range between 7 MHz and 0.02 Hz under illumination with forward bias potential controlled by the intensity of LED lights. The resulting impedance spectra were analysed with Z-view software (Scribner Associate Inc) version 3.3a on the basis of the two channel transmission line model. [22] The equivalent circuit in Z-view is shown in Figure 2.19.

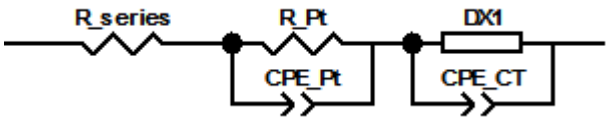

Figure 2.19 The equivalent circuit used to analyse impedance results

6.4 Intensity-modulated photocurrent spectroscopy (IMPS) and Intensity-modulated photovoltage spectroscopy (IMVS)

6.4.1 The technique

Like electrochemical impedance spectroscopy (EIS), intensity-modulated photocurrent spectroscopy (IMPS) and intensity-modulated photovoltage spectroscopy (IMVS) offer valuable information about electron transport and electron recombination in dye sensitised solar cells. Instead of modulating the amplitude of a current or potential as EIS, the intensity of light focused on a DSSC is modulated in both IMPS and IMVS.

During IMPS and IMVS measurements, a large bias background light intensity I_{DC} is focused on the DSSC and the cell is allowed to stabilise for some time to ensure that the DSSC has reached constant temperature. The short-circuit current (IMPS) and open-circuit potential (IMVS) are measured when they are constant. Then a sinusoidal waveform with amplitude I_0 is superimposed upon the constant base intensity, as shown in Equation 2.12. The cell's response is measured by changing the frequency of the light signal.

$$I = I_{DC} + I_0 sin\omega t \qquad \text{Equation 2.12}$$

IMPS is measured at short-circuit. Under this condition, electrons are extracted to the external circuit immediately after injection. The corresponding electron transport time constant τ_{tr} thus can be evaluated according to Equation 2.13.

$$\tau_{tr} = 1 / (2\pi f_{IMPS}) \qquad \text{Equation 2.13}$$

IMVS is measured at open-circuit. Under this condition, electrons cannot be extracted after injection and all electrons recombine with holes. The corresponding electron recombination lifetime constant τ_{rec} thus can be evaluated according to Equation 2.13.

$$\tau_{tr} = 1 / (2\pi f_{IMVS}) \qquad \text{Equation 2.14}$$

f_{IMPS} and f_{IMVS} are obtained from the maximum of Bode plot, where the imaginary part of the measured photocurrent is plotted against the frequency in a semi-logarithmic styles.

6.4.2 Experimental details

IMPS and IMVS were performed using a 625 nm LED driver at different light intensities and a Metrohm PGSTAT302N Autolab. All the measurements were carried out with the NOVA software.

6.5 Charge extraction

6.5.1 The technique

Charge extraction experiment is helpful in determining the quantity of charge stored within the cell under operational conditions, thus give information about the charge in TiO_2 conduction band.

The charge extraction experiment consists of multiple cycles as follow:

1) The potential is set to 0 V while the light is off in order to discharge the cell;
2) The potential is brought to open-circuit potential. The LED light is switched on for a defined time interval to build up charges in the conduction band;

3) The light is switched off and a given amount of time is waited, so the potential decayed to some extent depending on the defined decay time;
4) The potential is brought to short-circuit potential again when the light remains off. All the charges are being extracted at this step. In practice, the current is measured and the current output is integrated across a low drift analogue integration to obtain the extracted charge.

These four steps are repeated. In every cycle, the decay time is increased. Finally, the extracted charge and voltage at different decay time can be obtained from the resulting data. Charge density is obtained by extracted charge over the volume of TiO_2 film. By plotting charge density versus the voltage, we can fit the data using monoexponential. An example is given in Figure 2.20. Together with IMVS, the relationship between recombination lifetime and charge density can be plotted.

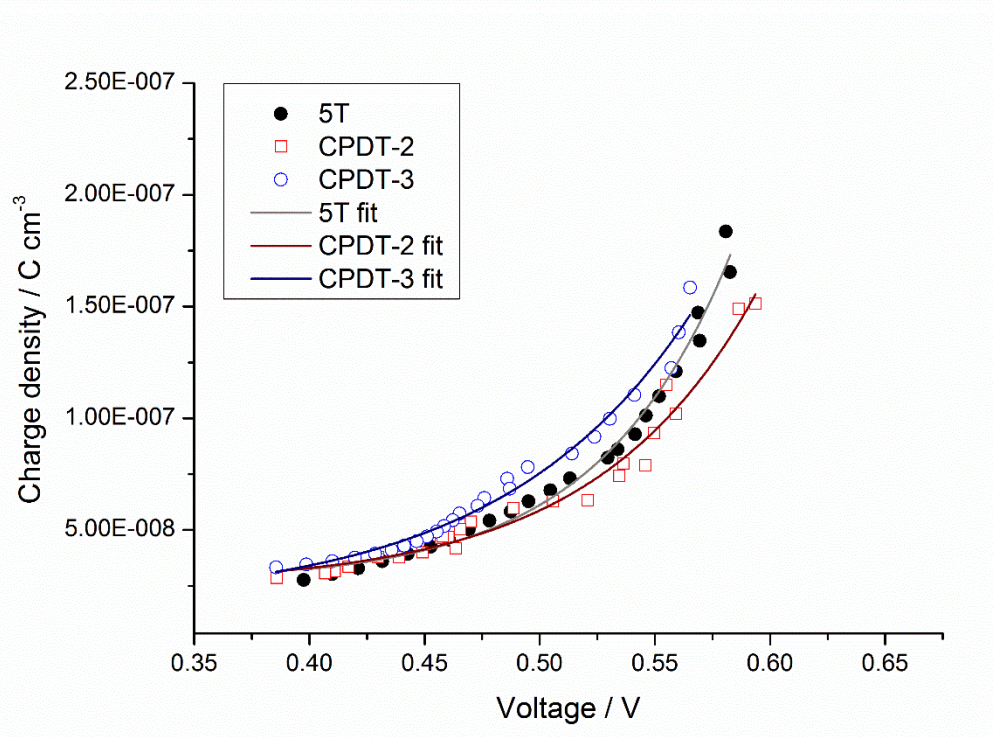

Figure 2.20 Example of charge extraction experiment. Plot of charge density vs. voltage

6.5.2 Experimental details

Charge extraction experiment was performed using a 625 nm LED and a Metrohm PGSTAT302N Autolab. The cell was allowed to equilibrate under steady state bias

illumination supplied by the LED for 2s under open circuit condition. The delay time was from 0.2s to 10s. All the measurements were carried out with the NOVA software.

Reference

1. Sheldrick, G.M., *A short history of SHELX.* Acta Crystallographica Section A, 2008. **64**: p. 112-122.
2. Macrae, C.F., et al., *Mercury: visualization and analysis of crystal structures.* Journal of Applied Crystallography, 2006. **39**: p. 453-457.
3. Kasha, M., *Characterization of Electronic Transitions in Complex Molecules.* Discussions of the Faraday Society, 1950(9): p. 14-19.
4. Chadwick, N., *Ruthenium dyes for Dye Sensitised Solar Cells (DSSCs). Exploring dye synthesis and TiO2-dye-I-/I3- electron transfer reactions in a DSSC*, in *University of Edinburgh*. 2014.
5. Zanello, P., C. Nervi, and F. Fabrizi de Biani, *Inorganic electrochemistry : theory, practice and application*. 2nd ed. 2012, Cambridge: Royal Society of Chemistry. xvi: p. 683.
6. Vlcek, A. and S. Zalis, *Modeling of charge-transfer transitions and excited states in d(6) transition metal complexes by DFT techniques.* Coordination Chemistry Reviews, 2007. **251**(3-4): p. 258-287.
7. Srinivas, K., et al., *A Combined Experimental and Computational Investigation of Anthracene Based Sensitizers for DSSC: Comparison of Cyanoacrylic and Malonic Acid Electron Withdrawing Groups Binding onto the TiO2 Anatase (101) Surface.* Journal of Physical Chemistry C, 2009. **113**(46): p. 20117-20126.
8. Magyar, R.J. and S. Tretiak, *Dependence of spurious charge-transfer excited states on orbital exchange in TDDFT: Large molecules and clusters.* Journal of Chemical Theory and Computation, 2007. **3**(3): p. 976-987.
9. *Avogadro 1.1.0*. Available from: http://sourceforge.net/projects/avogadro/.
10. Hanwell, M.D., et al., *Avogadro: an advanced semantic chemical editor, visualization, and analysis platform.* Journal of Cheminformatics, 2012. **4**: p. 17.
11. Gaussian 09, Revision E.01, Frisch, M. J., Trucks, G. W., Schlegel, H. B., Scuseria, G. E., Robb, M. A., Cheeseman, J. R., Scalmani, G., Barone, V., Mennucci, B., Petersson, G. A., Nakatsuji, H., Caricato, M., Li, X., Hratchian, H. P., Izmaylov, A. F., Bloino, J., Zheng, G., Sonnenberg, J. L., Hada, M., Ehara, M., Toyota, K., Fukuda, R., Hasegawa, J., Ishida, M., Nakajima, T., Honda, Y., Kitao, O., Nakai, H., Vreven, T., Montgomery, J. A., Jr., Peralta, J. E., Ogliaro, F., Bearpark, M., Heyd, J. J., Brothers, E., Kudin, K. N., Staroverov, V. N., Kobayashi, R., Normand, J., Raghavachari, K., Rendell, A., Burant, J. C., Iyengar, S. S., Tomasi, J., Cossi, M., Rega, N., Millam, J. M., Klene, M., Knox, J. E., Cross, J. B., Bakken, V., Adamo, C., Jaramillo, J., Gomperts, R., Stratmann, R. E., Yazyev, O., Austin, A. J., Cammi, R., Pomelli, C., Ochterski, J. W., Martin, R. L., Morokuma, K., Zakrzewski, V. G., Voth, G. A.; Salvador, P., Dannenberg, J. J., Dapprich, S., Daniels, A. D., Farkas, Ö., Foresman, J. B., Ortiz, J. V., Cioslowski, J., Fox, D. J., Gaussian, Inc., Wallingford CT, 2009.
12. Perdew, J.P., et al., *Atoms, Molecules, Solids, and Surfaces - Applications of the Generalized Gradient Approximation for Exchange and Correlation (Vol 46, Pg 6671, 1992).* Physical Review B, 1993. **48**(7): p. 4978-4978.

13. Perdew, J.P., K. Burke, and Y. Wang, *Generalized gradient approximation for the exchange-correlation hole of a many-electron system.* Physical Review B, 1996. **54**(23): p. 16533-16539.
14. Hay, P.J. and W.R. Wadt, *Abinitio Effective Core Potentials for Molecular Calculations - Potentials for K to Au Including the Outermost Core Orbitals.* Journal of Chemical Physics, 1985. **82**(1): p. 299-310.
15. Hay, P.J. and W.R. Wadt, *Abinitio Effective Core Potentials for Molecular Calculations - Potentials for the Transition-Metal Atoms Sc to Hg.* Journal of Chemical Physics, 1985. **82**(1): p. 270-283.
16. Wadt, W.R. and P.J. Hay, *Abinitio Effective Core Potentials for Molecular Calculations - Potentials for Main Group Elements Na to Bi.* Journal of Chemical Physics, 1985. **82**(1): p. 284-298.
17. Bauernschmitt, R. and R. Ahlrichs, *Treatment of electronic excitations within the adiabatic approximation of time dependent density functional theory.* Chemical Physics Letters, 1996. **256**(4-5): p. 454-464.
18. Tozer, D.J. and N.C. Handy, *Improving virtual Kohn-Sham orbitals and eigenvalues: Application to excitation energies and static polarizabilities.* Journal of Chemical Physics, 1998. **109**(23): p. 10180-10189.
19. O'Boyle, N.M., A.L. Tenderholt, and K.M. Langner, *cclib: A library for package-independent computational chemistry algorithms.* Journal of Computational Chemistry, 2008. **29**(5): p. 839-845.
20. Becke, A.D., *Density-Functional Thermochemistry .3. The Role of Exact Exchange.* Journal of Chemical Physics, 1993. **98**(7): p. 5648-5652.
21. Kalyanasundaram, K., ed. *Dye-sensitized Solar Cells*. 2010, EPFL Press.
22. Fabregat-Santiago, F., et al., *Influence of electrolyte in transport and recombination in dye-sensitized solar cells studied by impedance spectroscopy.* Solar Energy Materials and Solar Cells, 2005. **87**(1-4): p. 117-131.
23. Fabregat-Santiago, F., et al., *Decoupling of transport, charge storage, and interfacial charge transfer in the nanocrystalline TiO2/electrolyte system by impedance methods.* Journal of Physical Chemistry B, 2002. **106**(2): p. 334-339.
24. Barnes, P.R.F., et al., *Interpretation of Optoelectronic Transient and Charge Extraction Measurements in Dye-Sensitized Solar Cells.* Advanced Materials, 2013. **25**(13): p. 1881-1922.
25. Kern, R., et al., *Modeling and interpretation of electrical impedance spectra of dye solar cells operated under open-circuit conditions.* Electrochimica Acta, 2002. **47**(26): p. 4213-4225.
26. Wang, Q., J.E. Moser, and M. Gratzel, *Electrochemical impedance spectroscopic analysis of dye-sensitized solar cells.* Journal of Physical Chemistry B, 2005. **109**(31): p. 14945-14953.
27. Liu, J.Y., et al., *Mesoscopic titania solar cells with the tris(1,10-phenanthroline)cobalt redox shuttle: uniped versus biped organic dyes.* Energy & Environmental Science, 2011. **4**(8): p. 3021-3029.

28. O'Regan, B., X.E. Li, and T. Ghaddar, *Dye adsorption, desorption, and distribution in mesoporous TiO2 films, and its effects on recombination losses in dye sensitized solar cells.* Energy & Environmental Science, 2012. **5**(5): p. 7203-7215.

Chapter 3 Oligo(3-hexylthiophene) dyes

1 Introduction

1.1 First example of donor-free sensitiser

The overwhelming trend in designing metal-free organic sensitisers with high extinction coefficients is based on a donor-π spacer-acceptor (D-π-A) architecture. [1, 2] In such dyes, the donor and the π spacer part contain the HOMO of the dye while the LUMO is distributed on the acceptor part and the anchoring group. Upon excitation, the electrons move from donor to acceptor through the π-bridge. This modular design allows organic dyes to show great diversity and flexibility. Since Hagfeldt and co-workers [3] introduced bulky alkoxy substituents into the triphenylamine-based donor of the sensitizers and obtained 6.7% efficiency with cobalt electrolyte, it has become fashionable to make the donor part of D-π-A sensitizer bulkier and bulkier. The bulky donor is beneficial in order to reduce the electron recombination between redox electrolyte and the TiO_2 surface and to stabilize the oxidized dye. The influence of the donor size in D-π-A dye was studied by Yang et al. [2] A higher voltage was observed and reported when a bulky-indoline moiety was introduced as donor into the IQ4 dye. [4] However, at the same time, the complicated structure often results in difficult synthesis with low yield.

Previous study in our group on ssDSSCs using a 'donor-free' sensitiser, cyanoacrylic end-functionalized oligo(3-hexylthiophene) (5T) and 'donor- π-acceptor' sensitiser based on the same structure (MK-2) (Structure shown in Figure 1.17) showed that without an electron donor group, a significantly-higher open-circuit voltage (V_{OC}) could be achieved while the short-circuit current (J_{SC}) remained approximately the same. This resulted in a significantly higher over-all efficiency, comparable with the very best dyes for ssDSSCs. Devices using 5T as the sensitiser and spiro-OMeTAD as the hole-transport material gave an efficiency of 4.4% whereas the ones using MK-2 as the sensitiser gave only 2.8%. [5] With experimental and theoretical approaches, it was found that in the solid-state cells 5T sustains a significant fraction of oxidized dye under operating conditions and enhances the open-circuit voltage through the resulting large dipole on the dye.

1.2 Research Proposal

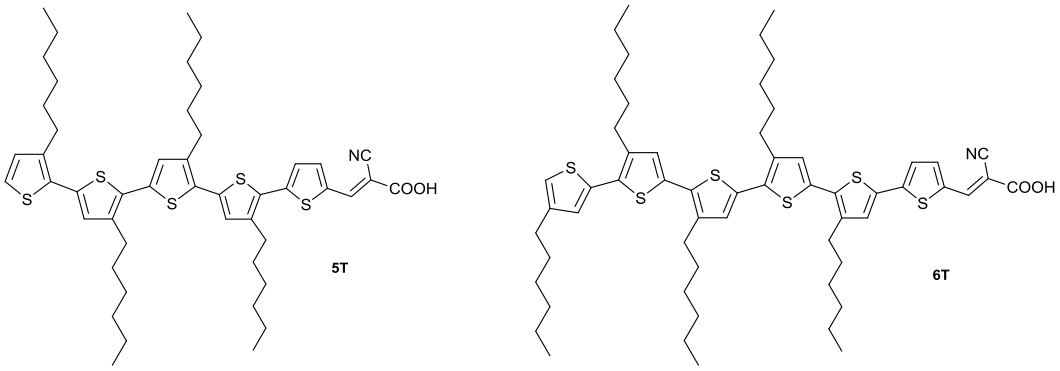

Figure 3.1 Chemical structures of 5T and 6T

To follow up the above work, in this chapter we have tested 5T in liquid-state dye-sensitised solar cells using classic I^-/I_3^- redox couple. Another donor-free dye, 6T (Figure 3.1), which has one more thiophene unit than 5T, as well as a simpler synthetic scheme is also designed, synthesised, characterised and tested. To compare the performance of 5T and 6T with the traditional D-π-A dyes, we also fabricated the liquid-state dye-sensitised solar cells based on MK2 dye and using I^-/I_3^- redox couple. The dyes studied in the present work have similar molecular backbone to MK2 - both use cyanoacrylic acid as an acceptor group and four thiophene derivatives as a π-spacer. While MK2 has a terminal carbazole donor group to complete the D-π-A structure, 5T and 6T have additional thiophene(s) to elongate the π-system to achieve a molecular size similar to MK2.

By removing the donor component from the traditional D-π-A structure, we aim to simplify the synthetic route with high yield, thus opening a new strategy of designing highly efficient 'donor-free' dyes in the future.

2 Results and Discussion

2.1 Synthesis

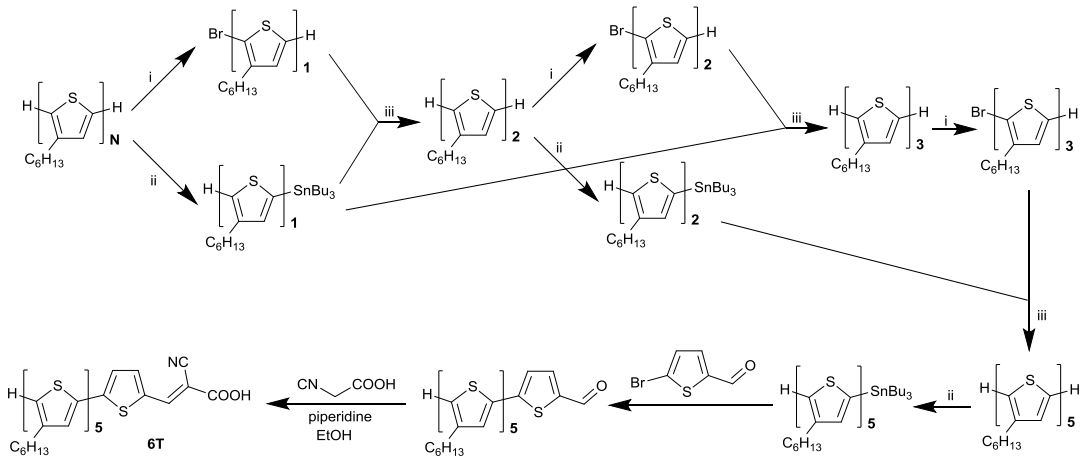

Scheme 3.1 the synthetic procedure for the synthesis of 6T

The synthesis of oligo(3-hexylthiophene)s and poly(3-hexylthiophene) has been reported using several routes and the challenge is to separate the high-purity monodisperse regioregular oligo(3-hexylthiophene)s in reasonable quantities. The previous work in our group was based on extending the oligomer stepwise by one unit per cross-coupling followed by activation of the newly formed chain end to give 5T. [6] This approach was part of a study to prepare shorter oligomers including 1 – 5 thiophene units [6], however it is not very efficient when the longer chains of 5T and 6T are specifically desired. In this work, 6T was therefore synthesised using a 'Fibonacci Route' reported by Heeney. [7] The synthetic route is shown in Scheme 3.1. The synthesis of the oligomer $(3HT)_n$ was achieved by the coupling of Br-$(3HT)_{n-x}$ and $(3HT)_x$-$SnBu_3$. Thus, $(3HT)_n$ with n=1,2,3,5,8,13 and 21 can be obtained more efficiently than adding one thiophene unit per cross-coupling. Also, this strategy allowed easy purification by vacuum distillation of solvent and column chromatography. Finally, in this work, a thiophene unit functionalized with a cyanoacrylic end group was added to enable appropriate attachment to the TiO_2. We note that this Fibonacci route leads to alkyl chains in a different position. The alkyl chains for 5T are at the 3-positions of the thiophene, however, for 6T, they are at the 2-positions. Alkyl chains were attached to the thiophene unit to avoid strong π-π interaction, [8] which has been proven to lead to a decreased electron injection in the

solar cells. [9] Furthemore, alkyl chains play a role in reducing charge recombination between electrons in TiO_2 and the redox electrolyte [10].

2.2 Optical properties

The optical properties of 5T and 6T were studied in dichloromethane at 2×10^{-6} M. For both dyes, the lowest energy absorption band is around 480 nm. The absorption band positions and their extinction coefficients are summarized in Table 3.1.

Table 3.1 Photophysical and Electrochemical properties of 5T and 6T

	λ_{max} / nm ($\varepsilon \times 10^{-4}$ / M^{-1} cm^{-1})	λ_{em} / nm	$E_{0\text{-}0}{}^{c}$ / eV
5T	478 (3.9), 376 (2.4)	660	2.15
6T	486 (3.9), 401 (3.1)	564	2.30

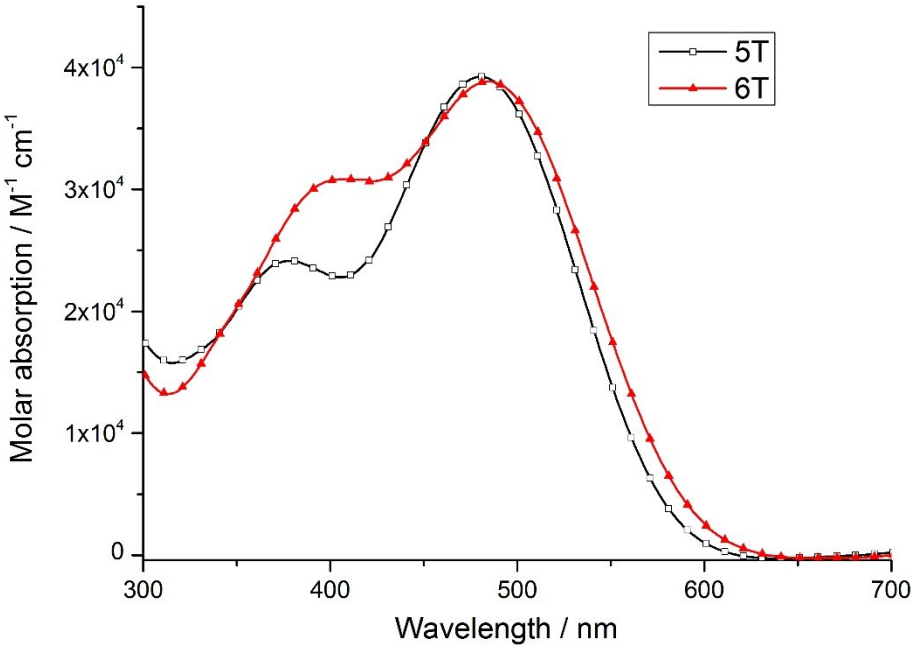

Figure 3.2 UV-vis spectra of 5T and 6T at 2×10^{-6} M in DCM

The addition of thiophene unit and extension of π-system does not lead to significant changes in either the position of the lowest energy absorption band or the extinction coefficient of this band but has a stronger influence on the higher energy band, which corresponds to a π- π* transition of the thiophene backbone and is more intense for 6T (Figure 3.2). This assignment was confirmed by measuring UV-vis spectra in different solvents (Figure 3.3). In a mixture of acetonitrile and butanol, the lowest energy absorption band of both compounds blue shifted significantly while the higher energy band remained at the same wavelength, indicating the charge transfer nature of the lowest energy absorption band.

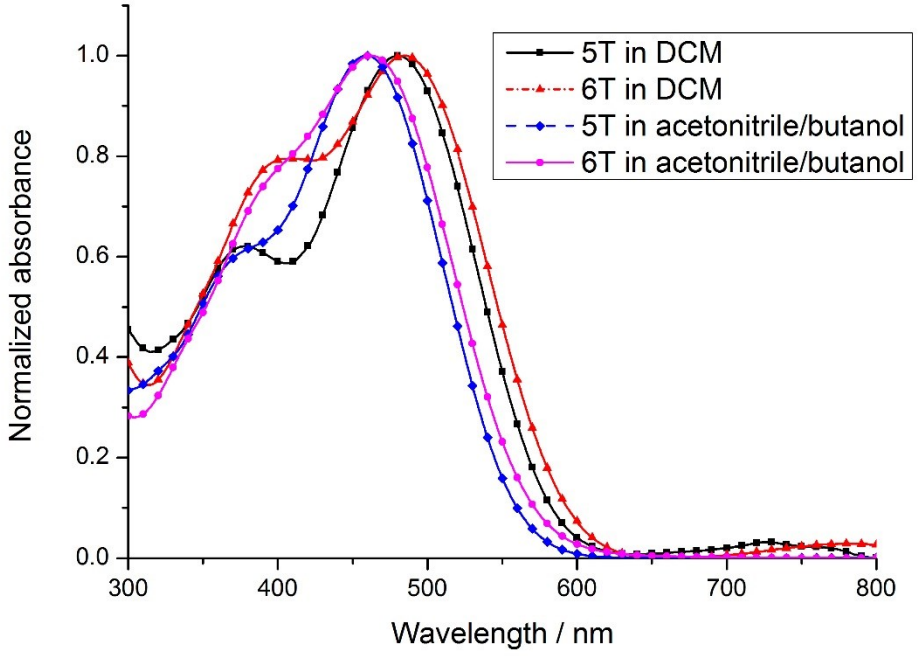

Figure 3.3 Normalized UV-vis spectra of 5T and 6T in DCM or a mixture of acetonitrile/butanol

Figure 3.4 gives the absorption spectra of 5T and 6T on 3 μm transparent TiO_2 films. Both spectra broadened, implying the dyes form herring-bone aggregates on TiO_2 films. [11] 6T showed broader absorption than 5T on TiO_2 film because of its extra conjugation. This has also been seen by Masumoto, et al. [12], who studied the optical properties of thiophene-based oligomers and found the effective conjugation length of oligothiophenes was six thiophene rings.

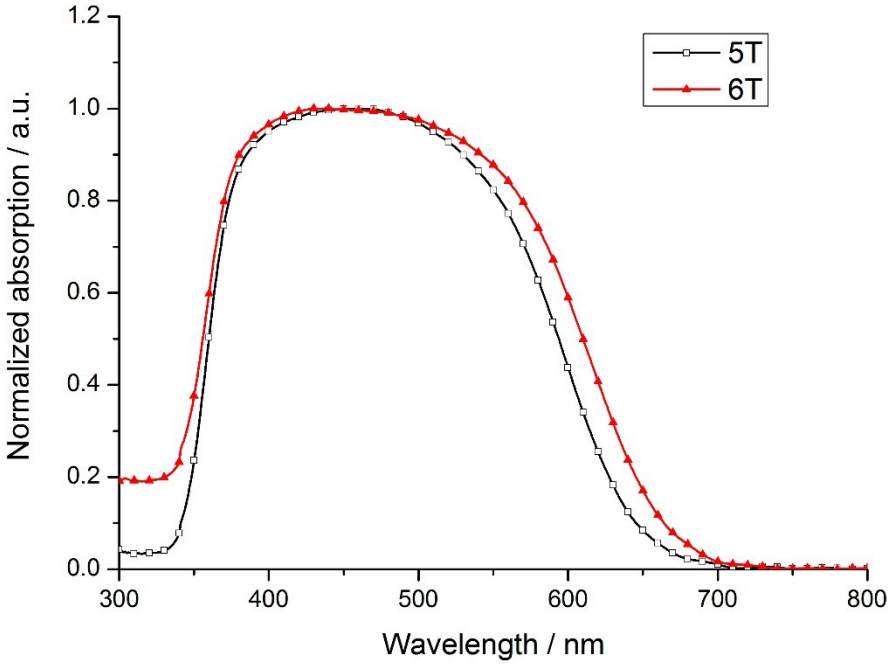

Figure 3.4 UV-vis spectra of 5T and 6T on 3 μm transparent TiO_2

Photoluminescence was also studied in solution. Table 3.1 shows the positions of the emission band and Figure 3.5 shows the spectra. Transition energy was then estimated from the intercept of the normalized absorption and emission spectra and is also shown in Table 3.1. 5T and 6T both showed very broad emission response, covering the visible and even near-IR region. 5T showed a bigger Stokes-shift than 6T (5973 cm^{-1} and 2908 cm^{-1}, respectively).

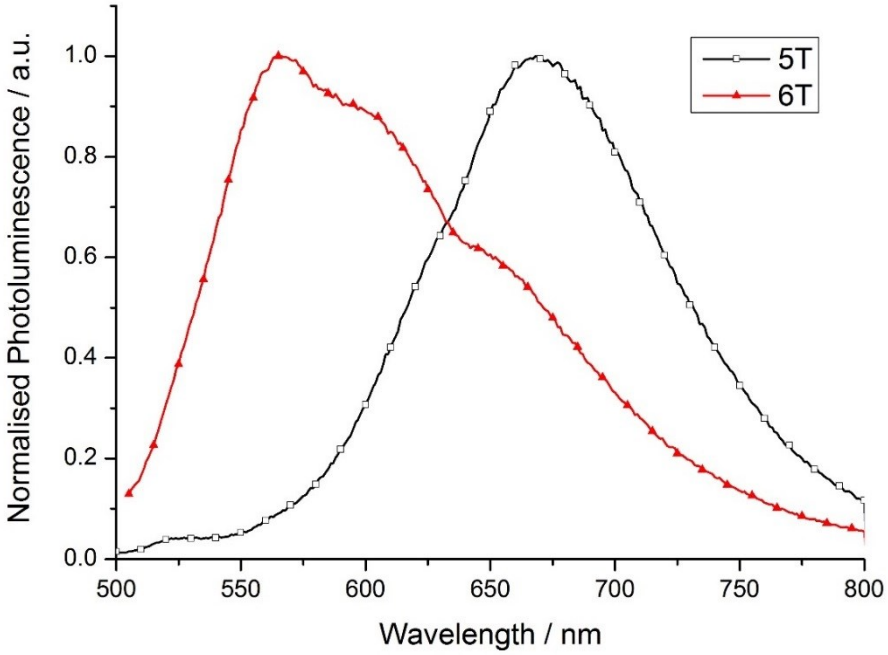

Figure 3.5 Emission spectra of 5T and 6T at 2×10^{-6} M in DCM

2.3 Electrochemistry

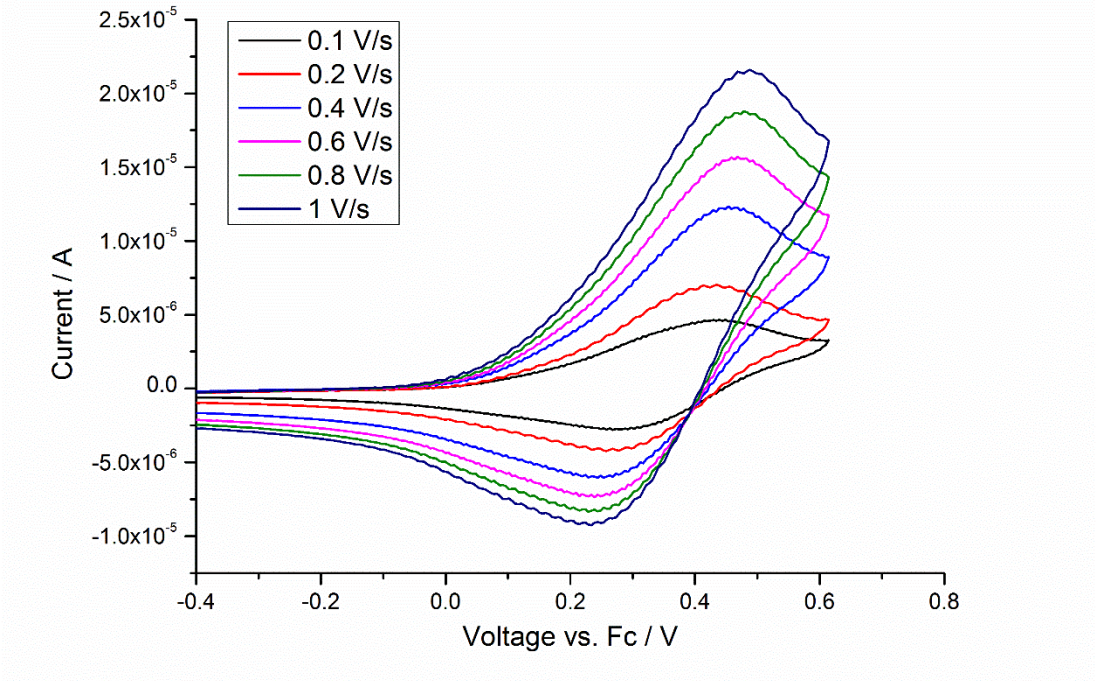

Figure 3.6 Cyclic Voltammetry of 6T recorded in CH_2Cl_2 solution containing 0.3 M [TBA][PF_6] at different rates.

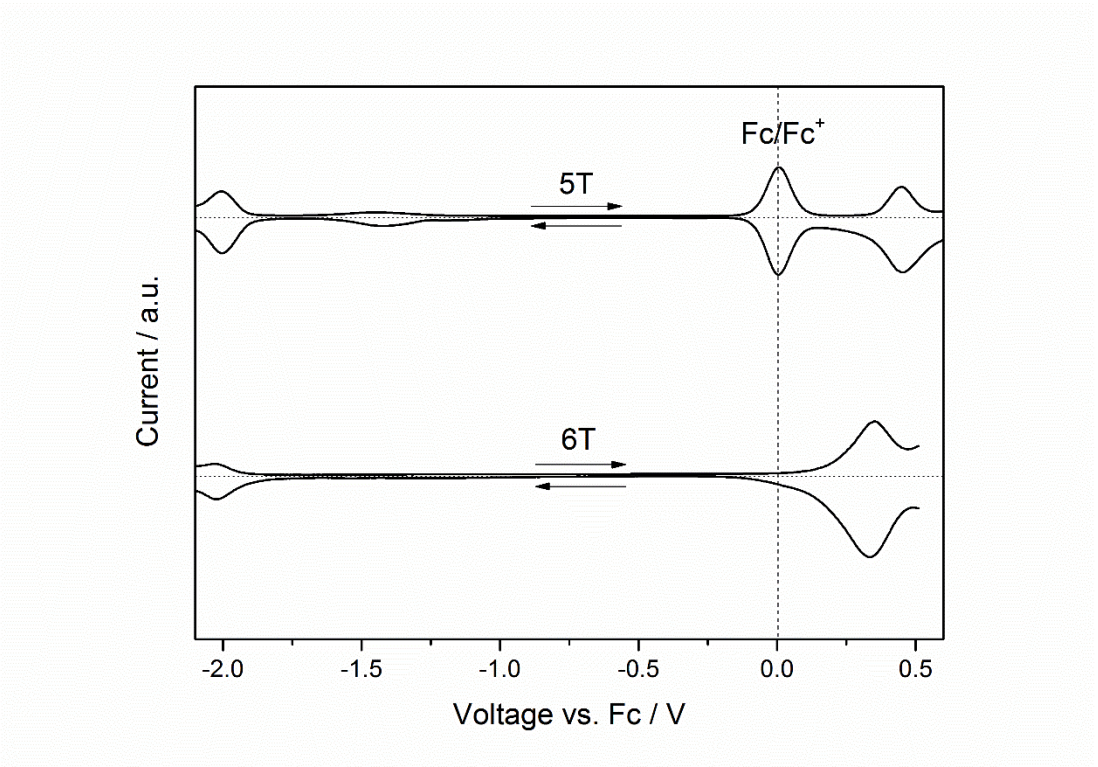

Figure 3.7 Square Wave Voltammetry recorded in CH_2Cl_2 solution containing 0.3 M [TBA][PF_6] and referenced internally to ferrocene (shown in the 5T trace).

Table 3.2 Electrochemical properties of 5T and 6T

	E_{ox} / V		E_{red} / V	
	vs. Fc	vs. NHE	vs. Fc	vs. NHE
5T	0.45	1.08	-1.92	-1.29
6T	0.35	0.98	-1.95	-1.32

Electrochemical properties for 5T and 6T were investigated by cyclic voltammetry (CV) (Figure 3.6) and square-wave voltammetry (SWV) (Figure 3.7). Despite the fact that 5T and 6T do not have donor groups, both the dyes showed a reversible first oxidation process. The cyclic voltammetry of 6T at different scan rates is shown in Figure 3.6. The potential was measured in DCM with 0.3 M [TBA][PF_6] as electrolyte and calibrated with ferrocene/ferrocenium (Fc/Fc^+) as an internal reference and converted to NHE by addition of 0.63 V. The values against ferrocene and NHE are presented in Table 3.2. The addition of one more thiophene unit in 6T

shifts the oxidation peak to less positive potential; 5T shows the first oxidation potential at 1.08V whereas 6T shows it at 0.98V vs. NHE. They are both higher than that of the iodide/triiodide (0.40 V vs. NHE) redox electrolyte energy level, guaranteeing good driving force for the dye regeneration. Little difference was observed for the reduction processes (5T: -1.29 V, 6T: -1.32 V vs. NHE). This is because the LUMO is localized mainly at the cyanoacrylic moiety and is little affected by the length of the thiophene chain.

2.4 Computational

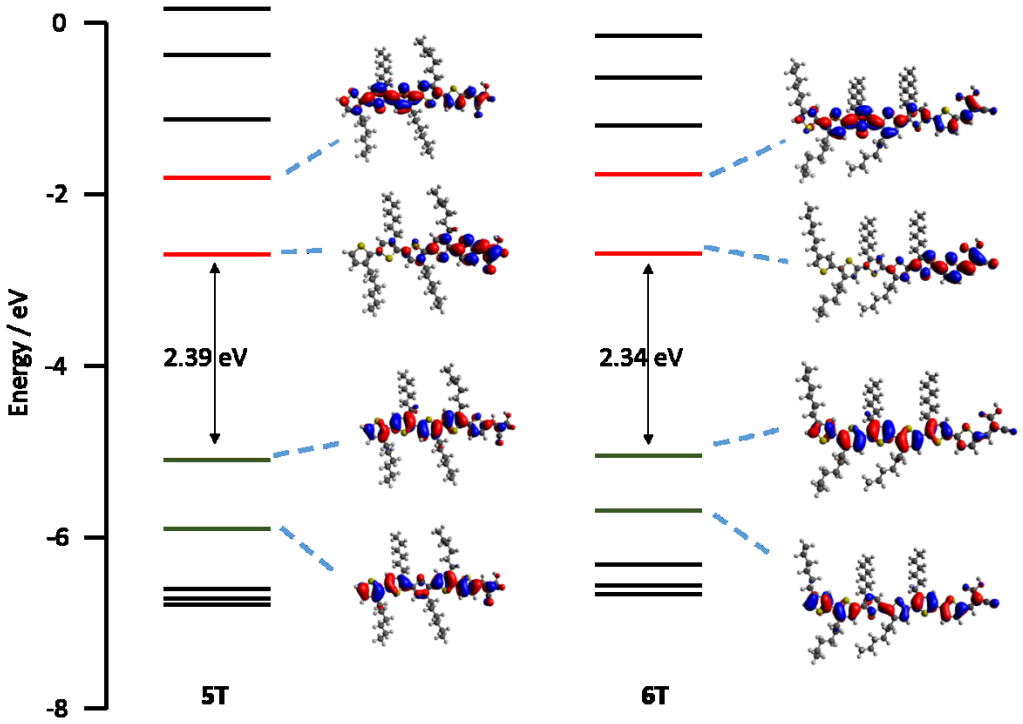

Figure 3.8 Energy level schemes for the Kohn-Sham orbitals of 5T and 6T, including selected Kohn-Sham orbitals and the HOMO-LUMO energy gap.

All calculations were carried out using the Gaussian 09 program [13] with the hybrid B3LYP functional [14] and the standard 6-31G(d) basis set. The energy level schemes for the Kohn-Sham orbitals of 5T and 6T, including selected Kohn-Sham orbitals and the HOMO-LUMO energy gap are shown in Figure 3.8. For both 5T and 6T, the HOMO is distributed along the conjugated π-system and the LUMO is located on the cyanoacetic acid unit through the thiophene, allowing good charge

separation and charge directionality after photo-excitation and minimising back recombination to the dye of the injected electrons. [15] Time-dependent DFT calculation was performed with a dichloromethane polarisable continuum model (PCM) [16] using the CAM-B3LYP functional [14]. The result is consistent with the experimental UV/Vis and is shown in Table 3.3 and Table 3.4.

Table 3.3 TD-DFT calculated energies and compositions of selected transitions of 5T

No	E(nm)	Composition	f
1	505	74% H→L, 12% H-1→L,	2.1401
2	380	60% H→L+1, 27 % H-1→L	0.1249

Table 3.4 TD-DFT calculated energies and compositions of selected transitions of 6T

No	E(nm)	Composition	f
1	498	64% H→L, 21% H-1→L,	2.2587
2	394	59% H→L+1, 21% H-1→L	0.2694

2.5 Device performance

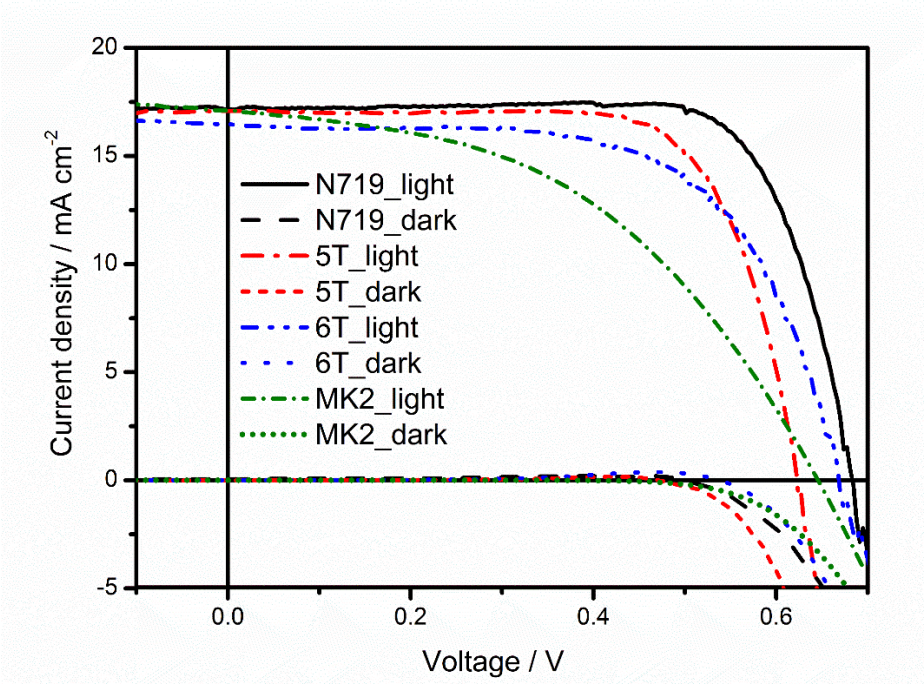

Figure 3.9 J-V characteristics and IPCEs of the DSSCs using MK2, N719, 5T and 6T under dark and under AM1.5 simulated sunlight of illumination of 100 mW cm^{-2}.

Table 3.5 Photovoltaic performance for the champion cells measured under AM 1.5 illumination. The photoelectrodes were soaked in the dye solution for 24 hours.

Dye	Jsc / mA cm^{-2}	Voc / V	FF / %	Efficiency / %	Dye loading / $\times 10^{7}$ mol cm^{-2}
N719	17.48	0.68	74.7	8.89	3.04
5T	17.15	0.62	72.0	7.64	5.09
6T	16.85	0.67	62.8	7.07	5.38

The solar cell devices were made by Dr. Aruna Ivaturi. The photovoltaic performance of the DSSCs based on iodide/triiodide redox electrolyte using the 5T and 6T dyes was analysed as a function of dye soaking time of 3-24 hours and compared with DSSCs using N719. The best performance for all the dyes was observed for the devices soaked for 24 hours. To compare the performance of 5T and

6T with the traditional D-π-A dyes, DSSCs based on MK2 dye were also fabricated. The J-V characteristics of the best cells are shown in Figure 3.9. The incident photon-to-electron conversion efficiencies (IPCEs) of 5T and 6T are shown in Figure 3.10. The corresponding device characteristics along with the estimated amount of dye loaded on 18 µm TiO_2 photoelectrodes soaked in the corresponding dyes for 24 hours are given in Table 3.5.

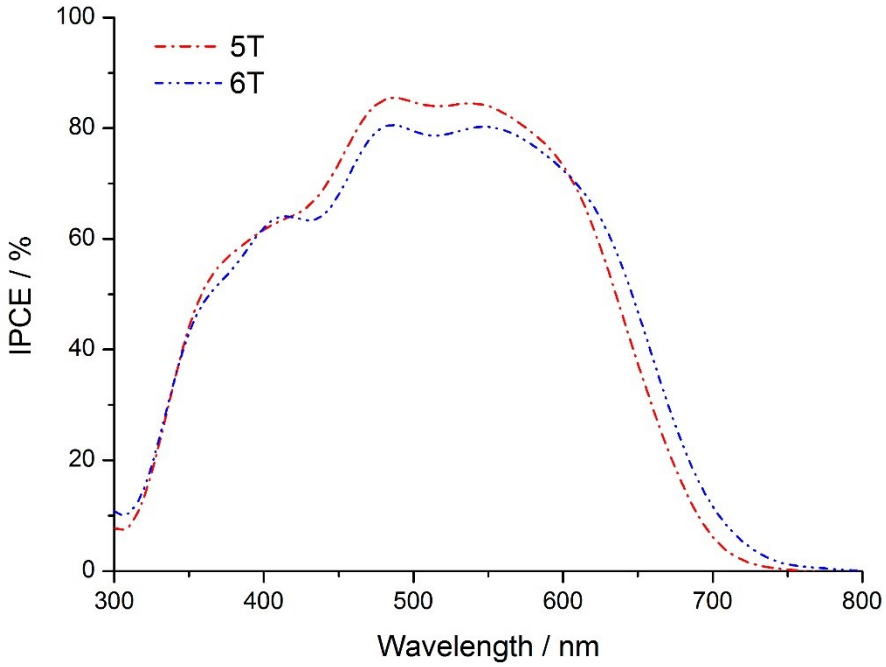

Figure 3.10 IPCE of DSSCs using 5T and 6T

N719 has the highest J_{SC} because it exhibits the widest absorption spectrum. The IPCE of DSSCs using 5T and 6T (Figure 3.10) exceeded 60% over most of the visible light region from 400 nm to 650 nm, with a maximum of ~80% at around 500 nm and the lowest values were between 650-700 nm. N719 showed better performance in this region. The slight shift in the absorption onset of the 6T as compared to 5T on TiO_2 (Figure 3.4) is also evident from the shift in the IPCE. A higher dye loading of the 6T compared to 5T on TiO_2 (Table 3.5), however, does not lead to a higher short circuit photocurrent as might be expected. Hagberg et al. observed similar trends in a series of organic chromophores when the π-conjugation between the donor (triphenylamine moiety) and the acceptor (cyanoacetic acid

moiety) were systematically extended. [17] A similar trend was also observed by Barea et al. in n-thiophene absorbers when increasing the conjugation length from 2 to 6. [15] Such a decrease in J_{SC} was attributed to the differences in dye binding and orientation affecting injection efficiency. Overall, the best PCE efficiencies obtained were N719 (8.94%), 5T (7.64%) and 6T (7.07%). 5T has a lower PCE than N719 mainly due to a loss in V_{OC}, which is not unusual in organic dyes. A significant decrease in the fill factor is observed when comparing the devices using 6T and others. In contrast, the best PCE efficiency obtained in DSSCs based on MK2 is 5.05%, with J_{SC} of 17.64 mA.cm^{-2}, V_{OC} of 0.64 V and FF of 45.0%. The best PCE value reported in literature for MK2 sensitised DSSCs is 8.3% with J_{SC} of 15.22 mA cm^{-2}, V_{OC} of 0.73 V and FF of 75.0%. [18] The higher J_{SC} and lower FF observed in the present study could be related to the photoelectrode thickness of 18 µm in contrast to the 16 µm reported in literature. Whereas the lower V_{OC} is related to the electrolyte composition, especially the iodine concentration of 0.2M in the former in contrast to 0.03M used in the present study.

2.6 Electrochemical impedance spectroscopy (EIS)

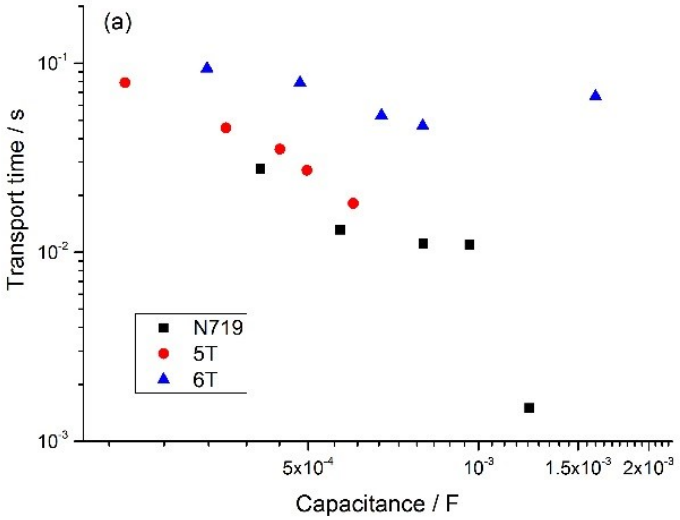

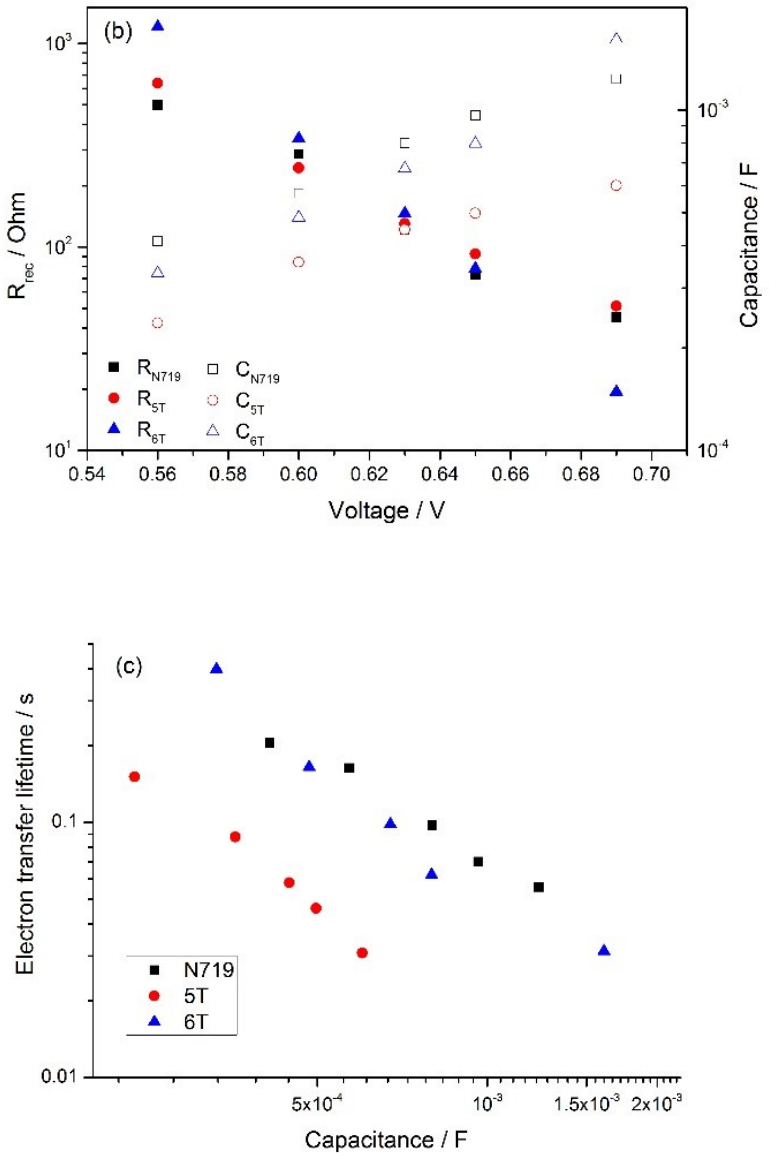

Figure 3.11 (a) Transport time plotted against capacitance of the TiO_2. (b) Charge transfer resistance and chemical capacitance of the TiO_2 plotted against the voltage. (c) Electron lifetime plotted against capacitance of the TiO_2.

In order to understand the reasons behind the observed photovoltaics performance as a function of thiophene chain length, detailed impedance spectroscopy measurements were performed on the best cells under illumination from a LED at different bias potentials in the frequencies between 1MHz and 0.1Hz. The data were fitted using

the transmission line model.[19, 20] Details of fitting can be found in Chapter 2. From the fittings, charge transfer resistance (R_{CT}), electron transport resistance (R_{trans}) and chemical capacitance of TiO_2 (C_{Chem}) were extracted. The electron lifetime and electron transport time were calculated according to the equations: $\tau_e = R_{CT} * C_{Chem}$ and $\tau_{trans} = R_{trans} * C_{Chem}$, respectively. Figure 3.11 shows the charge transfer resistance and the chemical capacitance of the TiO_2 as a function of voltage and the electron lifetime as a function of capacitance. Although it is increasingly common to use the chemical capacitance as a reference for the relative position of the conduction band edge in different devices, Barnes, et al.[21] have highlighted the need to analyse both charge and transport data in addition to simple electron lifetime measurements when drawing conclusions about DSSC behaviour, for the reason that some dyes may modify the distribution of trap states as well as shifting the semiconductor conduction band. Based on this knowledge, we first examine the relationship between transport time and capacitance. The longer transport time of 6T over 5T indicates more trap states in the presence of 6T, consistent with the higher capacitance for 6T shown in Figure 3.11(a). A low FF is generally ascribed to high series resistance, [22, 23] which includes the redox reaction resistance at the counter electrode, the resistance of electron transport by ions in the electrolyte and electron transport through the TiO_2. The longer transport time for 6T indicates a higher resistance for electron transport, which leads to a lower FF and a slightly lower J_{SC} for 6T than the other dyes. This may be caused by the extra conjugation of 6T compared to 5T, or the different position of the alkyl chains which modifies the TiO_2 surface differently. The longer electron lifetime for 6T over 5T [Figure 3.11(b)], despite the higher number of traps, corresponds with the experimental Voc which is slightly higher for 6T. In contrast, 5T and N719 have similar trap states, so any different device behaviour can be attributed to a shift of conduction band edge, possibly related to the different protonation state of N719 compared with 5T and 6T. From Figure 3.11(c) N719 has much longer electron lifetime than 5T and this leads to a final V_{OC} value trend of N719>6T>5T.

3 Conclusion

Two 'donor-free' cyanoacrylic end-functionalized oligo(3-hexylthiophene) dyes (5T and 6T) have been synthesised and used as effective sensitisers for liquid-state dye-sensitised solar cells with I^-/I_3^- redox couple, with power conversion efficiency of 7.64% and 7.07%, respectively. 6T showed a significantly higher V_{OC} than 5T but lower J_{SC} and FF. By using electrochemical impedance spectroscopy (EIS), it was found that 6T has more trapping states, attributed to the extra conjugation or different position of alkyl chain of 6T. These dyes can be easily synthesised using cross-coupling and showed reversible first oxidation processes even without donor groups, thus opening a new strategy of designing dyes in the future.

4 Experimental

The synthesis of the oligo(3-hexylthiophene) was based on literature report. [7] The ^{1}H NMR spectra of the products are in agreement with the literature.

Synthesis of Br-(3HT). 3-hexylthiophene (1.7g, 10mmol) was dissolved in 25 ml DMF and the solution was cooled down to -20℃. N-bromosuccinimide (1.8g, 10mmol) was added and the mixture was stirred at -10 ℃ for 1h before stirring at room temperature overnight. Ethyl acetate (10ml) was added and the mixture was washed with deionized water and brine. The organic phase was dried over magnesium sulphate. After filtration, the solvent was removed under pressure. The product (2.4g, 97% yield) was used without further purification. ^{1}H NMR (500 MHz, $CDCl_3$): 7.22 (d, J=5.7Hz, 2H), 6.85 (d, J=5.6Hz, 2H), 2.63(t, J=7.7Hz, 2H), 1.68-1.6 (m, 2H), 1.45-1.35(m, 6H), 1.00-0.95(t, 3H).

Synthesis of (3HT)-SnBu$_3$. 3-hexylthiophene (1.5g, 8.91mmol) was dissolved in 200ml THF and the solution was cooled down to -78℃. 1M solution of lithium diisopropylamide in THF/hexane (14.4ml, 13.37mmol) was added slowly into the solution and stirred for 2h. Then tributyltin chloride (2.88ml, 10.69mmol) was added dropwise. The mixture was stirred at -78℃ for another 1h before allowing to warm up to room temperature and washed with deionized water and brine. The organic phase was dried over magnesium sulfate. After filtration, the solvent was removed under pressure. The product was used without further purification. ^{1}H NMR (500

MHz, $CDCl_3$): 7.24-7.19 (m, 2H), 7.02-6.97 (m, 1H), 2.73-2.62 (m, 4H), 1.74-1.53 (m, 10H), 1.44-1.31 (m, 18H), 1.19-1.05 (m, 6H), 1.00-0.87 (m, 15H).

Synthesis of $(3HT)_2$. Br-(3HT) (4.5g, 18.2mmol) and (3HT)-$SnBu_3$ (8.3g, 18.8mmol) were dissolved in anhydrous toluene (150ml) and bubbled with N_2 for 30 mins. Tetrakis(triphenylphosphine) palladium ($Pd(PPh_3)_4$) (0.22g, 0.2mmol) was added and the solution was bubbled with N_2 for another 10 mins before stirring at 90℃ for 72h. The organic solvents were removed by vacuum, then the crude product was purified by column chromatography (SiO_2, hexane) to give a light yellow oil (5.26g, 90% yield). ^{1}H NMR (500 MHz, $CDCl_3$): 7.16 (d, J=5.1Hz, 1H), 6.96 (m, 1H), 6.94 (d, J=5.2Hz, 1H), 6.90 (m, 1H), 2.77 (t, J=8.1Hz, 2H), 2.64 (t, J=7.5 Hz, 2H), 1.71-1.61 (m, 4H), 1.44-1.25 (m, 12H), 0.97-0.87 (m, 6H).

Br-$(3HT)_2$ $(3HT)_2$ (3g, 9mmol) was dissolved in THF/DMF (20ml/ 40ml) and the solution was cooled down to -20℃. A solution of N-bromosuccinimide (1.6g, 9mmol) in DMF (15ml) was added and the mixture stirred at -20 ℃ for 4h before stirring at room temperature overnight. Hexane (10ml) was added and the mixture was washed with deionized water and brine. The organic phase was dried over magnesium sulphate. After filtration, the solvent was removed. The product (3.6g, 96% yield) was used without further purification. ^{1}H NMR (500 MHz, $CDCl_3$): 7.18 (d, J=5.2Hz, 1H), 6.93 (d, J=5.2Hz, 1H), 6.81 (s, 1H), 2.73 (t, J=7.8 Hz, 2H), 2.58 (t, J=7.5 Hz, 2H), 1.69-1.58 (m, 4H), 1.45-1.25(m, 12H), 0.97-0.85 (m, 6H).

$(3HT)_2$-$SnBu_3$ $(3HT)_2$ (2.7g, 8.0mmol) was dissolved in 200ml THF and the solution was cooled down to -78℃. 1M solution of lithium diisopropylamide in THF/hexane (12ml, 12mmol) was added slowly into the solution and stirred for 2h. Then tributyltin chloride (2.6ml, 9.6mmol) was added dropwise and the mixture was stirred at -78℃ for another 1h. The solution was allowed to warm up to room temperature and washed with deionized water and brine. The organic phase was dried over magnesium sulphate. After filtration, the solvent was removed. The product was used without further purification. ^{1}H NMR (500 MHz, $CDCl_3$): 7.35-7.28 (m, 1H), 7.26-7.19 (m, 1H), 6.97-6.95 (m, 1H), 2.78 (t, J=8.2 Hz, 2H), 2.62 (t, J=7.8 Hz, 2H), 1.73-1.57 (m, 10H), 1.45-1.28 (m, 18H), 1.20-1.08 (m, 6H), 1.01-0.89 (m, 15H).

(3HT)$_3$ Br-(3HT)$_2$ (4.2g, 10mmol) and (3HT)-SnBu$_3$ (8.3g, 18.8mmol) were dissolved in anhydrous toluene (150ml) and bubbled with N_2 for 30 mins. Tetrakis(triphenylphosphine) palladium (Pd(PPh$_3$)$_4$) (0.23g, 0.2mmol) was added and the solution was bubbled with N_2 for another 10 mins before stirring at 90℃ for 72h. The organic solvents were removed by vacuum, then the crude product was purified by column chromatography (SiO_2, hexane) to give a light yellow oil (1.7g, 34% yield). ^{1}H NMR (500 MHz, $CDCl_3$): 7.18 (d, J=5.1Hz, 1H), 6.99 (s, 1H), 6.98 (s, 1H), 6.96-6.94 (m, 2H), 6.92 (s, 1H), 2.78 (m, 4H), 2.63 (t, J=7.7 Hz, 2H), 1.75-1.61 (m, 6H), 1.47-1.37 (m, 6H), 1.37-1.26(m, 12H), 0.96-0.86 (m, 9H).

Br-(3HT)$_3$ (3HT)$_3$ (1.6g, 3.9mmol) was dissolved in THF/DMF (20 ml/ 10 ml) and the solution was cooled down to -20℃. A solution of N-bromosuccinimide (0.6g, 3.4mmol) in DMF (10ml) was added and the mixture stirred at -20 ℃ for 5h before stirring at room temperature overnight. Hexane (10ml) was added and the mixture was washed with deionized water and brine. The organic phase was dried over magnesium sulphate. After filtration, the solvent was removed. The product (1.9g, 84% yield) was used without further purification. ^{1}H NMR (500 MHz, $CDCl_3$): 7.18 (d, J=5.2Hz, 1H), 6.96-6.93 (m, 2H), 6.83 (s, 1H), 2.79 (t, J=7.7 Hz, 2H), 2.73 (t, J=7.6 Hz, 2H), 2.59 (t, J=7.4 Hz, 2H), 1.71-1.59 (m, 6H), 1.45-1.30 (m, 18H), 0.96-0.89 (m, 9H).

(3HT)$_5$ Br-(3HT)$_3$ (1.3g, 2.2mmol) and (3HT)$_2$-SnBu$_3$ (1.9g, 2.5mmol) were dissolved in anhydrous toluene (150ml) and bubbled with N_2 for 30 mins. Tetrakis(triphenylphosphine) palladium (Pd(PPh$_3$)$_4$) (0.075g, 0.07mmol) was added and the solution was bubbled with N_2 for another 10 mins before stirring at 90℃ for 72h. The organic solvents were removed by vacuum, then the crude product was purified by column chromatography (SiO_2, hexane) to give a red oil (0.5g, 27% yield). ^{1}H NMR (500 MHz, $CDCl_3$): 7.18 (d, J=5.2Hz, 1H), 7.03 (s, 1H), 7.01-6.94 (m, 4H), 6.92 (s, 1H), 2.84-2.76 (m, 6H), 2.64 (t, J=7.8 Hz, 2H), 2.59 (m, 2H), 1.78-1.63 (m, 10H), 1.47-1.26 (m, 30H), 0.98-0.86 (m, 15H).

(3HT)$_5$-SnBu$_3$ (3HT)$_5$ (0.5g, 0.6mmol) was dissolved in 30ml THF and the solution was cooled down to -78℃. 1M solution of lithium diisopropylamide in THF/hexane (0.4ml, 0.8mmol) was added slowly into the solution and stirred for 2h. Tributyltin chloride (0.2ml, 0.6mmol) was then added dropwise and the mixture was stirred at -

78℃ for another 1h. Then the solution was allowed to warm up to room temperature and washed with deionized water and brine. The organic phase was dried over magnesium sulphate. After filtration, the solvent was removed. The product was used without further purification. ^{1}H NMR (500 MHz, $CDCl_3$): 7.31 (s, 1H), 7.26 (s, 1H), 7.19 (s, 1H), 7.18 (s, 1H), 7.14 (s, 1H), 6.67 (s, 1H), 2.92-2.82 (m, 8H), 2.47 (t, J=7.9 Hz, 2H), 1.77-1.64 (m, 16H), 1.47-1.24 (m, 42H), 0.96-0.84 (m, 24H).

References

1. Gabrielsson, E., et al., *Convergent/Divergent Synthesis of a Linker-Varied Series of Dyes for Dye-Sensitized Solar Cells Based on the D35 Donor.* Advanced Energy Materials, 2013. **3**(12): p. 1647-1656.
2. Yang, J.B., et al., *Influence of the Donor Size in D-pi-A Organic Dyes for Dye-Sensitized Solar Cells.* Journal of the American Chemical Society, 2014. **136**(15): p. 5722-5730.
3. Feldt, S.M., et al., *Design of Organic Dyes and Cobalt Polypyridine Redox Mediators for High-Efficiency Dye-Sensitized Solar Cells.* Journal of the American Chemical Society, 2010. **132**(46): p. 16714-16724.
4. Pei, K., et al., *Constructing High-Efficiency D-A-pi-A-Featured Solar Cell Sensitizers: a Promising Building Block of 2,3-Diphenylquinoxaline for Antiaggregation and Photostability.* Acs Applied Materials & Interfaces, 2013. **5**(11): p. 4986-4995.
5. Abate, A., et al., *An Organic "Donor-Free" Dye with Enhanced Open-Circuit Voltage in Solid-State Sensitized Solar Cells.* Advanced Energy Materials, 2014. **4**(13): p. 201400166.
6. Planells, M., et al., *Oligothiophene Interlayer Effect on Photocurrent Generation for Hybrid TiO2/P3HT Solar Cells.* Acs Applied Materials & Interfaces, 2014. **6**(19): p. 17226-17235.
7. Koch, F.P.V., P. Smith, and M. Heeney, *"Fibonacci's Route" to Regioregular Oligo(3-hexylthiophene)s.* Journal of the American Chemical Society, 2013. **135**(37): p. 13695-13698.
8. Nazeeruddin, M.K., et al., *Engineering of efficient panchromatic sensitizers for nanocrystalline TiO2-based solar cells.* Journal of the American Chemical Society, 2001. **123**(8): p. 1613-1624.
9. Koumura, N., et al., *Alkyl-functionalized organic dyes for efficient molecular photovoltaics.* Journal of the American Chemical Society, 2006. **128**(44): p. 14256-14257.
10. Schmidt-Mende, L., et al., *Effect of hydrocarbon chain length of amphiphilic ruthenium dyes on solid-state dye-sensitized photovoltaics.* Nano Letters, 2005. **5**(7): p. 1315-1320.
11. Guo, M., et al., *Photoelectrochemical studies of nanocrystalline TiO2 co-sensitized by novel cyanine dyes.* Solar Energy Materials and Solar Cells, 2005. **88**(1): p. 23-35.
12. Kanemitsu, Y., et al., *Optical-Properties of Quasi-One-Dimensional Thiophene-Based Oligomers.* Physical Review B, 1994. **50**(4): p. 2301-2305.
13. Gaussian 09, R.A., M. J. Frisch, G. W. Trucks, H. B. Schlegel, G. E. Scuseria, M. A. Robb, J. R. Cheeseman, G. Scalmani, V. Barone, B. Mennucci, G. A. Petersson, H. Nakatsuji, M. Caricato, X. Li, H. P. Hratchian, A. F. Izmaylov, J. Bloino, G. Zheng, J. L. Sonnenberg, M. Hada, M. Ehara, K. Toyota, R. Fukuda, J. Hasegawa, M. Ishida, T. Nakajima, Y. Honda, O. Kitao, H. Nakai, T. Vreven, J. A. Montgomery, Jr., J. E. Peralta, F. Ogliaro, M. Bearpark, J. J. Heyd, E. Brothers, K. N. Kudin, V. N. Staroverov, R. Kobayashi, J. Normand, K. Raghavachari, A. Rendell, J. C. Burant, S. S. Iyengar, J. Tomasi, M. Cossi, N.

Rega, J. M. Millam, M. Klene, J. E. Knox, J. B. Cross, V. Bakken, C. Adamo, J. Jaramillo, R. Gomperts, R. E. Stratmann, O. Yazyev, A. J. Austin, R. Cammi, C. Pomelli, J. W. Ochterski, R. L. Martin, K. Morokuma, V. G. Zakrzewski, G. A. Voth, P. Salvador, J. J. Dannenberg, S. Dapprich, A. D. Daniels, O. Farkas, J. B. Foresman, J. V. Ortiz, J. Cioslowski, and D. J. Fox, Gaussian, Inc., Wallingford CT, 2009.

14. Becke, A.D., *A New Mixing of Hartree-Fock and Local Density-Functional Theories.* Journal of Chemical Physics, 1993. **98**(2): p. 1372-1377.
15. Barea, E.M., et al., *Bandgap Modulation in Efficient n-Thiophene Absorbers for Dye Solar Cell Sensitization.* Chemphyschem, 2010. **11**(1): p. 245-250.
16. Cossi, M. and V. Barone, *Time-dependent density functional theory for molecules in liquid solutions.* Journal of Chemical Physics, 2001. **115**(10): p. 4708-4717.
17. Hagberg, D.P., et al., *Molecular engineering of organic sensitizers for dye-sensitized solar cell applications.* Journal of the American Chemical Society, 2008. **130**(19): p. 6259-6266.
18. Wang, Z.S., et al., *Hexylthiophene-functionalized carbazole dyes for efficient molecular photovoltaics: Tuning of solar-cell performance by structural modification.* Chemistry of Materials, 2008. **20**(12): p. 3993-4003.
19. Fabregat-Santiago, F., et al., *Influence of electrolyte in transport and recombination in dye-sensitized solar cells studied by impedance spectroscopy.* Solar Energy Materials and Solar Cells, 2005. **87**(1-4): p. 117-131.
20. Fabregat-Santiago, F., et al., *Characterization of nanostructured hybrid and organic solar cells by impedance spectroscopy.* Physical Chemistry Chemical Physics, 2011. **13**(20): p. 9083-9118.
21. Barnes, P.R.F., et al., *Interpretation of Optoelectronic Transient and Charge Extraction Measurements in Dye-Sensitized Solar Cells.* Advanced Materials, 2013. **25**(13): p. 1881-1922.
22. Roy-Mayhew, J.D., et al., *Functionalized Graphene as a Catalytic Counter Electrode in Dye-Sensitized Solar Cells.* Acs Nano, 2010. **4**(10): p. 6203-6211.
23. Fabregat-Santiago, F., et al., *Correlation between photovoltaic performance and impedance spectroscopy of dye-sensitized solar cells based on ionic liquids.* Journal of Physical Chemistry C, 2007. **111**(17): p. 6550-6560.

Chapter 4 Oligo(4,4-dihexyl-4H-cyclopenta[1,2-b:5,4-b']dithiophene) dyes

1 Introduction

4H-cyclopenta[2,1-b:3,4-b']dithiophene (CPDT) has been used for constructing the π-conjugated skeleton of organic sensitisers in many cases because of its excellent co-planarity as well as the electron donating capability.[1] Compared to two thiophene units as π-bridge, the fused bithiophene π-group red-shifts the visible light absorption maximum of the sensitiser and increases its molar extinction coefficient at the same time.[2] For example, dye C218 not only showed a broader absorption spectrum, but also a 2-fold higher molar extinction coefficient than D21L6. (Figure 4.1) As a result, applying both dyes in ssDSSCs, the short-circuit current (J_{SC}) of the device using C218 was higher than that using D21L6 and thus led to an efficiency of 5.6% whereas the one using D21L6 has an efficiency of 4.4%.[3, 4]

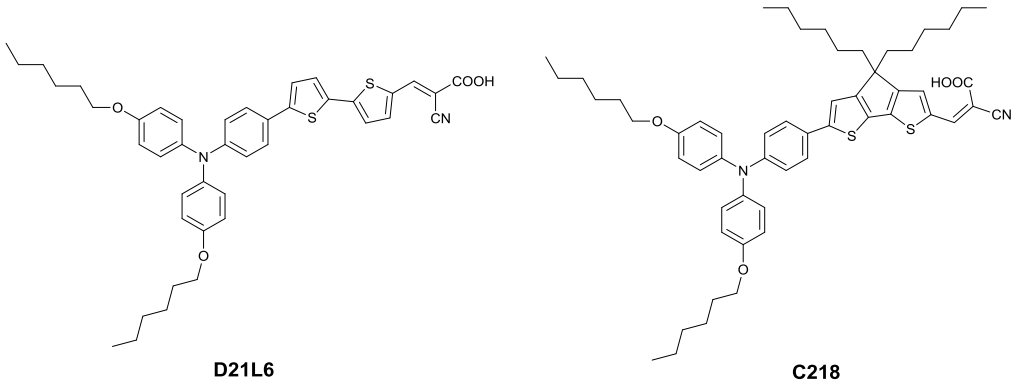

Figure 4.1 Chemical structures of D21L6 and C218.

In addition, the easy introduction of long alkyl chains at the bridging carbon atoms of CPDT can efficiently decrease the intermolecular interactions and retard the electron recombination, resulting in an obvious improvement of V_{OC}.[5, 6] Nazeeruddin et al [3] studied the influence of alkyl chain length on organic donor-π-acceptor sensitisers. They found that the dye with hexyl chains (D21L6) exhibited longer electron lifetime than methyl (D9L6) or dodecyl chains (D25L6). The structures are shown in Figure 4.1 and Figure 4.2. This conclusion was further supported by computational chemistry.[7]

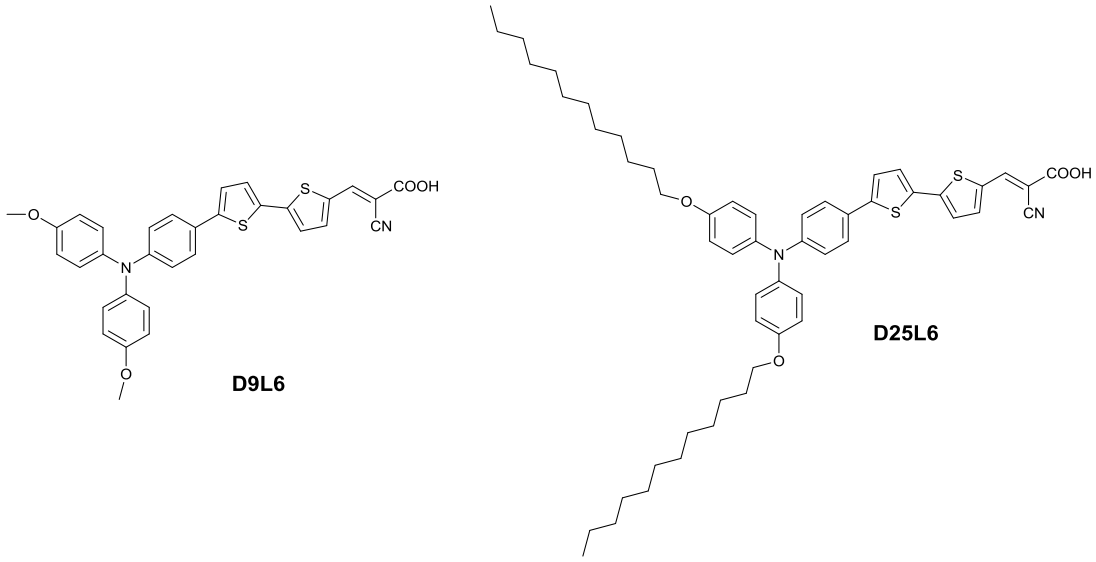

Figure 4.2 Chemical structures of D9L6 and D25L6.

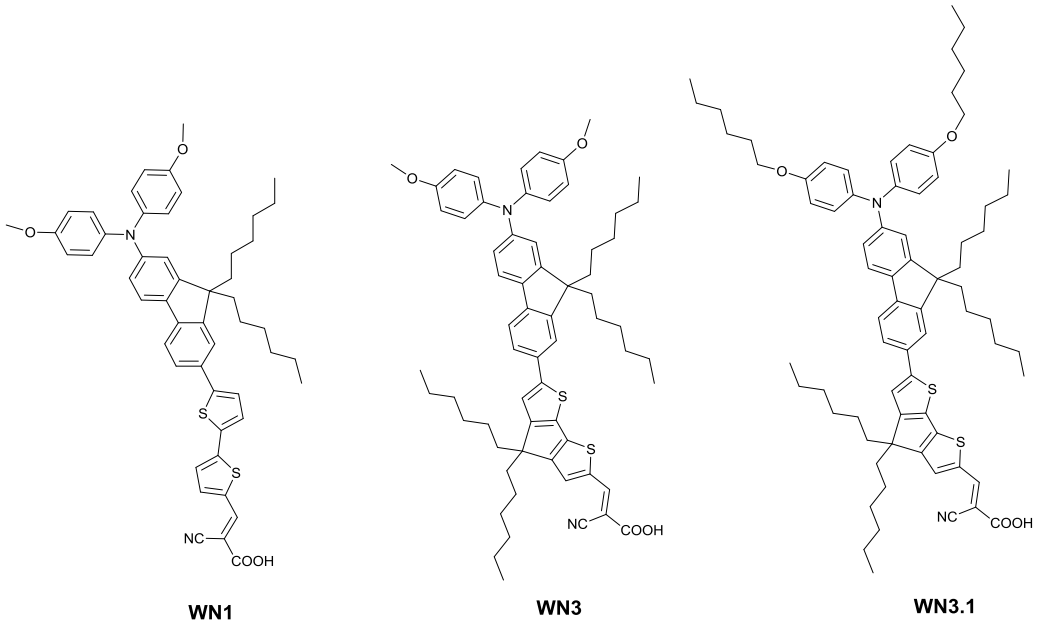

Figure 4.3 Chemical structures of WN1, WN3 and WN3.1

Nguyen [8] et al. studied the effects of the quantity and position of alkyl chains of sensitisers on the device performance of ssDSSCs. Through the study of three dyes, WN1, WN3 and WN3.1 (Figure 4.3), the quantity and placement of alkyl chains were found to play a significant role in the suppression of recombination. Among these three dyes, WN3.1 is shown, by transient photovoltage and photocurrent measurements, to be the most effective at suppressing recombination in ssDSSCs. As

a result, WN3.1 gave an efficiency of 6.3% using spiro-OMeTAD as the hole-transport material whereas WN1 achieved an efficiency of 4.9% and WN3 had 5.9%.

Based on this knowledge and the research in Chapter 3, a series of 'donor-free' oligo(4,4-dihexyl-4H-cyclopenta[1,2-b:5,4-b']dithiophene) functionalized with cyanoacrylic end groups (CPDT-1, CPDT-2 and CPDT-3) was designed, synthesised, characterised and checked thoroughly in solar cell devices based on different electrolytes.

2 Results and Discussion

2.1 Synthesis

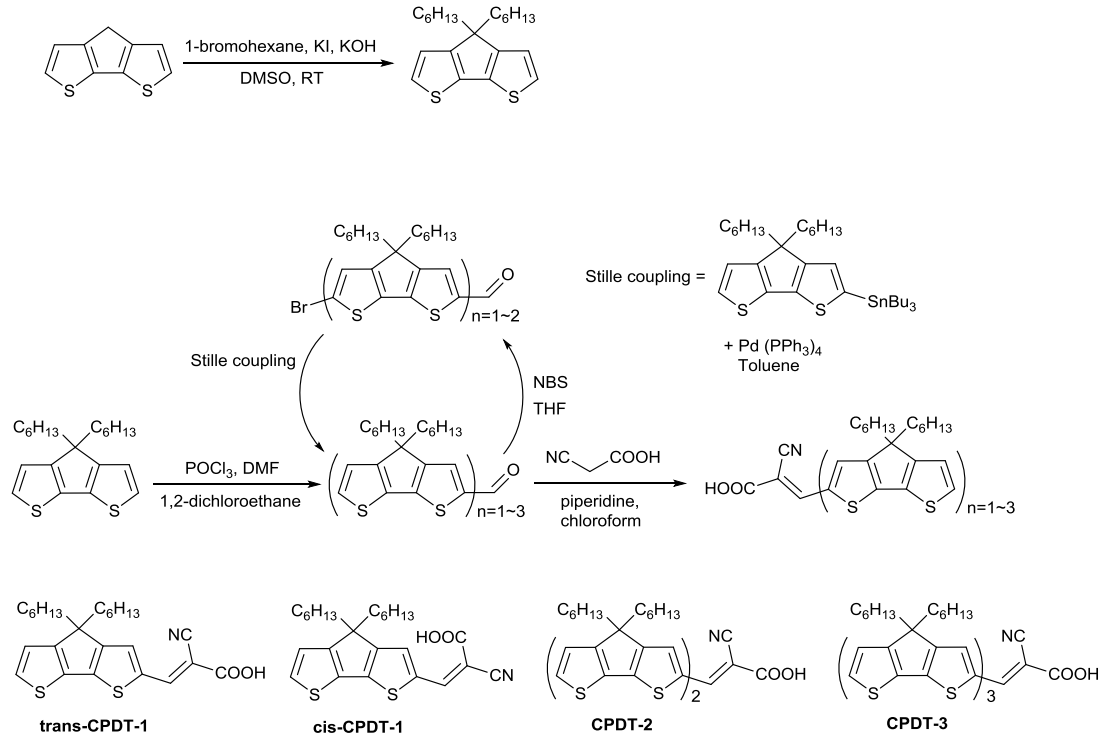

Scheme 4.1 Synthesis of CPDT series and isomers of CPDT-1

The synthetic route used to obtain the oligo-CPDT series is shown in Scheme 4.1. Two hexyl chains were first introduced on the CPDT unit to attenuate the interfacial recombination, followed by palladium catalysed Stille coupling reactions and then

Knoevenagel condensation to give CPDT-1, CPDT-2 and CPDT-3. CPDT-1 was obtained as an isomeric mixture in a 77:23 ratio between trans- and cis- cyanoacrylic acid (confirmed by ^{1}H NMR) and further separation was not possible by conventional purification techniques. This isomerization of the cyanoacrylic acid acceptor group has also been seen by Zietz, et al [9] using a simple D-π-A type dye where the donor triarylamine is connected with the cyanoacrylic acid acceptor via a double bond π-bridge. Despite this, no isomerization was observed for larger molecules, and in our case, CPDT-2 and CPDT-3 were found to be pure-trans by ^{1}H NMR.

2.2 Optical properties

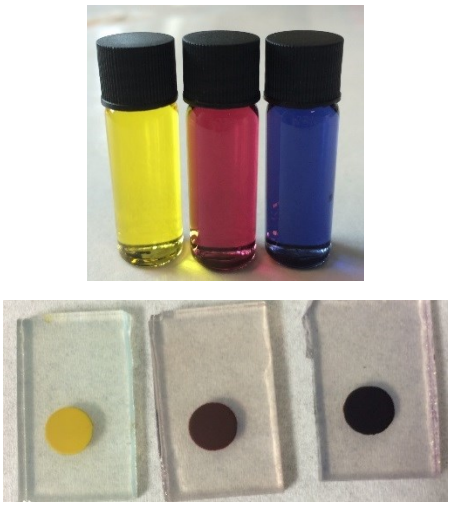

Figure 4.4 CPDT series in CH_2Cl_2 solution (upper) and on TiO_2 film (lower). From left to right: CPDT-1, CPDT-2 and CPDT-3.

Table 4.1 Summary of optical properties for CPDT series in CH_2Cl_2 solution

	λ_{max} / nm	ε / M^{-1} cm^{-1}	λ_{em} / nm	$E_{0\text{-}0}$[a] / V
CPDT-1	456	49000	516	2.55
CPDT-2	546	54000	676	1.94
CPDT-3	585	74000	682	1.99

[a] Optical gap estimated from the intersection of UV-vis spectrum and emission spectrum.

Optical properties of the CPDT series were studied in dichloromethane solution (Figure 4.4). The data are summarized in Table 4.1. The addition of each CPDT unit

led to an expected red shift in the UV-vis spectrum and also an increase in the extinction coefficient, as shown in Figure 4.5. This is the result of the extra conjugation and electron delocalization within the CPDT backbone, which reduces the molecular HOMO-LUMO gap. Therefore, the CPDT series appear yellow, red and blue in CH_2Cl_2 solution, respectively. Especially for CPDT-2 and CPDT-3, their superb absorption capability shows great potential for application as sensitisers in dye-sensitised solar cells.

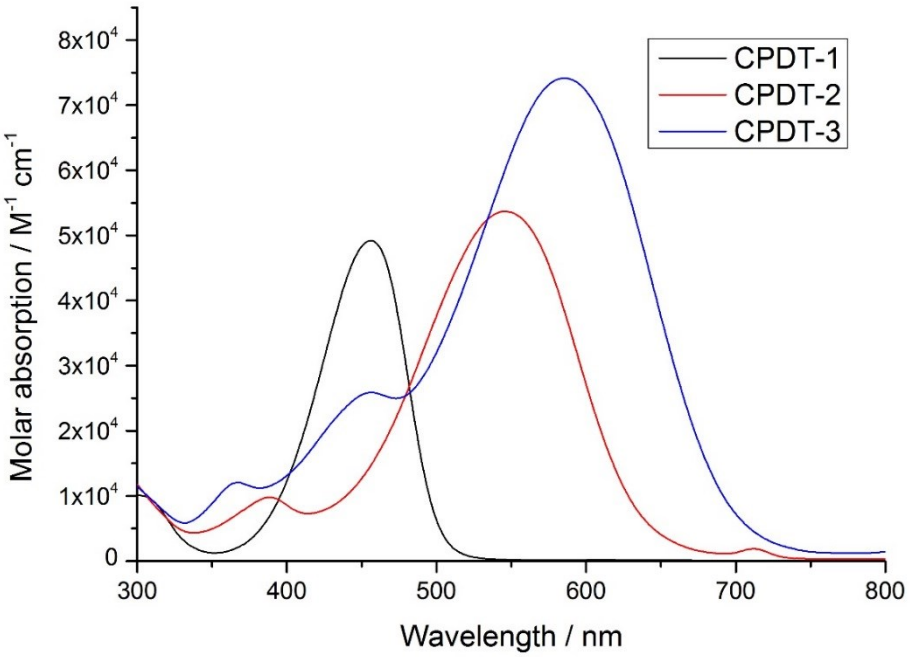

Figure 4.5 Absorbance spectra of oligo-CPDT molecules obtained in 2 × 10^{-5} M solution of DCM. A Beer-Lambert plot showed a linear response confirming no aggregation at this concentration.

Photoluminescence (PL) was also studied in dichloromethane solution and is shown in Figure 4.6. They all show broad emission bands covering visible and even the near-IR region. There is again a trend of red-shifting upon increasing the CPDT chain length. The optical gaps were estimated from the intersection of UV-vis spectrum and emission spectrum as shown in Table 4.1.

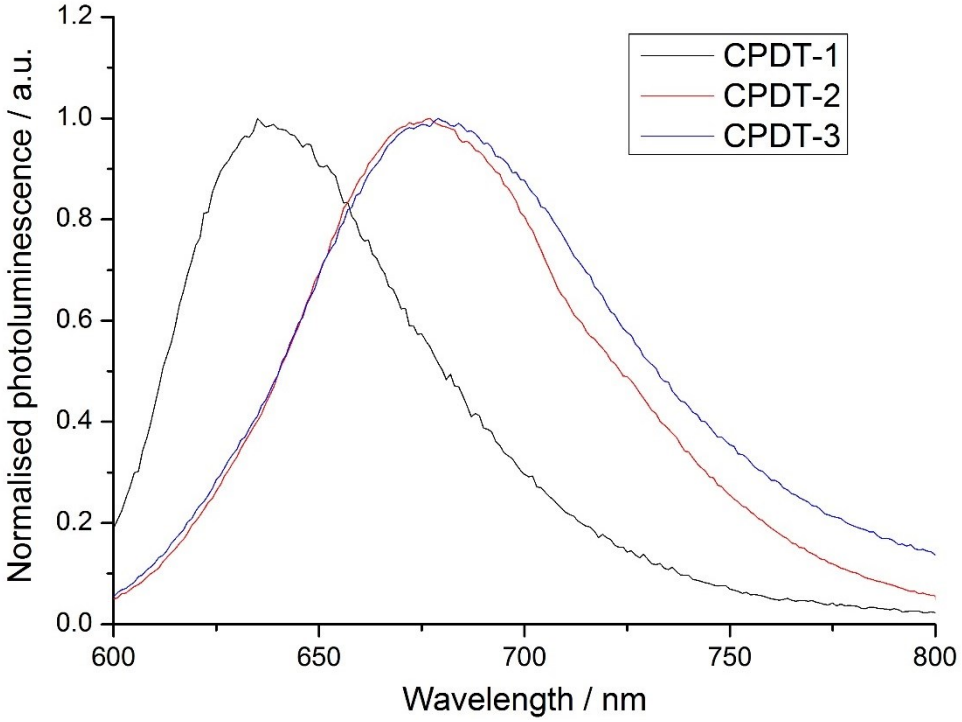

Figure 4.6 Photoluminescence (PL) spectra of CPDT series obtained in 5 × 10^{-6} M solution of DCM.

2.3 Electrochemistry

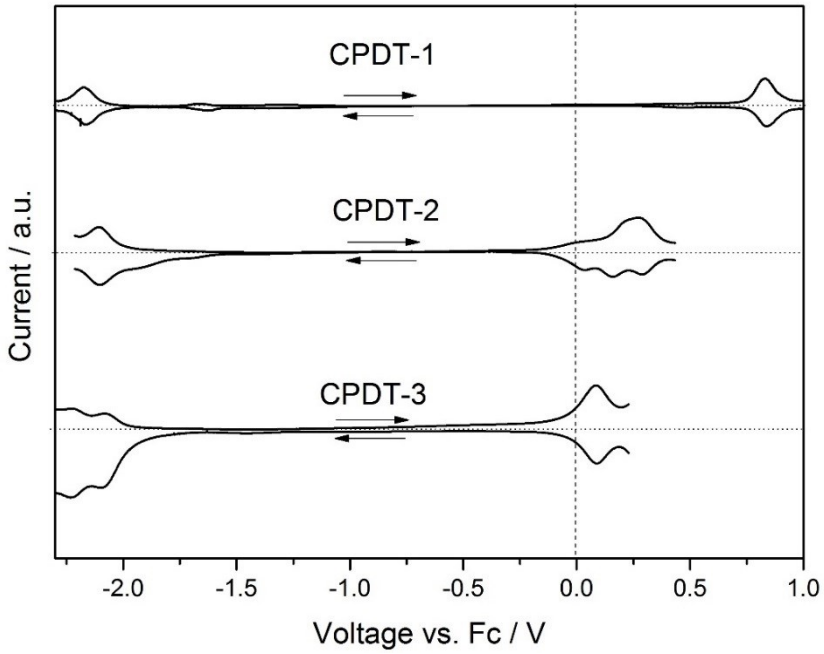

Figure 4.7 SWV of CPDT series recorded in DCM solution containing 0.3 M [TBA][BF_4] and referenced internally to ferrocene. Arrows indicate the direction of scan.

Table 4.2 Summary of electrochemical properties for CPDT series in CH_2Cl_2 solution and exciton binding energies, estimated by E_{gap}^{CV}- $E_{0\text{-}0}$

	E_{ox} / V		E_{red} / V		E_{gap}^{CV} / V	E_{gap}^{CV}- $E_{0\text{-}0}$
	vs. Fc	vs. NHE	vs. Fc	vs. NHE		
CPDT-1	0.83	1.46	-2.17	-1.54	3.00	0.45
CPDT-2	0.26	0.89	-2.11	-1.48	2.37	0.43
CPDT-3	0.08	0.71	-2.07	-1.44	2.15	0.16

The redox potentials for CPDT-1~3 were obtained by cyclic voltammetry (CV) and square-wave voltammetry (SWV) and are summarised in Table 4.2 and Figure 4.7. Upon increasing CPDT core length, a clear trend in the oxidation potentials can be observed. The oxidation peaks gradually shifted to less positive potentials and the electrochemical gap between the first oxidation and first reduction potentials was reduced. The first oxidation process for CPDT-1 (Figure 4.8) is irreversible on electrochemical time scales (0.1s to 1s). On the other hand, CPDT-2 and CPDT-3 (Figure 4.9 and Figure 4.10) show reversible electrochemical behaviour, although the first two oxidation processes are too close to each other to be studied separately by cyclic voltammetry. For the reduction processes, a slight shift to less negative potentials can be observed upon adding CPDT units. The change is much smaller than the oxidation processes change because the reduction processes is mainly controlled by the cyanoacrylic moiety where the LUMO is mainly localized in this series (see computational studies below).

In addition, the exciton binding energy was estimated by subtracting the optical gap from the electrochemical gap. The excition binding energy was reduced by increasing the CPDT chain length, indicating greater spatial separation of the electron-hole pair.

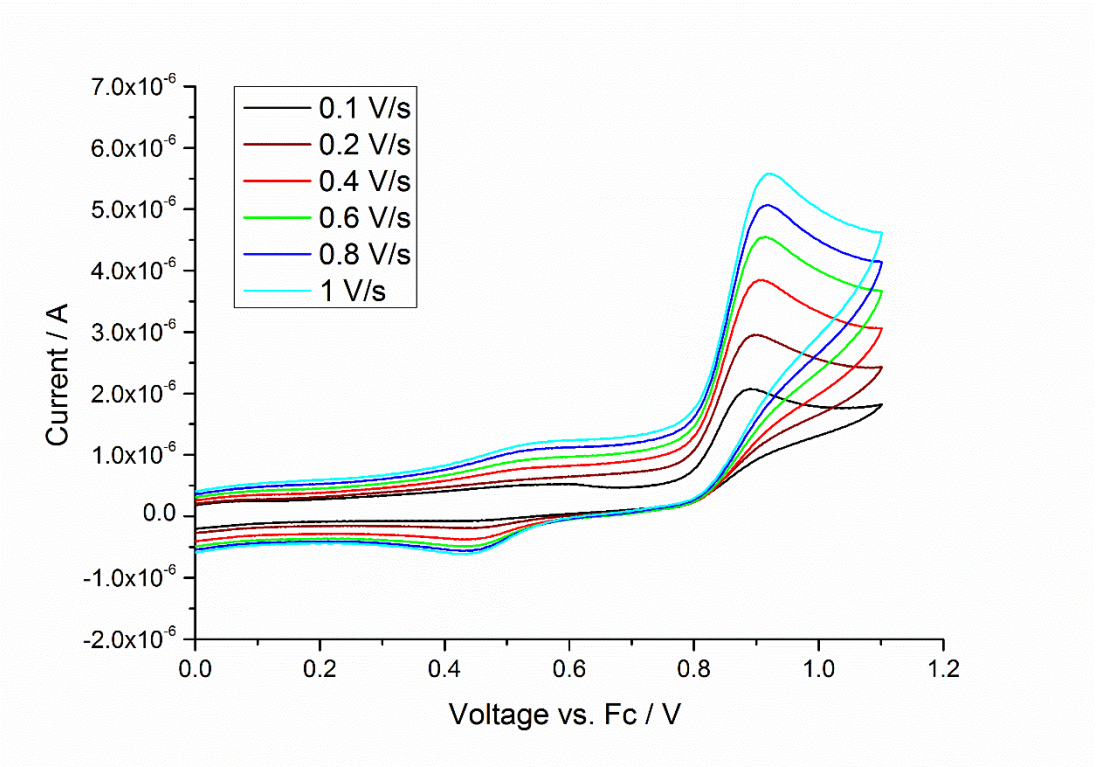

Figure 4.8 Cyclic voltammetry of CPDT-1 recorded in DCM solution containing 0.3 M [TBA][BF_4].

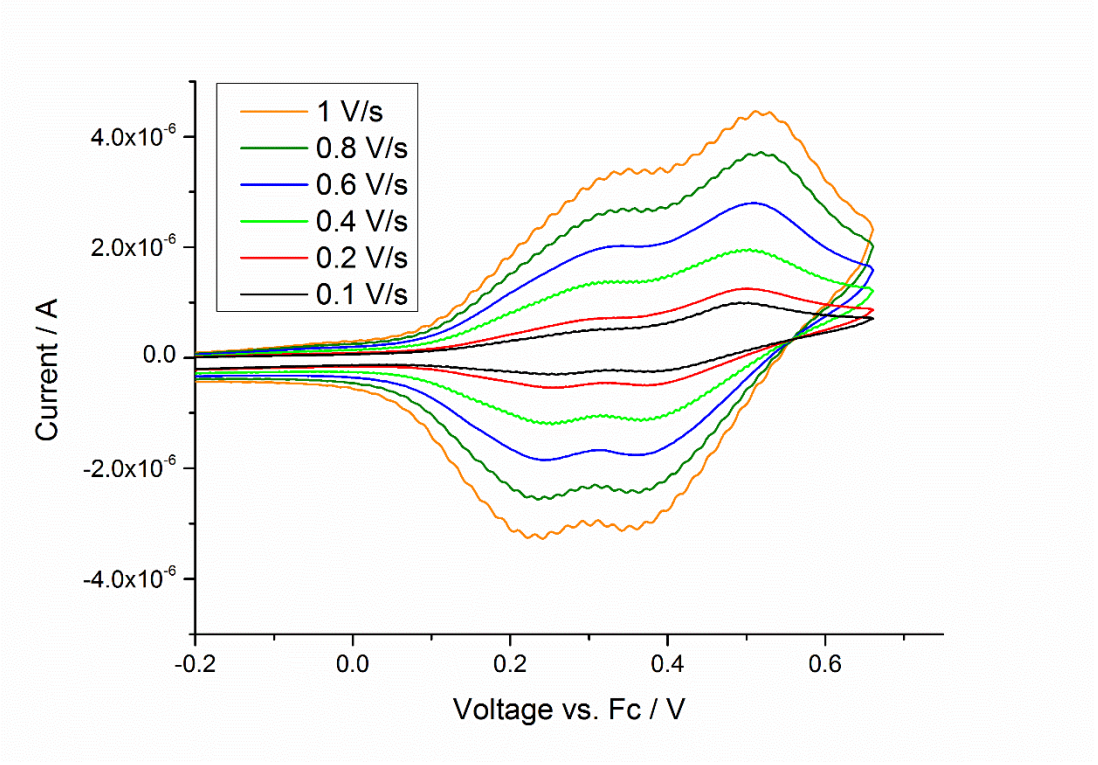

Figure 4.9 Cyclic voltammetry of CPDT-2 recorded in DCM solution containing 0.3 M [TBA][BF_4].

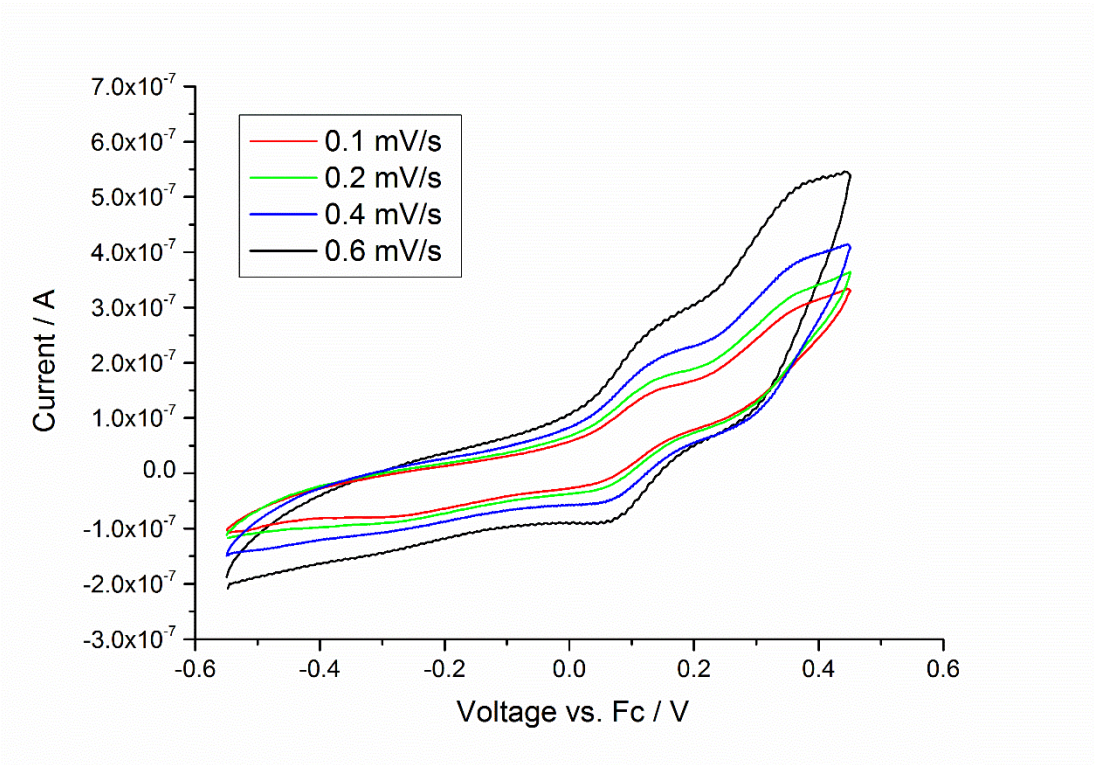

Figure 4.10 Cyclic voltammetry of CPDT-3 recorded in DCM solution containing 0.3 M [TBA][BF_4].

2.4 Computational

Hybrid DFT calculations were performed at B3LYP/6-31G(d) level of theory. Dipole moments are important for organic dyes since they can cause a shift of the TiO_2 conduction band, thus lead to a change in the V_{OC} in devices.[10] The dipole moment of each dye was calculated and compared in Table 4.3. Upon increasing the chain length, an increase of dipole moment was observed due to the increased distance between the 'electron rich' component and 'electron deficient' component.

Table 4.3 Calculated dipole moments both in vacuum and in DCM

	CPDT-1	CPDT-2	CPDT-3
In vacuum	8.87	10.42	12.62
In DCM	11.92	14.09	16.64

Table 4.4 and Figure 4.11 show the calculated energy levels of the CPDT series and the HOMO and LUMO molecular orbital distribution. In all cases, the HOMO is mainly located on the CPDT core chain and the LUMO is located on the cyanoacrylic moiety, indicating good charge separation and appropriate charge directionality. The calculated HOMO and LUMO energy levels followed the same trend as that measured using electrochemistry.

Table 4.4 Calculated energy levels in vacuum and in DCM

	CPDT-1		CPDT-2		CPDT-3	
	In vacuum	In DCM	In vacuum	In DCM	In vacuum	In DCM
LUMO+2	-0.35 eV	-0.27 eV	-0.85 eV	-0.81 eV	-1.29 eV	-1.28 eV
LUMO+1	-1.14 eV	-0.99 eV	-1.79 eV	-1.73 eV	-1.98 eV	-1.98 eV
LUMO	-2.83 eV	-2.80 eV	-2.80 eV	-2.85 eV	-2.74 eV	-2.84 eV
HOMO	-5.77 eV	-5.67 eV	-5.05 eV	-4.99 eV	-4.68 eV	-4.67 eV
HOMO-1	-7.31 eV	-7.17 eV	-6.05 eV	-6.02 eV	-5.41 eV	-5.41 eV
HOMO-2	-7.39 eV	-7.31 eV	-7.05 eV	-7.01 eV	-6.15 eV	-6.16 eV

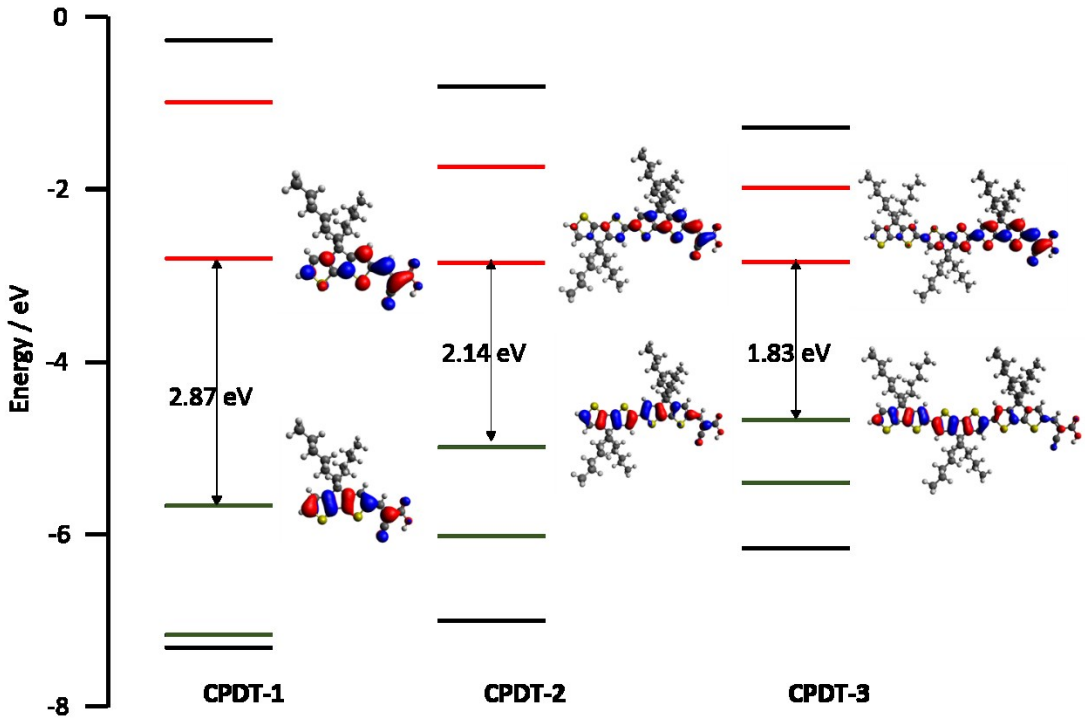

Figure 4.11 Molecular orbital distribution of HOMO (bottom) and LUMO (top) for CPDT series with their energy gap in DCM.

TD-DFT calculations were used to compare the theoretical and experimental electronic transitions through absorption spectroscopy. The calculations matched well with the experimental as shown in Figure 4.12. The lowest energy transitions of these dyes are dominated by HOMO→LUMO character. The maximum absorption band of CPDT-3 also has some contributions from HOMO-1→LUMO character. The calculation also agrees qualitatively well with experimental in the case of molar extinction coefficient, whereby the oscillator strength (f) increased with the increasing CPDT chain length.

Table 4.5 TD-DFT calculated energies and compositions of selected transitions

Compounds	E(nm)	Composition	f
CPDT-1	428	97% H→L	1.01
CPDT-2	542	89% H→L	1.81
CPDT-3	592	73% H→L, 13%H-1→L	2.62

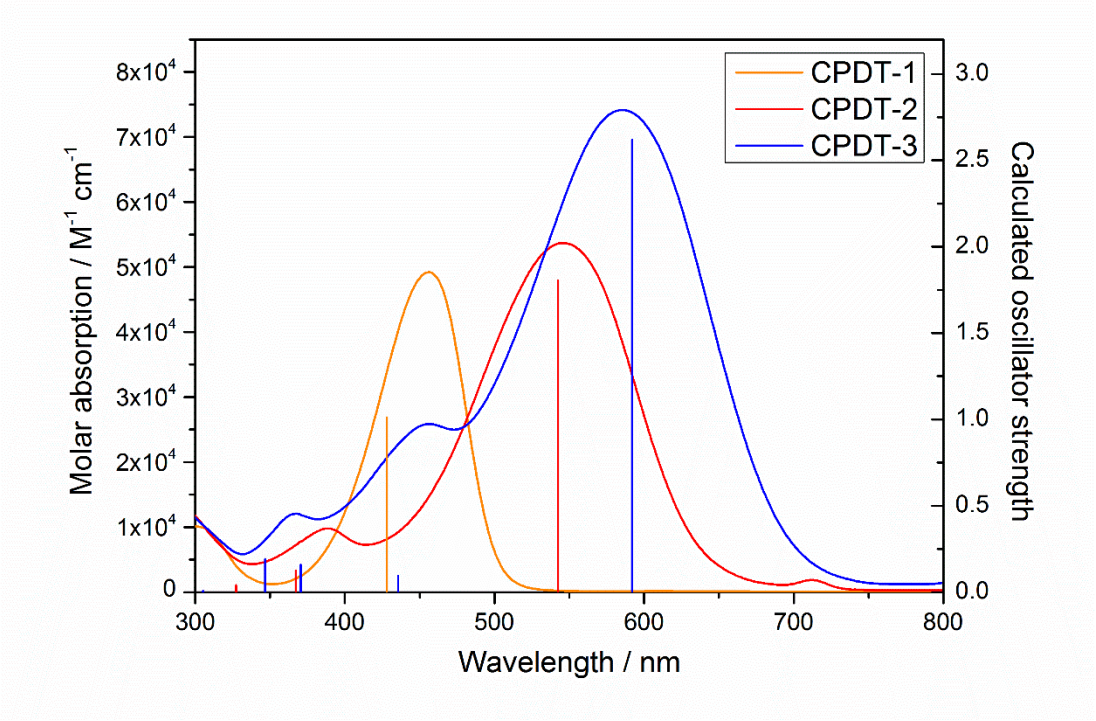

Figure 4.12 Experimental UV-vis absorption spectra of CPDT-1~3 with calculated electronic transitions represented as vertical lines.

2.5 Device performance

2.5.1 Cell optimisation

Not only is the solar cell performance dependent on the materials of each component in the device, but also on the cell fabrication process. The overall efficiency of the solar cell can be improved by optimising the cell construction. Namely, one can change the dye bath solvent [11], the concentration of the dye bath [12], co-absorber concentration [13], the soaking time [12], the film thickness [14] and the electrolyte component [15]. The first five methodologies will affect mostly the amount of dye loading and the way that dyes arrange on TiO_2 surface. The electrolyte contains several components and additives that can affect the open-circuit voltage (V_{OC}) and short-circuit current density (J_{SC}). Increasing 4-tert butylpyridine concentration usually improves the V_{OC} by shifting the conduction band edge of TiO_2 to higher energy but decreases the J_{SC} because of less driving force for charge injection. On the contrary, controlling lithium iodide concentration gives the opposite result. For solid-state cells, Co (III) complexes as p-type dopants are usually also added to enhance the charge transport within the HTM and usually result in a better fill factor of the device. [16]

2.5.2 I^-/I_3^- electrolyte based cells

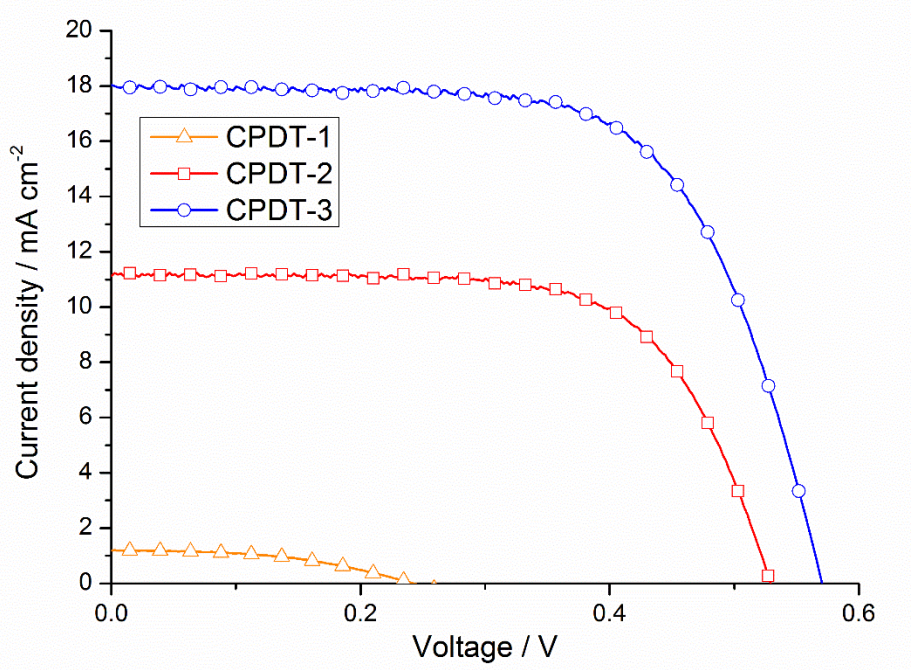

Figure 4.13 J-V curves of CPDT-1, CPDT-2 and CPDT-3

Table 4.6 Photovoltaic performance for cells based on I^-/I_3^- electrolyte under AM 1.5 illumination

Dye	J_{SC} / mA cm^{-2}	V_{OC} / V	FF / %	Efficiency / %
CPDT-1	1.2	0.25	43	0.1
CPDT-2	11.17	0.53	67	4.0
CPDT-3	17.99	0.57	66	6.7
5T	17.15	0.62	72	7.6

The CPDT sensitisers were first examined in I^-/I_3^- electrolyte based dye-sensitised solar cells. The dyes were fairly insoluble in most commonly used organic solvents for dye sensitisation, (*t*-butanol: acentonitrile (1:1)), so a 3:7 mixture of chloroform and ethanol was used as the dye bath solution. The 18 μm TiO_2 photoelectrodes (12 μm mesoporous layer + 6μm scattering layer) were soaked in the 0.5mM corresponding dyes for 3 hours. The electrolyte used in this study contains 1M BMII, 0.05M GuNCS, 0.03M I_2, 0.05M LiI and 0.25M tBP. J-V curves and data are shown in Figure 4.13 and Table 4.6. Upon addition of CPDT unit, we can see an increase in not only the J_{SC} but also V_{OC}, thus leading to an efficiency order of CPDT-3 > CPDT-2 > CPDT-1. 5T (Chapter 3) showed better overall performance than CPDT series mainly because of a higher V_{OC} and ff.

These dyes were further studied in cobalt electrolyte based devices and solid-state solar cells. Due to the yellow colour of CPDT-1 which does not cover most of the solar spectrum, only CPDT-2 and CPDT-3 were further studied in detail and compared with 5T.

2.5.3 $Co^{2+/}Co^{3+}$ electrolyte based cells

The cobalt electrolyte based cells were made by Dr. Yiming Cao from École Polytechnique Fédérale de Lausanne, Switzerland.

Thinner TiO_2 films (6μm of mesoporous layer + 4μm scattering layer) were used for cobalt-devices and the films were soaked in 0.15mM dye solution overnight. The electrolyte contains 0.25M Tris-(2,2'-bipyridine)cobalt(II) di(tetracyanoborate)

$[Co(bpy)_3][(B(CN)_4]_2$, 0.06M tris-(2,2'-bipyridine)cobalt(III) tri(tetracyanoborate) $[(Co(bpy)_3][(B(CN)_4)_3]$, 0.1M LiTFSI and 0.5M tBP.

The J-V data are summarized in Table 4.7 and J-V curves are shown in Figure 4.14. Comparing with the DSSCs using I^-/I_3^- electrolyte, the DSCs using Co^{2+}/Co^{3+} electrolyte showed a lower J_{SC} because of less dye adsorption form a thinner TiO_2 film. However, the V_{OC} of Co^{2+}/Co^{3+} electrolyte based cells increased significantly, resulting in higher overall efficiencies. This increase of V_{OC} is commonly seen [17] due to less loss-in-potential for the one electron Co^{2+}/Co^{3+} redox couple, which requires less overpotential to achieve rapid dye regeneration. Like in I^-/I_3^- based cells, CPDT-3 also showed a higher J_{SC}, V_{OC} and efficiency than CPDT-2 for the DSCs using Co^{2+}/Co^{3+} electrolyte. 5T showed both a higher J_{SC} and a higher V_{OC} than CPDT-3, leading to a superb efficiency of 9%. Figure 4.15 exhibits the incident photon-to-current conversion efficiency (IPCE) spectra recorded on these cells. The J_{SC} data integrated from the IPCE spectra over all wavelengths against the solar spectrum are in good agreement with the experimental values. Although CPDT-3 shows a broader IPCE spectra to 800nm which corresponds to the NIR spectrum, 5T has higher IPCE of ~65% from 400nm to 600nm than CPDT-3 (50%), thus resulting in a higher J_{SC}.

Table 4.7 Photovoltaic performance for cells using cobalt electrolyte

Dye	J_{SC} / mA cm^{-2}	V_{OC} / V	FF / %	Efficiency / %
5T	15.26	0.79	75	9.0
CPDT-2	9.65	0.67	76	4.9
CPDT-3	13.84	0.71	75	7.3

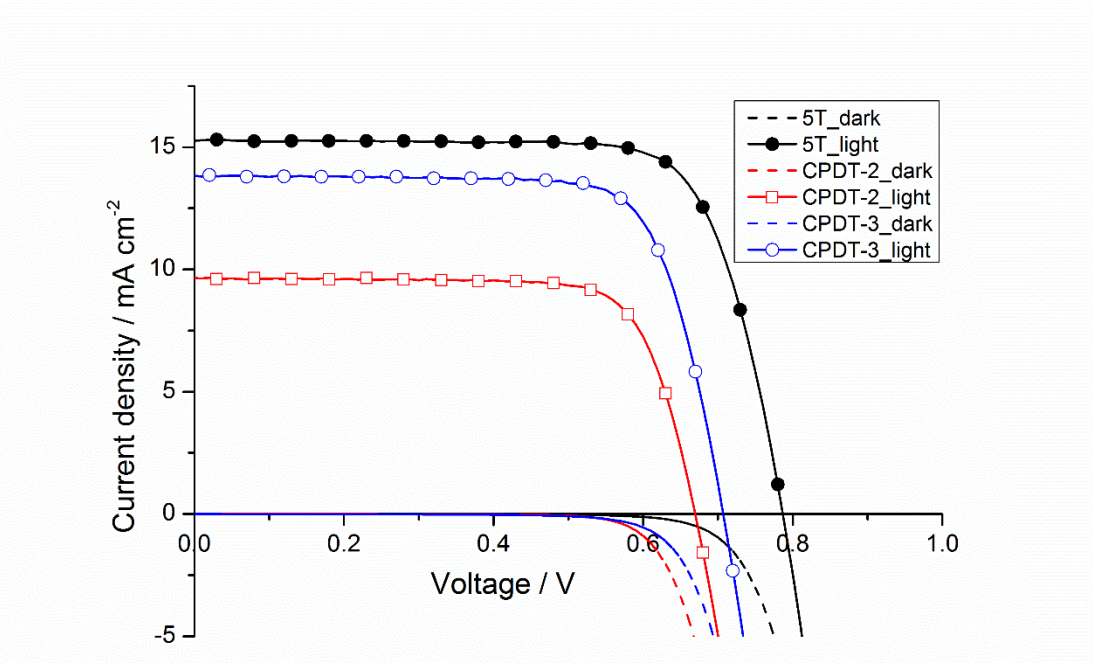

Figure 4.14 J-V curves of CPDT-2, CPDT-3 and 5T (with cobalt electrolyte)

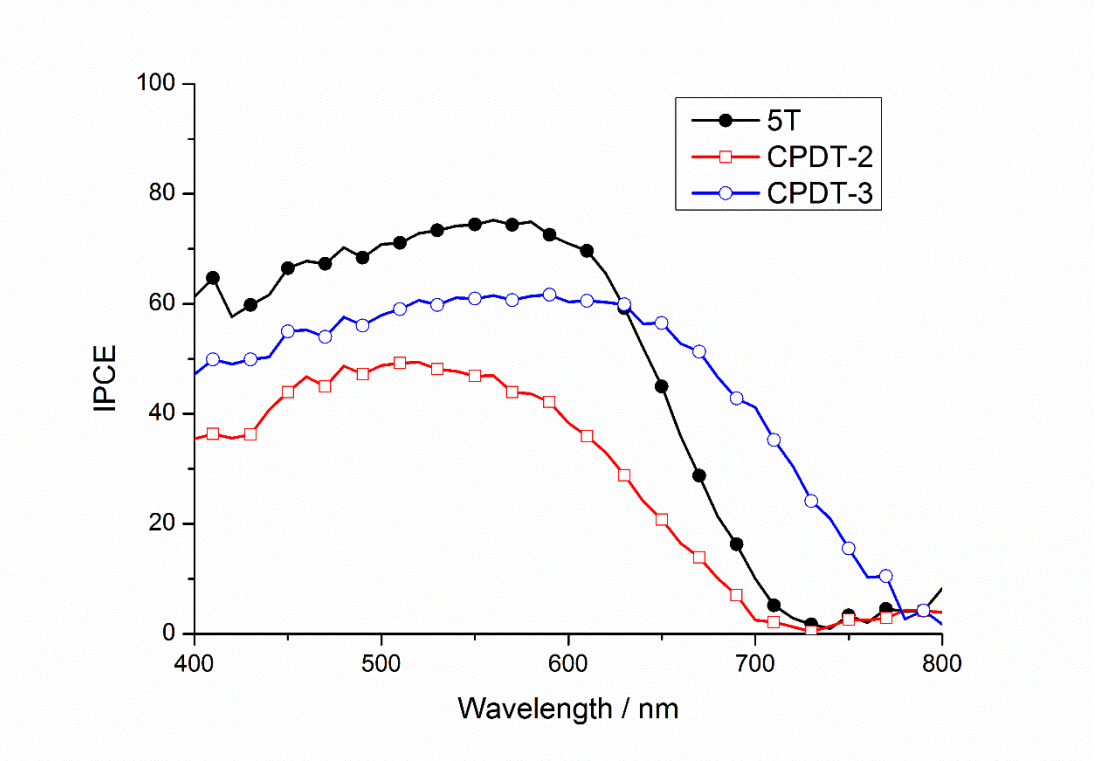

Figure 4.15 J-V curves of CPDT-2, CPDT-3 and 5T (with cobalt electrolyte)

2.5.4 Solid-state solar cells

Figure 4.16 Solid-state dye-sensitised solar cells based on CPDT-1 (yellow), CPDT-2 (orange) and CPDT-3 (purple)

The solid-state solar cells (Figure 4.16) studies were carried out during a research placement in École Polytechnique Fédérale de Lausanne, Switzerland. 5T was used as a comparison and the record dye Y123 was used as a control.

Although these oligo-CPDT dyes were engineered with hexyl chains in order to reduce the tendency towards aggregation, the difference between the absorption spectra in solution and on film revealed that the aggregation cannot be suppressed fully with hexyl chains, attributed to the planarity of CPDT unit. The maximum absorption peaks in dye-bath solution and on 0.9μm film are summarized in Table 4.8 and the spectra are shown in Figure 4.17 and Figure 4.18. In the case of 5T, a bathochromic shift was observed when the dye was bounded with TiO_2, indicating the formation of J-aggregation. On the contrary, hypsochromic shifts were seen in the case of CPDT-2 and CPDT-3, indicating the formation of H-aggregation.

Table 4.8 The maximum absorption peaks of 5T, CPDT-2 and CPDT-3 in solution and on film

	λ_{max} in solution/ nm	λ_{max} on film/ nm
5T	430	446
CPDT-2	494	482
CPDT-3	530	511

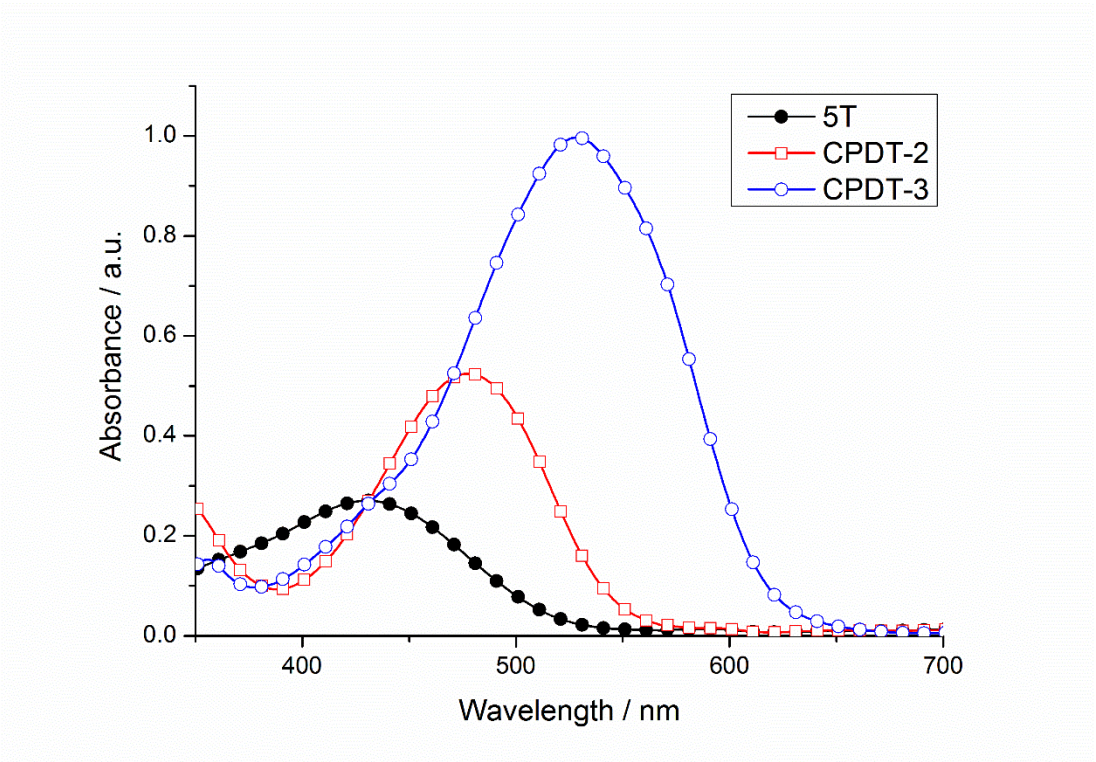

Figure 4.17 UV-vis spectra of 5T, CPDT-2 and CPDT-3 at 0.2mM in chloroform: ethanol (3:7)

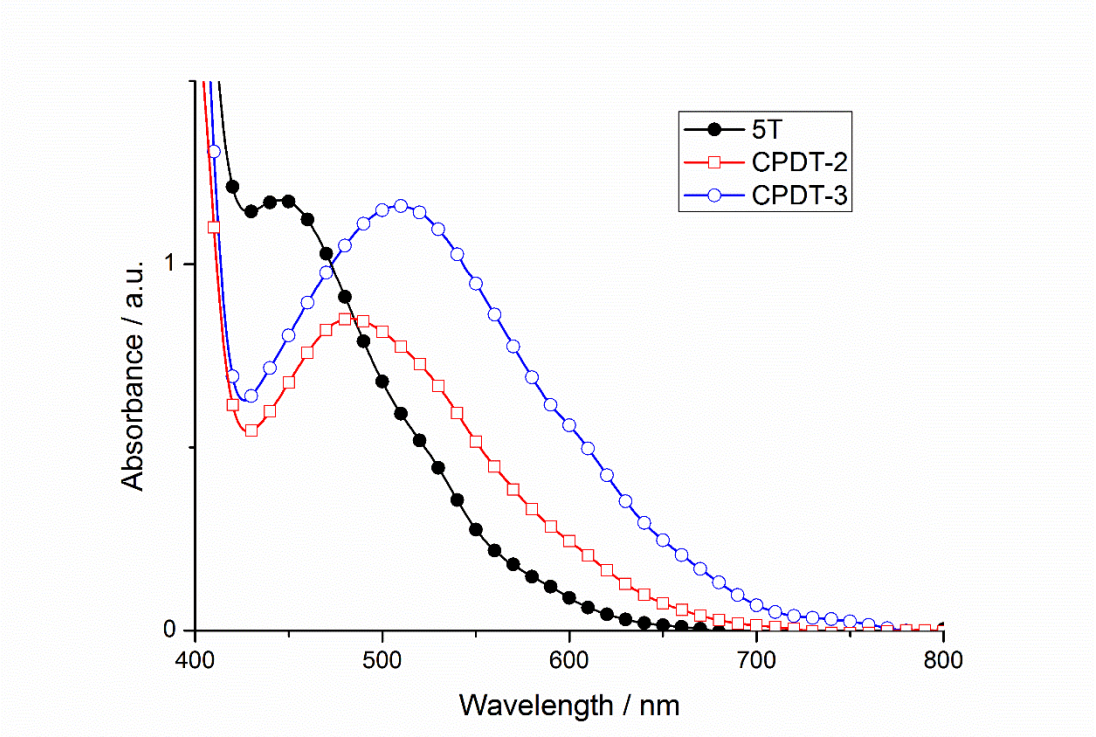

Figure 4.18 UV-vis spectra of 5T, CPDT-2 and CPDT-3 on 0.9μm TiO_2 film

Two different thicknesses of TiO_2 films (2μm or 0.9μm) were used to explore the effects of TiO_2 thickness on solar cell efficiencies. The electrolyte used in this study contains 70mM spiro-OMeTAD, 231mM tBP, 35mM LiTFSI and 2.1mM FK209. The J-V data are shown in Table 4.9.

Table 4.9 J-V data for devices using different thickness of TiO_2

Dye	Thickness of TiO_2/ μm	J_{SC} / mA cm^{-2}	V_{OC} / V	FF / %	Efficiency / %
CPDT-2	2	6.0	0.60	57	2.1
	0.9	5.2	0.67	59	2.1
CPDT-3	2	6.38	0.61	30	1.2
	0.9	8.56	0.64	53	3.1

Thinner films are desired because it means that charges need to travel a shorter distance to reach the electrode, thus are less likely to recombine with spiro-OMeTAD. In addition, thinner films lead to less aggregation. However, in most cases, current density is sacrificed when a thinner film is applied because of insufficient light absorption. Due to the extremely high extinction coefficient of the CPDT dye series, we are able to use a TiO_2 film as thin as 0.9μm. For CPDT-2, an increase in the V_{OC} and FF was observed while J_{SC} was slightly lower when using thinner films, resulting in the same overall efficiency. In the case of CPDT-3, all parameters increased when using thinner films because of less aggregation.

The solar cells were further optimised by varying the concentration of each component in the electrolyte. Finally, the electrolyte composed of 70mM spiro-OMeTAD, 112mM tBP, 14mM LiTFSI and 2.1mM FK209 was used. Co-absorption of chenodeoxycholic acid (CDCA) is often used to reduce dye aggregation, resulting in an improved electron injection efficiency, a decrease of charge recombination and an improved overall efficiencies.[13, 18] However, in the case of the CPDT dyes, addition of CDCA didn't result in either a higher V_{OC} or a higher J_{SC}. (Table 4.10) This could be because adsorption of CDCA leaves protons on the TiO_2 surface and positively shifts the conduction band.

Table 4.10 J-V data for devices using dye bath with different concentration of CDCA

Dye	Concentration of CDCA	J_{SC} / mA cm^{-2}	V_{OC} / V	FF / %	Efficiency / %
CPDT-2	0	7.8	0.72	59	3.5
	0.5mM	7.3	0.71	57	3.3
CPDT-3	0	10.9	0.73	47	3.9
	0.5mM	9.9	0.72	47	3.4

Finally, the cells were made under the optimised conditions and compared with oligo-thiophene dye 5T, with Y123 as control. The J-V data and dye-loading amount are summarised in Table 4.11 and the J-V curves in light and in dark are shown in Figure 4.19. The short-circuit current densities (J_{SC}) of CPDT-2 (7.8mA cm^{-2}) and CPDT-3 (10.9mA cm^{-2}) are higher than 5T (6.5mA cm^{-2}), as expected, due to the high extinction coefficient. CPDT-3 shows an extremely high current density on a TiO_2 film as thin as 0.9μm, which was not observed before on any other organic dyes and is 30% higher than Y123, the record dye in solid-state dye cells. IPCE data (Figure 4.20) correlated well with the photocurrent and UV results. CPDT-3 showed a significantly-broader IPCE spectrum which explains the larger photocurrent. However, the open-circuit voltage and fill factor of CPDT-2 (0.73V, 0.59) and CPDT-3 (0.72V, 0.47) could not compete with 5T (0.85V, 0.67).

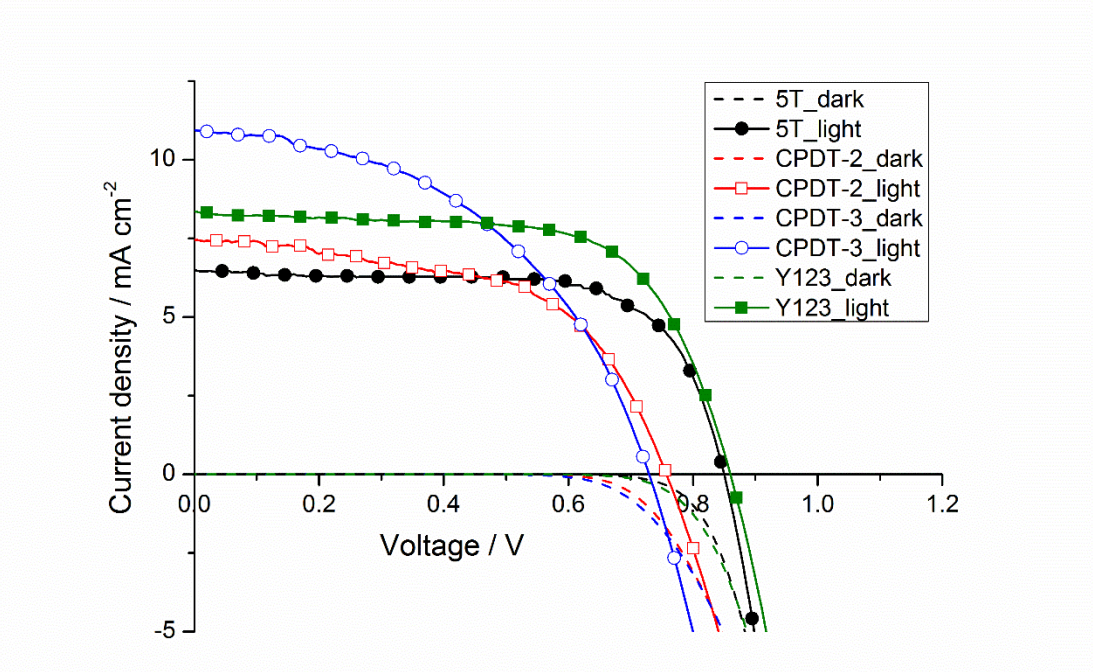

Figure 4.19 J-V curves and dark currents of 5T, CPDT-2, CPDT-3 and Y123

Table 4.11 Summary of J-V data and dye loading

Dye	Jsc / mA cm^{-2}	Voc / V	FF / %	Efficiency / %	Dye loading / $\times 10^{7}$ mol cm^{-2}
5T	6.5	0.85	67	4.0	1.62
CPDT-2	7.8	0.72	59	3.5	1.13
CPDT-3	10.9	0.73	47	3.9	1.88
Y123	8.4	0.86	66	5.0	1.46

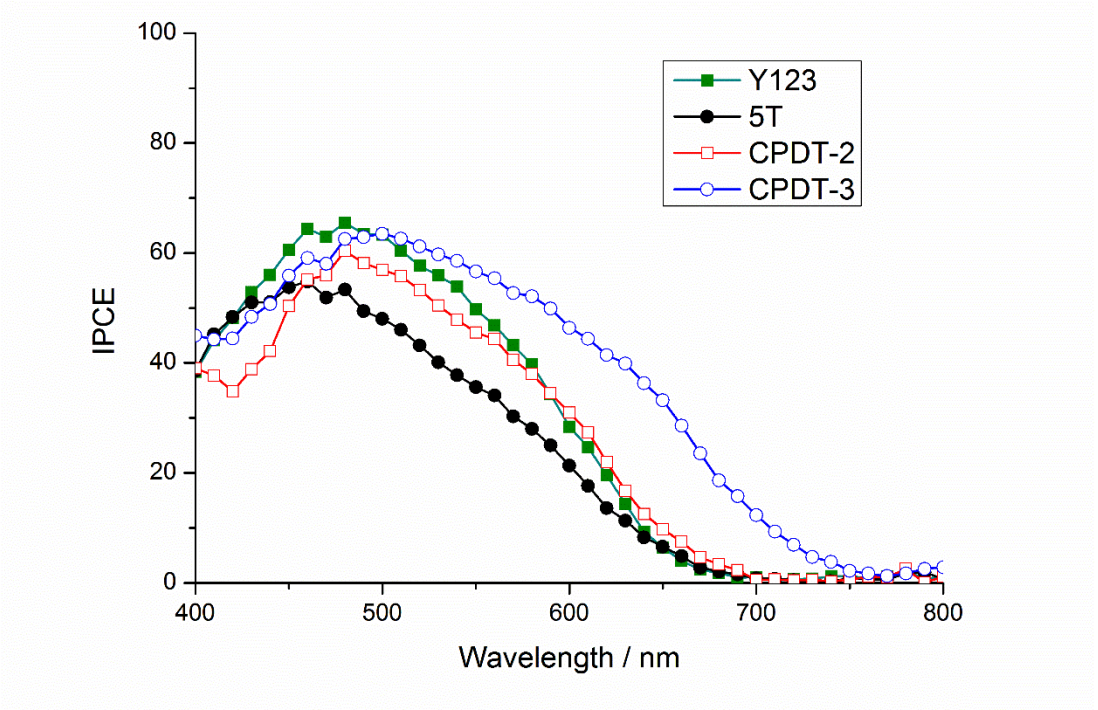

Figure 4.20 IPCE spectra for DSSCs based on oligo-CPDTs, 5T and Y123

2.6 Charge extraction, IMVS and IMPS

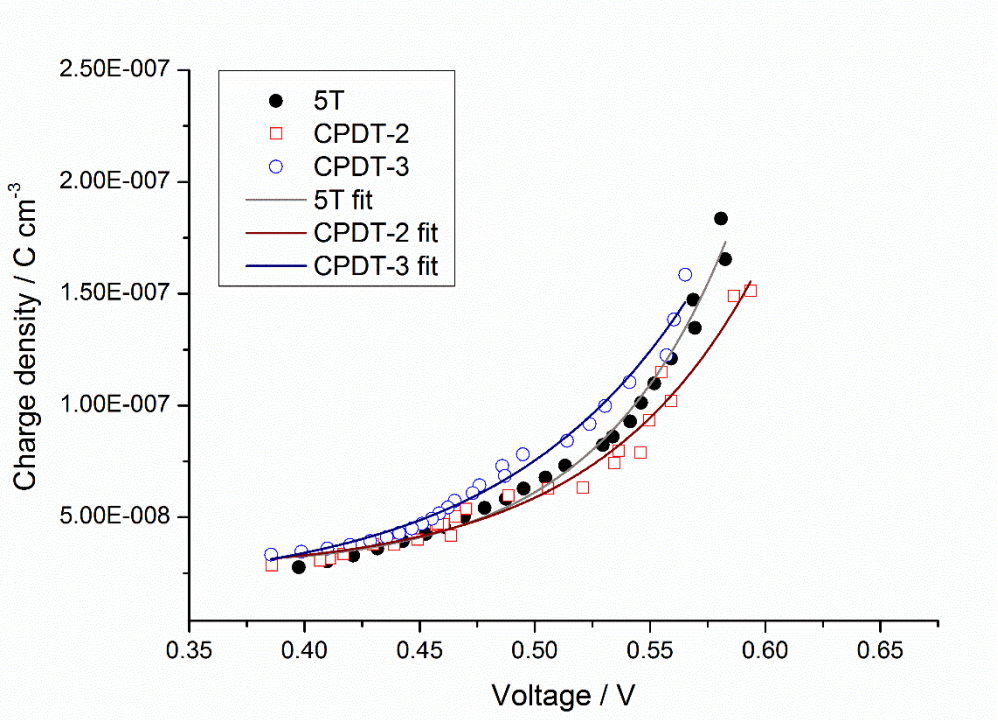

Figure 4.21 Charge extracted at a certain voltage for devices prepared with 5T and CPDT dyes. Data are fitted to a monoexponential function.

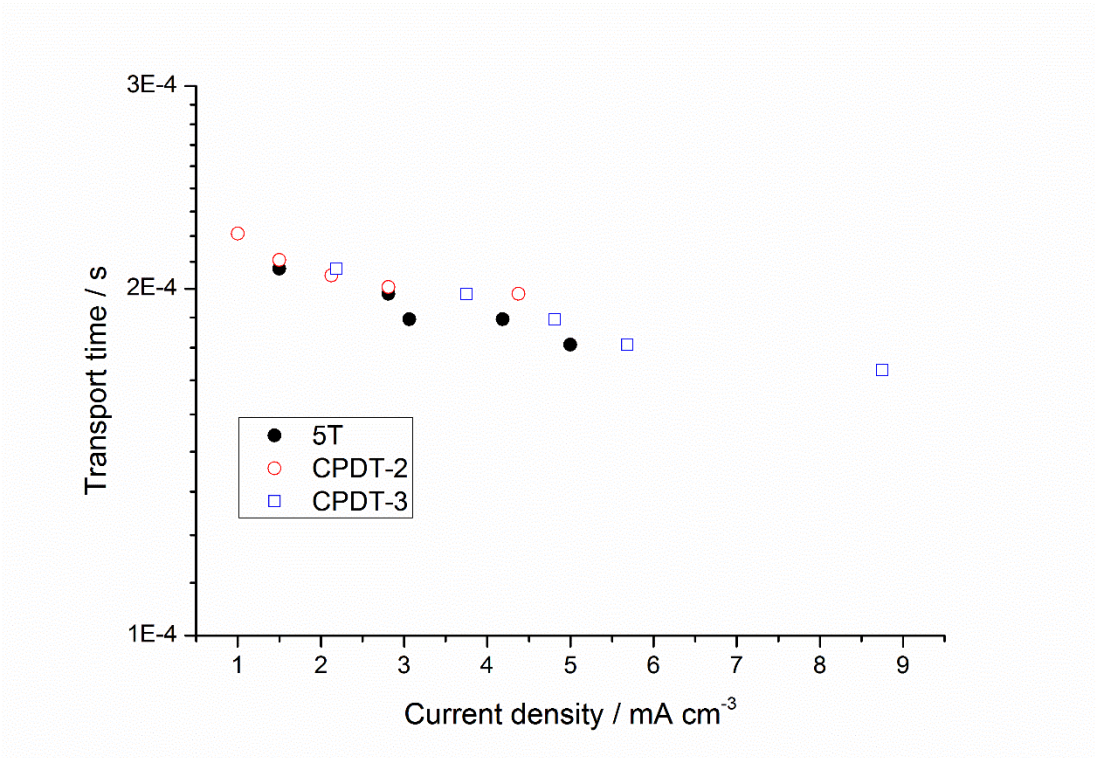

Figure 4.22 Transport time at short circuit conditions against current density

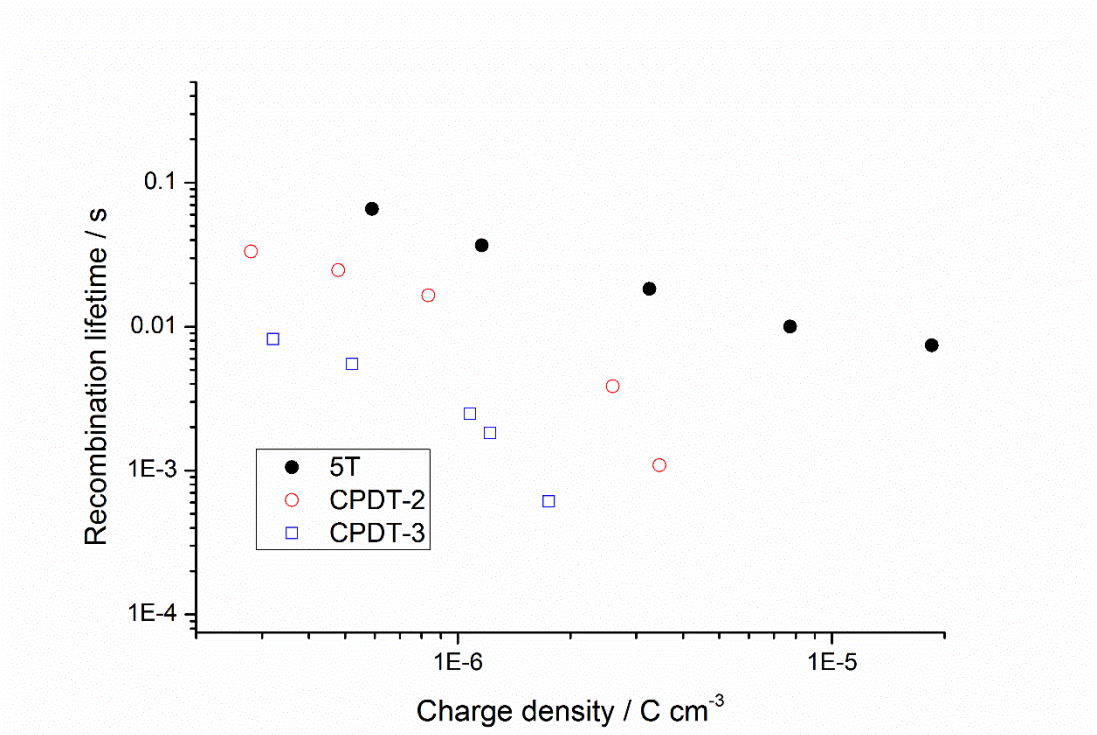

Figure 4.23 Recombination lifetime at open circuit conditions against charge density

After these dyes were checked thoroughly in devices using I^-/I_3^- electrolyte, Co^{2+}/Co^{3+} electrolyte and spiro-OMeTAD, it was found that the V_{OC} of these dyes always follows the same trend no matter what electrolyte was used, namely, 5T > CPDT-3 > CPDT-2. The open-circuit voltage is determined by the difference between the quasi-Fermi energy level of TiO_2 and the energy level of the HTM, which can be affected by 1) A shift of conduction band edge of TiO_2 caused by either dye attachment or additives like Li-TFSI and tBP; 2) The number of electron trap states in the TiO_2 conduction band; 3) The charge recombination rate. In order to gain further insight into variation of the TiO_2 conduction band and the rates of interfacial recombination, charge extraction (CE), intensity modulated photocurrent spectroscopy (IMPS) and intensity modulated photovoltage spectroscopy (IMPS) measurements were performed on the solid-state cells. Charge extraction measurements were first employed to find out the relationship between charge density and voltage. As shown in Figure 4.21, all the dyes have nearly identical charge density as a function of voltage. Additionally, IMPS measurement (Figure 4.22) shows no change of charge transport time. The charge extraction data were fitted to a monoexponential, enabling us to compare the recombination lifetimes measured from IMVS at the same charge density, as reported in Figure 4.23. Despite the fact that both 5T and CPDT series do not have any donor groups, a significant difference in the recombination lifetime can be seen, ordering 5T > CPDT-2 > CPDT-3, which corresponds to the open-circuit voltage and fill factor order we observed in devices. It is clear that replacing the thiophene units of 5T with CPDT units makes the recombination faster. CPDT-2 has the same number of alkyl chains as 5T and CPDT-3 has two more alkyl chains than 5T, so a simple relationship between alkyl chains and suppression of recombination cannot explain this result here.[8] One possibility is that 5T has a more twisted π-conjugated architecture than the CPDT dyes. Recently, the Li group designed a series of sensitisers with adjustment of the twist conformation through minor structural modifications and studied the effect of conjugation between the chromophore and anchoring group on the behaviour of solar cells. They found that sensitisers with better conjugation suffered from a severe back electron transfer although they showed better absorption properties.[19] In our case, computational calculations revealed that the dihedral

angles between the thiophene units in 5T are from 20° to 35°, while those between the CPDT units in CPDT-2 and CPDT-3 are from 1° to 5°. The better conjugation of the CPDT dyes could lead to a problem of back electron transfer. Another possibility is that the low regeneration driving force for CPDT-2 and CPDT-3 makes regeneration less competitive with recombination. Indeed, CPDT-2 (0.89V vs. NHE) and CPDT-3 (0.71V vs. NHE) are much easier to oxidise than 5T (1.02V vs. NHE). Especially for CPDT-3, the oxidation potential in solution is even slightly less positive than spiro-OMeTAD. Although energy levels may vary in a functional device, we can imagine that little or no regeneration driving force can cause slow regeneration hence a problem with charge recombination. This problem should be solved if an easier-to-oxidise hole-transport material can be used instead of spiro-OMeTAD, but so far, no such highly-performing HTM has been developed.

3 Conclusion

A series of 'donor-free' dyes oligo(4,4-dihexyl-4H-cyclopenta[1,2-b:5,4-b']dithiophene) (oligo-CPDTs) functionalized with cyanoacrylic end groups were easily synthesized using cross-coupling. They were used as effective sensitisers for liquid-state dye-sensitised solar cells with I^-/I_3^- redox couple, Co^{2+}/Co^{3+} redox couple and solid-state dye-sensitised solar cells. The J_{SC}, V_{OC} and power conversion increases upon addition of CPDT unit in all types of DSSCs. As a result, CPDT-3 shows the highest efficiency among this series (6.7% for I^-/I_3^- based cells, 7.3% for Co^{2+}/Co^{3+} based cells and 3.9% for solid-state cells). In solid-state dye-sensitised solar cells, CPDT-3 shows superb J_{SC} (10.9mA cm^{-2}) with only 900nm mesoporous TiO_2 film due to broad absorption over the solar spectrum and outstanding absorption coefficient up to 75000$M^{-1}cm^{-1}$. However, comparing with the oligo(3-hexylthiophene) dye (5T), CPDT dyes suffer from a low V_{OC}. By using charge extraction experiments, IMVS and IMPS, it was found upon replacing the thiophene unit with CPDT unit in donor-free dyes, the charge recombination across the TiO_2-dye-electrolyte interface enhanced significantly. We attribute this to a more planar conformation of CPDT-3 and/or less regeneration driving force compared with 5T. These dyes are promising if careful modification can be made towards the twist conformation and adjustment of energy levels, especially in super thin solid-state

dye-sensitised solar cells. The knowledge gained in this study can be helpful for future donor-free dyes.

4 Experimental

The compounds were synthesized based on the literature. [3,4]

4,4-dihexyl-4*H*-cyclopenta[2,1-b:3,4-b']dithiophene 4*H*-cyclopenta[2,1-b:3,4-b']dithiophene (3g, 16.8mmol), 1-bromohexane (5.56g, 33.6mmol) and potassium iodide (0.07g, 0.04mmol) were dissolved in 80ml DMSO and bubbled with N_2 for 15 mins. Potassium hydroxide (1.9g, 33.6mmol) was added and the mixture was stirred at room temperature for 3 days. Distilled water was added and the crude product was extracted into diethyl ether. The organic layer was washed with saturated ammonium chloride solution and water before drying over anhydrous sodium sulfate. After filtration, the solvent was removed and the residue was purified by column chromatography (SiO_2, petroleum ether 60-90 ℃) to give a light yellow oil (5.26 g, 90% yield). ^{1}H NMR (500 MHz, $CDCl_3$) δ_H: 7.16 (d, J=4.8 Hz, 2H), 6.95 (d, J=4.9 Hz, 2H), 1.63 (m, 4H), 1.15 (m, 12H), 0.97 (m, 4H), 0.83 (t, J=6.9 Hz, 6H).

4,4-dihexyl-4*H*-cyclopenta[2,1-b:3,4-b']dithiophene-2-carbaldehyde 4,4-dihexyl-4*H*-cyclopenta[2,1-b:3,4-b']dithiophene (0.27g, 0.80mmol) and DMF (0.068g, 0.94mmol) were dissolved in 2 ml 1,2-dichloroethane (2ml) and bubbled with N_2 at 0 ℃. Phosphorus chloride oxide (0.14g, 0.94mmol) was added. Then the mixture was stirred in ice-bath for 4 h before saturated sodium acetate solution (4ml) was added. The mixture was warmed up to room temperature and stirred for another 2 h. The crude product was extracted into dichloromethane, washed with water, and dried over anhydrous sodium sulfate. After filtration, the solvent was removed, then the residue was purified by column chromatography (SiO_2, DCM/Hexane, 2/3, v/v) to give a light yellow oil (0.29g, 97%). ^{1}H NMR (500 MHz, $CDCl_3$) δ_H: 9.86 (s, 1H), 7.59 (s, 1H), 7.42 (d, J=5.1 Hz, 1H), 7.01 (d, J=5.1 Hz, 1H), 1.89 (m, 4H), 1.18 (m, 12H), 0.91 (m, 4H), 0.84 (t, J=7.2 Hz, 6H).

2-Cyano-3-(4,4-dihexyl-4*H*-cyclopenta[2,1-b:3,4-b']dithiophene) acrylic acid (CPDT-1) 4,4-dihexyl-4*H*-cyclopenta[2,1-b:3,4-b']dithiophene-2-carbaldehyde (300mg, 0.8mmol) and cyanoacetic acid (204mg, 2.4mmol) were dried under vacuum. Then chloroform (50ml) was added and the solution was bubbled with N_2

for 10 mins. Piperidine (477mg, 5.6mmol) was added and the reaction was refluxed overnight. Then, the mixture was poured into 100 ml of aqueous HCl 1M and extracted with chloroform. The crude product was purified by column chromatography (SiO_2, DCM/methanol/acetic acid 400/25/2) to give a mixture of isomers as red solid (0.19g, 54% yield). ^{1}H NMR (500 MHz, $CDCl_3$): 8.35 (s, 1H), 7.69 (s, 1H), 7.50 (d, J= 4.9Hz, 1H), 7.02 (d, J= 4.9Hz, 1H), 1.89 (m, 4H), 1.18 (m, 12H), 0.94 (m, 4H), 0.84 (t, J = 7.7Hz, 6H). MS ESI (m/z): $[M-H]^+$ calcd 440.17962. Found: 440.17235. Anal. Calc. for $C_{25}H_{31}NO_2S_2$: C 67.99, H 7.08, N 3.17. Found: C 67.92, H 7.15, N 3.32%.

6'-bromo-4,4-dihexyl-4*H*-cyclopenta[2,1-b:3,4-b']dithiophene-2-carbaldehyde 4,4-dihexyl-4*H*-cyclopenta[2,1-b:3,4-b']dithiophene-2-carbaldehyde (1.25g, 3.30mmol) was dissolved in anhydrous THF (100ml) and bubbled with N_2 at 0 ℃. *N*-bromosuccinimide (0.65g, 3.67mmol) was added and the mixture was stirred in an ice-bath for 1 h before warming up and stirring overnight. Distilled water was then added into the mixture and the crude product was extracted into dichloromethane. The crude product was purified by column chromatography (SiO_2, DCM) to give a yellow oil (1.48g, 98%). ^{1}H NMR (600 MHz, $CDCl_3$) δ_H: 9.86 (s, 1H), 7.58 (s, 1H), 7.03 (s, 1H), 1.86 (m, 4H), 1.19 (m, 12H), 0.95 (m, 4H), 0.85 (t, J=7.0 Hz, 6H).

Tributyl-(4,4-dihexyl-4a,7a-dihydro-4H-cyclopenta[2,1-b;3,4-b']dithiophen-2-yl)-stannane 4,4-dihexyl-4*H*-cyclopenta[2,1-b:3,4-b']dithiophene (0.52g, 1.50mmol) was dissolved in anhydrous THF (40ml) and stirred at -78℃ for 30 mins under N_2. 1.6 M solution of n-butyllithium in hexane (1ml, 1.6mmol) was added slowly. The mixture was stirred for 1h before tributyltin chloride (0.6ml, 1.8mmol) was added dropwise and the mixture was stirred for another 1 h. Then the solution was allowed to warm up to room temperature and stirred for 2 h. Saturated brine (2ml) was added to quench the reaction and the solvents were removed. The crude product was dissolved in DCM and washed with water. The organic phase was dried over magnesium sulfate, filtered, then the solvents were removed. The product (1g, 67% stannylation) was used without further purification.

4,4,4',4'-Tetrahexyl-4a,7a,4',7'b-tetrahydro-4H,3'aH-[2,2']bi[cyclopenta[2,1-b;3,4-b']dithiophenyl]-6-carbaldehyde

6’-Bromo-4,4-dihexyl-4*H*-cyclopenta[2,1-b:3,4-b’]dithiophene-2-carbaldehyde (0.45g, 1mmol) and tributyl-(4,4-dihexyl-4a,7a-dihydro-4H-cyclopenta[2,1-b;3,4-b']dithiophen-2-yl)-stannane (0.64g, 1mmol) were dissolved in chloroform (30ml) and bubbled with N_2 for 30 mins. Tetrakis(triphenylphosphine) palladium ($Pd(PPh_3)_4$) (0.11g, 0.1mmol) was added and the solution was bubbled with N_2 for another 10 mins before the solution was refluxed for 72h. The organic solvents were removed by vacuum. Then the crude product was purified by column chromatography (SiO_2, DCM) to give a red oil (0.6g, 83% yield). ^{1}H NMR (500 MHz, $CDCl_3$): 9.85 (s, 1H), 7.57 (s, 1H), 7.23 (d, J=4.8Hz, 1H), 7.11 (s, 1H), 7.05 (s, 1H), 6.97 (d, J=4.8Hz, 1H), 1.88 (m, 8H), 1.18 (m, 24H), 1.02 (m, 8H), 0.85 (m, 12H).

2-Cyano-3-(4,4,4',4'-tetrahexyl-4a,7a,4',7'b-tetrahydro-4H,3'aH-[2,2']bi[cyclopenta[2,1-b;3,4-b']dithiophenyl]-6-yl)-acrylic acid (CPDT-2) 4,4,4',4'-Tetrahexyl-4a,7a,4',7'b-tetrahydro-4H,3'aH-[2,2']bi[cyclopenta[2,1-b;3,4-b']dithiophenyl]-6-carbaldehyde (300mg, 0.42mmol) and cyanoacetic acid (107.2mg, 1.26mmol) were dried under vacuum. Then chloroform (30ml) was added and the solution was bubbled with N_2 for 10 mins. Piperidine (250mg, 2.94mmol) was added and the reaction was refluxed overnight. Then, the mixture was poured into 300ml of aqueous HCl 1M and extracted with chloroform. The organic layer was washed with water and brine. The crude was purified by column chromatography (SiO_2, DCM/methanol/acetic acid 400/25/2) to give a shining black solid (0.21g, 63 % yield). ^{1}H NMR (500 MHz, $CDCl_3$): 8.41 (s, 1H), 7.61 (s, 1H), 7.21 (m, 1H), 7.07 (s, 1H), 7.00 (s, 1H), 6.95 (d, J= 4.6Hz, 1H), 1.88 (m, 8H), 1.18 (m, 24H), 1.01 (m, 8H), 0.83 (m, 12H). MS ESI (m/z): $[M]^+$ calcd 789.37416. Found: 789.34512. Anal. Calc. for $C_{46}H_{63}NO_2S_4$: C 69.91, H 8.04, N 1.77. Found: C 69.95, H 7.71, N 1.85%.

6'-Bromo-4,4,4',4'-tetrahexyl-4a,7a,4',7'b-tetrahydro-4H,3'aH-[2,2']bi[cyclopenta[2,1-b;3,4-b']dithiophenyl]-6-carbaldehyde 4,4,4',4'-Tetrahexyl-4a,7a,4',7'b-tetrahydro-4H,3'aH-[2,2']bi[cyclopenta[2,1-b;3,4-b']dithiophenyl]-6-carbaldehyde (300mg, 0.42mmol) was dissolved in anhydrous THF (10ml) and bubbled with N_2 at 0 ℃. *N*-bromosuccinimide (82mg, 0.46mmol) was added and the mixture was stirred in ice-bath for 1 h before warming up and

stirred overnight. Distilled water was then added into the mixture and the crude product was extracted into dichloromethane. The crude product was purified by column chromatography (SiO_2, DCM/hexane 1/2) to give a orange oil (150g, 98%). ^1H NMR (500 MHz, $CDCl_3$) δ_H: 9.88 (s, 1H), 7.58 (s, 1H), 7.36 (s, 1H), 7.00 (s, 1H), 1.85 (m, 8H), 1.18 (m, 24H), 1.01 (m, 8H), 0.91 (m, 12H).

4,4,4',4',4'',4''-Hexahexyl-4a,7a,4',7'b,4'',7''b-hexahydro-4H,3'aH,3''aH-[2,2';6',2'']ter[cyclopenta[2,1-b;3,4-b']dithiophene]-6-carbaldehyde 6'-Bromo-4,4,4',4'-tetrahexyl-4a,7a,4',7'b-tetrahydro-4H,3'aH-[2,2']bi[cyclopenta[2,1-b;3,4-b']dithiophenyl]-6-carbaldehyde (150mg, 0.2mmol) and tributyl-(4,4-dihexyl-4a,7a-dihydro-4H-cyclopenta[2,1-b;3,4-b']dithiophen-2-yl)-stannane (130mg, 0.2mmol) were dissolved in toluene (20ml) and bubbled with N_2 for 30 mins. Tetrakis(triphenylphosphine) palladium ($Pd(PPh_3)_4$) (20mg, 0.05mmol) was added and the solution was bubbled with N_2 for another 10 mins before refluxing for 72h. The organic solvents were removed by vacuum. Then the crude product was purified by column chromatography (SiO_2, DCM/ hexane 2/1) to give a red oil (100mg, 47 % yield). ^1H NMR (500 MHz, $CDCl_3$): 9.85 (s, 1H), 7.57 (s, 1H), 7.20 (d, J=4.8Hz, 1H), 7.11 (s, 1H), 7.06 (s, 1H), 7.05 (s, 1H), 7.04 (s, 1H), 6.96 (d, J=4.8Hz, 1H), 1.88 (m, 12H), 1.19 (m, 36H), 1.02 (m, 12H), 0.85 (m, 18H).

2-Cyano-3-(4,4,4',4',4'',4''-hexahexyl-4a,7a,4',7'b,4'',7''b-hexahydro-4H,3'aH,3''aH-[2,2';6',2'']ter[cyclopenta[2,1-b;3,4-b']dithiophene]-6-yl)-acrylic acid (CPDT-3)

4,4,4',4',4'',4''-Hexahexyl-4a,7a,4',7'b,4'',7''b-hexahydro-4H,3'aH,3''aH-[2,2';6',2'']ter[cyclopenta[2,1-b;3,4-b']dithiophene]-6-carbaldehyde (400mg, 0.38mmol) and cyanoacetic acid (96.1mg, 1.13mmol) were dried under vacuum. Then chloroform (50ml) was added and the solution was bubbled with N_2 for 10 mins. Piperidine (226mg, 2.66mmol) was added and the reaction was refluxed overnight. Then, the mixture was poured into 300ml of aqueous HCl 1M and extracted with chloroform. The organic layer was washed with water and brine. The crude was purified by column chromatography (SiO_2, DCM/methanol/acetic acid 400/25/2) to give a shining black solid (0.21g, 63 % yield). ^1H NMR (500 MHz, $CDCl_3$): 8.33 (s, 1H), 7.63 (s, 1H), 7.21 (d, J=4.9Hz, 1H), 7.15 (s, 1H), 7.07 (s, 2H), 7.04 (s, 1H), 6.97 (d, J= 4.8Hz, 1H), 1.89 (m, 12H), 1.20 (m, 36H), 1.03 (m, 12H),

0.85 (m, 18H). MS ESI (m/z): $[M]^+$ calcd 1129.50611. Found: 1129.50556. Anal. Calc. for $C_{67}H_{87}NO_2S_6$: C 71.17, H 7.76, N 1.24. Found: C 70.93, H 7.78, N 1.26%.

References

1. Chai, Q.P., et al., *Rational molecular engineering of cyclopentadithiophene-bridged D-A-pi-A sensitizers combining high photovoltaic efficiency with rapid dye adsorption.* Scientific Reports, 2015. **5**: p. 11330.
2. Li, R.Z., et al., *Synchronously Reduced Surface States, Charge Recombination, and Light Absorption Length for High-Performance Organic Dye-Sensitized Solar Cells.* Journal of Physical Chemistry B, 2010. **114**(13): p. 4461-4464.
3. Moon, S.J., et al., *Highly Efficient Organic Sensitizers for Solid-State Dye-Sensitized Solar Cells.* Journal of Physical Chemistry C, 2009. **113**(38): p. 16816-16820.
4. Dualeh, A., et al., *Influence of Donor Groups of Organic D-pi-A Dyes on Open-Circuit Voltage in Solid-State Dye-Sensitized Solar Cells.* Journal of Physical Chemistry C, 2012. **116**(1): p. 1572-1578.
5. Cui, Y., et al., *Incorporating Benzotriazole Moiety to Construct D-A-pi-A Organic Sensitizers for Solar Cells: Significant Enhancement of Open-Circuit Photovoltage with Long Alkyl Group.* Chemistry of Materials, 2011. **23**(19): p. 4394-4401.
6. Koumura, N., et al., *Alkyl-functionalized organic dyes for efficient molecular photovoltaics.* Journal of the American Chemical Society, 2006. **128**(44): p. 14256-14257.
7. Mosconi, E., et al., *Cobalt Electrolyte/Dye Interactions in Dye-Sensitized Solar Cells: A Combined Computational and Experimental Study.* Journal of the American Chemical Society, 2012. **134**(47): p. 19438-19453.
8. Nguyen, W.H., et al., *Molecular Engineering of Organic Dyes for Improved Recombination Lifetime in Solid-State Dye-Sensitized Solar Cells.* Chemistry of Materials, 2013. **25**(9): p. 1519-1525.
9. Zietz, B., et al., *Photoisomerization of the cyanoacrylic acid acceptor group - a potential problem for organic dyes in solar cells.* Physical Chemistry Chemical Physics, 2014. **16**(6): p. 2251-2255.
10. Pandey, S.S., et al., *Investigating the Role of Dye Dipole on Open Circuit Voltage in Solid-State Dye-Sensitized Solar Cells.* Japanese Journal of Applied Physics, 2011. **50**(6): p. 1-4.
11. Tian, H.N., et al., *Effect of different dye baths and dye-structures on the performance of dye-sensitized solar cells based on triphenylamine dyes.* Journal of Physical Chemistry C, 2008. **112**(29): p. 11023-11033.
12. Tang, X., Y.X. Wang, and G.Z. Cao, *Effect of the adsorbed concentration of dye on charge recombination in dye-sensitized solar cells.* Journal of Electroanalytical Chemistry, 2013. **694**: p. 6-11.
13. Li, J., et al., *Effect of chenodeoxycholic acid (CDCA) additive on phenothiazine dyes sensitized photovoltaic performance.* Science China-Chemistry, 2011. **54**(4): p. 699-706.
14. Zhang, H.M., et al., *Effect of TiO2 nanoparticles on the structure and activity of catalase.* Chemico-Biological Interactions, 2014. **219**: p. 168-174.

15. Hara, K., et al., *Effect of additives on the photovoltaic performance of coumarin-dye-sensitized nanocrystalline TiO2 solar cells.* Langmuir, 2004. **20**(10): p. 4205-4210.
16. Burschka, J., et al., *Co(III) Complexes as p-Dopants in Solid-State Dye-Sensitized Solar Cells.* Chemistry of Materials, 2013. **25**(15): p. 2986-2990.
17. Wu, K.L., et al., *Dye sensitized solar cells with cobalt and iodine-based electrolyte: the role of thiocyanate-free ruthenium sensitizers.* Journal of Materials Chemistry A, 2014. **2**(45): p. 19556-19565.
18. Lu, H.P., et al., *Control of Dye Aggregation and Electron Injection for Highly Efficient Porphyrin Sensitizers Adsorbed on Semiconductor Films with Varying Ratios of Coadsorbate.* Journal of Physical Chemistry C, 2009. **113**(49): p. 20990-20997.
19. Chai, Z.F., et al., *Similar or Totally Different: the Adjustment of the Twist Conformation Through Minor Structural Modification, and Dramatically Improved Performance for Dye-Sensitized Solar Cell.* Advanced Energy Materials, 2015. **5**(18): p. 1500846.

Chapter 5 Ruthenium dyes with azo ligands

1 Introduction

1.1 Ru complexes with azo ligands

Octahedral, six co-ordinate ruthenium(II) complexes play an important role in the development of fundamental understanding and applications in photochemistry, photocatalysis and photophysics. [1-3] The most highly studied Ru complex, $[Ru(bpy)_3]^{2+}$ (Figure 5.1) was first reported by Burstall in 1936 [4], although its luminescence behaviour was not observed until 1959. [5] Since then, hundreds, if not thousands, of these types of complexes have been synthesised and studied. These are d^6, low-spin complexes with tunable photophysical and electrochemical properties through modification of the coordinating ligands. Due to the heavy metal centre, Ru complexes allow the excited singlet complex to relax to the triplet state via intersystem crossing (ISC) and thus produce long-lived phosphorescence. Besides the excited-state lifetime, Ru complexes also have the advantages of reversible redox, good stability, low aggregation and directional electron and energy transfer. All these features give Ru complexes promising potential in different photophysical and photoelectrochemical applications, such as photochemical water splitting [6], nonlinear optics [7], photoswitching [8, 9], imaging [10], as well as dye-sensitized solar cells (DSSC) [11, 12].

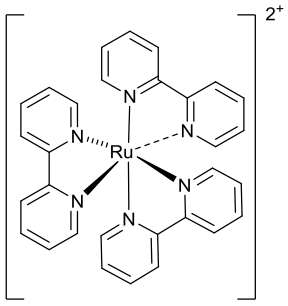

Figure 5.1 Molecular structure of $[Ru(bpy)_3]^{2+}$

Azo compounds, such as 2-phenylazopyridine (azpy), which contain the functional group –N=N-C=N-, have been used as ligands in metal complexes due to their ability to stabilise metals in their lower oxidation states. The first report of using azpy as a ligand in the synthses of ruthenium complexes is from 1980, when Krause [13] published the synthesis and characterisation of three isomers of $[Ru(azpy)_2Cl_2]$ (Figure 5.2).

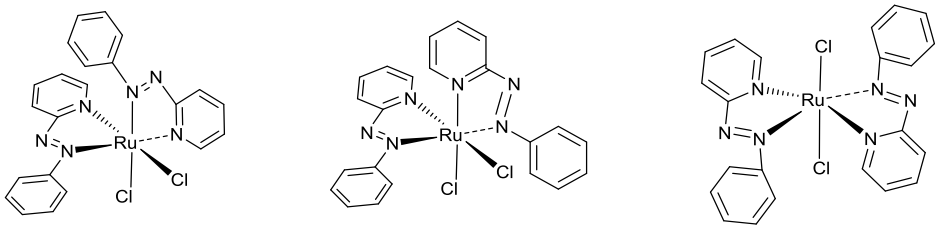

Figure 5.2 Molecular structures of three isomers of $[Ru(azpy)_2Cl_2]$.

The structural and spectroscopic properties of these isomers were further investigated by Velders. [14] Further ruthenium complexes with azo ligands were synthesized and studied, regarding their synthesis, spectra, electrochemistry and X-ray crystal structures by different groups, including dichloro bis[1-alkyl-2-(arylazo)imidazole] ruthenium complexes (Figure 5.3) [15] and dichloro bis[2-(arylazo)pyrimidine] ruthenium complexes (Figure 5.4) [16] by Sinha, and dithiocyanato-bis{1-(alkyl)-2-(arylazo)imidazole} ruthenium (Figure 5.5) by Byabartta. [17] Other ruthenium complexes with mixed ligands, normally one or two azo ligands and another bipyridine or terpyridine ligand have been studied also by Lahiri [18, 19], Goswami [20], Al-Noaimi [21] and Sinha [22].The cytotoxic activity of ruthenium complexes containing azo ligands against a series of human tumor cell lines were by different groups, such as $[Ru(azpy)_2Cl_2]$ by Velders [23], $[Ru(azpy)(bpy)Cl_2]$ by Reedijk [24] and a series of ruthenium complexes containing an η^6-coordinated arene and azpy or phenylazopyrazole derivatives by Sadler. [25]

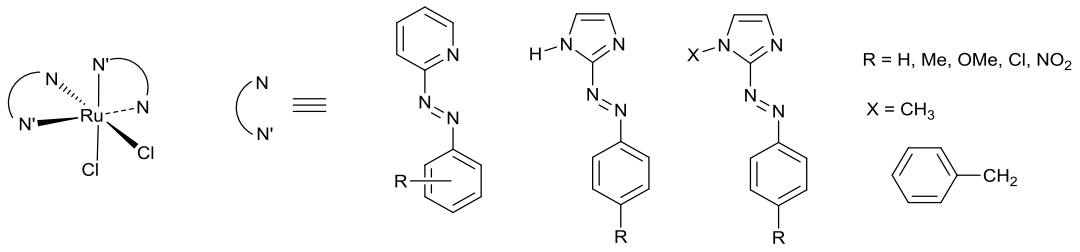

Figure 5.3 Molecular structures of dichloro bis[1-alkyl-2-(arylazo)imidazole] ruthenium complexes.

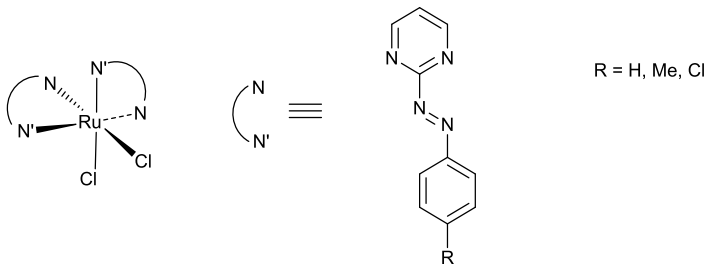

Figure 5.4 Molecular structures of dichloro bis[2-(arylazo)pyrimidine] ruthenium complexes.

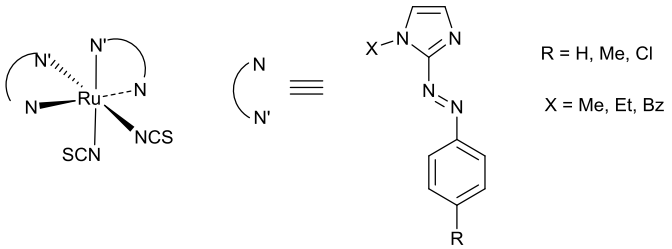

Figure 5.5 Molecular structures of dithiocyanato-bis{1-(alkyl)-2-(arylazo)imidazole ruthenium complexes.

1.2 Research proposal

Some of the focus of these prior studies was on biological function [23-25], however the work also illustrated the enhanced light harvesting achieved by introducing azo ligands into such Ru complexes, and reversible Ru(II)/Ru(III) oxidation process, thus indicating potential for application in photophysical devices such as DSSCs. These new sensitisers should allow a combination of the best aspect of organic dyes, which is the high absorption coefficient, with those of Ru dyes, which are good stability, low aggregation, better red absorption and long excited-state lifetime, thus resulting in an improvement of efficiency when applied to dye-sensitised solar cells.

In order to use the complex as a sensitiser, the dye excitation should be a charge-transfer transition with the electron density moving towards the anchoring group to the TiO_2 surface in order to facilitate electron injection. However, in previous studies containing both azpy ligand and bipyridine ligand in one Ru complex, the first reduction process is always based on azpy ligand. This may cause a problem of wrong charge directionality when the dye is used in a solar cell. Thus, in contrast to

previously-reported complexes, we need to modify the azo ligand to enable charge directionality towards the bipyridine ligand, as well as also providing a bipy ligand able to bind to the mesoporous TiO_2. To address this, we have designed a series of ruthenium complexes that include specifically designed azo ligands as an additional chromophore, and studied their photophysical and electrochemical properties in detail. To the best of our knowledge, this is the first specific design and trial application of Ru complexes with azo ligands for DSSCs

2 Results and Discussion

Five Ru(II) dyes containing the chelating phenylazopyridine or phenylazoimidazole ligands 2-phenylazopyridine (azpy), 4-(2-pyridylazo)-N,N-dimethylaniline (dmazpy), [4-(N,N-dimethylamino)benzeneazo]imidazole (pai) and 1-methyl-2-[4-(N,N-dimethylamino)benzeneazo]imidazole (pai-Me) were synthesised. The structures are shown in Figure 5.6.

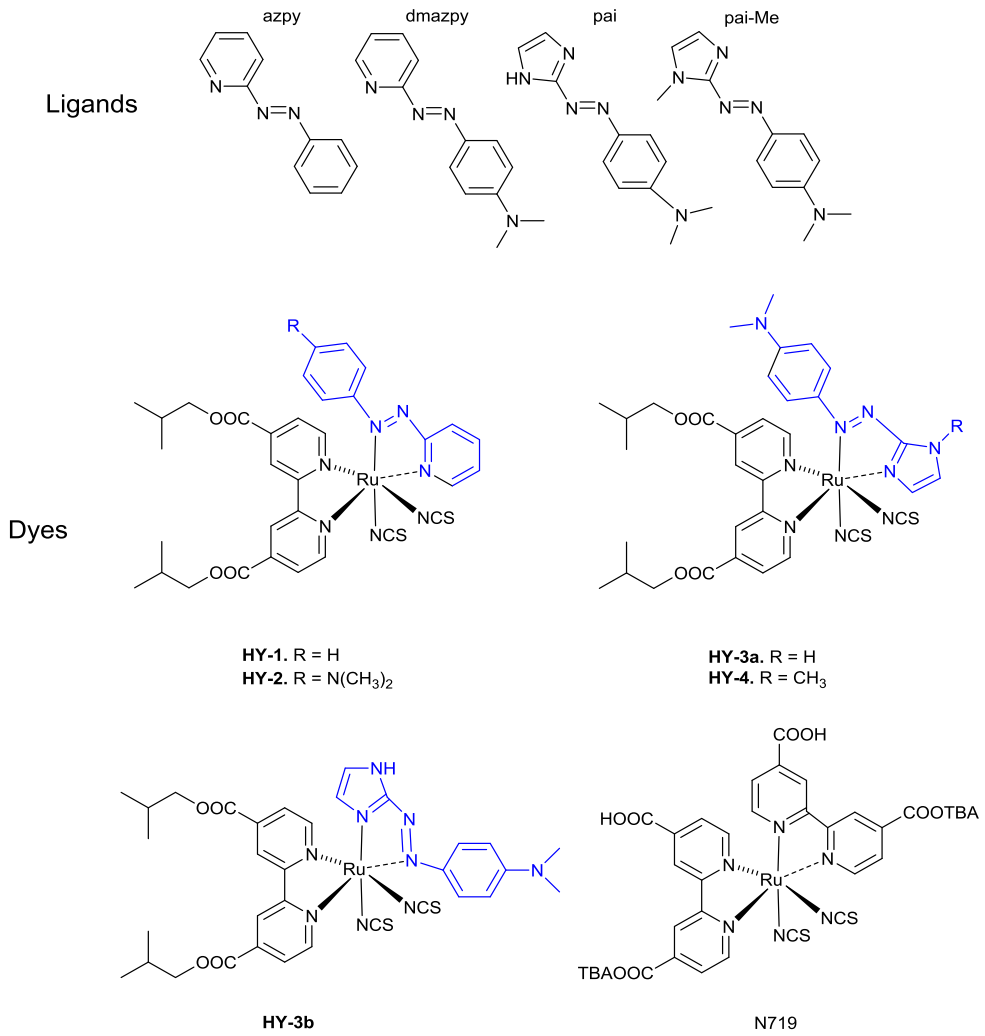

Figure 5.6 Structures of the studied Ru(II) sensitisers HY-1~4 and for comparison N719, an analogous dye with no azo-ligand previously developed for dye-sensitised solar cells.

2.1 Synthesis

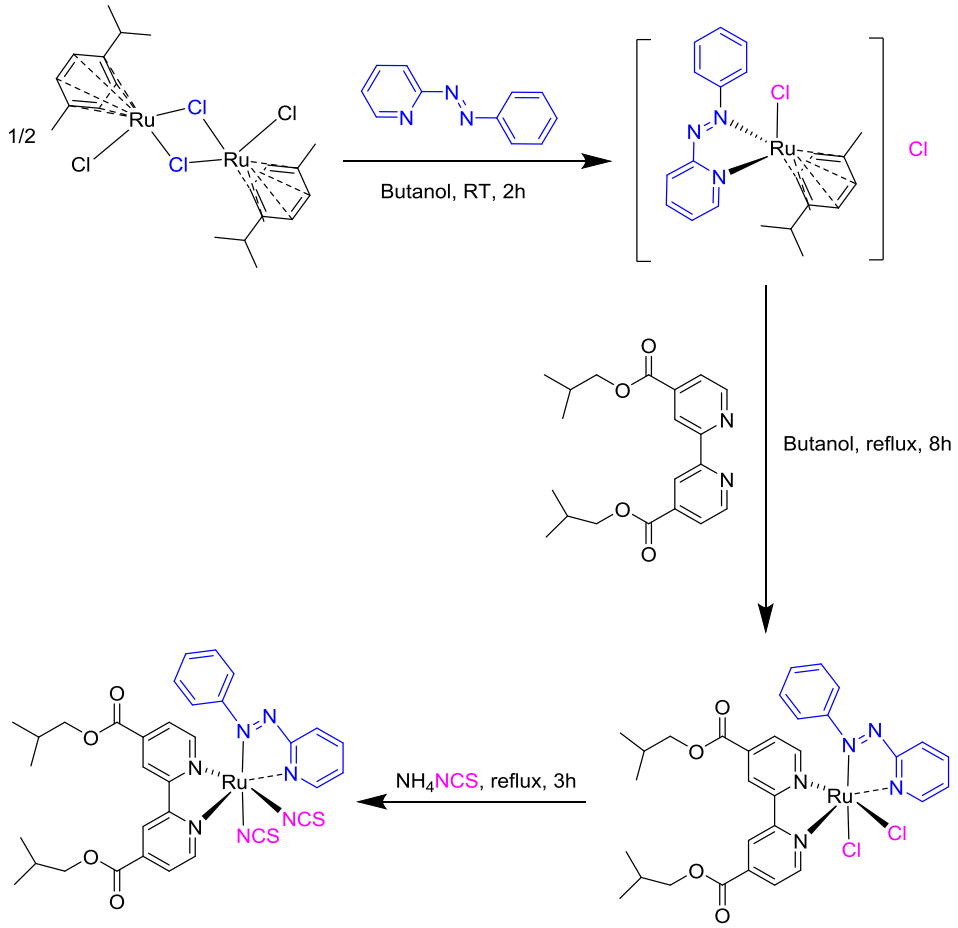

Scheme 5.1 Synthesis of HY-1

The synthetic procedure for HY-1 is given as an example in Scheme 5.1. It is based on an established one-pot literature method used to prepare [Ru(bipy)(bipy')X_2] dyes.[26] [Ru(p-cymene)Cl_2]$_2$ dimer was used as a starting material.[42] The [Ru(azo)(p-cymeme)Cl]$^+$ intermediate was formed at room temperature and substitution of the p-cymene ligand by ^{i}Bu$_2$dcbpy was performed at a high temperature, followed by substitution of the two Cl ligands by NCS. The order of ligand addition is crucial to obtain a relatively clean crude product in the synthesis. In this case, it was discovered that the azo ligand can react with dichloro(*p*-cymene)ruthenium(II) dimer at ambient temperature while the ^{i}Bu$_2$dcbpy ligand cannot unless the temperature is over 60°C. This suggests that the azo ligands bond with ruthenium to form a more stable intermediate. In keeping with this, if the ^{i}Bu$_2$dcbpy ligand is added first, we observed that it can be replaced by the azo ligand in the next step to give a mixture of substitution products. (Figure 5.7) The

complexes were prepared with carboxylate groups to enable their subsequent study as sensitisers in DSSCs, however they were initially prepared in ester form, enabling the use of conventional silica gel chromatography for the isolation of pure products on a large scale.[27] Butanol was used as solvent rather than DMF to avoid hydrolysis of the ester during the reaction.[28] Butanol is also a high-boiling solvent (118℃) so when refluxing in the final step, we were able to obtain the complex with N-bound thiocyanate ligands, rather than S-bound since the N-bound isomer is more thermodynamically favored.

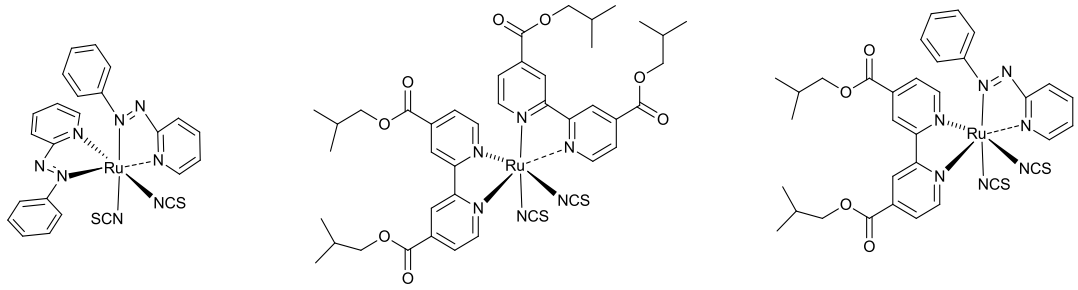

Figure 5.7 Schematic structures of $Ru(azpy)_2(NCS)_2$ (left), $Ru(^iBu_2dcbpy)_2(NCS)_2$ (middle) and $Ru(^iBu_2dcbpy)(azpy)(NCS)_2$ (right).

All complexes were examined by ^1H NMR, 2D COSY and 2D NOESY spectroscopy to confirm their structures. HY-1 and HY-2 also showed the correct number of carbon peaks in the appropriate part of the ^{13}C NMR spectrum. ^{13}C NMR spectra were not able to be obtained for HY-3 and HY-4 due to their lower solubility. The unsymmetrical nature of the ligands leads to three possible isomers (excluding optical isomers and S-bound linkage isomers of NCS) for each complex as shown in Figure 5.8. Only the α-*cis* isomer was obtained pure for $Ru(^iBu_2dcbpy)(azpy)(NCS)_2$, $Ru(^iBu_2dcbpy)(dmazpy)(NCS)_2$ and $Ru(^iBu_2dcbpy)(pai\text{-}Me)(NCS)_2$ to give HY-1, HY-2 and HY-4, respectively. However, for $Ru(^iBu_2dcbpy)(pai)(NCS)_2$, two isomers were observed in the ^1H NMR of the crude product and they were successfully separated to give the α -*cis* isomer (HY-3a) and β-*cis* isomer (HY-3b). The ^1H NMR spectra of all the α-*cis* isomers were very similar, while in the β-*cis* isomer, the characteristic ortho-proton signal on the phenyl group shifted significantly downfield compared to the corresponding α-*cis* isomer.

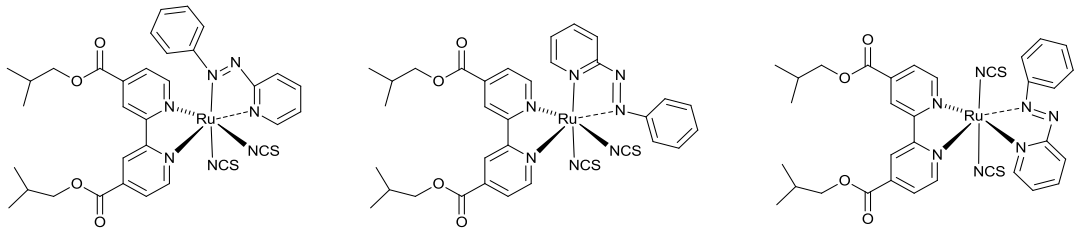

Figure 5.8 Theoretical possible isomers of Ru(^{i}Bu$_2$dcbpy)(azpy)(NCS)$_2$: α-*cis*-Ru(^{i}Bu$_2$dcbpy)(azpy)(NCS)$_2$ (left), β-*cis*-Ru(^{i}Bu$_2$dcbpy)(azpy)(NCS)$_2$ (middle), *trans*-Ru(^{i}Bu$_2$dcbpy)(azpy)(NCS)$_2$ (right).

Crystal structures for two of the complexes were obtained (Figure 5.9) and were consistent with the structures found by NMR spectroscopy. Table 5.1 shows selected bond distances for HY-2 and HY-3b. The Ru(51)-N(56) is longer than Ru(51)-N(51) in HY-2 and the Ru(1)-N(2) is longer than Ru(1)-N(6) in HY-3b. This can be explained by the stronger π-interaction with azoimine (-N=N-C=N-) than with the diimine (-N=C-C=N-) function,[29] which is consistent with the strengths of ligand coordination we observed during synthesis.

Table 5.1 Selected bond distances (Å) for HY-2 and HY-3b

HY-2		HY-3b	
Ru(51)-N(51)	2.023(8)	Ru(1)-N(1)	2.001(15)
Ru(51)-N(53)	2.040 (10)	Ru(1)-N(2)	2.075(16)
Ru(51)-N(55)	2.039(9)	Ru(1)-N(3)	1.995(17)
Ru(51)-N(56)	2.075(9)	Ru(1)-N(6)	2.029(17)
Ru(51)-N(57)	2.058(10)	Ru(1)-N(8)	1.98(2)
Ru(51)-N(58)	2.037(10)	Ru(1)-N(9)	2.001(18)

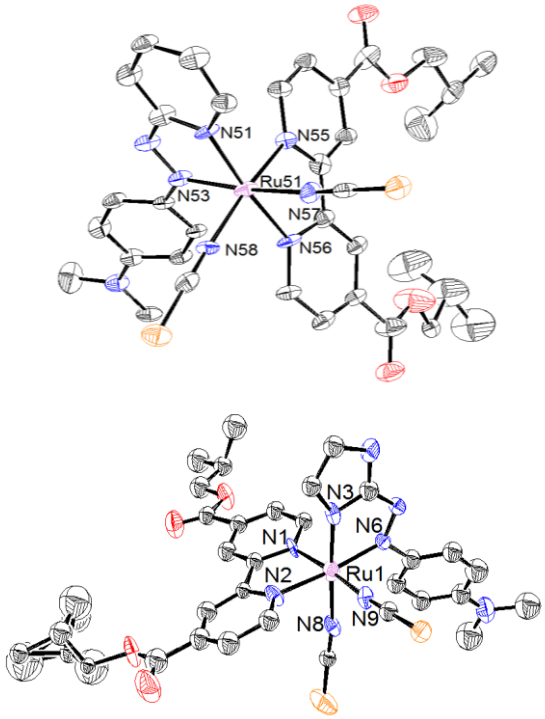

Figure 5.9 Single crystal X-ray structures of HY-2 (upper) and HY-3b (lower)

2.2 Absorption Spectroscopy

2.2.1 UV-vis spectroscopy of the ligands

Table 5.2 UV-Vis spectral data for the ligands

Ligand	λ_{max} [nm] ($\varepsilon/10^4$ M^{-1} cm^{-1})
azpy	318 (1.9), 444 (0.9)
dmazpy	433 (3.8)
pai	268 (0.4), 318 (0.3), 456 (2.4)

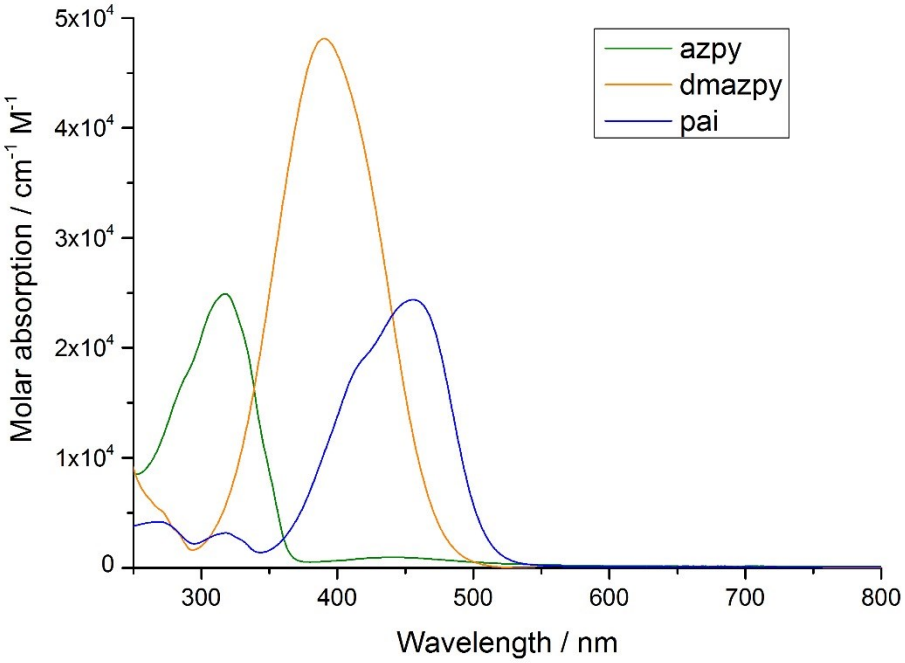

Figure 5.10 UV-vis spectra of ligand azpy (green line), dmazpy (orange line) and pai (blue line) in methanol

The UV-Vis spectra of all the uncomplexed pro-ligands were measured in methanol and the details are summarized in Table 5.2 and Figure 5.10. The azo ligands showed intense absorption bands in the region of 200-500 nm. According to the explanation of Yoopensuk et al.,[30] the absorption band of azpy at 318nm is due to π- π* transition and the one at around 450nm is due to n- π* transition. In contrast to azpy, dmazpy shows an intense π- π* band at lower energy at 433nm. With the help of TD-PBE0 calculation,[30] these π- π* transition peaks can be assigned as a mainly HOMO → LUMO transition. The π- π* bands of the ligand pai is the most red-shifted due to increased charge transfer character of the transition.[31, 32]

2.2.2 UV-vis spectroscopy of the complexes

The UV-vis spectra of the ruthenium complexes were measured in methanol (Figure 5.11). The introduction of the azo ligand leads to an enhanced light harvesting compared to N719 which lacks any azo ligand. The band that appears in the UV region, shows little variation in energy for all the complexes and can be assigned to π_{bpy}- π_{bpy}* ligand-centred transitions. Other bands in the visible light region in such Ru-bipy complexes are usually assigned to MLCT and details for the new dyes in this work are discussed later with the help of computational chemistry.

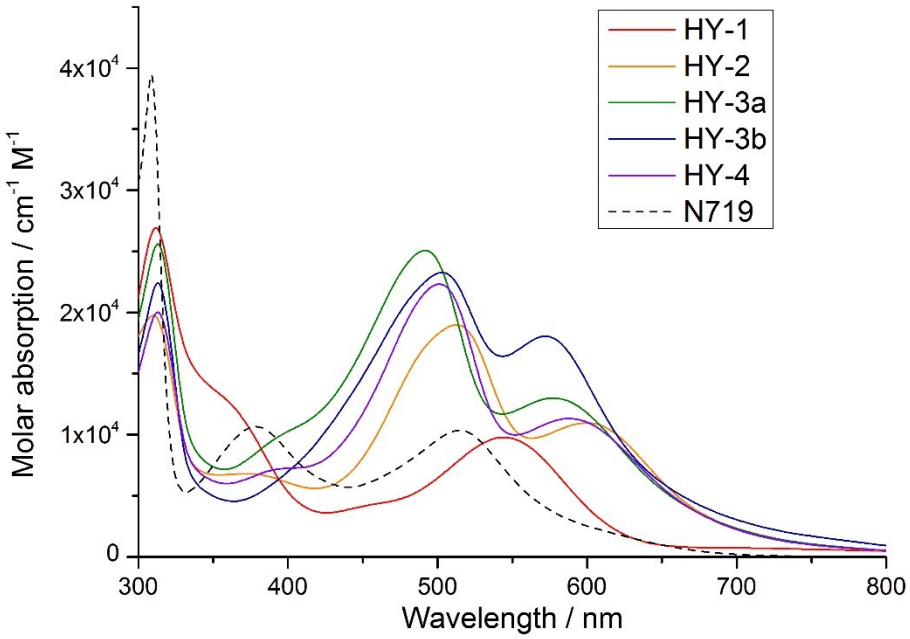

Figure 5.11 UV-visible spectra of HY-1 (red), HY-2 (orange), HY-3a (green), HY-3b (blue), HY-4 (purple) and N719 (dash) in methanol

Table 5.3 UV-Vis spectral data of HY1-4 in different organic solvents

Compound	λ_{max} [nm] ($\varepsilon \times 10^4$ M^{-1} cm^{-1})					
	MeOH	MeCN	DMSO	DMF	DCM	Chloroform
N719	307(4.0)					
	377(1.0)					
	514(1.0)					
HY-1	313(2.7)	311(2.2)	316(2.4)	315(2.8)	315(2.9)	316(2.8)
	544(1.0)	546(0.8)	551(0.9)	553(1.0)	558(1.1)	564(1.1)
HY-2	314(2.1)	310(2.3)	314(2.0)	313(1.0)	313(2.3)	314(2.2)
	372(0.7)	376(0.8)	380(0.7)	383(0.4)	394(0.9)	403(0.9)
	513(1.9)	514(2.2)	524(1.9)	519(0.9)	520(2.5)	521(2.6)
	601(1.1)	603(1.2)	613(1.1)	610(0.5)	611(1.4)	614(1.3)
HY-3a	313(2.6)	313(2.3)	318(2.5)	317(3.1)	314(2.3)	315(2.4)
	492(2.5)	493(2.1)	495(2.3)	435(3.4)	506(2.5)	510(2.9)
	577(1.3)	585(1.2)	587(1.3)	587(1.4)	600(1.3)	608(1.4)
HY-3b	313(2.2)	313(2.2)	318(2.0)	318(2.1)	315(2.2)	315(2.2)
	503(2.3)	504(2.1)	478(1.9)	455(2.9)	521(2.5)	527(2.6)
	572(1.8)	582(1.6)	582(1.3)	591(1.0)	598(2.1)	608(2.2)
HY-4	313(2.0)	313(2.3)	317(2.5)	316(1.4)	315(1.9)	315(2.1)
	501(2.2)	502(2.6)	511(2.9)	507(1.6)	510(2.3)	512(2.8)
	588(1.1)	592(1.3)	601(1.5)	600(0.8)	603(1.1)	607(1.3)
Z values	83.6	71.3	70.2	68.5	64.2	63.2

The high solubility in most solvents allowed a detailed investigation of the solvatochromic behaviour of these compounds. Solvatochromism has been previously reported in ruthenium organometallic compounds.[33, 34] Six solvents were used in the study, namely, methanol (MeOH), dichloromethane (DCM), acetonitrile (MeCN), dimethylformamide (DMF), dimethylsulfoxide (DMSO) and chloroform. The results are summarized in Table 5.3 and examples of HY-1 and HY-3a are given in Figure 5.12 and Figure 5.13. All compounds HY-1~4 showed negative solvatochromism, i.e., absorption bands blue-shifted with increasing solvent polarity. This phenomenon was especially remarkable in the bands between 450-

700nm. This means the ground state of the dyes is better stabilized than the excited state in solvents with higher polarity. The solvent-dependent absorption data of the dyes in these six solvents were analysed in respect to different solvent parameters. However, no linear correlations could be found with dielectric constant, or dipole moment. A moderate correlation could be observed with Kosower's Z value[35] (R^2 between 0.48 and 0.82), which corresponds to solvent polarity. The fits are shown in Figure 5.14. This solvatochromic behavior is consistent with the usual phenomenon of Ru complexes that contain ligands with lone pairs of electrons.[36, 37] In addition to the solvatochromic behaviour, we note unusually large differences in some cases in extinction coefficients of the charge-transfer transitions (Table 5.3). The greatest differences arise when comparing chloroform with DMF or DMSO, for example, the lowest-energy transitions for HY-4, are around 70% more intense in chloroform compared with DMF. We suggest this may relate to the ability of the solvent to form hydrogen bonds, although further study would be required to substantiate this.

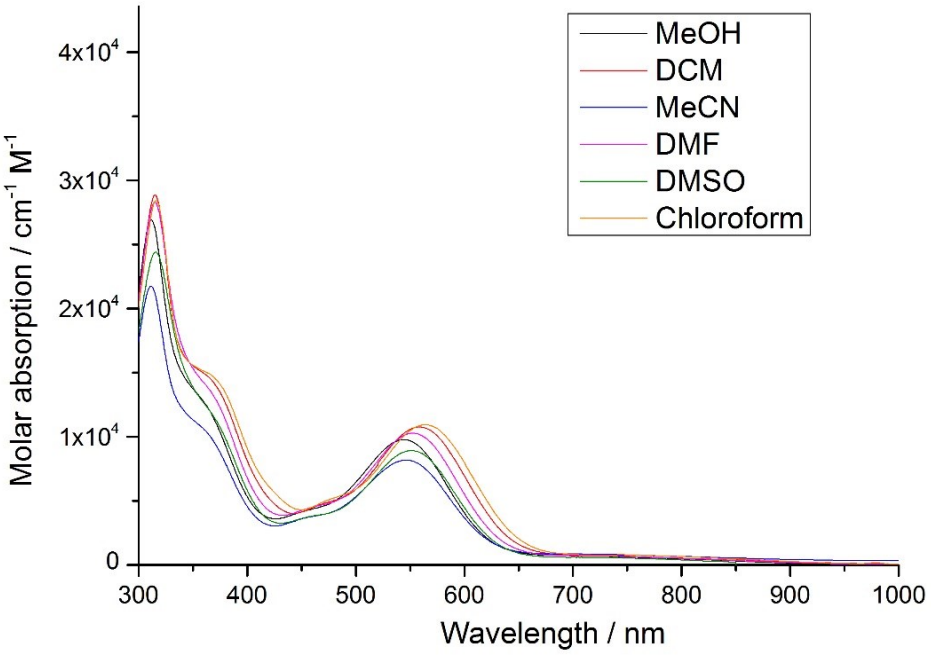

Figure 5.12 The solvatochromic behaviour of HY-1 in different solvents.

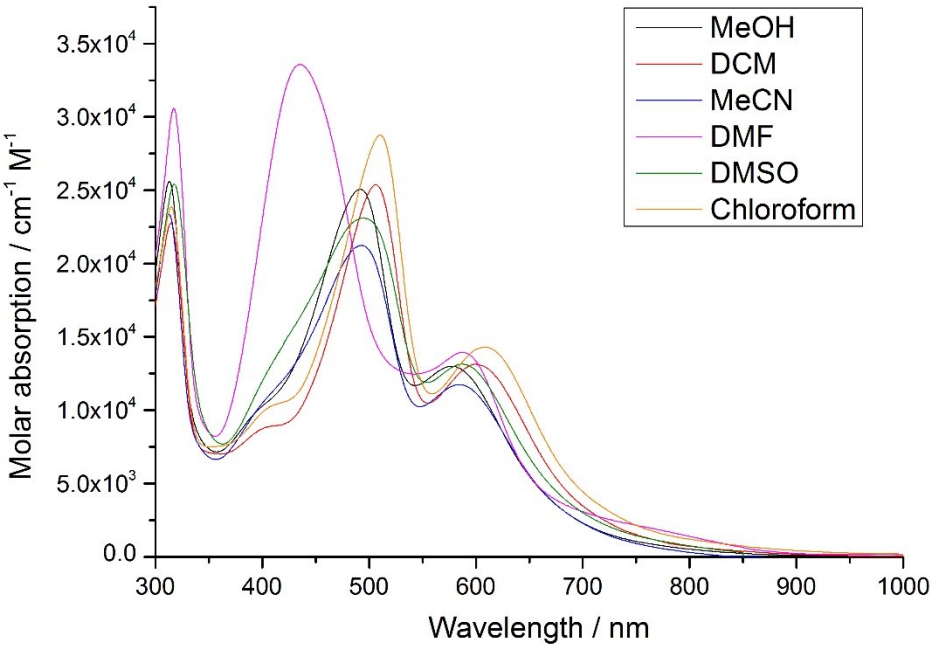

Figure 5.13 The solvatochromic behaviour of HY-3a in different solvents.

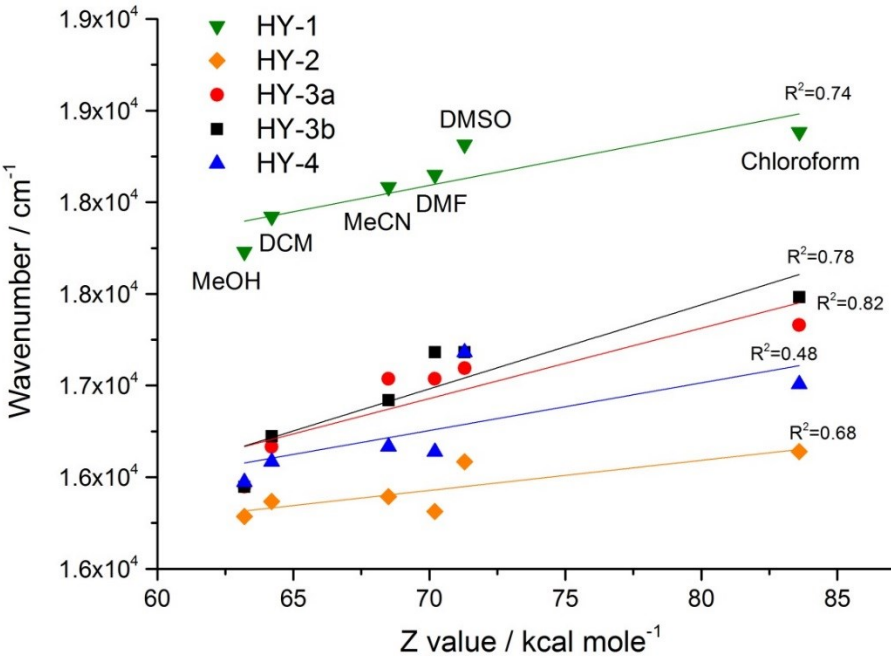

Figure 5.14 The effect of the solvent polarity on the lowest energy MLCT transition of the dyes.

2.3 Electrochemistry

The redox behaviour of the complexes in acetonitrile solution was examined by cyclic voltammetry. The electrochemical data for the first oxidation potential and the first two reduction potentials are summarised in Table 5.4 and the cyclic voltammograms of the first oxidation processes are given in Figure 5.15.

Table 5.4 Electrochemistry results of the ligands, esters and salts

Compounds	E_{ox} vs. NHE / V	1st E_{red} vs. NHE / V	2nd E_{red} vs. NHE / V
HY-1	1.34	-0.43	-0.94
HY-2	1.17	-0.54	-0.99
HY-3a	1.09	-0.66	-1.02
HY-3b	0.99	-0.66	-1.02
HY-4	1.07	-0.66	-1.07
N719[a]	1.12[a]	-0.60[a]	-

a. See reference 38.[38]

The first oxidation potential was assigned to the ruthenium(II)/ruthenium(III) couple and was irreversible for all the dyes. Comparing within the same isomers, the ruthenium(II)/ruthenium(III) redox potential follows the trend HY-4 < HY-3a < N719 < HY-2 < HY-1. This is correlated with the π-acidity order of the ligands. [15, 39] The bipyridine ligands thus better stabilize the reduced Ru(II) than pai and pai-Me but less effectively than azopyridines. This observation also corresponds with the calculations since the location of the LUMO gradually changes from the azo ligand to the bipyridine ligand from HY-1 to HY-4 (see later in Section 2.5).

When working in the dye-sensitized solar cells, the dyes are in neither ester nor salt form. Instead, the reality should be the product obtained when dye combines with TiO_2. However, using esters as models can provide us some estimation towards the HOMO and LUMO level energies.

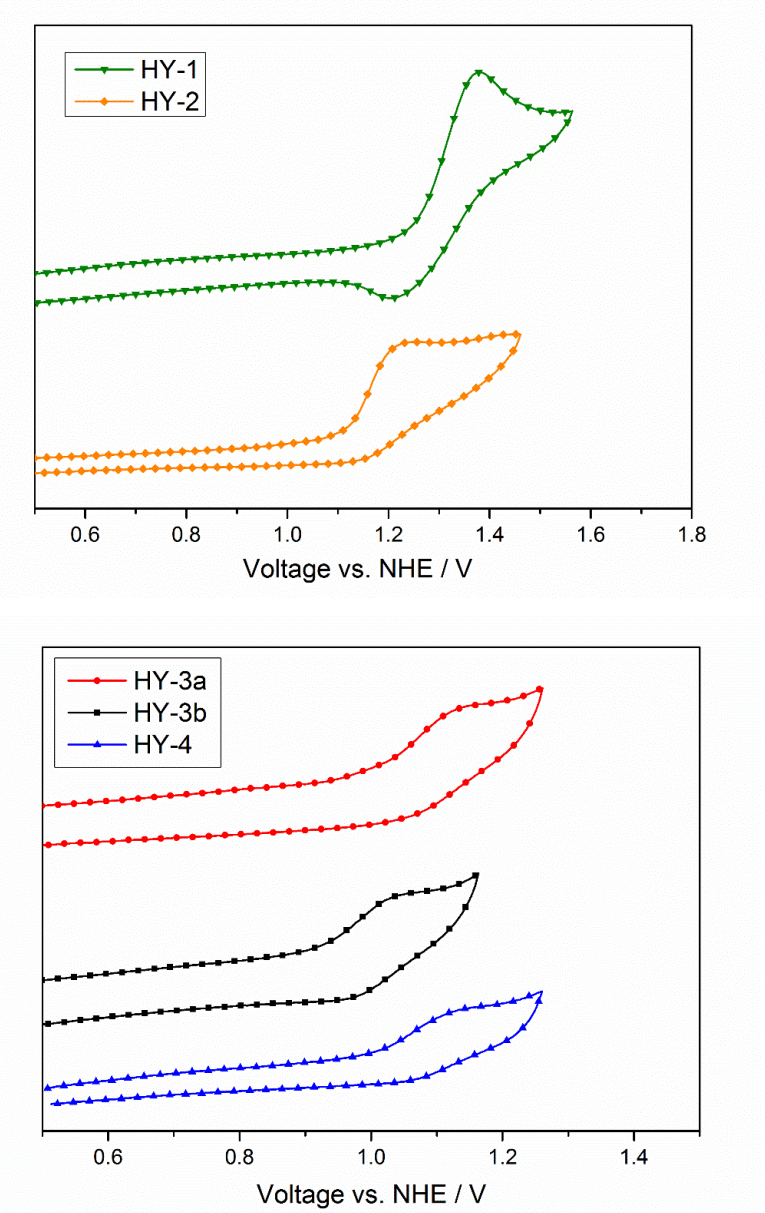

Figure 5.15 Cyclic voltammograms of the first oxidation processes in acetonitrile solution containing 0.1 M [TBA][PF_6] at scan rate 0.1 V/s.

2.4 Device performance

The complexes were tried as sensitisers in dye-sensitised solar cells and full details of cell fabrication were given in Chapter 2. The *iso*-butyl group was easily removed by stirring in a tetrabutylammonium hydroxide (TBAOH) solution for 20 mins, followed by careful addition of nitric acid to precipitate the product with carboxylic acid as the anchoring group. An example is given in Scheme 5.2. NMR and

elemental analysis of the precipitate in each case are consistent with the proposed structure $[Bu_4N][Ru(azo)(dcbpy)(NCS)_2]$.

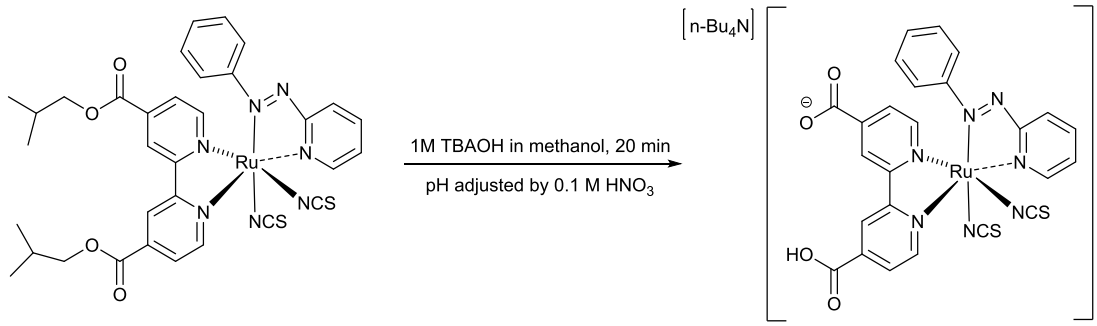

Scheme 5.2 Hydrolysis of HY-1

Dye-sensitised solar cells were prepared by standard methods and tested under AM1.5 radiation and the commercial dye, N719, was used as a comparison. Surprisingly, the new complexes all showed very poor power-conversion efficiency of <0.2%. N719-sensitized DSSCs performed significantly better in every aspect including photocurrent, voltage and efficiency with a highest observed efficiency of 7.0%. The J-V curve of the devices using HY-1 and HY-2 are shown in Figure 5.18 compared with that of the N719-sensitised device. The photovoltaic data summarized in Table 5.5 are shown for the best device fabricated for each dye and overall efficiencies are not optimized. Three different electrolytes- ***a*** to ***c***, where the percentage of LiI and t-BP was systematically varied- were also prepared to tune the acceptor levels within the TiO_2, which should decrease in energy from the one treated with electrolyte ***a*** to the one treated with electrolyte ***c***. As a consequence, the J_{SC} of the solar cells increased, V_{OC} decreased and the overall efficiency increased. This result also indicates that charge injection to the TiO_2 is a problem inherent for the dyes.

Table 5.5 Photovoltaic data for DSSCs using N719 and compounds HY-1~4

Compounds	J_{SC} / mA cm^{-2}	V_{OC} / V	ff	η / %
HY-1[a]	0.15	0.41	0.65	0.04
HY-2[a]	0.3	0.43	0.70	0.1
HY-3a[a]	0.19	0.36	0.46	0.03
HY-3a[b]	0.52	0.31	0.52	0.08
HY-3a[c]	1.24	0.30	0.54	0.20
HY-3b[c]	0.7	0.32	0.54	0.12
HY-4[c]	0.18	0.23	0.48	0.02
N719	13.6	0.73	0.71	7.0

Electrolyte: a 1.0M BMII, 0.1M GuNCS, 0.03M I_2, 0.5 M t-BP in MeCN/VN (85:15); b 1.0M BMII, 0.1M GuNCS, 0.05M LiI, 0.03M I_2 in MeCN/VN (85:15); c 1.0M BMII, 0.1M GuNCS, 0.4M LiI, 0.03M I_2 in MeCN/VN (85:15).

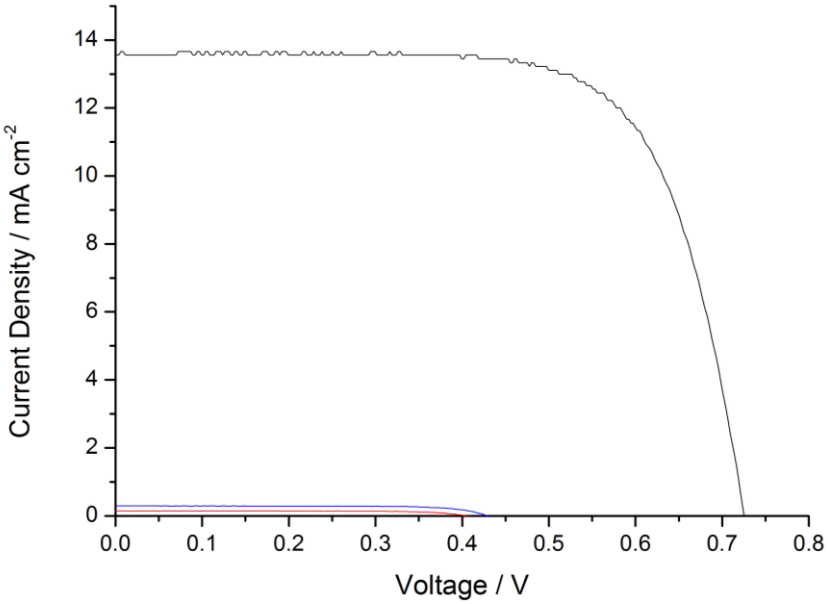

Figure 5.16 J-V curves for DSSCs using N719 (black), HY-1 (red) and HY-2 (blue)

2.5 Computational Study

Despite the appropriate redox properties and light harvesting of these dyes, the DSSC performance was poor. To understand this and to explore the electronic structures of these dyes in more detail, we undertook a study of the photophysical properties of the

dye series, interpreted in the context of DFT and TD-DFT calculations. The calculations were performed on the hydrolyzed dyes.

The orbital distributions of HY-1 and HY-2 are shown in Tables 5.6 and Table 5.7. For both complexes HY-1 and HY-2, the HOMO is mainly localised on the Ru atom with a strong *d* character and on the NCS ligands with strong π character. Also, a small contribution of the azo ligand can be seen to contribute to the HOMO. In HY-1, the LUMO is mainly localised on the azo ligand with the LUMO+1 on the bipy ligand. As the azo ligand becomes more electron rich from azpy to dmazpy, a larger contribution from the bipy can be observed for the LUMO for HY-2. This result suggests a charge separation in an inappropriate direction for DSSCs. However, although these two complexes are not suitable for DSSCs, the results show a promising method to modify the molecule. A larger contribution from dcbpy can be observed for LUMO in HY-2 than HY-1, which means $N(CH_3)_2$ is making the azo ligand more electron rich and raising its energy. In addition, it can be observed that the $N(CH_3)_2$ group raises the energy of both LUMO and LUMO+1 compared with the simple azpy ligand. Crucially, it raises the LUMO energy more, making it closer to the LUMO+1. Thus, if the energy of LUMO can be raised a bit more, then the dcbpy ligand, which is the LUMO+1 now, will become the LUMO.

Table 5.6 Molecular orbital distribution of HY-1 (isodensity = 0.02)

MO	HOMO–4	HOMO–3	HOMO–2	HOMO–1	HOMO
MO picture		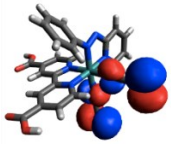		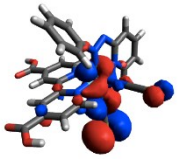	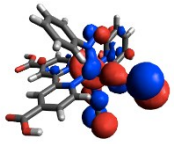
Energy / eV	-6.86	-6.66	-5.97	-5.89	-5.63
MO	LUMO	LUMO+1	LUMO+2	LUMO+3	LUMO+4
MO picture	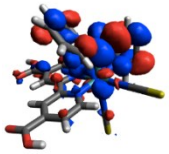	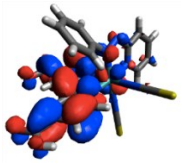	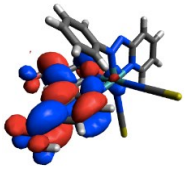	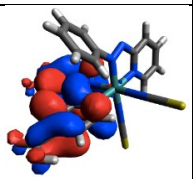	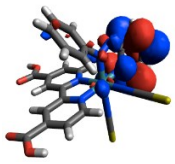
Energy / eV	-3.85	-3.19	-3.08	-1.71	-1.39

Table 5.7 Molecular orbital distribution of HY-2 (isodensity = 0.02)

MO	HOMO–4	HOMO–3	HOMO–2	HOMO–1	HOMO
MO Picture	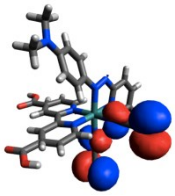	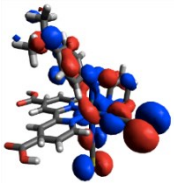	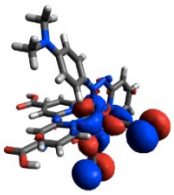	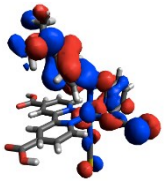	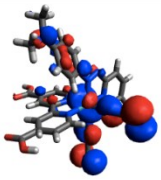
Energy / eV	-6.15	-5.92	-5.74	-5.67	-5.29
MO	LUMO	LUMO+1	LUMO+2	LUMO+3	LUMO+4
MO picture	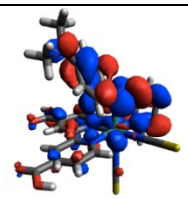	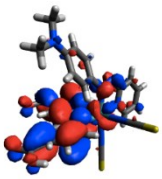	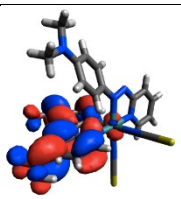	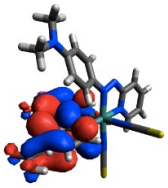	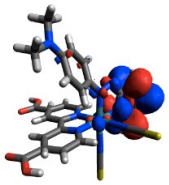
Energy / eV	-3.41	-2.98	-2.55	-2.22	-1.38

Based on this logic, HY-3 and HY-4, which contain the more electron-rich pai and pai-Me ligands, were designed. As a result, the lowest unoccupied level of the azo ligand is higher than that of the bipy. The molecular orbital distributions of HY-3a, HY-3b and HY-4 are shown in Table 5.8 ~ Table 5.10. The LUMO of HY-3 and HY-4 lies on the bipy ligand and LUMO+1 is mainly located on the azo ligand with a very similar energy. The pai and pai-Me ligands were deliberately chosen to favour location of the LUMO on the bipy ligand so this is as expected from the design strategy.

Table 5.8 Molecular orbital distribution of HY-3a (isodensity = 0.02)

MO	HOMO–4	HOMO–3	HOMO–2	HOMO–1	HOMO
MO picture	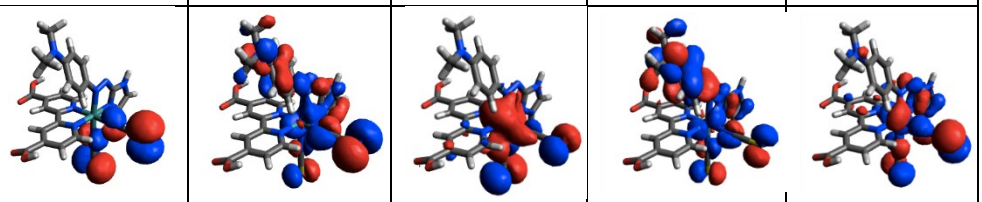				
Energy / eV	-6.22	-5.96	-5.88	-5.73	-5.62
MO	LUMO	LUMO+1	LUMO+2	LUMO+3	LUMO+4
MO picture	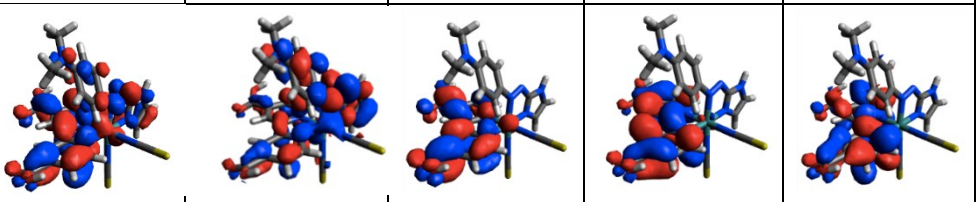				
Energy / eV	-3.26	-3.11	-2.60	-2.34	-0.94

Table 5.9 Molecular orbital distribution of HY-3b (isodensity = 0.02)

MO	HOMO–4	HOMO–3	HOMO–2	HOMO–1	HOMO
MO picture	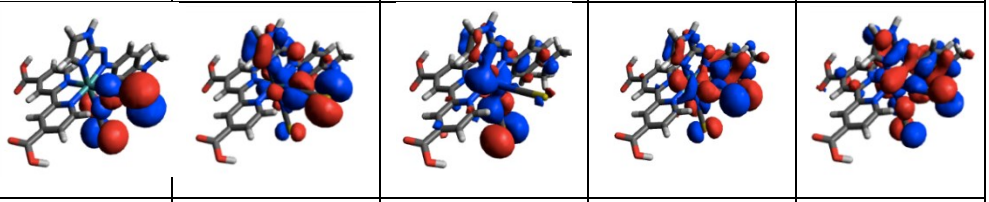				
Energy / eV	-6.21	-5.93	-5.85	-5.78	-5.53
MO	LUMO	LUMO+1	LUMO+2	LUMO+3	LUMO+4
MO picture	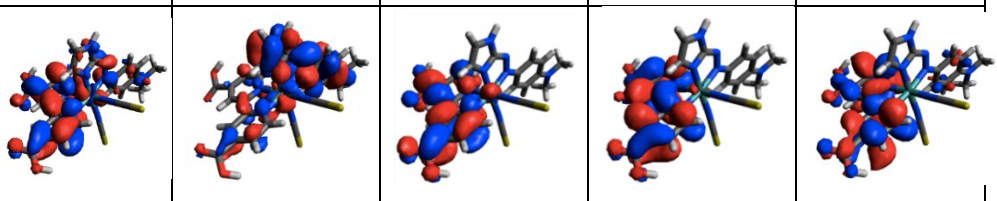				
Energy / eV	-3.21	-3.12	-2.57	-2.31	-0.91

Table 5.10 Molecular orbital distribution of HY-4 (isodensity = 0.02)

MO	HOMO–4	HOMO–3	HOMO–2	HOMO–1	HOMO
MO picture	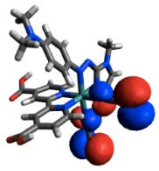	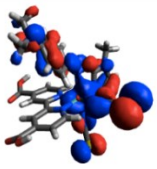	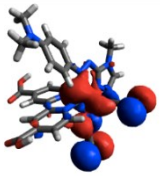	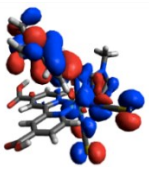	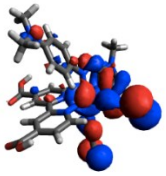
Energy / eV	-6.22	-5.93	-5.86	-5.71	-5.60
MO	LUMO	LUMO+1	LUMO+2	LUMO+3	LUMO+4
MO picture	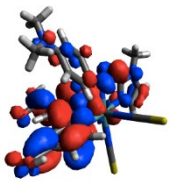	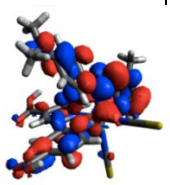	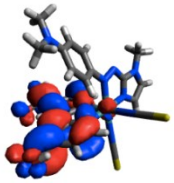	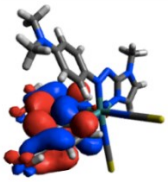	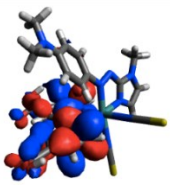
Energy / eV	-3.24	-3.08	-2.59	-2.33	-0.91

As mentioned before, the transitions in the visible region are typical of Ruthenium dyes and are typically assigned to metal-to-ligand charge transfers (MLCT), as exemplified by N719. In that case this transition takes place from the metal centre to the bipyridine and allows rapid electron injection into the TiO_2 when the dye is incorporated into a DSSC device.

In the case of the new dyes, TDDFT calculations showed the complexity of these compounds. Seventy singlet-singlet transitions were calculated using the optimised geometry surrounded by a MeOH polarisable continuum model. The calculated and experimental UV-Vis absorption spectra are shown in Figure 5.17 ~ Figure 5.21. TDDFT simulated absorption spectra matched well with the experimental, giving confidence in the assignment of transitions through the computational results. Table 5.11 summarizes selected low-energy singlet-singlet transitions. More transitions can be found in Section 5.

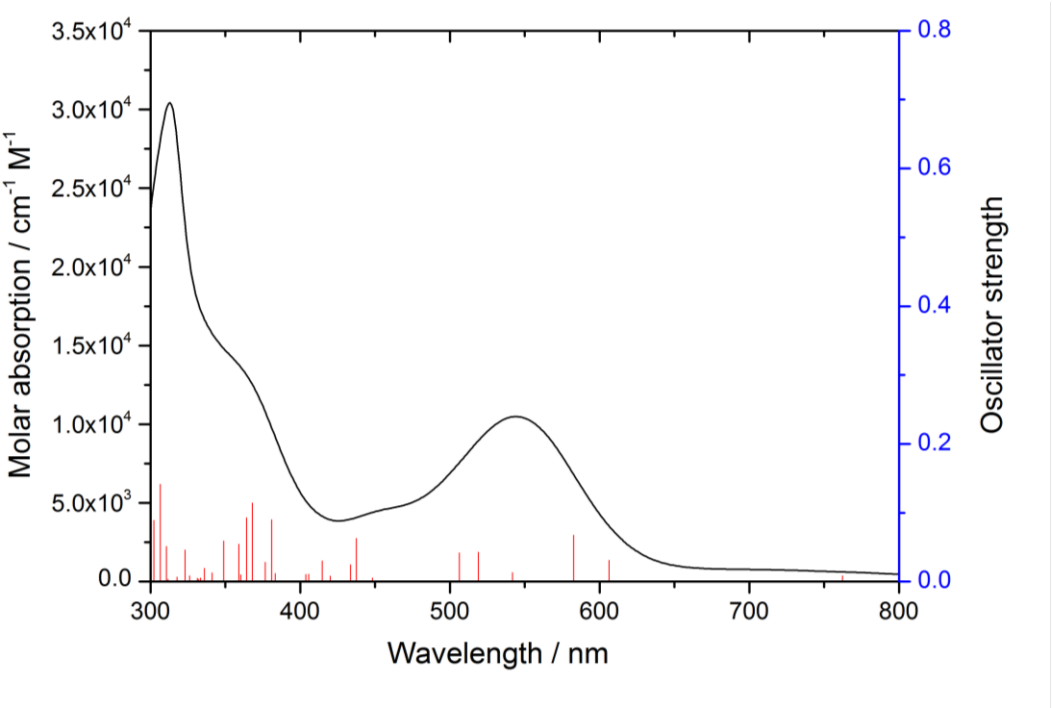

Figure 5.17 Experimental UV-visible spectra (black line) and computational simulated oscillator strength (red line) of HY-1 in methanol

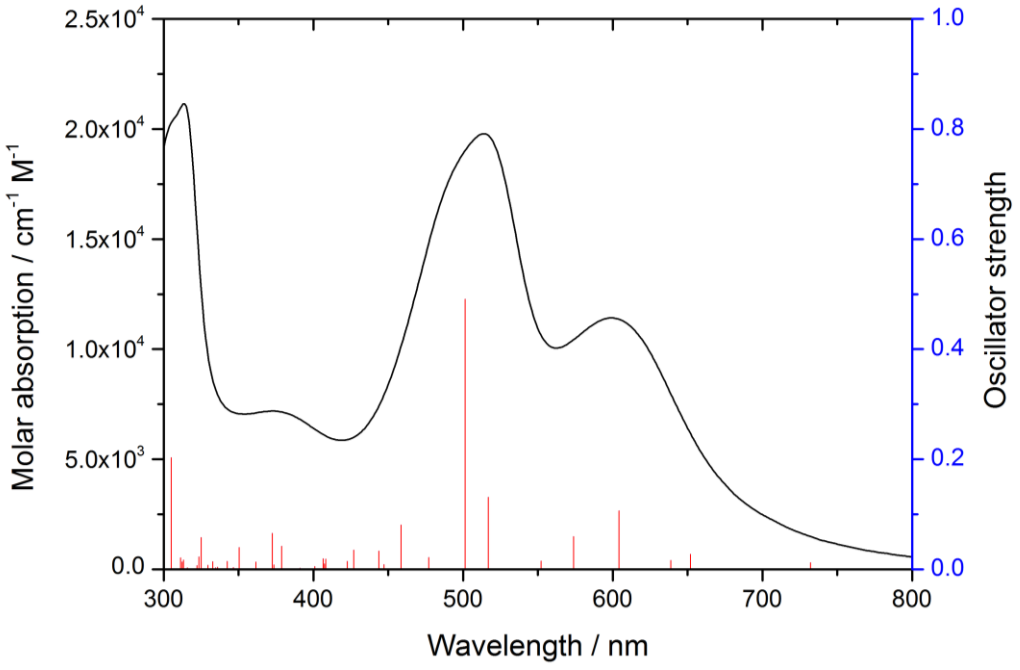

Figure 5.18 Experimental UV-visible spectra (black line) and computational simulated oscillator strength (red line) of HY-2 in methanol

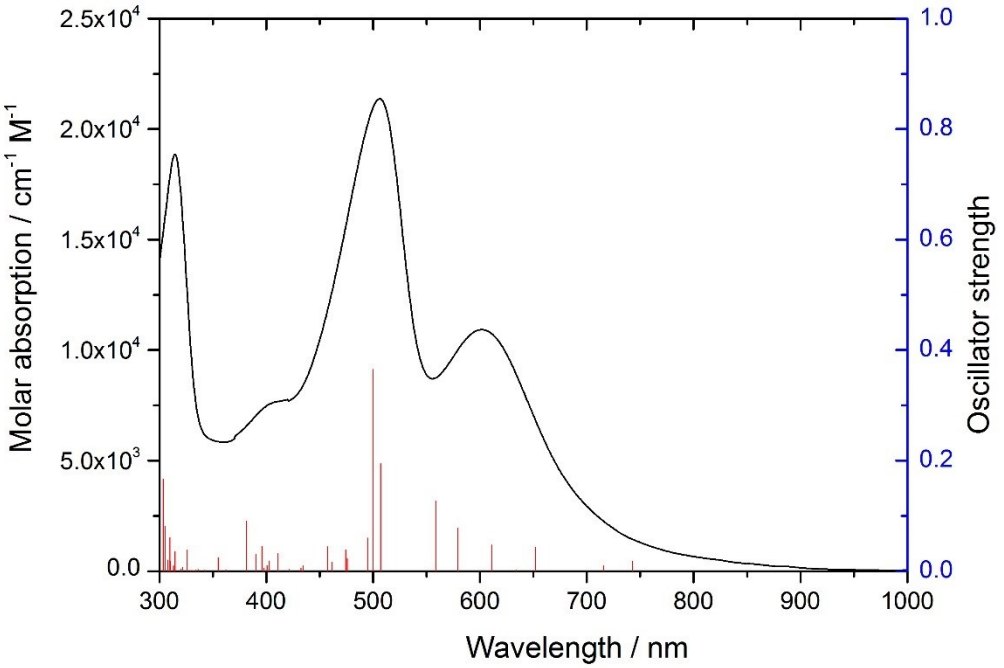

Figure 5.19 Experimental UV-visible spectra (black line) and computational simulated oscillator strength (red line) of HY-3a in methanol

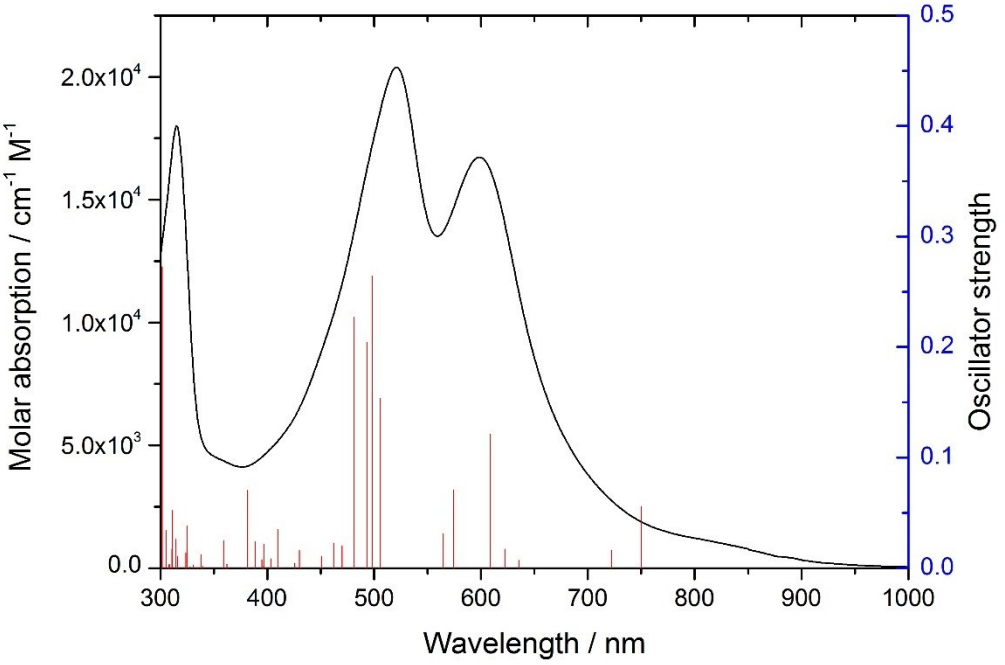

Figure 5.20 Experimental UV-visible spectra (black line) and computational simulated oscillator strength (red line) of HY-3b in methanol

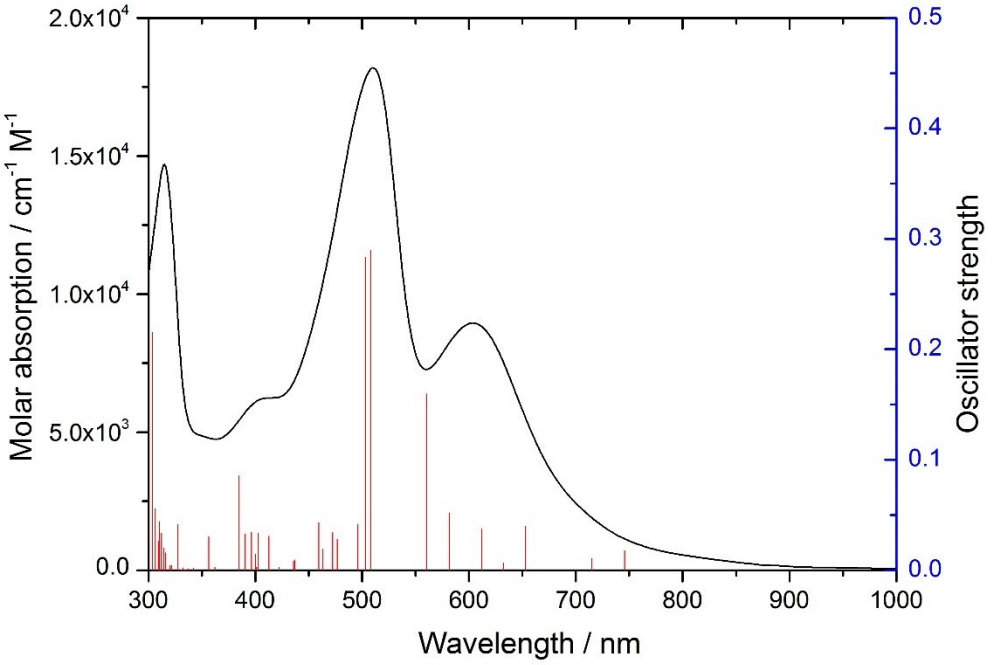

Figure 5.21 Experimental UV-visible spectra (black line) and computational simulated oscillator strength (red line) of HY-4 in methanol

Table 5.11 Wavelengths, oscillator strengths and major contributions to selected singlet optical transitions calculated by TDDFT.

	Wavelength (nm)	Osc. Strength	Nature of transition (major contribution, %)[a,b]	Primary character
HY-1	582.74	0.0674	H-2→LUMO (19%) HOMO→L+1 (64%)	$ML_{azo}CT$ $ML_{bp}CT$ ILCT
	519.00	0.0427	H-2→L+1 (34%) H-1→L+1 (58%)	$ML_{azo}CT$ $ML_{bp}CT$
	506.20	0.0417	H-3→LUMO (17%) H-2→L+1 (49%) H-1→L+1 (24%)	$ML_{azo}CT$ $ML_{bp}CT$
HY-2	604.15	0.1064	H-2→LUMO (24%) H-1→LUMO (27%) H-1→L+1 (24%)	$ML_{azo}CT$ LC ILCT LLCT

	501.37	0.491	H-3→LUMO (38%) H-3→L+1 (21%) H-1→LUMO (22%)	$ML_{bp}CT$ ILCT LLCT
HY-3a	611.1	0.0471	H-2→LUMO (16%) H-2→L+1 (67%)	$ML_{azo}CT$ $ML_{bp}CT$
	579.1	0.078	H-3→LUMO (36%) H-1→L+1 (45%)	$ML_{azo}CT$ $ML_{bp}CT$ ILCT LLCT
	558.6	0.1268	H-3→LUMO (41%) H-3→L+1 (26%)	$ML_{azo}CT$ $ML_{bp}CT$ ILCT LLCT
	506.9	0.1947	H-4→LUMO (41%) H-3→L+1 (27%) HOMO→L+2 (18%)	$ML_{azo}CT$ $ML_{bp}CT$ ILCT LLCT
	500.0	0.3648	H-4→LUMO (23%) H-3→L+1 (32%) HOMO→L+2 (16%)	$ML_{azo}CT$ $ML_{bp}CT$ ILCT LLCT
HY-3b	608.8	0.121	H-3→LUMO (14%) H-2→LUMO (59%)	$ML_{bp}CT$ $ML_{azo}CT$ ILCT
	505.4	0.1536	H-4→LUMO (30%) H-3→L+1 (17%) HOMO→L+2 (36%)	$ML_{azo}CT$ ILCT LLCT
	498.5	0.2646	H-4→L+1 (16%) HOMO→L+2 (39%)	$ML_{bp}CT$ LLCT
	493.2	0.2042	H-4→LUMO (65%) H-3→L+1 (16%)	$ML_{azo}CT$ $ML_{bp}CT$ ILCT

				LLCT
HY-4	560.6	0.1596	H-3→LUMO (28%) H-3→L+1 (24%) H-1→L+1 (25%)	$ML_{bp}CT$ $ML_{azo}CT$ ILCT LLCT
	508.3	0.2898	H-4→LUMO (22%) H-3→L+1 (42%)	$ML_{azo}CT$ $ML_{bp}CT$ ILCT LLCT
	502.9	0.2835	H-4→LUMO (22%) H-3→L+1 (17%) HOMO→L+2 (37%)	$ML_{azo}CT$ $ML_{bp}CT$ ILCT LLCT

For all the complexes, the highly-intense bands between 450 nm and 600 nm are due to mixed character transitions, composed of some $d\pi - \pi^*_{azo}$ metal-to-ligand charge transfer ($ML_{azo}CT$), $d\pi - \pi^*_{bp}$ metal-to-ligand charge transfer ($ML_{bp}CT$), $\pi_{azo} - \pi^*_{bp}$ ligand-to-ligand charge transfer (LLCT), $n- \pi_{azo}^*$ intra-ligand charge transfer (ILCT) and $\pi_{azo}- \pi_{azo}^*$ ligand-centered (LC) character. This complexity may arise from a splitting of d orbitals of Ru metal due to the presence of different acceptor orbitals. The lower symmetry splitting may then result in a mixing of singlet and triplet configurations in the excited state through spin-orbit coupling. [18]

For HY-1, the band at 544 nm is assigned to a combination of $ML_{azo}CT$ and $ML_{bp}CT$. In the case of HY-2, this band red-shifted and split into two bands. The red-shift is explained by the introduction of the electron-donating N,N'-dimethyl group on the phenyl ring of the azo ligand. The band at the longer wavelength is mainly due to $ML_{azo}CT$ and the other one is mainly based on $ML_{bp}CT$. ILCT and LLCT also contributes in both transitions.

HY-3 and HY-4 have two bands between 450 and 700 nm. However, since the LUMO for HY-3 and HY-4 were localised on bpy instead of azo ligands, unlike HY-

1 and HY-2, the lower energy transition is largely due to $ML_{bpy}CT$ and the higher energy transition to $ML_{azo}CT$. However, again, both also contained a large contribution from ILCT and LC.

The two isomers of HY-3 behaved similarly both experimentally and computationally. The main difference is that HY-3b has a higher extinction coefficient at the lower energy band.

2.6 Emission

Emission spectroscopy measurement was carried out by Dr. Irene Sanchez-Molina in Imperial College. Emission was recorded in methanol, with and without the presence of O_2 from air. In general, the samples were degassed and cooled down in liquid nitrogen and measurements were taken at 77K. Control measurements were taken at room temperature, and without degassing, in order to identify emission from triplet states. All emission spectra were corrected for inner filter effects [40] and the data can be found in Table 5.12 and Figure 5.24.

Table 5.12 Summary of the emission bands (nm) for HY-1~4 observed at room temperature in degassed solutions (black), non-degassed solutions (red) and frozen in degassed MeOH at 77 K (blue), with λ_{exc} = 500 nm

HY-1	536, 585 536, 585 536, 585
HY-2	538^{sh}, 591 538^{sh}, 591 538^{sh}, 591
HY-3a	621, 665 621,665 535^{sh}, 582^{sh}, 625, 670
HY-3b	536, 585 536, 585 537, 582, 625^{sh}, 670^{sh}
HY-4	538, 583 538, 583 534, 584, 626^{sh}, 666^{sh}

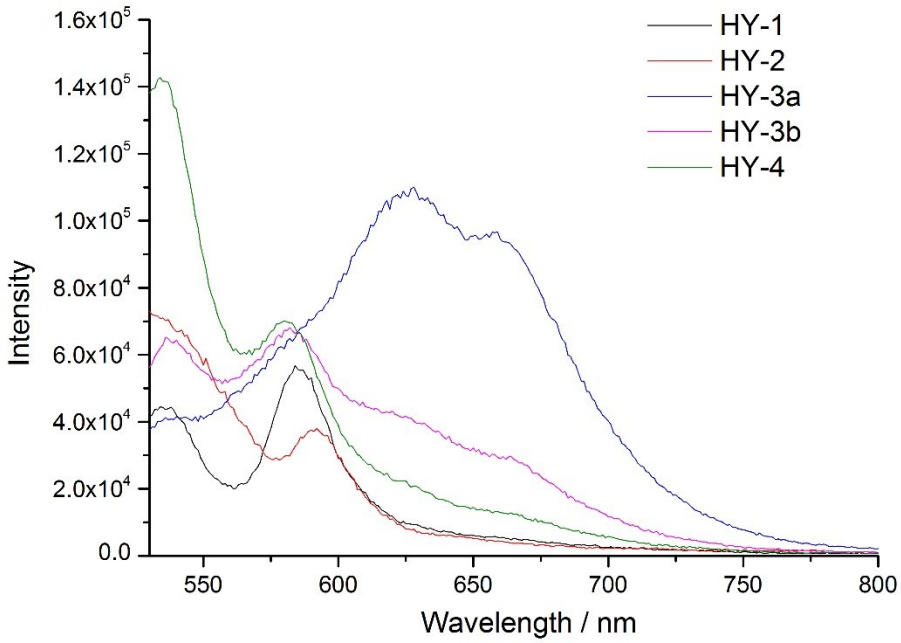

Figure 5.24 Emission spectra for HY-1~4 recorded in MeOH degassed solutions at 77K when excited at 500 nm.

For all the complexes, no emission could be observed when excited at the lowest energy absorption band (ca. 550nm). This is unusual but has been observed before in the case of cycloruthenated carbonyl complexes by Kumar [41] where strong chromophore groups were chelated to Ru complexes. Excitation at 500 nm, however, led to observable emission in solution and frozen glass. In the case of HY-1 and HY-2, comparatively strong emission around 540 and 580 nm was observed. This small Stokes shift emission may arise through ^{1}MLCT that relaxes rapidly to the ground state before intersystem crossing occurs to ^{3}MLCT, and/or from deactivation of any ^{3}MLCT state by mixing with low lying non-emitting azo-ligand-based excited states. Large singlet character in the emission is consistent with significant ligand character through the strong contribution of the azo chromophore. In HY-3a,b and HY-4, similar bands were seen around 530 and 585 nm; however, additional peaks or shoulders were also seen around 625 and 670 nm that were absent from HY-1 and HY-2.

To explore the capability of the dyes to inject electrons into TiO_2, emission of complexes on mesoporous oxide substrates was tested. Thin films of selected complexes, HY-2 and HY-4 were spin-coated onto mesoporous ZrO_2 and TiO_2. Emission quenching on TiO_2 would indicate that the electrons inject into TiO_2, with ZrO_2 used as a control since the higher conduction band would preclude charge injection. Emission spectra were recorded upon excitation at 500 nm and partial, although not complete, quenching of emission for the dyes on TiO_2 was observed in both cases. Time-correlated single photon counting measurements were performed on the samples to determine the emission lifetimes of the signals observed. Dyes were excited at 282nm and emission was monitored at 460 nm. A long pass filter at 420 nm was set in the emission channel. Reference measurements were taken on TiO_2 and ZrO_2 films. The lifetimes of both HY-2 and HY-4 were seen to decrease from 22.12 ns and 21.8 ns to 15.11 ns and 12.34 ns respectively going from ZrO_2 to TiO_2, consistent with the reduction in emission intensity. Overall, the weak emission, short lifetimes and only-partial quenching suggest that charge injection in the DSSC may be the limiting factor in cell performance.

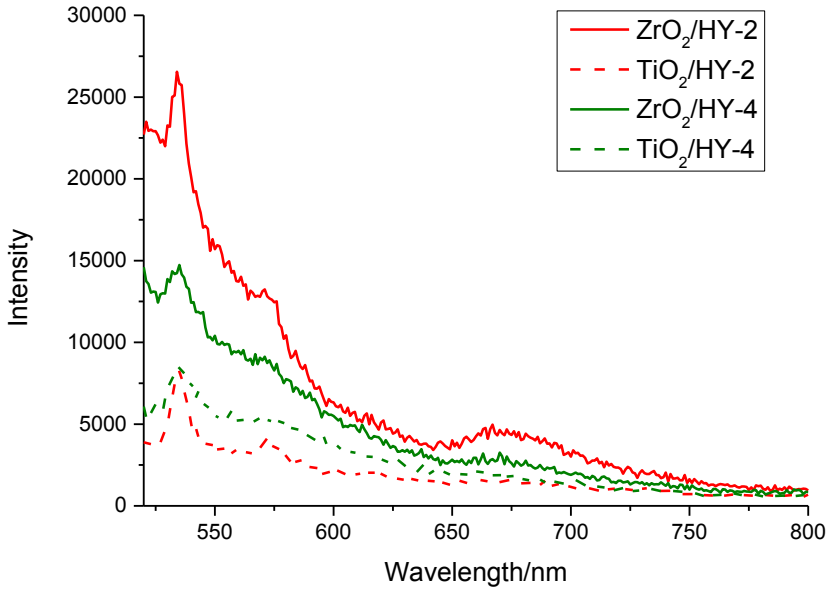

Figure 5.25 Emission of HY-2 and HY-4 on mesoporous TiO_2 and ZrO_2 excited at 500 nm.

3 Conclusion

A series of novel Ru(II) complexes with bis(2-methylpropyl)-2,2'-bipyridine-4,4'-dicarboxylate ($^{i}bu_2dcbpy$) as one chromophore and phenylazopyridine derivatives (azpy and dmazpy) or [4-(N,N-dimethylamino)benzeneazo]imidazole derivatives (pai and pai-Me) as an additional chromophore and thiocyanate as ligand have been synthesized (HY-1~HY-4). These dyes are all intensely colored in the visible region. For simple Ru-bipyridyl complexes, such transitions would be due to $d\pi - \pi^*$ metal-to-ligand charge transfer (MLCT) occurring in the visible region. However, the photophysical study of the new dyes showed unexpected features including intense solvatochromism, and also solvent-dependence of extinction coefficient.

The absorption spectrum of the dyes showed an enhanced light harvesting compared to the N719 dye that lacks the azo ligand and electrochemical study also showed properties suitable for application as sensitisers in DSSCs. Following hydrolysis, the complexes were investigated in DSSCs, with performance investigated using I-V measurements. Poor performance was observed and we attribute this as mostly likely

due to poor charge injection due to short excited-state lifetime. Although the application of these current dyes in DSSCs is not feasible due to their poor performance, this study allowed us to determine the positions of the HOMO and LUMO orbitals and correlate it to the π-acidity of the dyes. It is expected that this will help the design of related dyes for DSSC or similar optoelectronic fields, and highlight the approach of joining together an additional chromophore to enhance light harvesting with a ruthenium complex.

4 Experimental

The preparation of the starting materials dichloro(*p-cymene*)ruthenium(II) dimer [42], and all ligands including 4, 4'-dicarboxylic acid-2,2'-bipyridine (dcbpy) [43], bis(2-methylpropyl)-2,2'-bipyridine-4,4'-dicarboxylate (^{i}bu$_2$dcbpy) [44], 2-Phenylazopyridine (azpy) [24, 25], [4-(N,N-dimethylamino)benzeneazo]imidazole (pai) and 1-Methyl-2-[4-(N,N-dimethylamino)benzeneazo]imidazole (pai-Me) [45] were based on literature reports. 4,4'-Dimethyl-2,2'-bipyridyl, 2-aminoimidazole suflate, $NaNO_2$, NaH, methyl iodide and N,N-dimethylaniline were purchased from Sigma-Aldrich. 2-Aminopyridine and nitrosobenzene were purchased from Merck (MDA) incl Schuchard. 4-(2-pyridylazo)-N,N-dimethylaniline and 1M tetra-n-butylammonium hydroxide in methanol was purchased from Alfa (Aesar). All chemicals were used without further purification. All solvents were reagent grade except for the ones for emission, which were spectroscopic grade. They were all used as received.

The UV/vis studies were recorded using a Jasco V670 UV-Visible-NIR spectrophotometer and analysed using UVwinlab software. All measurements were made using a quartz cell of 1 cm path length using methanol, dichloromethane, acetonitrile, dimethylformamide, dimethylsulfoxide and chloroform as the solvents. Emission was recorded with a Flourolog-3 Horiba Yobin-Ybon spectrometer and analysed with OriginPro 9. Concentration of 2×10^{-5} M and 1.5×10^{-5} M were used for UV-Visible and emission, respectively.

Electrochemical studies were obtained by cyclic voltammetry (CV) using a μ autolab type III potentistat, controlled using General Purpose Electrochemical System (GPES) software. A platinum rod counter electrode, a 0.5mm diameter platinum working electrode and an Ag/AgCl reference electrode were used. Ferrocene/ferrocenium (Fc/Fc^+) redox couple was used as an internal standard. Tetrabutylammonium tetrafluoroborate ($TBABF_4$) or tetrabutylammonium hexafluorophosphate was used as the supporting electrolyte. The experiment was performed in nitrogen purged 0.1M $[TBA]^+[BF_4]^-$ or 0.1 M $[TBA]^+[BF_6]^-$ solution in acetonitrile. The data were recorded against ferrocene and converted to NHE by addition of 0.63V.

The hydrolysed molecular structures were optimised in vacuum, using the software Avogadro [46, 47] to enter the starting geometry. Then the structure was optimised using the methanol polarisable-continuum model, starting from the optimised structure from vacuum. All calculations were carried out using the Gaussian 09 program [48] with the Becke three parameter exchange functional with the Perdew Wang 1991 correlation functional (B3PW91) [49, 50] level of theory together with 6-31+G* basis set for C, H, N, O and S atoms. The Ru atom was treated with the Hay-Wadt VDZ (n+1) ECP basis set.[51-53] Time-dependent DFT calculations (TD-DFT) [54, 55] were performed using Gaussian 09 program [48] with a methanol polarisable continuum model (PCM).[56] The 70 lowest singlet electronic transitions were calculated and processed with the GaussSum software package.[57]

Black plate crystals of HY-2 and thin black needle crystals of HY-3b were grown by slow diffusion from acetone/hexane. Single crystal data were collected using Cu-Kα radiation (λ=1.54184Å) on a Bruker Smart Apex CCD diffractometer equipped with an Oxford Cryostreams low temperature device operating at 120 K. An absorption correction was applied using numerical for HY-2 and Gaussian for HY-3b.[58] The structure was solved by Patterson synthesis and refined by Full-matrix least-squares on F^2.[59] Figures were prepared using the programme Mercury.[60]

HY-2: $C_{35}H_{38}N_8O_4RuS_2 \cdot C_3H_6O \cdot CH_4O$ (moieties), $C_{40}H_{52}N_8O_7RuS_2$ (total), *T/K* =

120(2), space group *P* -1, *a* = 10.6502(3), *b* = 19.9039(10), *c* = 20.9841(11) Å, α = 80.449(4)°, β = 83.371(3)°, γ = 81.622(3)°, *V* = 4320.7(4) Å^3, reflections for cell refinement: 9185 (θ = 4.2~74.3°), *Z* = 4, D_c = 1.418 mg m^{-3}, μ = 4.312 mm^{-1}, reflections collected = 49305 (R_{int} = 0.0886), no. $F^2 > 2\ \sigma$ = 11292, T_{min}/T_{max} = 0.572/0.937, data/restraints/parameters : 15456/150/908, R_1 ($F^2 > 2\ \sigma$) = 0.1320, *wR2* = 0.3202, *S* = 1.088, $\Delta\rho_{max}/e$ Å^{-3} = 3.00, $\Delta\rho_{min}/e$ Å^{-3} = -3.35.

HY-3b C_{36} H_{43} $N_9O_5RuS_2$, *T/K* = 120(2), space group *P* -1, *a* = 7.5548(8), *b* = 15.6015(19), *c* = 17.570(2) Å, α = 79.549(10)°, β = 89.788(9)°, γ = 77.335(10)°,*V* = 1985.6(4) Å^3, reflections for cell refinement=2113 (θ = 3.5~38.1°), *Z* = 2, D_c = 1.417 Mg m^{-3}, μ = 4.611 mm^{-1}, reflections collected = 12607 (R_{int} = 0.1293), T_{min}/T_{max} = 0.998/1.000, data/restraints/parameters : 2113/42/321, R_1 ($F^2 > 2\ \sigma$) = 0.0867, *wR2* = 0.2235, *S* = 1.144, $\Delta\rho_{max}/e$ Å^{-3} = 0.880, $\Delta\rho_{min}/e$ Å^{-3} = -0.475.

CCDC-1027610 and -1027609 contain the supplementary crystallographic data for this chapter. These data can be obtained free of charge from the The Cambridge Crystallographic Data Centre via www.ccdc.cam.ac.uk/data_request/cif.

4, 4'-Dicarboxylic acid-2,2'-bipyridine Synthesis of the dcbpy ligand was carried out following the procedure in the literature.[61] 4,4'-Dimethyl-2,2'-bipyridyl (1.0g, 5.4mmol) was added to concentrated sulphuric acid (25ml) and heated to 70-80 °C. Potassium dichromate (4.8g, 0.47mol) was added slowly with constant stirring at 70-80 °C. The resultant deep green mixture was poured over 200 ml of ice/distilled water, affording a light yellow precipitate that was collected by filtration and washed with water. The solid was then refluxed in 50% HNO_3 (30ml) for 4 hours at 120 °C. The solution was allowed to cool and poured over ice and diluted with distilled water. A white powder was collected by filtration and washed with water followed by acetone and finally diethyl ether, yielding 0.84g (64%). ^{1}H NMR (400 MHz, DMSO-d_6): 8.95 (d, J=5.0Hz, 2H), 8.85 (s, 2H), 7.95 (d, J=5.0Hz, 2H). Anal. Calc. for $C_{12}H_8N_2O_4$: C 59.02, H 3.30, N 11.47. Found: C 58.90, H 3.35, N 11.36%.

Bis(2-methylpropyl)-2,2'-bipyridine-4,4'-dicarboxylate (^{i}Bu$_2$dcbpy) ^{i}Bu$_2$dcbpy was synthesized according to an adaptation of literature procedures. [44] 2,2'-Bipyridine-4,4'-dicarboxylic acid (0.5g, 2.05mmol) was suspended in isobutyl alcohol (50ml) followed by concentrated sulfuric acid (1ml). The mixture was refluxed for 6 hours, during which time the solution became clear. Then the solution was cooled down to room temperature and the solvent was removed under vacuum to give a pink liquid. Distilled water (30ml) was added giving an immediate precipitate. Saturated aqueous Na_2CO_3 was added slowly until a pH of 8~9 was obtained. The precipitate was collected by filtration and washed with water until no trace of the pink colour remained and a beige power was obtained, yielding 0.67g (91%). ^{1}H NMR (400MHz, $CDCl_3$): 8.97(s, 2H), 8.88(d, 2H), 7.92(d, 2H), 4.20(d, 4H), 2.17(sep, 2H), 1.06(d, 12H). ^{1}H NMR (500MHz, [D_6]DMSO): 8.98(dd, 2H), 8.89(dd, 2H), 7.93(dd, 2H), 4.21(d, 4H), 2.17(sep, 2H), 1.08(d, 12H). MS EI (m/z): $[M]^+$ 356. Anal. Calc. for $C_{20}H_{24}N_2O_4$: C 67.40, H 6.79, N 7.86. Found: C 67.22, H 6.91, N 8.03%.

2-Phenylazopyridine 2-Phenylazopyridine was synthesized according to an adaptation of literature procedures.[24, 25]2-Aminopyridine (0.47g, 5mmol) was dissolved in 5ml benzene. The solution was heated at 80℃ for 10 min, and then 25M NaOH (6 ml) was added dropwise into the solution. Nitrosobenzene (0.54g, 5mmol) was added slowly to the warm solution mixture during which, the temperature was kept constant at 80℃ and the solution mixture continuously stirred. After this, more benzene (5ml) was added and the solution was refluxed for 1h. The mixture was filtered and the two layers were separated. The aqueous layer was then extracted by 3x25 ml toluene. The solution was concentrated and purified by silica gel column chromatography. The reddish-orange band was eluted by hexane/ethylacetate (9:1, 8:2 and 7:3). An oil was obtained after removal of solvent under vacuum. The oil was dissolved in hot petroleum ether (40-60℃) and decanted to leave a brown residue. The solution was cooled in dry ice overnight to give orange-red crystals in 0.38g (41%) yield. ^{1}H NMR (500MHz, $CDCl_3$): 8.78(d, 1H), 8.09(d, 2H), 7.95(t, 1H), 7.87(d, 1H), 7.57(t, 1H), 7.56(d, 2H), 7.44(t, 2H). MS EI (m/z): $[M]^+$ 183.1. Anal. Calc. for $C_{11}H_9N_3$: C 72.11, H 4.95, N 22.94. Found: C 72.27, H 4.93, N 22.85.

2-[4-(N,N-dimethylamino)benzeneazo]imidazole (pai) 2-Aminoimidazole suflate (0.54g, 2.5mmol) was dissolved in 8ml 33% HNO_3. The solution of $NaNO_2$ (0.35g, 5mmol) in 2ml H_2O was dropped in in salt/ice bath. The resultant solution was run slowly into a well-stirred solution of N,N-dimethylaniline (6.05g, 50mmol) in 25ml H_2O, previously cooled to 2^0C. Then the solution was alkalized with concentrated aqueous ammonia, during which time, bright red precipitates came out. The mess was extracted with diethyl ether and recrystallized from ethanol to give a red crystal (0.56g, 52.1%).[62] ^{1}H NMR (500MHz, MeOD): 7.87(d, J=9.1Hz, 2H), 7.19(s, 2H), 6.84(d, J=9.1Hz, 2H), 3.13(s, 6H). MS EI (m/z): $[M]^+$ calcd for $C_{11}H_{13}N_5$: 215.1; found: 215.1. Anal. Calc. for $C_{11}H_{13}N_5$: C 61.38, H 6.09, N 32.54. Found: C 61.15, H 6.24, N 32.66%.

1-Methyl-2-[4-(N,N-dimethylamino)benzeneazo]imidazole (pai-Me) To a dry THF solution (50ml) of 2-[4-(N,N-dimethylamino)benzeneazo]imidazole (0.21g, 1mmol) was added NaH (0.06g, 2.5mmol). The mixture was stirred in ice bath for 1h. Methyl iodide (0.15g, 1.04mmol) was dissolved in dry THF (20ml) and dropped slowly through a pressure equalizing system for over 1h. The ice bath was then removed and the mixture continued stirring in room temperature for 4h. The excess NaH was destroyed by adding some water and the solvent was removed under vacuum. The residue was extracted with choloroform and washed with 10% NaOH three times followed by water 3 times. The chloroform extract was purified silica gel column chromatography eluting with acetonitrile/toluene (1:3). On slow evaporation in air, a reddish-orange crystal was obtained (0.17g, 73.4%). ^{1}H NMR (500MHz, $CDCl_3$): 7.97(d, J=9.1Hz, 2H), 7.20(d, J=1.0Hz, 1H), 7.05 (d, J=1.0Hz, 1H), 6.76(d, J=9.2Hz, 2H), 4.00(s, 3H), 3.12(s, 6H). ^{13}C NMR (500MHz, $CDCl_3$): 153.28, 152.75, 129.48, 125.52, 122.27, 111.44, 40.31, 32.50. MS EI (m/z): $[M]^+$ calcd for $C_{12}H_{15}N_5$: 229.1; found: 215.1. Anal. Calc. for $C_{12}H_{15}N_5$: C 62.86, H 6.59, N 30.54. Found: C 63.00, H 6.50, N 30.41%.

Dichloro(p-cymene)ruthenium(II) dimer Dichloro(p-cymene)ruthenium(II) dimer was synthesized according to a literature.[42] $RuCl_3.xH_2O$ (2.01 g, 9.67 mmol) was dissolved in ethanol (100 ml) and α-phellandrene (10 ml, 61.4 mmol) was added. The mixture was heated at reflux for four hours, and cooled. The solvent was evaporated to half volume and the mixture was refrigerated overnight and filtered yielding an

orange brown solid (2.01g, 67.3%). ^{1}H NMR (500 MHz, $CDCl_3$) δ (ppm): 5.50(d, J=6.1Hz, 2H), 5.36(d, J=6.1Hz, 2H), 2.95(sep, J=6.9Hz, 2H), 2.18(s, 6H), 1.30(d, J=7.0Hz, 12H).

All complexes were synthesised using a similar procedure. Typically, the ruthenium dimer $[Ru(p\text{-cymene})Cl_2]_2$ (1 mol equiv) and azo ligand (2 mol equiv) were dissolved in dry butanol. The solution immediately changed color and was stirred at ambient temperature for 2h. Then $^{i}bu_2dcbpy$ (2 mol equiv) was added and the mixture refluxed under a nitrogen atmosphere in the dark overnight. Excess ammonium thiocyanate (30 mol equiv) was added to the reaction mixture and heated at reflux for 4h. The solution was cooled to room temperature. After filtration, the solvent was removed under vacuum and the residue was stirred in water overnight. The solid was collected by filtration and purified by silica gel column chromatography. Details of the amounts of reactants, volumes of butanol, eluent and nature of the product are described below for the individual reactions.

$Ru(^{i}Bu_2dcbpy)(azpy)(NCS)_2$ (HY-1) $[Ru(p\text{-cymene})Cl_2]_2$ (0.36, 0.58mmol), azpy (0.21g, 1.17mmol), $^{i}bu_2dcbpy$(0.42g, 1.17mmol) in 60ml butanol; methano/dichloromethane (1:25); dark red powder. Yield: 0.21g (24%). ^{1}H NMR (500MHz, $CDCl_3$): 9.33(d, J=5.7Hz, 1H), 9.29(d, J=5.7Hz, 1H), 8.61(s, 1H), 8.59(d, J=8.1Hz, 1H), 8.57(s, 1H), 8.20(t, J=7.7Hz, 1H), 8.08(d, J=6.0Hz, 1H), 7.91(t, J=6.7Hz, 1H), 7.77(d, J=5.8Hz, 1H), 7.26(t, J=7.5Hz, 1H), 7.15(d, J=5.8Hz, 1H), 7.09(t, J=7.7Hz, 2H), 6.78(d, J=8.4Hz, 2H), 4.29(d, 2H), 4.23(d, 2H), 2.21(sep, J=6.3Hz, 1H) , 2.13(sep, J=6.6Hz, 1H) , 1.11(d, J=6.7Hz, 6H) , 1.04(d, J=6.7Hz, 6H). ^{13}C NMR (500MHz, $CDCl_3$): 166.57, 163.22, 162.66, 158.46, 155.90, 155.59, 154.44, 152.02, 151.03, 139.20, 138.57, 138.38, 128.76, 126.04, 125.89, 125.60, 125.17, 121.97, 121.92, 121.18, 72.99, 72.84, 27.87, 27.80, 19.13, 19.08. MS FAB (m/z): $[M]^+$ calcd for $C_{33}H_{33}O_4N_7RuS_2$: 757.10789, found: 757.10779. Anal. Calc. for $C_{33}H_{33}O_4N_7RuS_2$: C 52.37, H 4.39, N 12.95. Found: C 52.42, H 4.32, N 13.01%.

$Ru(^{i}Bu_2dcbpy)(dmazpy)(NCS)_2$ (HY-2) $[Ru(p\text{-cymene})Cl_2]_2$ (0.18g, 0.3mmol), dmazpy (0.14g, 0.6mmol), $^{i}bu_2dcbpy$(0.21g, 0.6mmol) in 40ml butanol; methano/dichloromethane (1:25); dark purple powder. Yield: 0.19g (53%). ^{1}H NMR (500MHz, $CDCl_3$): 9.61(d, J=5.8Hz, 1H), 9.32(d, J=5.7Hz, 1H), 8.67(s, 1H), 8.59(s,

1H), 8.42(d, J=8.1Hz, 1H), 8.21(d, J=5.7Hz, 1H), 8.10(t, J=15.7Hz, 1H), 7.70,7.68(t, 1H; d, 1H), 7.10(d, J=5.9Hz, 1H), 7.03(d, J=9.1Hz, 2H), 6.23(d, J=9.3Hz, 2H), 4.32(d, J=6.9Hz, 2H), 4.20(d, J=6.9Hz, 2H) 2.98(s, 6H), 2.23(sep, J=6.6Hz, 1H) , 2.11(sep, J=6.6Hz, 1H) , 1.13(d, J=6.7Hz, 6H) , 1.03(d, J=6.7Hz, 6H). ^{13}C NMR (500MHz, $CDCl_3$): 166.41, 163.64, 163.01, 158.75, 156.52, 154.64, 152.41, 151.91, 151.04, 147.45, 139.54, 138.03, 137.99, 137.91, 136.91, 125.76, 125.19, 124.88, 124.14, 124.08, 121.92, 121.82, 110.58, 72.75, 40.23, 27.91, 27.80, 19.18, 19.08. MS FAB (m/z): $[M]^+$ calcd for $C_{33}H_{38}O_4N_8RuS_2$: 800.15009, found: 800.14954. Anal. Calc. for $C_{35}H_{38}O_4N_8RuS_2$: C 52.55, H 4.79, N 14.01. Found: C 52.62, H 4.84, N 13.85%.

[Ru(^{i}Bu$_2$dcbpy)(pai)(NCS)$_2$] $[Ru(p\text{-}cymene)Cl_2]_2$ (0.18g, 0.3mmol), pai (0.13g, 0.6mmol), ^{i}bu$_2$dcbpy(0.21g, 0.6mmol) in 50ml butanol; ethyl acetate/dichloromethane (1:8). A dark red fraction eluted first, followed by a blue-violet fraction and then a red-violet fraction. The solvent was removed from all three fractions. The red fraction was determined to be Ru(^{i}Bu$_2$dcbpy)$_2$(NCS)$_2$ by NMR. The blue-violet fraction yielded 30mg (13%) of β-[Ru(^{i}Bu$_2$dcbpy)(pai)(NCS)$_2$], while the green-violet fraction yielded 40 mg (17%) of α-[Ru(^{i}Bu$_2$dcbpy)(pai)(NCS)$_2$].

α-[Ru(^{i}Bu$_2$dcbpy)(pai)(NCS)$_2$] (HY-3a) ^{1}H NMR (600MHz, $CDCl_3$): 12.04(br, 1H), 9.59(d, J=5.7Hz, 1H), 8.68(s, 1H), 8.60(s, 1H), 8.16(d, J=6.0Hz, 1H), 7.70(d, J=6.0Hz, 1H), 7.64(s, 1H), 7.62(s, 1H), 7.43(d, J=5.9Hz, 1H), 6.90(d, J=9.0Hz, 2H), 6.22(d, J=9.1Hz, 2H), 4.31(m, 2H), 4.19(d, J=6.2Hz, 2H), 2.96(s, 6H), 2.23(m, 1H) , 2.11(m, 1H) , 1.13(d, J=6.7Hz, 6H) , 1.03(d, J=6.7Hz, 6H). MS ESI (m/z): $[M+Na]^+$ calcd for $C_{33}H_{37}O_4N_9RuS_2Na$: 812.13511, found: 812.13560. Anal. Calc. for $C_{33}H_{37}O_4N_9RuS_2$: C 50.24, H 4.73, N 15.98. Found: C 50.34, H 4.72, N 15.87%.

β-[Ru(^{i}Bu$_2$dcbpy)(pai)(NCS)$_2$] (HY-3b) ^{1}H NMR (600MHz, $CDCl_3$): 11.54(br, 1H), 9.67(d, J=5.6Hz, 1H), 8.77 (s, 1H), 8.61(s, 1H), 8.37(d, J=8.6Hz, 2H), 8.14(d, J=3.6Hz, 1H), 7.92(d, J=5.6Hz, 1H), 7.59(d, J=5.6Hz, 1H), 7.02(s, 1H), 6.75(d, J=8.6Hz, 2H), 6.22(s, 1H), 4.32(d, J=6.7Hz, 2H), 4.17(d, J=6.7Hz, 2H), 3.13(s, 6H) 2.23(m, 1H) , 2.09(m, 1H) , 1.12(dd, J=3.7Hz, 2.7Hz, 6H) , 1.01(d, J=6.6Hz, 6H). MS ESI(m/z): $[M+H]^+$ calcd for $C_{33}H_{38}O_4N_9RuS_2$: 790.15317, found: 790.15270.

Anal. Calc. for $C_{33}H_{37}O_4N_9RuS_2$: C 50.24, H 4.73, N 15.98. Found: C 50.34, H 4.70, N 15.88%.

Ru(^{i}Bu$_2$dcbpy)(pai-Me)(NCS)$_2$ (HY-4) [Ru(p-cymene)Cl$_2$]$_2$ (0.31g, 0.5mmol), pai-Me (0.23g, 1mmol), ^{i}bu$_2$dcbpy(0.36g, 1mmol) in 50ml butanol; ethyl acetate/dichloromethane (1:8) and ethyl acetate/petroleum ether (3:2); dark green-violet powder. Yield: 63.2mg (8%). ^{1}H NMR (500MHz, $CDCl_3$): 9.53(d, J=5.9Hz, 1H), 8.67(s, 1H), 8.61(s, 1H), 8.12(d, J=6.0Hz, 1H), 7.74(d, J=1.5Hz, 1H), 7.72(d, J=5.9Hz, 1H), 7.55(d, J=1.4Hz, 1H), 7.50(d, J=5.8Hz, 1H), 6.84(d, J=9.2Hz, 2H), 6.24(d, J=9.2Hz, 2H), 4.31(m, 2H), 4.21(m, 5H), 2.95(s, 6H), 2.23(m, 1H) , 2.13(m, 1H) , 1.12(d, J=6.8Hz, 6H) , 1.05(d, J=6.8Hz, 6H). MS ESI(m/z): $[M+Na]^+$ calcd for $C_{34}H_{39}O_4N_9RuS_2Na$: 826.15076, found: 826.14610. Anal. Calc. for $C_{34}H_{39}O_4N_9RuS_2$: C 50.86, H 4.90, N 15.70. Found: C 50.93, H 4.84, N 15.62%.

[Bu$_4$N][Ru(azpy)(dcbpy)(NCS)$_2$] Ru(^{i}Bu$_2$dcbpy)(azpy)(NCS)$_2$ (45mg, 0.06mmol) was dissolved in 1M tetra-n-butylammonium hydroxide solution in methanol (5ml) and stirred at ambient temperature for 20 min. The solvent was then removed under vacuum. The residue was dissolved in water and pH of the solution adjusted to 3.0 using 0.1M nitric acid, at which point precipitation occurred. The solid was separated from the solution by centrifugation and then freeze-dried to give 52.1mg (99%) of the desired compound. ^{1}H NMR (500MHz, MeOD): 9.24(d, J=5.7Hz, 1H), 9.09(d, J=5.7Hz, 1H), 8.87(s, 1H), 8.83(s, 1H), 8.73(d, J=8.3Hz, 1H), 8.36(t, J=7.8Hz, 1H), 8.10(d, J=5.9Hz, 1H), 8.07(t, J=6.7Hz, 1H), 7.83(d, J=5.8Hz, 1H), 7.36(d, J=5.7Hz, 1H), 7.26(t, J=7.1Hz, 1H), 7.15(t, J=8.0Hz, 2H), 6.80(d, J=7.7Hz, 2H), 3.26(t, J=8.1Hz, 13H), 1.68(quin, J=8.7Hz, 12.6H) , 1.43(hex, J=7.6Hz, 12.2H) , 1.04(t, J=7.2Hz, 19.3H). ^{13}C NMR (500MHz, MeOD): 166.92, 166.16, 165.81, 157.87, 156.50, 155.69, 153.07, 152.06, 150.15, 144.18, 141.98, 141.22, 138.87, 136.30, 129.22, 128.39, 126.18, 126.00, 125.81, 125.08, 122.44, 122.31, 120.97, 58.06, 23.40, 19.37, 12.66. MS ESI (m/z): $[M+H^+]$ calcd for $C_{41}H_{53}O_4N_8{}^{102}Ru^{32}S_2$: 887.26692; found: 887.26796. Anal. Calc. for $C_{41}H_{52}O_4N_6RuS_2$: C 55.57, H 5.91, N 12.65. Found: C 55.37, H 5.75, N 12.57%.

[Bu$_4$N][Ru(dmazpy)(dcbpy)(NCS)$_2$] Ru(^{i}Bu$_2$dcbpy)(dmazpy)(NCS)$_2$ (30mg, 0.038mmol) was dissolved in 1M tetra-n-butylammonium hydroxide solution in methanol (6ml) and stirred at ambient temperature for 20 min. The solvent was then

removed under vacuum. The residue was dissolved in water and pH of the solution adjusted to 2.85 using 0.1M nitric acid, at which point precipitation occurred. The solid was separated from the solution by centrifugation and then freeze-dried to give 35mg (98%) of the desired compound. ^{1}H NMR (500MHz, MeOD): 9.40(t, J=5.5Hz, 1H), 9.24(d, J=5.6Hz, 1H), 8.89(d, J=7.0Hz, 1H), 8.82(s, 1H), 8.54(t, J=7.4Hz, 1H), 8.27-8.25(m, 2H), 7.86(m, 1H), 7.74(d, J=6.3Hz, 1H), 7.20(m, 1H), 7.00(d, J=9.2Hz, 1H), 6.95(d, J=8.9Hz, 1H), 6.37(d, J=9.2Hz, 1H), 6.21(d, J=9.2Hz, 1H), 3.26(t, J=8.1Hz, 16.5H), 2.96(s, 3H), 2.72(s, 1.7H), 1.67(quin, J=8.7Hz, 13.9H) , 1.44(hex, J=7.6Hz, 12.9H) , 1.05(t, J=7.2Hz, 27.3H). ^{13}C NMR (500MHz, MeOD): 166.95, 165.81, 158.37, 157.03, 156.99, 153.35, 153.10, 152.51, 151.68, 150.20, 147.63, 147.34, 138.95, 138.19, 135.49, 125.68, 125.59, 124.62, 124.28, 124.20, 123.73, 122.32, 122.25, 110.30, 110.16, 58.12, 38.86, 28.44, 23.41, 19.36, 12.57. MS FAB (m/z): $[M+ Na^{+}- (n\text{-}Bu_4N)]^{-}$ 710.00562. Anal. Calc. for $C_{43}H_{57}O_4N_9RuS_2$: C 55.58, H 6.18, N 13.57. Found: C 55.49, H 6.25, N 13.49%.

α-[Bu$_4$N][Ru(pai)(dcbpy)(NCS)$_2$] α-Ru(^{i}Bu$_2$dcbpy)(pai)(NCS)$_2$ (20mg, 0.03mmol) was dissolved in 1M tetra-n-butylammonium hydroxide solution in methanol (5ml) and stirred at ambient temperature for 20 min. The solvent was then removed under vacuum. The residue was dissolved in water and pH of the solution adjusted to 2.12 using 0.1M nitric acid, at which point precipitation occurred. The solid was separated from the solution by centrifugation and then freeze-dried to give 13.2mg (57%) of the desired compound. ^{1}H NMR (600MHz, MeOD): 9.34(d, J=5.7Hz, 1H), 8.81(s, 1H), 8.77(s, 1H), 8.16(d, J=5.7Hz, 1H), 7.92(d, J=1.4Hz, 1H), 7.75(d, J=5.7Hz, 1H), 7.69(d, J=1.6Hz, 1H), 7.39(d, J=5.8Hz, 1H), 6.82(d, J=9.1Hz, 2H), 6.32(d, J=9.1Hz, 2H), 3.26(t, J=8.1Hz, 12H), 2.91(s, 6H), 1.68(quin, J=8.7Hz, 8.2H) , 1.43(hex, J=7.6Hz, 8.8H) , 1.04(t, J=7.2Hz, 17.3H). MS ESI(m/z): $[M]^{+}$ calcd for $C_{41}H_{56}O_4N_{10}RuS_2$: 918.29709, found: 918.29823. Anal. Calc. for $C_{41}H_{56}O_4N_{10}RuS_2$: C 53.63, H 6.15, N 15.26. Found: C 53.48, H 6.36, N 15.15%.

β-[Bu$_4$N][Ru(pai)(dcbpy)(NCS)$_2$] β-Ru(^{i}Bu$_2$dcbpy)(pai)(NCS)$_2$ (20mg, 0.03mmol) was dissolved in 1M tetra-n-butylammonium hydroxide solution in methanol (5ml) and stirred at ambient temperature for 20 min. The solvent was then removed under vacuum. The residue was dissolved in water and pH of the solution adjusted to 1.44 using 0.1M nitric acid, at which point precipitation occurred. The solid was separated

from the solution by centrifugation and then freeze-dried to give 22.8mg (98%) of the desired compound. ^{1}H NMR (600MHz, MeOD): 9.57(d, J=5.9Hz, 1H), 9.06(s, 1H), 8.88(s, 1H), 8.44(d, J=9.3Hz, 2H), 8.33(d, J=5.7Hz, 1H), 7.91(d, J=5.9Hz, 1H), 7.67(d, J=5.7Hz, 1H), 7.38(d, J=1.6Hz, 1H), 6.93(d, J=9.2Hz, 2H), 6.49(d, J=1.4Hz, 1H), 3.25(t, J=8.1Hz, 19H), 3.20(s, 6H), 1.68(quin, J=8.7Hz, 14.4H) , 1.43(hex, J=7.6Hz, 15.8H) , 1.04(t, J=7.2Hz, 30.1H). MS ESI(m/z): [M- (n-Bu_4N)]$^{-}$ calcd for $C_{25}H_{20}O_4N_9RuS_2$: 676.01286, found: 676.01275. Anal. Calc. for $C_{41}H_{56}O_4N_{10}RuS_2$: C 53.63, H 6.15, N 15.26. Found: C 53.53, H 6.24, N 15.16%.

[Bu_4N][Ru(pai-Me)(dcbpy)(NCS)$_2$] Ru($^{i}Bu_2$dcbpy)(pai-Me)(NCS)$_2$ (30mg, 0.04mmol) was dissolved in 1M tetra-n-butylammonium hydroxide solution in methanol (5ml) and stirred at ambient temperature for 20 min. The solvent was then removed under vacuum. The residue was dissolved in water and pH of the solution adjusted to 2.53 using 0.1M nitric acid, at which point precipitation occurred. The solid was separated from the solution by centrifugation and then freeze-dried to give 21.2mg (61%) of the desired compound. ^{1}H NMR (600MHz, $CDCl_3$): 9.42(d, J=5.9Hz, 1H), 8.91(s, 1H), 8.83(s, 1H), 8.34(d, J=5.9Hz, 1H), 7.91(d, J=1.5Hz, 1H), 7.82(d, J=5.9Hz, 1H), 7.63(d, J=1.4Hz, 1H), 7.55(d, J=5.8Hz, 1H), 7.03(d, J=9.2Hz, 2H), 6.54(d, J=9.2Hz, 2H), 4.41(t, J=3.9Hz, 3H), 3.27(t, J=8.1Hz, 9H), 3.21(s, 6H), 1.72(quin, J=8.7Hz, 10H) , 1.41(hex, J=7.6Hz, 12H) , 1.09(t, J=7.2Hz, 14H). MS ESI(m/z): [M- (n-Bu_4N)]$^{-}$ calcd for $C_{26}H_{22}O_4N_9RuS_2$: 690.02851, found: 690.02932. Anal. Calc. for $C_{42}H_{58}O_4N_{10}RuS_2$: C 54.12, H 6.27, N 15.03. Found: C 53.91, H 5.99, N 14.88%.

Reference

1. Vos, J.G. and J.M. Kelly, *Ruthenium polypyridyl chemistry; from basic research to applications and back again.* Dalton Transactions, 2006(41): p. 4869-4883.
2. Juris, A., et al., *Ru(Ii) Polypyridine Complexes - Photophysics, Photochemistry, Electrochemistry, and Chemi-Luminescence.* Coordination Chemistry Reviews, 1988. **84**: p. 85-277.
3. Willner, I., et al., *Photoinduced electron transfer in supramolecular assemblies of transition metal complexes.* Coordination Chemistry Reviews, 1998. **171**: p. 261-285.
4. Burstall, F.H., *Optical activity dependent on co-ordinated bivalent ruthenium.* Journal of the Chemical Society, 1936: p. 173-175.
5. Paris, J.P. and W.W. Brandt, *Charge Transfer Luminescence of a Ruthenium(Ii) Chelate.* Journal of the American Chemical Society, 1959. **81**(18): p. 5001-5002.
6. Gersten, S.W., G.J. Samuels, and T.J. Meyer, *Catalytic-Oxidation of Water by an Oxo-Bridged Ruthenium Dimer.* Journal of the American Chemical Society, 1982. **104**(14): p. 4029-4030.
7. Sahraoui, B., et al., *Nonlinear optics and surface relief gratings in alkynyl-ruthenium complexes.* Journal of Optics a-Pure and Applied Optics, 2009. **11**(2): p. 024005.
8. Oszajca, M.F., et al., *Photocurrent Switching Effects in TiO2 Modified with Ruthenium Polypyridine Complexes.* Journal of Physical Chemistry C, 2011. **115**(24): p. 12187-12195.
9. Kwolek, P., M. Oszajca, and K. Szacilowski, *Catecholate and 2,3-acenediolate complexes of d(0) ions as prospective materials for molecular electronics and spintronics.* Coordination Chemistry Reviews, 2012. **256**(15-16): p. 1706-1731.
10. Gill, M.R. and J.A. Thomas, *Ruthenium(II) polypyridyl complexes and DNA-from structural probes to cellular imaging and therapeutics.* Chemical Society Reviews, 2012. **41**(8): p. 3179-3192.
11. Hagfeldt, A., et al., *Dye-Sensitized Solar Cells.* Chemical Reviews, 2010. **110**(11): p. 6595-6663.
12. Gratzel, M., *Photoelectrochemical cells.* Nature, 2001. **414**(6861): p. 338-344.
13. Krause, R.A. and K. Krause, *Chemistry of Bipyridyl-Like Ligands - Isomeric Complexes of Ruthenium(Ii) with 2-(Phenylazo)Pyridine.* Inorganic Chemistry, 1980. **19**(9): p. 2600-2603.
14. Velders, A.H., et al., *Dichlorobis(2-phenylazopyridine)ruthenium(II) complexes: characterisation, spectroscopic and structural properties of four isomers.* Dalton Transactions, 2004(3): p. 448-455.
15. Misra, T.K., et al., *Chemistry of azoimidazoles: Synthesis, spectral characterization, electrochemical studies, and X-ray crystal structures of isomeric dichloro bis[1-alkyl-2-(arylazo)imidazole] complexes of ruthenium(II).* Inorganic Chemistry, 1998. **37**(8): p. 1672-1678.

16. Santra, P.K., et al., *Chemistry of azopyrimidines. Part II. Synthesis, spectra, electrochemistry and X-ray crystal structures of isomeric dichloro bis[2-(arylazo)pyrimidine] complexes of ruthenium(II).* Polyhedron, 1999. **18**(22): p. 2869-2878.
17. Byabartta, P., *Ruthenium azo complexes: Synthesis, spectra, and electrochemistry of dithiocyanato-bis{1-(alkyl)-2-(arylazo)imidazole}ruthenium(II).* Russian Journal of Coordination Chemistry, 2009. **35**(9): p. 687-691.
18. Mondal, B., M.G. Walawalkar, and G.K. Lahiri, *Ruthenium terpyridine complexes incorporating azo-imine based ancillary ligands. Synthesis, crystal structure, spectroelectrochemical properties and solution reactivities.* Journal of the Chemical Society-Dalton Transactions, 2000(22): p. 4209-4217.
19. Das, A., et al., *Application of a Structure/Oxidation-State Correlation to Complexes of Bridging Azo Ligands.* Chemistry-a European Journal, 2012. **18**(35): p. 11007-11018.
20. Das, C., et al., *Ruthenium complexes of 2-[(4-(arylamino)phenyl)azo]pyridine formed via regioselective phenyl ring amination of coordinated 2-(phenylazo)pyridine: Isolation of products, X-ray structure, and redox and optical properties.* Inorganic Chemistry, 2003. **42**(1): p. 198-204.
21. Al-Noaimi, M.Z., et al., *Syntheses, crystallography and spectroelectrochemical studies of ruthenium azomethine complexes.* Polyhedron, 2007. **26**(14): p. 3675-3685.
22. Pal, S., et al., *Ruthenium(II) complexes of alpha-diimines: synthesis, spectral characterisation, electrochemical properties and single-crystal X-ray structure of bis(2,2'-bipyridine){1-benzyl-2-(p-tollylazo)imidazole}-ruthenium(II) perchlorate.* Polyhedron, 2000. **19**(16-17): p. 1925-1933.
23. Velders, A.H., et al., *Strong differences in the in vitro cytotoxicity of three isomeric dichlorobis(2-phenylazopyridine)ruthenium(II) complexes.* Inorganic Chemistry, 2000. **39**(14): p. 2966-2967.
24. Hotze, A.C.G., et al., *Coordination of 9-ethylguanine to the mixed-ligand compound alpha-[Ru(azpy)(bpy)Cl-2] (azpy=2-phenylazopyridine and bpy=2,2'-bipyridine). An unprecedented ligand positional shift, correlated to the cytotoxicity of this type of [RuL2Cl2] (with L = azpy or bpy) complex.* Inorganic Chemistry, 2004. **43**(16): p. 4935-4943.
25. Dougan, S.J., et al., *Phenylazo-pyridine and phenylazo-pyrazole chlorido ruthenium(II) arene complexes: Arene loss, aquation, and cancer cell cytotoxicity.* Inorganic Chemistry, 2006. **45**(26): p. 10882-10894.
26. Nazeeruddin, M.K., et al., *Stepwise assembly of amphiphilic ruthenium sensitizers and their applications in dye-sensitized solar cell.* Coordination Chemistry Reviews, 2004. **248**(13-14): p. 1317-1328.
27. Rawling, T., et al., *Ruthenium Phthalocyanine-Bipyridyl Dyads as Sensitizers for Dye-Sensitized Solar Cells: Dye Coverage versus Molecular Efficiency.* Inorganic Chemistry, 2009. **48**(7): p. 3215-3227.
28. Armarego, W.L.F. and C.L.L. chai, eds. *Purification of laboratory chemicals*. 5 ed. 2003, Elsevier. 609.

29. Byabartta, P., et al., *Heteroleptic tris-chelates of ruthenium(II)-bipyridine-arylazo-imidazoles: Synthesis, spectral characterisation and electrochemical properties. Single crystal X-ray structure of [(2,2 '-bipyridine)-bis{1-methyl-2-(p-tolylazo)imidazole}ruthenium(II)] perchlorate.* Journal of the Chemical Society-Dalton Transactions, 2001(19): p. 2825-2832.
30. Yoopensuk, S., et al., *Photoactive azoimine dyes: 4-(2-Pyridylazo)-N,N-diethylaniline and 4-(2-pyridylazo)-N,N-dimethylaniline: Computational and experimental investigation.* Spectrochimica Acta Part a-Molecular and Biomolecular Spectroscopy, 2012. **86**: p. 538-546.
31. Rau, H., *Spectroscopic Properties of Organic Azo-Compounds.* Angewandte Chemie-International Edition in English, 1973. **12**(3): p. 224-235.
32. Santos, F.D., et al., *Evidence for excited state intramolecular charge transfer in benzazole-based pseudo-stilbenes.* Physical Chemistry Chemical Physics, 2012. **14**(31): p. 10994-11001.
33. Kim, H.B., N. Kitamura, and S. Tazuke, *Excited-State Relaxation of Ru(Bpy)3-2+ at Low-Temperature - Time Evolution of the Emission Quantum Yield.* Chemical Physics Letters, 1988. **143**(1): p. 77-80.
34. Timpson, C.J., et al., *Influence of solvent on the spectroscopic properties of cyano complexes of ruthenium(II).* Journal of Physical Chemistry, 1996. **100**(8): p. 2915-2925.
35. Kosower, E.M., *The Effect of Solvent on Spectra .1. A New Empirical Measure of Solvent Polarity - Z-Values.* Journal of the American Chemical Society, 1958. **80**(13): p. 3253-3260.
36. Nazeeruddin, M.K., et al., *Engineering of efficient panchromatic sensitizers for nanocrystalline TiO2-based solar cells.* Journal of the American Chemical Society, 2001. **123**(8): p. 1613-1624.
37. Indelli, M.T., et al., *Design of long-lived Ru(II) terpyridine MLCT states. Tricyano terpyridine complexes.* Inorganic Chemistry, 1998. **37**(23): p. 6084-6089.
38. Daeneke, T., et al., *High-efficiency dye-sensitized solar cells with ferrocene-based electrolytes.* Nature Chemistry, 2011. **3**(3): p. 211-215.
39. Constable, E.C. and P.J. Steel, *N,N'-Chelating Biheteroaromatic Ligands - a Survey.* Coordination Chemistry Reviews, 1989. **93**(2): p. 205-223.
40. Lakowicz, J.R., *Principles of fluorescence spectroscopy*. 2006, Springer: New York.
41. Kumar, K.N., R. Ramesh, and Y. Liu, *Synthesis and structure of cycloruthenated carbonyl complexes and their emission, redox and biological properties.* Journal of Inorganic Biochemistry, 2006. **100**(1): p. 18-26.
42. Bennett, M.A., et al., *(Eta-6-Hexamethylbenzene)Ruthenium Complexes.* Inorganic Syntheses, 1982. **21**: p. 74-78.
43. Donnici, C.L., et al., *Synthesis of the Novel 4,4 '- and 6,6 '-dihydroxamic 2,2 '-bipyridines and improved routes to 4,4 '- and 6,6 '- substituted 2,2 '-bipyridines and mono-N-opxide-2,2 '-bipyridine.* Journal of the Brazilian Chemical Society, 1998. **9**(5): p. 455-460.

44. Rawling, T., F. Buchholz, and A.M. McDonagh, *Convenient synthesis and purification of [Bu(4)N](2)[Ru(4-carboxy-4-carboxylate-2,2'-bipyridine)(2)(NCS)(2)]: a landmark DSC dye.* Australian Journal of Chemistry, 2008. **61**(6): p. 405-408.
45. Salwinska, E. and J. Suwinske, *Synthesis of 4,5-dialkyl-2,2'-azoimidazoles.* Polish Journal of Chemistry, 1983. **57**: p. 547-549.
46. *Avogadro 1.1.0*. Available from: http://sourceforge.net/projects/avogadro/.
47. Hanwell, M.D., et al., *Avogadro: an advanced semantic chemical editor, visualization, and analysis platform.* Journal of Cheminformatics, 2012. **4**.
48. Gaussian 09, R.A., et al.
49. Perdew, J.P., et al., *Atoms, Molecules, Solids, and Surfaces - Applications of the Generalized Gradient Approximation for Exchange and Correlation (Vol 46, Pg 6671, 1992).* Physical Review B, 1993. **48**(7): p. 4978-4978.
50. Perdew, J.P., K. Burke, and Y. Wang, *Generalized gradient approximation for the exchange-correlation hole of a many-electron system.* Physical Review B, 1996. **54**(23): p. 16533-16539.
51. Hay, P.J. and W.R. Wadt, *Abinitio Effective Core Potentials for Molecular Calculations - Potentials for K to Au Including the Outermost Core Orbitals.* Journal of Chemical Physics, 1985. **82**(1): p. 299-310.
52. Hay, P.J. and W.R. Wadt, *Abinitio Effective Core Potentials for Molecular Calculations - Potentials for the Transition-Metal Atoms Sc to Hg.* Journal of Chemical Physics, 1985. **82**(1): p. 270-283.
53. Wadt, W.R. and P.J. Hay, *Abinitio Effective Core Potentials for Molecular Calculations - Potentials for Main Group Elements Na to Bi.* Journal of Chemical Physics, 1985. **82**(1): p. 284-298.
54. Bauernschmitt, R. and R. Ahlrichs, *Treatment of electronic excitations within the adiabatic approximation of time dependent density functional theory.* Chemical Physics Letters, 1996. **256**(4-5): p. 454-464.
55. Tozer, D.J. and N.C. Handy, *Improving virtual Kohn-Sham orbitals and eigenvalues: Application to excitation energies and static polarizabilities.* Journal of Chemical Physics, 1998. **109**(23): p. 10180-10189.
56. Vlcek, A. and S. Zalis, *Modeling of charge-transfer transitions and excited states in d(6) transition metal complexes by DFT techniques.* Coordination Chemistry Reviews, 2007. **251**(3-4): p. 258-287.
57. O'Boyle, N.M., A.L. Tenderholt, and K.M. Langner, *cclib: A library for package-independent computational chemistry algorithms.* Journal of Computational Chemistry, 2008. **29**(5): p. 839-845.
58. *CrysAlisPRO*. 2013, Oxford Diffraction / Agilent Technologies UK Ltd, Yarnton, England.
59. Sheldrick, G.M., *A short history of SHELX.* Acta Crystallographica Section A, 2008. **64**: p. 112-122.
60. Macrae, C.F., et al., *Mercury: visualization and analysis of crystal structures.* Journal of Applied Crystallography, 2006. **39**: p. 453-457.
61. Donnici, C.L., et al., *Synthesis of the novel 4,4'- and 6,6'-dihydroxamic-2,2'-bipyridines and improved routes to 4,4'- and 6,6'-substituted 2,2'-bipyridines*

and mono-N-oxide-2,2'-bipyridine. Journal of the Brazilian Chemical Society, 1998. **9**(5): p. 455-460.
62. Salwinska, E. and J. Suwinski, *Synthesis of 4,5-dialkyl-2,2'-azoimidazoles.* Polish Journal of Chemistry, 1983. **57**(4-5-6): p. 547-9.

Chapter 6 Conclusion

Series of 'donor-free' dyes including oligo(3-hexylthiophene) (oligo-3HT) (Chapter 3) and oligo(4,4-dihexyl-4H-cyclopenta[1,2-b:5,4-b']dithiophene) (oligo-CPDTs) (Chapter 4) functionalized with cyanoacrylic end groups were prepared. These dyes do not follow the overwhelming trend of designing organic sensitisers for dye-sensitised solar cells, namely, 'donor-π-acceptor' structure. The novel dyes can be synthesized easily using stille coupling. They were fully characterised through electrochemical, spectroscopic and computational techniques, showing versatile colour-tuning, as well as outstanding absorption properties.

Liquid DSSC devices using oligo-3HT (5T and 6T) as sensitiser and I^-/I_3^- redox couple as electrolyte were fabricated, with power conversion efficiency of 7.64% and 7.07%, respectively. 6T showed a significantly higher V_{OC} than 5T but lower J_{SC} and FF. By using electrochemical impedance spectroscopy (EIS), it was found that 6T has more trapping states, attributed to the extra conjugation or different position of alkyl chain of 6T.

Oligo-CPDTs were used as effective sensitisers for liquid-state dye-sensitised solar cells with I^-/I_3^- redox couple, Co^{2+}/Co^{3+} redox couple and solid-state dye-sensitised solar cells. The J_{SC}, V_{OC} and power conversion increases upon addition of CPDT unit in all types of DSSCs. As a result, CPDT-3 shows the highest efficiency among this series (6.7% for I^-/I_3^- based cells, 7.3% for Co^{2+}/Co^{3+} based cells and 3.9% for solid-state cells). In solid-state dye-sensitised solar cells, CPDT-3 shows superb J_{SC} (10.9 mA cm^{-2}) with only 900 nm mesoporous TiO_2 film due to broad absorption over the solar spectrum and outstanding absorption coefficient up to 75000 $M^{-1}cm^{-1}$. However, comparing with the oligo(3-hexylthiophene) dye (5T), CPDT dyes suffer from a low V_{OC}. By using charge extraction experiments, IMVS and IMPS, it was found upon replacing the thiophene unit with CPDT unit in donor-free dyes, the charge recombination across the TiO_2-dye-electrolyte interface enhanced significantly. We attribute this to a more planar conformation of CPDT-3 and/or less regeneration driving force compared with 5T.

A series of novel Ru(II) complexes with bis(2-methylpropyl)-2,2'-bipyridine-4,4'-

dicarboxylate ($^{i}bu_2dcbpy$) as one chromophore and phenylazopyridine derivatives (azpy and dmazpy) or [4-(N,N-dimethylamino)benzeneazo]imidazole derivatives (pai and pai-Me) as an additional chromophore and thiocyanate as ligand have been synthesized (HY-1~HY-4). These dyes were prepared using a protection/deprotection strategy that allows for convenient purification. These dyes are all intensely colored in the visible region, showing an enhanced light harvesting compared to the N719 dye that lacks the azo ligand. Electrochemical study also showed properties suitable for application as sensitisers in DSSCs. Following hydrolysis, the complexes were investigated in DSSCs, with performance investigated using I-V measurements. Poor performance was observed and we attribute this as mostly likely due to poor charge injection due to short excited-state lifetime.

In conclusion, novel 'donor-free' oligomers and ruthenium complexes have been designed to absorb in both visible and near-IR region with high extinction coefficient. They were synthesized easily and studied as sensitisers for both liquid state and solid state dye-sensitised solar cells in this thesis. The knowledge gained in this study can be helpful for future sensitisers design.